UTS UNIVERSITY OF TECHNOLOGY SYDNEY

Neural cell responses to wear debris from spinal instrumentation and devices

by David Jiawei Wen

Thesis submitted in fulfilment of the requirements for the degree of

Doctor of Philosophy

under the supervision of Prof. Joanne Tipper, Dr. Javad Tavakoli, Dr. Carmine Gentile

University of Technology Sydney
Faculty of Engineering and Information Technology

August 2024

Certificate of Original Authorship

I, David Jiawei Wen, declare that this thesis is submitted in fulfilment of the requirements for the award of Doctor of Philosophy, in the School of Biomedical Engineering/ Faculty of Engineering and Information Technology at the University of Technology Sydney.

This thesis is wholly my own work unless otherwise referenced or acknowledged. In addition, I certify that all information sources and literature used are indicated in the thesis.

This document has not been submitted for qualifications at any other academic institution.

This research is supported by the Australian Government Research Training Program.

Signature: Production Note:
Signature removed prior to publication.

Date: 21/08/2024

Acknowledgements

Firstly, I would like to sincerely acknowledge my main PhD supervisor, Prof. Joanne Tipper for giving me an opportunity to work with her and providing me guidance and encouragement throughout my PhD candidature. I would also like to thank my PhD co-supervisors, Dr. Javad Tavakoli and Dr. Carmine Gentile for their support and motivation throughout my PhD candidature. Specifically, the knowledge and insights I gained from Prof. Joanne Tipper in the field of joint arthroplasty and wear debris has been enormous. Additionally, the information I learnt and practical skills I developed in 3D bioprinting from Dr. Carmine Gentile has been very helpful for me in the laboratory. Also, I would like to give a special thanks to my colleague, Aswini Madhavan, who continually supported me during my PhD candidate, especially in laboratory work and also providing new insights and information about our research field. I am grateful for the financial support provided by University of Technology Sydney, Faculty of Engineering and IT and also thank the School of Biomedical Engineering for providing great support to PhD students as well as providing the necessary facilities to conduct PhD research. I would also like to thank my PhD colleagues and academics for their support and help in the BMT, Science and MAU laboratories.

I would also like to express my deepest gratitude to my closest friends and family for their support over the past few years. In particular, I would like to thank Tony and Haimin for their support and motivation. Having them around during my during my PhD years, made my life a lot more fun and interesting. Also, I would like to deeply thank Helen, who has given me great motivation and care during my PhD. I cannot express how much excitement and joy you have brought to my life. Your kind and vibrant soul has made my PhD journey a lot more enjoyable and less stressful.

Finally, my family has been the biggest support during my PhD years. I would not have completed my PhD without their unconditional love and support. I would like to thank my father, Prof. Li Ming Wen for sharing your expertise in the research field and giving me extra motivation when I needed it. I also would like to thank my mother, Jo Hua Liang and brother, Henry Wen for their care and keeping me sane during my PhD. Without them, I would not be where I am today.

Format of Thesis

This is a conventional thesis consisting of 7 chapters. The overall aim was to investigate the neural cell responses to model particles in a novel *in vitro* 3D bioprinted hydrogel model. The summary of chapters are as follows:

- Chapter 1 consists of an introduction, including background research, impact of COVID-19, aims, objects and significance.

- Chapter 2 consists of a narrative literature review of the research field my PhD project is based on.

- Chapter 3 consists of the general materials and methods used in this research.

- Chapter 4 investigates the clinical performance of lumbar total disc replacements on treating patients with degenerative disc disease. This chapter was conducted in response to the limited access to practical facilities during the NSW lockdowns implemented during the COVID-19 pandemic.

- Chapter 5 summaries the sizes and morphologies of model particles, as well as the development of the novel *in vitro* 3D bioprinted hydrogel model.

- Chapter 6 investigates the neural cell responses to model particles by conducting experiments on cell viability, oxidative stress and DNA damage.

- Chapter 7 summaries the outcomes of the PhD, including a discussion of results in this work with previous studies, and also provides insights into the future direction of this work.

List of Publications and Conference Presentations

Publication

- D. J. Wen, J. Tavakoli, and J. L. Tipper, "Lumbar Total Disc Replacements for Degenerative Disc Disease: A Systematic Review of Outcomes With a Minimum of 5 years Follow-Up," (in eng), *Global Spine J,* p. 21925682241228756, Jan 23 2024.

Conference Presentations

- Lumbar Total Disc Replacements for Degenerative Disc Disease: A Systematic Review of Outcomes With a Minimum of 5 years Follow-Up. Spineweek conference, Melbourne, Australia, May, 2023 (Oral presentation)

- Development of a 3D Bioprinted Model to Investigate Neural Cell Responses to Wear Debris from Spinal Instrumentation and Devices. Australian & New Zealand Research Society conference, Auckland, New Zealand, December 2023 (Poster presentation)

List of Abbreviations

2D……...Two-Dimensional

3D……Three-Dimensional

ATP……...Adenosine Triphosphate

CNS……...Central Nervous System

CoCr……....Cobalt Chrome

CoCrMo……Cobalt Chrome Molybdenum

DDD……..Degenerative Disc Disease

DMEM……...Dulbecco's Modified Eagle Medium

DMSO……..Dimethyl Sulfoxide

DNA……...Deoxyribonucleic Acid

ELISA……Enzyme Linked Immunosorbent Assay

FBS……Foetal Bovine Serum

GelMA……..Gelatin Methacryloyl

H_2O_2……Hydrogen Peroxide

KPa……Kilopascal

KV……..Kilovolt

LDPE……Low Density Polyethylene

MOM……Metal-On-Metal

MOP……..Metal-On-Polymer

MTT…….3-(4,5-dimethylthiazol-2-yl)-2,5-diphenyltetrazolium bromide

ODI……Oswestry Disability Index

PBS……...Phosphate Buffered Saline

PEEK……Polyetheretherketone

ROS……Reactive Oxygen Species

SEM……Scanning Electron Microscopy

TDR……...Total Disc Replacement

UHMWPE…….Ultra Heigh Molecular Weight Polyethylene

VAS……Visual Analog Scale

v/v……Volume per Volume

w/v……...Weight per Volume

ZTA……..Zirconia Toughened Alumina

Table of Contents

List of Figures

List of Tables

Abstract

Back pain is now the leading cause of disability worldwide and affects approximately 619 million people globally. The prevalence of spinal surgery involving the implantation of spinal implants and/or instrumentation continues to increase due to advancements in medical technologies and increased incidence of spine-related degenerative conditions. Despite the successes and increased use of spinal surgery for patients with back pain, the longevity of spinal implants may be compromised by issues including mechanical challenges and biological factors. One of the mechanical problems causing spinal implant failures is the generation of wear debris resulting in adverse biological responses including inflammation and osteolysis. In addition, the proximity of neural tissues and cells of the central nervous system poses a challenge as the tissues and cells may be damaged if exposed to wear debris. By understanding how neural cells respond to wear debris from spinal devices, researchers and clinicians can improve outcomes of spinal surgeries and support the development of more spinal implants that improve patient quality of life.

Most of the knowledge currently known regarding the biological responses of neural cells to wear debris has been studied within a 2D environment, which has the limitation of not being representative of the *in vivo* environment. As a result, 3D *in vitro* models have emerged as an alternative to study cell responses. The aim of this study was to use a novel 3D bioprinted *in vitro* model to examine biological responses of model wear particles representative of wear debris from spinal implants on neural cells including NG108-15 neuronal and C6 astrocyte-like cells.

For proof of concept, the 3D model was developed using extrusion-based bioprinting of Gelatin Methacryloyl (GelMA) at 5% (w/v) embedded with NG108-15 neuronal cells and C6 astrocyte-like cells combined with model wear particles including metals, polymers and ceramics. The size and morphology of these particles were characterised using scanning electron microscopy and Image J. The biological responses of neural cells to model wear particles were investigated using cell viability, reactive oxygen species production, and DNA damage assays.

The proof of concept of 3D bioprinting GelMA hydrogels embedded with neural cells and model wear particles was successful, as neural cell survival was observed over 5 days. The sizes of the model particles for polymers, ceramics and metals used in the investigation of neural cell response to wear particles ranged from 0.1 – 0.8 μm. The results from the assays demonstrated that there was no significant reduction in cell viability of C6 astrocyte-like cells when exposed to either polymer, ceramic or metal model particles dosed at 100 μm^3, 50 μm^3 and 50 μm^3 per cell, respectively. However, a significant reduction in cell viability of NG108-15 neuronal cells was observed when exposed to metallic model particles, dosed at 50 μm^3 per cell over a duration of 5 days. In addition, there was no significant increase in reactive oxygen species production and no significant DNA damage in either cell type when exposed to either polymer, ceramic or metal model particles dosed at 100 μm^3, 50 μm^3 and 50 μm^3 per cell, respectively. In summary, our novel 3D bioprinted model was successful in establishing a 3D environment to examine the interaction of neural cells and model wear particles. In addition, this study demonstrated that the model wear particles did not have adverse biological effects on neural cells.

Chapter 1

Introduction

1.1 Introduction

In the past 20 years, the incidence of spinal surgery has increased substantially in numerous Western countries [1]. Globally, low back pain is now the main cause of disability and has seen a 54% increase in disability-adjusted-life years between 1990 and 2015 [1, 2]. The use of spinal implants in spinal fusion and total disc replacements have continued to increase. Although the successes and advantages of spinal surgery are recognised, obstacles remain for the use of spinal devices [3]. One of the main challenges is the increase in patient demand, due to the media publicity provided for advancements in spinal surgery [4]. Another challenge is the problems with spinal revision surgery, due to post-operative complications [5], which suggests the need for long-term success of spinal devices. Additionally, the failure of spinal instrumentation and devices may lead to harmful effects on surrounding neural tissues.

The biological impact of wear particles from spinal implants have not been studied widely compared to other orthopaedic implants, including the knee and hip. However, comparisons of the effects of spinal implant wear debris with knee and hip implants are important and justified due to common biomechanical principles and material considerations. Important biomechanical goals among all orthopaedic implants include mechanical load bearing and osseointegration, which refers to the ability of the implant to integrate with surrounding bone tissue. In addition, essential material considerations for orthopaedic implants include the biocompatibility, strength and corrosion resistance of a biomaterial. The interfaces of in spinal devices, including the bearing surfaces, and endplate/bone interface may generate wear debris, which have the potential to induce adverse biological responses. The detrimental effects from wear debris may lead to implant failure and ultimately revision surgery. Wear particles have been observed to be associated with the inflammatory response in periprosthetic tissue of total disc replacements from long-term follow-up studies [6]. The presence of polyethylene wear particles produced from metal-on-polyethylene devices can ultimately lead to osteolysis

and aseptic loosening of the implant. The polyethylene wear particles generated in total disc replacements and the periprosthetic inflammatory reactions are comparable to those observed in total hip and total knee replacements [7].

Furthermore, metallosis has been reported in metallic spinal instrumentation and metal-on-metal artificial disc arthroplasty [8, 9]. Previous case studies have demonstrated an association between metal wear particles produced from spinal fusion instrumentation and inflammatory reactions [9, 10]. In addition, pseudotumours have been reported in patients with metal-on-metal disc replacements [11]. Recently, clinically-relevant metal wear particles, produced via a wear simulator, have been demonstrated to cause DNA damage in glial cells and astrocytes *in vitro* [12]. Furthermore, Co-Cr wear particles have also been shown to decrease cell viability in glial cells *in vitro* [12].

In a previous animal model, titanium particles were reported to have the capacity of cross the blood-spinal cord barrier [13]. Additionally, nanoparticles have the ability to cross the Blood-Brain-Barrier (BBB) [14]. Thus, these findings suggest the potential for nano-sized wear particles to access neural tissues. Due to issues arising from wear debris of spinal instrumentation and implants, and the potential of wear particles causing detrimental effects on neural tissue, there is a need to investigate how neural cells are affected when exposed to wear particles. In addition, the effects of wear debris produced from spinal implants has been studied relatively rarely compared to wear debris generated from hip and knee total joint replacements.

Most of the knowledge on the biological responses of neural cells to wear particles has been studied with in a 2D monolayer environment, which has the limitation of not being representative of the *in vivo* environment. As a result, 3D *in vitro* models have emerged as an alternative to study cell responses. Recently, collagen hydrogels have been used to model a 3D cell culture environment using the gel casting method to study neural cell responses to clinically relevant metallic wear particles in a study conducted by Lee *et al* [12]. However, there are some limitations to this 3D model including batch-to-batch variability, the lack of controlling mechanical parameters and lack of precision in cell positioning. In particular, 3D bioprinting has recently become an attractive technique to generate 3D environments due to its greater precision in spatial control compared to

traditional 3D cell culture methods. For example, the automated process of 3D bioprinting allows bioprinted 3D constructs to have higher precision and consistency of the volume of biomaterial and number of cells, due to the absence of human error and variability. In addition, 3D bioprinting offers more time efficient production of cell encapsulated 3D construct, when compared to traditional manual cell seeding methods. The current project aims to investigate the biological interactions between wear debris and neural cells, using an advanced 3D bioprinted *in vitro* model.

The following literature review will be a discussion on the spine structures, degeneration of intervertebral discs, current treatment options with spinal implants and the biomaterials used. Furthermore, there will be further discussion on the biomaterial wear debris produced from spinal devices and instrumentation, the characteristics of wear particles, and current *in vitro*, *in vivo*, and animal models used to study the effects of wear debris on neural cells.

1.2 The impact of the COVID-19 pandemic on my PhD

As a PhD student conducting research in biomedical engineering, my work heavily relied on access to laboratory facilities for cell biology experiments, data collection, and analysis. Unfortunately, the lockdown measures during 2020 and 2021 in New South Wales, Australia implemented in response to the COVID-19 pandemic have severely limited my ability to carry out essential laboratory-based activities at the rate which was initially planned. As a result, a systematic review was conducted as part of this PhD as an alternative to the inability to access laboratories at the Faculty of Engineering and IT and the Faculty of Science at University of Technology Sydney (UTS). The following issues described below occurred during my PhD:

- The NSW COVID-19 lockdown from March 2020 to July 2020 delayed my laboratory induction and training.
- The NSW COVID-19 lockdown from June 2021 to October 2021 which consisted of restrictions of travelling over 5 km from home and a curfew in my local government area delayed my experiments involving characterisation of wear particles, 3D bioprinting and cell viability.

- The 1.5 metre social distancing rule and the "1 person per four square metre" rule imposed during the easing of restrictions, resulted in limited access to laboratories and reduced training with colleagues.
- Significant delay for the induction and training for wear particle generation at the implant testing facility located at the Tech lab.

1.3 Hypothesis

Model particles from materials used in spinal devices and instrumentation will have adverse biological effects on neural cells assessed in a 3D bioprinted model.

1.4 Aims and objectives

Due to the COVID-19 pandemics, PhD students in Sydney, Australia were unable to access university laboratory facilities and could only conduct research at home due to the strict lockdown measures implemented by the government. In response to this, a systematic review was conducted to understand the effectiveness of total disc replacements for patients with low back pain in regard to clinical outcomes. The first aim of this PhD project was to review the clinical outcomes, re-operation, and complication rates of different lumbar total disc replacement devices at mid- to long-term follow-up studies for the treatment of lumbar degenerative disc disease. The specific objectives that addressed this aim were:

1) To determine the clinical outcomes in patients with lumbar total disc replacements for a minimum of 5 years
2) To determine the complication and reoperation rates in patients with lumbar total disc replacements for a minimum of 5 years
3) To compare the long-term clinical outcomes and safety profile of patients with mid-term outcomes

The second aim of this PhD project was to investigate the biological responses of neural cells to model particles, using an advanced multicellular 3D tissue culture model. The specific objectives that address this aim were:

1) To characterise the morphology and size of wear particles using scanning electron microscopy and image analysis.
2) To develop an advanced 3D neural cell model using 3D bioprinting techniques.
3) To investigate the biological responses of wear particles to neural cells via cell viability, and DNA damage.

1.5 Significance and novelty

The significance of this project is in addressing growing patient concerns with spinal implants, and the effectiveness and longevity of spinal implants currently used. The use of a bioprinted 3D cell culture model will allow more representative neural cell responses under physiologically relevant conditions, compared to traditional 2D cell culture methods. We envisage this will generate new knowledge about the cellular responses to spinal implant materials, reveal novel biological failure mechanisms and lead to recommendations for the use of particular materials for spinal instrumentation and devices. This potentially will result in longer lasting, more reliable devices and improved quality of life for patients. The knowledge gained from this project will be of interest to surgeons, patients, and the medical device industry.

Although many studies over the past decades have investigated the biological or cellular responses associated with macrophages and fibroblasts to wear particles retrieved from total joint replacements or total joint simulation, less is currently understood about the biological responses of neural cells after exposure to different biomaterials released from spinal devices both *in vitro* and *in vivo.* The most recent literature on this area of research have examined how neural cells respond to clinically relevant metallic wear particles, using collagen hydrogels to model a 3D cell culture environment. However, the use of collagen hydrogel presented limitations, including, batch-to-batch variability and inadequate long-term stability. Consequently, the novelty and rationale in the current project to utilise a 3D bioprinted model is to overcome the limitations in previous studies and also provide advantages including greater precision in spatial control, increased complexity, and mimicry of *in vivo* organisation of tissues.

Chapter 2

Literature Review

2.1 The Spine

2.1.1 Anatomy and physiology

The spine, also known as the vertebral column, is composed of 33 vertebrae, which are divided into different regions, the cervical vertebrae, thoracic vertebrae, lumbar vertebrae, sacrum and coccyx. The upper 24 vertebrae, consisting of 7 cervical vertebrae (C1 – C7), 12 thoracic vertebrae (T1 – T12) and 5 lumbar vertebrae (L1 – L5), are each separated by intervertebral discs. The lower 9 vertebrae consist of the sacrum (S1 – S5) and coccyx, both of which lack intervertebral discs. The smallest and lightest vertebrae are in the cervical region and have highest bone density compared to the other regions, in order to support the weight of the head and allow flexibility of the neck. The thoracic vertebrae are larger than cervical vertebrae and have thicker intervertebral discs, which allows for shock absorption. Lumbar vertebrae are the strongest and largest and have the thickest intervertebral discs, which provides the most substantial shock absorption.

The cervical vertebrae located directly inferior to the skull are the smallest in size. These provide structural support and allow controlled movement of the head and neck [15]. The thoracic vertebrae are located in the middle section of the spine and are situated in between the cervical and lumbar vertebrae. The thoracic vertebrae provide rib articulation to permit changes in the rib cage volume, and also protection of thoracic viscera, including the heart and lungs [16, 17]. The lumbar vertebrae, located in the lower vertebral column, contain the largest vertebral segments in the spine. The lumbar vertebrae provide substantial load bearing capacity of the head, neck, trunk and upper extremities, as well as movement and stability of the trunk [18]. The sacrum is connected to the pelvis and is comprised of five vertebrae, which are fused together in adulthood at the age of 25 – 30 [19]. The sacrum is important for supporting the load of the upper body and connecting the hip with the lower spine [18]. The coccyx, also known as the tailbone, is a fusion of three to five vertebrae and allows attachment to pelvic muscles, tendons and ligaments. The fundamental biomechanical goals of the spine are to provide structural

support, protect the spinal cord and maintain an upright body position. The vertebral column ultimately provides support by transfer of weight of the head, neck and trunk to the lower extremities of the human body.

The adult spine consists of four curvatures, including the cervical curve, thoracic curve, lumbar curve, and sacral curve. The thoracic and sacral curves, which are maintained from the foetal spinal curvature, form a C-shape, and are classified as primary curves, which are present in the spine at birth. The primary curves assist in shifting the weight of the vertebral column to allow a vertical posture [19]. The lumbar and cervical curves, appearing a few months postnatal, are classified as the secondary curves. The secondary curves are concave and in the opposite direction of the primary curves. A schematic diagram of the vertebral column is shown in Figure 1.1.

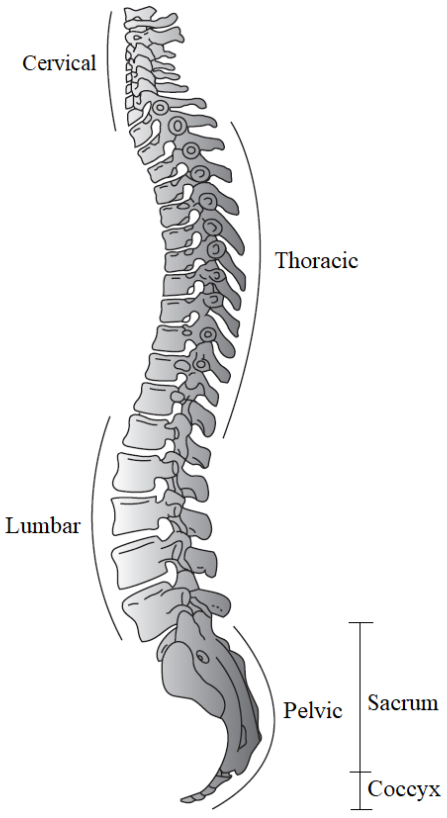

Figure 2.1. The vertebral column. A sagittal view of the vertebral column, displaying the four curvatures of the spine: cervical (C1 – C7), thoracic (T1 – T12), lumbar (L1 – L5) an pelvic, which is split into the sacrum region and the coccyx region. Diagram adapted from [20].

2.1.2 Intervertebral discs

Intervertebral discs are located between the vertebral bodies in the vertebral column and function mechanically by acting as a shock absorber during spinal compression and facilitating joint mobility [21]. A schematic diagram of the adult intervertebral disc is shown in Figure 2.2. The discs connect adjacent vertebrae together via a fibrocartilaginous joint, also known as a symphysis and allow limited vertebral movement, including flexion and extension. These discs are not present in the fused vertebrae of the sacrum and coccyx, or between the first two cervical vertebrae, due to the absence of a vertebral body and spinous process (permits attachment of muscles and ligaments).

The intervertebral disc is a complex structure, which comprises of an outer fibrous cartilage ring, the annulus fibrosis, surrounding a gel-like inner core, called the nucleus pulposus [22]. The annulus fibrosis (AF) is a laminate structure, constructed of 15 – 25 concentric layers of fibrocartilage and comprises 65 – 90% water, 50 – 70% (dry weight) collagen, 10 – 20% (dry weight) proteoglycans and non-collagenous proteins [23]. The main role of the annulus fibrosis is to protect the nucleus pulposus (NP) and prevent the gel-like material from leaking out of the disc (herniation). The nucleus pulposus, essential for weight bearing and shock absorption, is comprised mainly of water (66 – 86%), collagen fibres (type II collagen), as well as chondrocyte-like cells and proteoglycans. These components allow the nucleus pulposus to play an important role in resisting compressive forces in the spine [24]. The discs are mostly covered with vertebral end plates, which serve as the interface of the vertebral body and intervertebral disc. Vertebral end plates are cartilaginous and consists of a thin layer of hyaline cartilage [25].

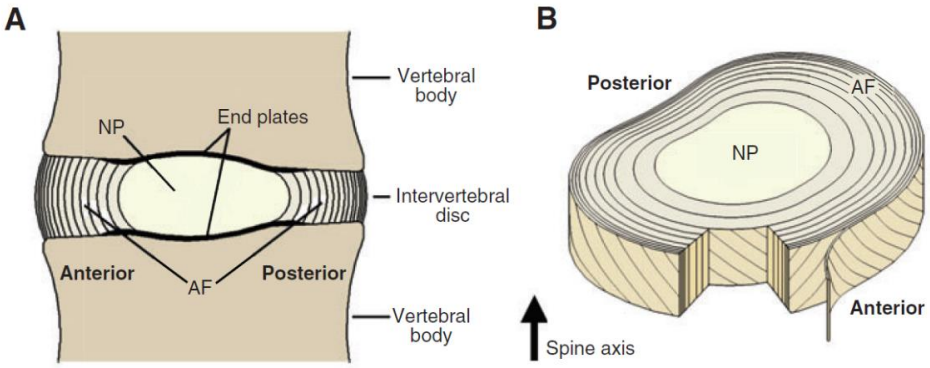

Figure 2.2. The adult intervertebral disc. (A) Sagittal cross-section showing the anatomical features of the intervertebral joint. (B) Cross-section of annulus fibrosis (AP) and nucleus pulposus (NP). Figure adapted from [21].

2.2 Degeneration of the intervertebral discs

The degeneration of intervertebral discs, also known as degenerative disc disease (DDD) is a spinal condition indicated by the breakdown of the discs and is commonly associated with neck or back pain [22, 26]. The intervertebral discs gradually deteriorate with increasing age, due to the reduction of water content in the nucleus pulposus, which leads to progressive impairment of mechanical function [21]. The water loss in the nucleus pulposus also causes the thinning of the discs and ultimately reducing the height of the vertebral column [19]. Decreased hydration in the nucleus pulposus also creates an imbalance in the distribution of compressive forces across adjacent vertebral bodies, which can result in non-uniform transferal of forces to the annulus fibrosis [27]. This ultimately can lead to modification of mechanical properties of the annulus fibrosis and the occurrence of radial and circumferential tears in the structure. Radial tears in the discs could potentially develop into a herniated nucleus pulposus, leading to pain [21].

The implications in the initiation and development of disc degeneration involve several factors, including abnormal mechanical loading, inadequate nutrient supply and genetic factors [21, 22, 28]. Modifications in the extracellular matrix composition, including lower pH and oxygen concentrations, caused by reduced nutrient supply can lead to increased death of disc cells [22, 29, 30]. Although the direct mechanisms are not fully understood, previous research *in vitro* and *in vivo* have suggested that the failure of

maintaining sufficient nutrient supply to the disc cells will eventually result in disc degeneration [31, 32]. Abnormal mechanical loading is also thought to play a crucial role in the pathway to disc degeneration. Mechanical stimulation is essential in encouraging extracellular matrix synthesis and stimulating nutrient diffusion through endplates [21]. Mechanical stimulation refers to the application and transmission of various loads including compressive, tensile and shear stresses to the intervertebral discs. These mechanical forces are detected by cells of the intervertebral discs, transduce these forces into biochemical signals. Mechanical loading of the intervertebral discs is important in maintaining the integrity of the discs, e.g. balancing the degradation and synthesis of components of the extracellular matrix including collagen, proteoglycans, hyaluronic acid, fibronectin, and laminin. However, overloading can generate localised tissue injury, causing a decline in repair rate, which may ultimately lead to disc degeneration [33]. Genetic predisposition has been demonstrated in previous research, including twin studies, to have associations with disc degeneration and herniation [34-37]. However, further studies on heredity factors have been limited due to the costs accumulated with the need for larger sample sizes participating in gene analysis [21].

Although degeneration of intervertebral discs is a normal part of the aging process, the presence of disc degeneration has been linked with the symptoms of low back pain [38]. In a study conducted by Brinjiki *et al* [39], patients who were aged 50 years or younger with back pain reported higher proportion of patients with lumbar degenerative changes from magnetic resonance imaging (MRI) of 57.4% compared to asymptomatic patients which reported 34.4%. Similarly, Berg *et al* [38] reported that 58.6% of patients aged 20 – 30 who had low back pain, showed MRI evidence of lumbar disc degeneration. Consequently, with the increase of younger patients having low back pain, there is a need to have a greater understanding of disc degeneration, and interventions associated with it.

2.3 Spinal instrumentation and implants

2.3.1 Spinal fusion

Spinal fusion is a surgical technique utilised to stabilise and fix two or more vertebra together, in order to improve spine stability or decrease back pain. Spinal fusion was first introduced in 1911 by Hibbs and Albee [40, 41] for the treatment of Potts disease, also

known as spinal tuberculosis [42]. Since then, lumbar spinal fusion has become the most common type of spinal fusion and is used as a treatment option for pathologies including degenerative scoliosis, spinal stenosis, spondylolisthesis and degenerative disc disease [43]. In 2014, spinal fusion was ranked the 6th most frequent operating room procedure in U.S.A hospitals with approximately 463,200 spinal fusion operations conducted annually [44].

In lumbar spinal fusion, a mixture of biologic material (bone graft) and spinal instrumentation including interbody spacers, plates, rods, wires and screws, are required to provide support and stability of the spine, as well as promoting osseous growth [45, 46]. Examples of spinal instrumentation are shown in Figure 2.1 and Figure 2.2. Spinal interbody spacers, also known as interbody cages, were introduced in the late 1980s and are implanted between vertebral bodies to assist with bone graft fusion, as well as providing additional biomechanical stabilisation of the spine [47]. Wires, cables and tapes are also used for the fusion of spinal segments. Furthermore, screws, rods and plates provide additional assistance with spinal stability. The rods or plates are placed over vertebral segments with the bone graft and are anchored into vertebral bodies or pedicles by screws.

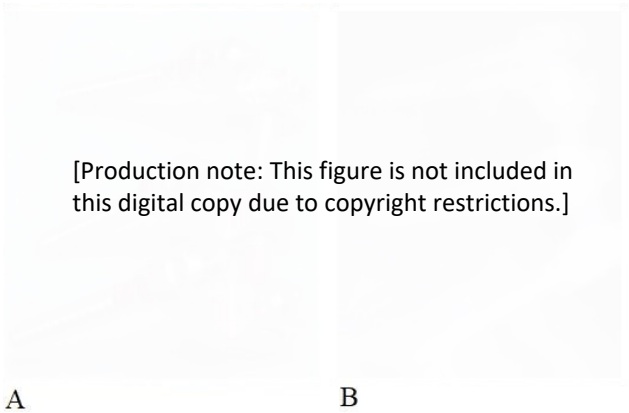

Figure 2.3 Metal rods and screws. (A) A photograph of a screw and rod device. (B) A radiograph of metal screw and rod positioned at L4-S1 level. Figure adapted from [45].

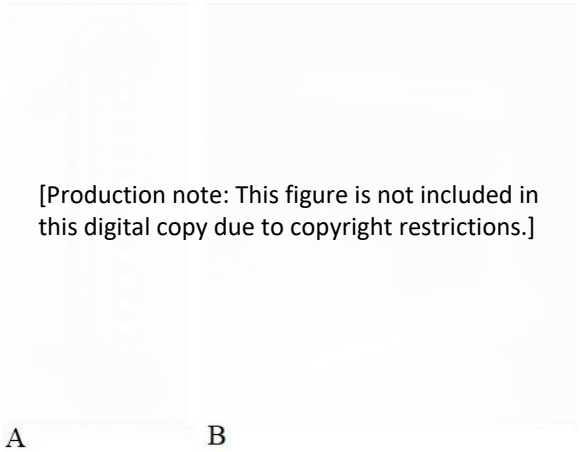

Figure 2.4 Metal plate and screws. (A) A photograph of a plate and rod device. (B) A radiograph of metal screw and rod positioned at L3-L5 level. Figure adapted from [45]

2.3.2 Total disc replacements

Total disc replacement is a surgical procedure that replaces degenerated intervertebral discs with artificial disc implants. The types of total disc arthroplasty include, cervical total disc replacement (CTDR) and lumbar total disc replacements (LTDR). The biomechanical aims of disc replacements are to relieve pain caused by disc degeneration, and to restore and maintain normal spine biomechanics and motion. The design of these implants requires consideration of several biomechanical parameters. These include the restoration of mobility and accurate spinal alignment, protection of adjacent biological structures, implant stability and wear properties.

Similar to hip and knee replacements, artificial discs are also designed based on a bearing system. The bearing comprises of two endplates (inferior and superior) and an inner core, together acting like a "ball and socket" joint. Common bearing couples of artificial discs include metal-on-metal and metal-on-polyethylene. The materials used to design artificial discs are generally inspired by materials used in total hip replacements. The material considered for endplate components needs to be able to endure repetitive loads. Currently, most endplates are manufactured from cobalt chrome alloys, due to its high wear resistance. In addition, titanium is currently being widely utilised for coating surfaces. The material selection for bearing surfaces of artificial discs is important, because can determine the longevity and stability of the implant. Currently, ultra-high molecular weight polyethylene (UHMWPE) is used as a bearing material in several implants. There

are numerous artificial disc devices available in the market for both CTDR and LTDR, which are outlined in Table 1.

Table 2.1 Summary of current artificial disc replacements. Co-Cr = cobalt-chrome alloys; UHMWPE = ultra-high molecular weight polyethylene

Implant	Articulation	Biomaterial	Manufacturer
Charité	Metal-on-Polymer	Co-Cr & UHMWPE	DePuy Synthes
ProDisc	Metal-on-Polymer	Co-Cr & UHMWPE	DePuy Synthes
Activ-L	Metal-on-Polymer	Co-Cr & UHMWPE	Aesculap Implant Systems
Maverick	Metal-on-Metal	Co-Cr	Medtronic
Flexicore	Metal-on-Metal	Co-Cr	Stryker
Prestige® LP	Metal-on-Metal	Stainless steel	Medtronic

2.4 Evaluation of current total disc replacements

2.4.1 Metal-on-Polymer devices

One of the current devices is the SB Charité artificial disc, which has undergone the longest clinical trials and is the oldest existing disc implant [47]. Initially, the endplates of the first two generations of this implant were made from stainless steel. The current Charité implant design, marketed by DePuy Synthes, consists of two Co-Cr alloy endplates, with protruding teeth for bone fixation, articulating against a UHMWPE inner core. The clinical outcomes of this implant have been mixed. Excellent clinical and radiographic results were reported in a 10 year follow-up study by Lemaire *et al* [48], in which a clinical success rate of 90% was reported in patients. In addition, a short-term follow-up study by Scott-Young [49] also demonstrated statistically significant pain improvement and a revision surgery rate of 2.7% reported in patients with the Charité implant. However, these results conflicted with a study by Zeegers *et al* [50], in which these authors reported that 24% of patients required secondary surgery after a 2-year follow-up. Furthermore, late complications including, implant subsidence and adjacent disc degeneration have occurred in patients [51]. Another study on Charité disc replacements was conducted by Putzier *et al* [52] with a 17-year average follow-up time

of patients with different types of the Charité implant. They concluded that the clinical or radiological outcomes of the SB Charité III implant (Figure 2.5), currently on the market, had no significant differences to the previous Charité generations. Interestingly, the first and second Charité generation implants were replaced, because of inadequate contact between the bone implant and high fracture rates of the endplate, respectively [52].

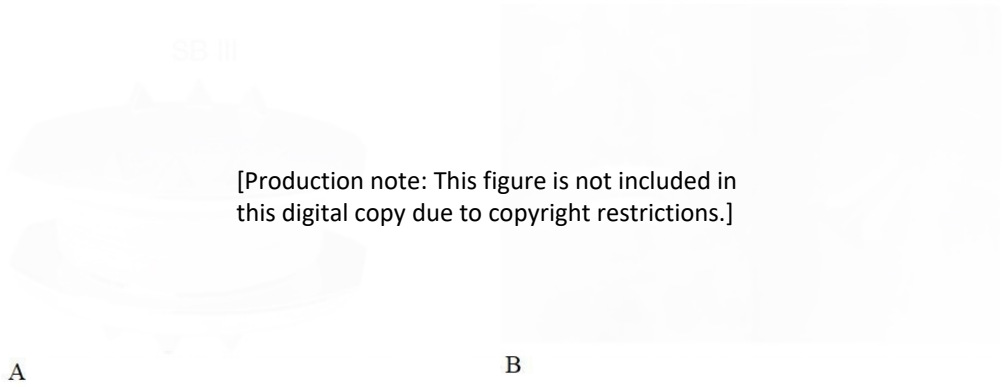

Figure 2.5 (A) SB Charité artificial disc. (B) Radiographic image of implanted disc. Adapted from [47].

Similar to the Charité disc, the ProDisc (Synthes Spine) utilises Co-Cr alloy endplates with a UHMWPE inner core. However, it utilises a locking mechanism to attach the disc to the interior endplates. The ProDisc has undergone two generations of design, with the second one currently available on the market. A follow-up (1 year minimum) study on the ProDisc II was conducted by Tropiano *et al* [53], who reported a clinical success rate of 71.4% in patients. The implants did not present mechanical failure or loosening. However, Park *et al* [54] conducted a 10-year-average follow-up study on the long-term clinical outcomes of the Pro-Disc II and reported a clinical success rate of 76.9%. Since the approval of the ProDisc-L (Figure 2.6) in 2006, Zigler *et al* [55] reported a randomised, 5-year follow-up, FDA Investigational Device Exemption (IDE) study. The study reported that patients with total disc replacements demonstrated higher satisfaction than patients with spinal fusion, even though both groups showed improvement in their Oswestry Disability Index (ODI) scores, which is a quantification of low back pain using a questionnaire.

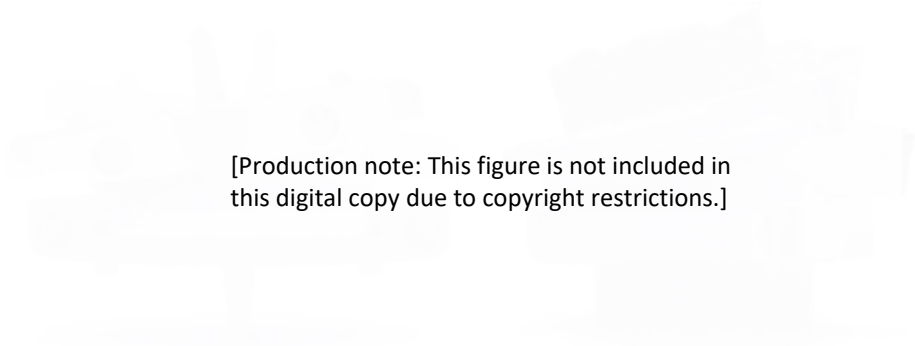

Figure 2.6 ProDisc-L artificial disc. Adapted from [47].

The Activ-L artificial disc is also currently commercialised for LTDR. This implant utilises Co-Cr alloy endplates, with a titanium and dicalcium phosphate mixed coating, and a UHMWPE inner core. A follow-up study of 6 years on the clinical outcomes of patients with Activ-L or ProDisc-L was reported by Yue *et al* [56]. The study reported that Activ-L patients had a decrease of 89% and 76% in back pain and ODI scores, respectively, which was greater than ProDisc-L patients. More recently, Yue *et al* [57] demonstrated safe and effective use of Activ-L for 5 years in patients with lumbar DDD. Additionally, the study reported that the range of motion in Activ-L patients was significantly better, compared to controls, including the Charité or ProDisc-L.

2.4.2 Metal-on-Metal

Metal-on-metal disc implants for LDTR, including Maverick (Medtronic) and Flexicore (Stryker Spine) have been developed, but are still undergoing the process of FDA approval. Both implants utilise Co-Cr alloys, with the Maverick having an additional hydroxyapatite coating of the endplates. The Maverick implant has demonstrated clinical success in follow-up studies, with improvements in ODI scores and Visual Analog Scores (VAS) [58, 59]. However, long-term complications, including revision surgery, discectomy, and suspicion of infection, have been reported in 11.2% of patients from a 10-year follow-up study [59]. Clinical studies for Flexicore are currently ongoing, thus the clinical outcomes of this implant are not yet available [47].

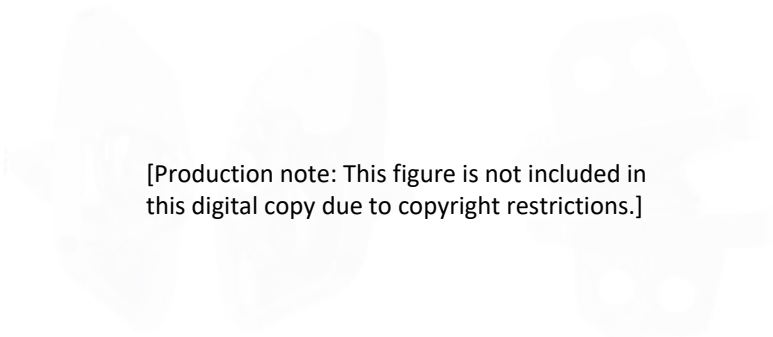

Figure 2.7 Maverick artificial disc. Adapted from [47].

Another metal-on-metal artificial disc implant is the Prestige, which uses stainless steel and is indicated for CDTR. Clinical results from a 2-year pilot study on patients have demonstrated improvements in VAS scores, as well as maintained mobility [60]. In addition, long-term follow-up studies have reported satisfactory clinical outcomes and high patient satisfaction with this implant [61, 62]. In a minimum 6-year follow study, Zeng *et al* [61], reported mobility was maintained in 80.5% of patients. However, incidences of adjacent segmentation degeneration were detected in some patients. Gornet *et al* [62] also reported patients with revision surgery and implant-related adverse events with 10-year cumulative rates of 10.3% and 13.8%, respectively.

2.5 Biomaterials used in spinal implants

2.5.1 Metals

Metallic biomaterials, including stainless steel, cobalt chromium and titanium alloys were introduced in orthopaedic applications throughout the twentieth century [63]. The first type of modern alloy used in orthopaedic applications was stainless steel [47, 64]. During the late 1950s and early 1960s, the first truly successful artificial joint replacement was the total hip replacement developed by John Charnley. The femoral stem of the hip joint prothesis was made of stainless steel [63, 65]. Due to the extensive and successful use of metals in orthopaedic devices, including hip implants, metals were introduced in early spinal instrumentation and implants.

The first use of stainless steel in spinal devices was the implantation of steel balls by Fernstrom as an approach for lumbar total disc replacement. However, a decrease in disc height often occurred which resulted in revision surgery [66]. Stainless steel was also introduced in cervical disc arthroplasty during 1989-1991 in the development of the Bristol-Cummins device, which evolved into the Prestige® disc replacement, approved by the Food and Drug Administration (FDA) in 2007 [66, 67]. It uses a metal-on-metal, ball-and-socket system designed to preserve the distance between the vertebrae and maintain mobility in a normal disc. The most commonly used stainless steel in clinical applications is AISI 316L, also known as austenitic stainless steel. The composition of 316L stainless steel mainly is 17-20 wt% Cr, 12-14 wt% Ni, 2-3 wt% Mo and 0.03 wt% C. In addition, the high chromium content in stainless steels allows the material to be corrosion resistant, because of the formation of chromium oxide providing a coating on the outer surface [63]. However, stainless steels are still susceptible to localised corrosion due to damage of the protective coating during articulation. Although, the use of austenitic stainless steel is restricted in permanent orthopaedic devices, it is relatively easy to process, strong and low cost, which makes it an ideal material for temporary, fracture-fixation devices, including plates, screws, rods and wires, commonly used in spinal instrumentation [47, 63, 64].

Stainless steel was suggested to have good biocompatibility due to the clinical success of its use in total hip arthroplasty, during the 1960s and 1970s. Since then, further research on 316L stainless steel has demonstrated biocompatibility [68-70]. However, due to poor wear resistance, many metal-on-metal bearing couples in total hip replacements produced high volumes of wear debris particles, which caused the rapid onset of aseptic loosening [63, 64]. As a result, the biocompatibility of austenitic stainless steel has been overridden by titanium-based and cobalt-chrome-based alloys, because of greater wear resistance and corrosion properties [71]. Furthermore, due to the greater mechanical and enhanced corrosion resistant properties of titanium-based and cobalt-chrome-based alloys, the use of stainless steel in arthroplasty has declined [63].

Cobalt-chrome (Co-Cr) or cobalt-chromium-molybdenum (Co-Cr-Mo) alloy, also known as Vitallium was introduced in orthopaedic applications (ASTM-F75 standard) in the 1940s and has now become one of the main materials utilised in artificial hip implants

[71]. The Co-Cr used in orthopaedic implants consists of approximately 27-30 wt% Cr, 5-7 wt% Mo and maximum 2.5 wt% Ni. Co-Cr based alloys have excellent corrosion resistance, to a greater extent than that of stainless steels and they also exhibit superior mechanical properties [63]. Both Co-Cr and stainless steel possess similar elastic moduli, 220-230 GPa and approximately 200 GPa, respectively, which are significantly higher than cortical bone (20-30 GPa). Due to the higher moduli of those metals, they absorb most of the mechanical load when in contact with bone. This phenomenon is called stress shielding, which occurs when the mechanical load is mostly absorbed by the load-bearing devices, leading to a decrease in load bearing experienced by the surrounding bones. Stress shield can ultimately cause a reduction in bone density and strength over time [63]. The reduction of mechanical load on bone may lead to bone resorption and ultimately implant failure and loosening [63, 72, 73]. However, with the high fatigue strength of Co-Cr alloys, they make a suitable material for total joint replacements and fracture-fixation devices [71]. Wrought Co-Cr alloys (ASTM-F75) have been used in long-term orthopaedic applications, including femoral stems and for joint bearing systems. Currently for spinal implants, there are several cervical disc replacements using Co-Cr in a Metal-on-Polymer bearing system, approved by the FDA including the, Depuy-Synthes and ProDisc-C [74].

Titanium and its alloys have been of great interest in orthopaedic applications and has been popular in total hip replacements. Titanium possesses excellent properties including, high mechanical strength, low density, good corrosion resistance and biocompatibility. Titanium and its alloys have a lower elastic modulus (110 GPa), compared with Co-Cr and stainless steel alloys [63]. In addition, titanium alloys have better biocompatibility compared to Co-Cr and stainless-steel alloys, due to excellent corrosion resistance. However, titanium alloys have poor wear resistance, due to its low shear resistance, which has limited its use as an articulating component in total joint replacement [74]. The most commonly used titanium alloys in orthopaedics are pure titanium grade 4 (ASTM F67) and titanium-6AI-4 V alloy (ASTM F136). In the late 1960s and early 1970s, Branemark demonstrated the osseointegration phenomenon of titanium when working on dentistry implants. Osseointegration is defined as a *"structural and functional connection between ordered, living bone and the surface of a load-carrying implant"* [75]. With titanium alloys having the ability to tightly interact with bone, implants can be longer-lasting,

reducing the risk of device failure [63]. In spinal fusion, pedicle screws have used titanium surface treatments to improve fatigue strength and also help screw-bone interaction. Additionally, pure titanium and titanium alloys are a popular material choice for spinal interbody cages, due to their high fracture resistance [76]. Titanium has been used in total disc replacement, as a coating material for artificial disc endplates [47, 74]. Some examples include the Depuy-Synthes ProDisc-C and the Stryker Flexicore, which both utilise titanium plasma-spray coating for endplates to stimulate bone growth [74].

Table 2.2. A summary of the mechanical properties of various metallic materials used in orthopaedic applications [63, 77]. GPa = Gigapascals; MPa = Megapascals

Metallic material	Composition of elements (weight %)	Elastic modulus (GPa)	Yield strength (MPa)	Ultimate tensile strength (MPa)	Fatigue strength
Stainless steel (316L)	17 -20 Cr 12 – 14 Ni 2 – 3 Mo 0.03 C Balance Fe	190 – 210	170 – 310	465 – 950	241 – 820
Co-Cr-Mo (F-75)	27 – 30 Cr 5 – 7 Mo 2.5 Ni Balance Co	220 – 240	275 – 1585	600 – 1785	207 – 950
Pure titanium grade 4	0.4 O Balance Ti	105 – 110	485 – 692	760 – 785	300
Titanium alloy (Ti4A16V)	5.5 – 6.5 Al 3.5 – 4.5 V Balance Ti	110 – 116	850 – 1034	960 – 1103	620

2.5.2 Polymers

Polymers have been utilised for several decades in orthopaedic applications, including, total joint replacements. The most commonly used polymers in orthopaedics are ultra-high molecular weight polyethylene (UHMWPE) and polyether-ether-ketone (PEEK). In

the early 1960s, Charnley introduced PTFE in total hip arthroplasty for the acetabular cup. PTFE has high flexural strength, high thermal stability and is water resistant [78]. However, due to low wear resistance and adverse foreign biological responses from wear debris, PTFE was prevented for further use in acetabular cups [78, 79]. Consequently, UHMWPE was introduced in acetabular cups by Charnley in 1962, due to displaying superior properties [79].

UHMWPE has been commonly utilised in bearing surfaces in total joint replacements, including the acetabular component of total hip replacements, the tibial insert of total knee replacements and the inlay component of artificial disc replacements [63]. There are several artificial disc implants, which use a UHWMPE and metal bearing system, including the Charité, ProDisc and ActivL. UHWMPE is generally manufactured to have a molecular weight of 2 – 10 million g/mol and possesses superior properties including, high impact strength, excellent toughness, high chemical and abrasion resistance [63, 78]. However, the limitation is that wear particles generated from UHWMPE bearings, mainly < 1μm, can result in adverse biological effects [63, 78-80]. Additionally, gamma radiation sterilisation of UHWMPE, which is used in most devices, can lead to oxidative degradation, causing increased rate of wear particle generation and fatigue damage [63]. In order to address this issue, other sterilisation and processing methods have been utilised, including, ethylene oxide sterilisation and gas plasma sterilisation, which show no significant impacts on UHMWPE structure [81].

Crosslinking of UHWMPE has been introduced in total joint arthroplasty and is demonstrated to improve wear resistance [80]. Galvin *et al* [82] reported that high levels of cross-linking (10MRad) of UHWMPE significantly lowered the wear rate, when tested against smooth and scratched countersurfaces. This result is consistent with a study by Muratogula [83], which demonstrated a decrease of 85% in 10MRad cross-linked UHWMPE wear. Galvin *et al* [84] also found that highly cross-linked UHWMPE had a significantly lower functional biological activity for the wear particles, compared to moderately cross-linked and non-cross-linked UHWMPE. However, the downside of cross-linking is that it can negatively impact the mechanical properties of this material, including reducing fracture toughness and tensile strength [80].

PEEK has been increasingly adopted as a biomaterial in orthopaedic implants, especially in spinal devices [85]. PEEK is a thermoplastic with excellent thermal stability, and resistance to chemical and radiation damage. Additionally, the radiolucent property of this material, makes it an attractive substitute to metallic materials used in spinal devices, as surgeons can observe possible movements of the implant [76]. PEEK is commonly used in spinal instrumentation, including, cages and rods. The advantage of PEEK over titanium rods is that it provides more interaction between the bone graft and endplate, because of the comparable elasticity of PEEK with bone [76]. PEEK was firstly introduced in the spine, with carbon reinforcement, as a design for a spinal cage. Brantigan and Steffee [86] reported 54.5% of patients with the posterior lumbar interbody fusion reinforced with a cage-like implant, showed statistically significant radiographic fusion after 2 years follow-up compared to pre-operation. In addition to carbon reinforcement, bioactive materials, including hydroxyapatite, have been combined with PEEK as a coating to promote osseointegration, which improves the bonding between the implant surface and surrounding bone tissue [47]. PEEK has also been examined in other spinal implants, including total disc arthroplasty and dynamic stabilisation, which is the flexible stabilisation of the spine using spinal instrumentation to provide some motion retention [47].

2.5.3 Ceramics

Ceramic biomaterials, including Zirconia and Alumina have been used in orthopaedic applications for several decades. One of the first applications of ceramics in total joint arthroplasty was the introduction of Alumina in total hip arthroplasty in 1971 by Boutin [63]. Alumina was utilised as a replacement for the metallic femoral head. Furthermore, ceramics were also introduced in acetabular cups in alumina-on-alumina bearing systems, due to the excellent wear and corrosion resistance of alumina, as well as favourable biocompatibility [63, 78]. Although, ceramics possess high strength and hardness properties, early failures in ceramic components occurred because of their lack of fracture toughness. A limitation of alumina is the stress shielding concern, due to the high modulus of elasticity, compared to bone. This has led to aseptic loosening of alumina acetabular cup in patients with osteoporosis [63].

Zirconia toughened alumina (ZTA) was introduced in 1980s when there was ongoing issues of brittle fractures of alumina in total hip replacements [87]. Zirconia was considered to be a more appropriate ceramic material for medical use, due to its increased strength and toughness, approximately double that of alumina [63, 87]. Silicon nitride (Si_3N_4) is another ceramic material that is used in orthopaedic implants. Similar to zirconia, silicon nitride also possesses excellent tensile strength and toughness [87]. Silicon nitride was initially used in patients, who underwent a clinical trial to investigate its viability as an intervertebral spacer for the lumbar spine [88]. More recently, silicon nitride has been implemented in spinal cages for spinal fusion, showing little adverse outcomes [89].

2.6 Wear

Wear is the steady loss of material, creating wear particles, which results from relative motion of two contacting surfaces. In total joint arthroplasty, the common types of wear include, abrasion, adhesion, fatigue, fretting and corrosion. Abrasive wear refers to the removal of material, produced from two contacting materials with different surface hardnesses, i.e. the asperities of the harder material surface cuts through the asperities of the softer material surface, producing wear debris. Adhesive wear occurs when there is removal of material from asperities of opposing material surfaces bonding together and sliding over another, creating a shear force. Fatigue wear occurs from cyclic loading and unloading between contact surfaces. The constant cyclic stress on a material may induce the propagation of surface and subsurface cracks. Fretting wear is similar to fatigue wear in that two contacting material surfaces undergo cyclic motion, however at a small amplitude. Corrosive wear occurs when the material surface is damaged, due to chemical or electrochemical reactions.

2.6.1 Wear debris

It is important to understand wear particles released from biomedical implants, especially in artificial joint arthroplasty, because they have been demonstrated to cause detrimental effects, including osteolysis and implant loosening [90]. Wear debris is one of the major indicators in the reduction of artificial joint implant lifetime and rising revision surgeries [91]. The generation of wear debris in total joint replacement mainly occurs at the bearing

surfaces, the interface of modular components and at the connection of bone fixation [91, 92]. Furthermore, characterisation of wear debris provides essential information for implant material selection, implant design and understanding the mechanism of wear, as well as the biological effects of the wear particles. A summary of the issues with different wear particle material

2.6.2 Metal wear particles

Metallic materials have been commonly used in artificial joint replacements, including hip and knee replacements. Initially, metal-on-metal hip replacements were used with stainless steel. However, Co-Cr alloys were introduced to replace stainless steel to prevent excessive friction from previous bearings. With the early success of metal-on-polyethylene hip replacements in the 1970s and 1980s, the use of metal-on-metal implants declined. However, in the early 1990s, the second generation, metal-on-metal bearings were introduced, as the volume of wear debris produced was significantly lower than the volume of polyethylene wear debris generated from metal-on-polyethylene bearings. Data from wear simulation conducted by Kenneth *et al* [93] demonstrated that the volumetric wear of Co-Cr alloy in metal-on-metal hip replacement was 110-180 times lower than that of metal-on-polyethylene bearing systems.

Adhesive and abrasive wear are the major types of wear that occur in metal-on-metal articulations [94]. Malpositioning of the implant can also cause enhanced wear [95]. The generation of metal wear debris initially begins in a high wear environment, via a process called “bedding in” of the components. The wear rate slows down once one of the metal components finds the optimal contact area on the other component. During the “bedding in” phase, radial clearance and sphericity are key factors in determining the quantity of wear production [96]. The bearing radial clearance is a relative radial movement between an outer and inner component, e.g. in a total hip replacement that would be the acetabular component and femoral head, respectively. Finally, the “bedding in” phase transitions into a “steady-state” phase, where the wear rate decreases and sustains for the life of the metal-on-metal bearing couple [94, 96].

Wear and corrosion have a synergistic effect on the breakdown of metals in proteinaceous solutions, such as synovial fluid. This breakdown process is known as tribo-corrosion, which is a permanent transformation of a material, due to the concurrent action of wear and corrosion. For metal-on-metal articulations, the reaction of metallic surfaces and synovial fluid create a tribo-material. The susceptibility of metal ion release from these articulations is elevated, as a result of impairments of the surface oxide layers, which occurs due to motion and articulation that removes the oxide layer [94]. In addition, tribo-corrosion and metal ion release also occurs in metal-on-polyethylene articulations. In a previous study conducted by Savarino *et al* [97], patients with metal-on-polyethylene total joint replacement demonstrated a significant increase in Co and Cr levels in serum, compared to the control which included patients without implants.

2.6.2.1 Characterisation of metal wear particles

Characterisation of metal wear particles from tissue samples retrieved from revision surgeries are generally conducted via light microscopy and transmission electron microscopy [98]. Metal wear particles have been previously reported to have a size range of 0.1 – 400 μm, using light microscopy. However, light microscopy has limitations of not being able to accurately detect sub-micron size particles. Therefore, previous studies have also used TEM, which have reported particle size ranges 10 – 15 nm and 10 – 400 nm.

A study was conducted by Doorn *et al* [99] to analyse the metal wear particles obtained from metal-on-metal total hip replacements. The study found that the Co-Cr-Mo particle sizes ranged from 51 – 116 nm and were round to oval in shape, with sharp, elongated boundaries. In addition, Doorn *et al* [99] were able to calculate the wear particle production rate, ranging approximately from 6.7×10^{12} – 2.5×10^{14} particles per year. These results can be compared with a study conducted by Firkins *et al* [100], who utilised a physiological hip stimulator to characterise metal wear particles, produced in serum by metal-on-metal hip replacements. The study found that the metal wear particles were 25 – 36 nm in size and mainly oval to round shaped, similar to the shape reported for *in vivo* generated particles by Doorn *et al* [99]. However, the study did demonstrate a similar production of metal wear particles per year with 4×10^{12} – 6×10^{13}. It can be deduced

that the size of wear particles generated from metal-on-metal implants are consistently in the nanometre scale range and are uniform in shape.

Generally, metal-on-metal articulations in arthroplasty have a lower volumetric wear rate than metal-on-polymer articulations [101]. An example of a metal-on-metal spinal implant is the Medtronic MAVERICK^{TM} lumbar disc replacement (Cr-Cr-Mo alloy). A study using a spine wear simulator was conducted by Philippe *et al* [102] that investigated the characterisation of wear from a A-MAV^{TM} anterior motion replacement.

In a more recent study by Lee *et al* [12], these authors conducted *in vitro* characterisation of Co-Cr and stainless steel wear particles, using a pin-on-plate tribometer. The study demonstrated that most of the Co-Cr wear particles generated ranged from 10 – 120 nm in size, with a mode of 30 – 39nm. Similarly, the size range of stainless-steel wear particles also had mode of 30 – 39nm, but with a larger range of 10 nm – 1 mm. Co-Cr wear particles were oval to round in shape and stainless steel wear particles included irregular granules and round particles. The particles characterised in this study were similar to those analysed by Pasko [103], who characterised Co-Cr wear particles in an *in vitro* spine simulator with four degrees of freedom. The study reported oval to round Co-Cr particles ranging from 20 – 120 nm in size, with the majority within 30 – 60 nm. The characterisation of Co-Cr wear particles generated by spine simulation show similarities with wear particles produced via hip simulation in a study conducted by Catelas *et al* [104].

2.6.3 Polymer wear particles

Metal-on-polymer bearing systems produce wear particles, which have led to implant failure in total hip and knee replacements. In addition, metal-on-polymer articulations produce a greater volumetric wear rate, compared to metal-on-metal articulations [105]. The wear debris generated by UHMWPE components have been associated with osteolysis, which is the progressive loss of bone tissue and implant loosening, occurring when there is a deterioration of the implant-bone bond [78].

There are several mechanisms of UHMWPE wear in total joint arthroplasty, including abrasive, adhesive, fatigue and third-body wear. The type of wear produced in the

UHMWPE articulating component of the Charité disc replacement, was reported to be mainly adhesion and abrasion [106]. Adhesion between a UHMWPE surface and a metal counter-surface produces fibrils, which can be separated from the surface via mechanical movement and subsequently form sub-micron wear particles [91]. Wang *et al* [107] reported that the wear rate of UHMWPE is affected by its elongation at break and ultimate tensile strength. Wear particles can be separated from material surfaces through mechanical actions (cyclic loading) or chemical effects (microstructural modifications of surface) [78].

2.6.3.1 Characterisation of UHMWPE wear particles

Characterisation of UHMWPE wear particles both *in vitro* and *in vivo* is generally studied using polarised light microscopy and scanning electron microscopy. The presence of macrophages in tissues obtained from around total joint replacement components, have been demonstrated to be linked with UHMWPE wear particles [108]. Initial findings from *in vivo* studies were limited, due to the resolution of light microscopy. Consequently, isolation of UHMWPE wear particles via tissue digestion methods and characterisation using scanning electron microscopy were encouraged.

Wear particles generated from UHMWPE in total joint arthroplasty, ranging from 0.1 – 1.0 μm have been demonstrated to cause adverse biological effects, resulting in implant loosening [109, 110]. Maloney *et al* [111] utilised scanning electron microscopy to characterise polyethylene wear particles, retrieved from failed total hip implants. The authors reported that the majority of those particles were sub-micron sized, with a mean of 0.5 μm and were spherical or globular in shape. Likewise, other studies, including Campbell *et al* [112] and Margevicius *et al* [113], demonstrated that UHMWPE wear particles were submicron in size, mainly in the 0.3 – 0.5 μm range. However, these studies generally neglected to analyse larger sized wear particles (>10 μm), which were often observed in histological sections. Furthermore, Tipper *et al* [114] conducted a quantification of UHMWPE wear particles of all sizes (0.1 – 1000 μm), from revised Charlney hip replacements. Comparable to previous studies, they reported that the size of wear particles most frequently found, was 0.1 – 0.5 μm, although particles greater than 1 mm were also observed.

The wear particles generated from cross-linked UHMWPE are different to the convention UHMWPE. Both Scott *et al* [115] and Endo *et al* [116] produced wear particles via hip simulation and demonstrated cross-linked UHMWPE produced particles of smaller size, compared to non-cross-linked UHMWPE. Scott *et al* [115] also reported that increasing levels of cross-linking leads to reduced volume and surface area of wear particles. Consistent with these *in vitro* findings, *in vivo* studies on total hip arthroplasties and total knee arthroplasties, conducted by Baxter *et al* [117] and Iwakiri *et al* [118], have shown that highly cross-linked polyethylene produce fewer and smaller wear particles, compared to conventional polyethylene. Iwakiri *et al* [118] also reported rounder wear particles generated by highly cross-linked polyethylene.

More recently, nanometre-sized UHMWPE wear particles have been characterised, due to the advancements in higher resolution, scanning electron microscopy. Previous studies have defined nanometre-sized particles as particles with a size less than 100 nm. Liu *et al* [119] reported UHMWPE wear particle sizes of < 100 nm. Similarly, another study by Liu *et al* [110], demonstrated wear particles (< 50 nm). Both studies generated UHMWPE wear particles via wear simulation, using a UHMWPE pin against a Co-Cr alloy plate. These findings are consistent with other studies that demonstrated nanometre-sized UHMWPE wear particles [120, 121]. UHMWPE wear particles have been characterised down to 10 nm in size, via hip and knee simulators in a study by Tipper *et al* [120]. Similarly, Lapcikova *et al* [121] reported UHMWPE wear particles less than 50 nm, with the majority ranging 30 – 40 nm in size, from retrieved tissues of revised total joint replacements. The authors also found consistent mode sizes from *in vitro* characterisation, using pin-on-plate wear simulation.

The morphology of UHMWPE wear particles have been characterised both *in vitro* and *in vivo*. *In vitro* UHMWPE wear particles, obtained from hip and knee simulators were observed by Tipper *et al* [120] as spherical and flake shaped. The morphology of *in vivo* UHMWPE wear particles have been commonly described as round, flake-like and fibril-like [122-124]. These wear particles were retrieved from periprosthetic tissue at revision in total hip replacements. Similarly, Punt *et al* [7] demonstrated that the morphology of *in vivo* generated UHMWPE wear particles from total hip replacements were comparable to wear particles retrieved from SB Charité III total disc replacements, which generally

appeared round to oval shaped [125]. Additionally, Punt *et al* [7] also reported that the average wear particle size were similar between total hip replacements and total disc replacement, with average sizes of 0.53 μm and 0.46 μm, respectively [125]. An *in vitro* study by Eckold *et al* [109] found that UHMWPE wear particles, obtain from spine simulation, mostly generated sizes within 0.1 – 1 μm, with a mode of 0.88 μm.

2.6.4 Ceramic wear particles

Ceramic wear particles obtained from ceramic-on-ceramic total hip arthroplasties have been previously investigated in histological studies [126]. However, compared to metal and polymer wear particles, information on ceramic wear particles in periprosthetic tissues is less well characterised, due to the very low wear rates of ceramics and the inadequate characterisation methodologies to retrieve very low volumes of very small particles [108].

2.6.4.1 Characterisation of ceramic wear particles

In vivo studies of ceramic wear particles from surrounding tissues in ceramic-on-ceramic total joint replacements have been carried out using light microscopy. Alumina wear particles have been reported to have a size of 5 μm and a sharp-edged polygonal shape [127, 128]. However, other studies have demonstrated submicron-sized ceramic wear particles. This was seen in a study by Lerouge *et al* [129], where the authors used scanning electron microscopy, an average particle size of 0.44 μm was reported. This result was comparable to another study conducted by Yoon *et al* [130], who reported a mean particle size of 0.71 μm. Similarly, Williams *et al* [126] also demonstrated submicron-sized ceramic wear particles, with a mean size range of 0.2 – 0.6 μm. Nano-sized ceramic wear particles were firstly characterised *in vivo* by Hatton *et al* [131]. The authors utilised transmission electron microscopy to demonstrated alumina wear particle sizes, ranging 5 – 90 nm [131].

In vitro characterisation of ceramic wear particles has been conducted previously using hip joint simulation. Tipper *et al* [132] examined wear debris from different types bearings used in total hip implants. They reported that ceramic wear particles, with a mode size of 9 ± 0.5 nm, were the smallest compared to metal and polymer wear particles.

More recently, Asif *et al* [133] characterised commercial ceramic wear, including BIOLOX Delta particles and demonstrated that larger alumina wear particles had a polygonal shape, with a bimodal size range of 0.5 – 2 μm. Whilst, smaller zirconia wear particles of 60 – 70 nm were round in shape.

Table 2.3. A summary of the characterisation of wear particles from different biomaterials

Biomaterial	**Particle type**	**Size**	**Shape**
Metal	CoCrMo [lee, asif]	10 – 120 nm [12], 50 – 130 nm [134]	Round and oval
Metal	Stainless Steel [lee]	10 nm – 1 mm [12]	Irregular and round
Polymer	UHMWPE [liu and lap]	<50 nm [119, 121]	Spherical and globular
Polymer	PEEK [Stratton]	10 nm – 50 μm [135]	Granular
Ceramic	Alumina [hatton]	5 – 90 nm [136]	Polygonal
Ceramic	ZTA [asif]	20 – 90 nm [134], 0.5 – 2.0 μm [134]	Polygonal and round

2.7 Biological responses to wear particles

2.7.1 Biological responses to metal wear particles

Although metallic implants are widely used in total joint replacements, metal wear particles may cause adverse biological effects, as well as accumulating in periprosthetic structures. Even with the lower volumetric wear of metal-on-metal implants, higher numbers of metal wear particles were observed compared to metal-on-polymer implants [105, 137]. Additionally, metal wear particles released from metal-on-metal implants present the risk of causing metallosis, metal hypersensitivity and pseudotumours. Metallosis is a severe complication of total joint replacements and occurs when there is an accumulation of metal debris in periprosthetic tissues [138]. It can induce a chronic inflammatory response, resulting in local or systemic effects including, aseptic implant loosening and osteolysis [138]. Metallosis has been reported in metallic spinal instrumentation and metal-on-metal artificial disc arthroplasty [8, 9]. Yang *et al* [8] reported a case of implant loosening, causing metallosis in a Bryan cervical disc replacement, made of Ti_6Al_4V. Similarly, Takahashi *et al* [9] reported two cases of

intraspinal metallosis in patient, who undertook spinal fusion surgery, using stainless steel Cotrel-Dubousset instrumentation. Furthermore, detrimental effects of metal wear debris in metal-on-metal hip replacements have led to patients requiring revision surgery, with the rates significantly higher than patients with metal-on-polymer bearings [139]. Around 1 in 5 metal-on-metal replacements, require revision surgery after 10 – 13 years, whilst only <4% of metal-on-polymer hip replacements required revision after 10 years [139]. Based on studies reporting adverse reactions and high failure rates in metal-on-metal hip replacements, the Zimmer Durom and DePuy Articular Surface Replacement (ASR) hip bearings were recalled in 2008 and 2010, respectively [139].

One of the main concerns in metal-on-metal arthroplasty is the complication of soft tissue inflammatory response from metal wear debris. The adverse reactions to metal wear debris can range from small asymptomatic cysts to pseudotumours, which refers to a granulomatous solid or a destructive cystic mass in the periprosthetic tissues [139, 140]. In revised, first and second generation, metal-on-metal hip prostheses, previous histological studies have demonstrated tissues infiltrated by macrophages with metal wear debris inside them [108]. The ingestion of metal debris by macrophages led to a cascade of pro-inflammatory responses, including stimulation of pro-inflammatory mediators, metal-reactive T lymphocytes, oxidative stress, DNA damage and cytotoxicity [101]. Furthermore, metal particles in necrotic cells and tissue have been observed [108]. Similarly, other studies including, Milosev *et al* [141] and Aroukatos *et al* [142] also reported extensive necrosis in the periprosthetic tissues of a metal-on-metal hip replacement. These findings are consistent with a study by Mahendra *et al* [143], which demonstrated inflammatory and necrotic changes, due to accumulation of Co-Cr wear debris in periprosthetic tissue. Metal wear debris plays a role in stimulating a reaction, which results in necrosis in surrounding tissues [142]. In addition, many studies have demonstrated that device failure can be associated with extensive necrosis [143-146].

The discharge of chemically active metal particles from total joint arthroplasty is a major issue, because the metals ions may induce toxic and biological reactions, including osteolysis, metallosis and inflammation [101, 105]. The wear particles from metal-on-metal bearings produce metal ions and nanoparticles, including Co and Cr [147]. The fine particulate wear debris can produce a large surface area for electrochemical processes,

causing further corrosion [105, 148]. Dissemination of metal particles into surrounding tissue, including lymph nodes, liver and kidney can occur via metal ions binding to proteins [101, 108]. The levels of metal ions in the bloodstream have demonstrated to increase after total joint replacement and sustained throughout the duration of implantation [101, 147]. Previous studies of metal-on-metal total disc arthroplasty have reported significant increases in Co and Cr ions of 3 – 4 ng/ml and 1 – 2 ng/ml, respectively. These results are consistent in patients with metal-on-metal hip arthroplasty [101]. Although, Co and Cr are important trace metals for maintaining normal homeostasis, excessive amounts may lead to cardiomyopathy, hypothyroidism, nephropathy and carcinogenesis [149, 150]. Furthermore, high levels of Ti have been reported in the liver of patients with failed Ti-based implants [149]. Ti wear particles can lead to increased osteolytic activity and stimulate pro-inflammatory responses via elevated TNF-α expression [151].

2.7.2 Biological responses to polymer wear particles

Osteolysis and aseptic loosening in artificial joint replacement failures are primarily associated with the release of UHMWPE wear particles [81, 152]. The earliest reports linking polyethylene wear particles with bone loss and implant loosening was by Revell *et al* [153] and Mirra *et al* [154]. Histological examinations of revised implants, due to aseptic loosening, have shown high numbers of macrophages and multi-nucleated giant cells accumulated inside thickened, highly vascularised fibrous periprosthetic membranes [154]. Many previous studies have consistently shown that UHMWPE wear particles are associated with the manifestation of macrophages and multi-nucleated giant cells [155]. Additionally, UHMWPE wear particles have been identified inside these cells.

Schmalzried *et al* [156] reported periprosthetic bone loss and macrophages infiltrated with polyethylene wear particles (mostly <10 μm in length) in patients with total hip arthroplasty. Furthermore, they also reported direct correlation between macrophage infiltration and the quantity of polyethylene wear particles [156]. Similarly, other histological studies, including Benz *et al* [157] have reported wear particles (< 3 – 5 μm), accumulated inside macrophages [157-159]. Whilst, multinucleated giant cells were observed to neighbour wear particles with sizes larger than 3 – 5 μm [157]. In retrieved

hip implants, the size of UHMWPE wear particles is generally 0.1 – 1.0 μm, which have been demonstrated to be the main reason for implant loosening [109]. The *in vitro* studies of wear particles generated, via hip joint simulation have reported that there was a greater mass of particles with a size, ranging 0.1 – 1.0 μm, compared to the wear particles obtained *in vitro* [116, 132]. The differences in these results may suggest that dissemination of submicron sized wear particles occur *in vivo.*

There have been *in vitro* studies conducted on the cellular responses to UHMWPE wear particles. Previous *in vitro* studies have investigated the reaction of macrophages to polyethylene wear particles [155]. When macrophages engulf wear particles, they release pro-inflammatory mediators. These consist of cytokines, including tumour necrosis factor α (TNF-α), interleukin-1 β (IL-1β), interleukin-6 (IL-6), which trigger the differentiation and proliferation of other cells in the immune system [108, 160, 161]. The inflammatory mediators stimulate osteoblasts to encourage the production of osteoclast-promoting factors, including granulocyte-macrophage colony-stimulating factor (GM-CSF) and Prostaglandin E_2 (PGE_2) [160, 161]. Consequently, the activation of osteoclasts, leads to bone resorption at close proximity to the joint replacement. In a previous study by Shanbhag *et al* [162], the authors reported that commercial UHMWPE wear particles generated higher levels of IL-1α, IL-1β and IL-6, compared with explanted wear particles. Furthermore, Green *et al* [163] demonstrated *in vitro* that different sizes and doses of UHMWPE wear particles have an effect on macrophage-induced bone resorption activity. A ratio of $(10\ \mu m)^3$ GUR1120 grade UHMWPE particles per macrophage, co-cultured with macrophages, induced bone resorption activity, when the mean size of particles were 0.24 μm, whilst larger particles did not. Additionally, when macrophages were co-cultured with a ratio of $(100\ \mu m)^3$ GUR1120 grade UHMWPE particles per macrophage, mean particle sizes of 0.45 μm and 1.7 μm increased bone resorption activity, whereas the 0.24 μm particles were inactive [163].

Cross-linking of UHMWPE was introduced to improve the wear resistance of the conventional UHMWPE. A previous *in vitro* study by Ingram *et al*, investigated the effects of cross-linking on the production of TNF-α in response to UHMWPE wear particles [164]. Ingram *et al* [164] reported that highly cross-linked UHMWPE wear particles had higher biological activity, compared to non-cross-linked material.

Specifically, 0.1 μm^3/cell of highly cross-linked UHMWPE achieved a significant increase in TNF-α production, whilst non-cross-linked UHMWPE required 10 μm^3/cell. Likewise, Illegen *et al* [165] showed that macrophages exposed to highly cross-linked UHMWPE produced significantly higher TNF-α than the conventional material.

More recently, there have been studies on the biological response to UHMWPE wear particles from spinal implants. In a study by Veruva *et al* [166], they compared the biological activity of UHMWPE wear particles in patients with LTDR and healthy patients. The authors found that the wear particles promoted inflammation, vascularisation and innervation [166]. The UHMWPE wear particles in total disc replacements, including the Mobidisc and Activ-L devices have been reported to stimulate an inflammatory reaction.

2.7.3 Biological responses to ceramic wear particles

Compared to metal and polymer wear particles, fewer studies have been conducted on the biological responses to ceramic wear particles both *in vivo* and *in vitro*. Additionally, studies on whether ceramic wear particles are associated with osteolysis have been inconsistent. Hernigou *et al* [167] compared wear and osteolysis between ceramic-on-ceramic and ceramic-on-polyethylene bearings in a 20-year follow-up study. Hernigou *et al* [167] showed that the volume of osteolysis was lower in the alumina-on-alumina hip implant than the alumina-on-polyethylene devices. Similarly, a follow-up study conducted by Huo *et al* [168] reported no incidence of osteolysis in patients using ceramic-on-ceramic total hip replacements. In contrast to those findings, Yoon *et al* [130] reported radiographic evidence of osteolysis in 22% of ceramic femoral heads and ~48% of acetabular components. Yoon *et al* [130] deduced that osteolysis was due to the stimulation of foreign body reactions from ceramic wear particles. Furthermore, Lerouge *et al* [129] examined pseudomembranes retrieved from ceramic-on-ceramic hip replacements using histology. Cellular infiltration was reported to be similar, compared to failed UHMWPE-on-metal devices. The characterisation of the ceramic wear particles showed 76% zirconia wear particles and 12% alumina wear particles. Therefore, Lerouge *et al* [129] deduced that zirconia wear particles caused the cellular response and alumina had no effect.

In vitro studies on the biological responses to ceramic wear particles have been limited [108]. Similar to the findings by Lerouge *et al* [129], Li *et al* [169] demonstrated that alumina particles had no cytotoxic effects on human fibroblasts *in vitro* but zirconia particles reduced cell viability [170]. Furthermore, Kim *et al* [171] reported that alumina wear particles (3 μm) stimulated the production of IL-1, IL-6 and resorption of bone in rabbit synoviocytes. Submicron-sized alumina wear particles *in vitro* (mean of 0.5 ± 0.19 μm) have shown to stimulate TNF-α production from peripheral blood mononuclear cells [136]. These studies suggest that the biological response elicited by ceramic wear particles show some similarities to responses triggered by UHMWPE wear particles.

2.8 Animal models of biological responses to wear debris

The biological responses to wear debris in biomaterials used in total joint replacements have been investigated in animal models. One of the first studies, conducted by Meachim and Brooke [172], investigated the tissue responses to Co-Cr particles in guinea pig knee joints. The authors reported phagocytosis of smaller Co-Cr particles (0.5 – 50 μm) by macrophages, giant cells, intimal cells and fibroblasts. Cells infiltrated with Co-Cr particles were present in synovium for a few months, which suggests slow wear particle clearance [172]. Additionally, dissemination of Co-Cr particles to the inguinal lymph nodes were also observed. One of the limitations to this study by Meachim and Brooke [172] was the imprecise size and morphology of milled particles that would be characterised *in vivo*, which were not clinically relevant.

In response to the limitations of previous studies regarding non-clinically relevant particle characterisation, Papageorgiou *et al* [173] conducted an organ culture study of porcine dura mater to investigate the biological impacts of clinically relevant nanometre-sized Co-Cr particles (20 – 60 nm). The dura mater is the outermost layer of the meninges and it protects tissues of the brain and spinal cord from harmful foreign objects and mechanical injury [174]. Although Co-Cr nanoparticles in the dura mater did not show significant reduction in cell viability, significant structural changes including, loosening of the epithelial and collagen layers were observed [173]. The structural damage of the dura mater could ultimately lead to local inflammation of neural tissue.

The biological effects of titanium wear debris have previously been investigated in animal models. In a study by Chang *et al* [13], titanium debris were acquired from a spine wear simulator and were inserted into the lumbar region of 23 New Zealand white rabbits (10 placed in a retroperitoneal group and 13 in an epidural grouped). Under histological examination, titanium wear particles produced minimal biological response with no adverse effects observed. One of the drawbacks of this study was the absence of a control group for comparison. In a similar animal study with the use of a control group (autograft alone), Cunningham *et al* [175] reported elevated levels of pro-inflammatory cytokines (TNF-α) in response to titanium-treated autograft for spinal arthrodesis (L5-L6) in New Zealand white rabbits. In a more recent study conducted by Cunningham *et al* [176], the neurotoxicity of wear particles from different types of biomaterials used in spinal instrumentation were investigated in 120 New Zealand white rabbits. The rabbits were randomised into 12 equal groups including a control (epidural exposure alone) and 11 treatment groups based on the biomaterial and the wear particles were administrated epidurally. The treatment groups demonstrated elevated levels of epidural fibrosis, compared with the control group. Under histopathological examination, local inflammation and phagocytosed inert wear particles were observed in the fibrous tissues. After 3 months of particle implantation, the metallic and UHMWPE wear particle groups demonstrated increased levels of the pro-inflammatory cytokine, IL-6, and the stainless steel and UHMWPE groups displayed the highest levels of macrophage activity [176]. However, at 6 months post-operation, the cytokine and macrophage activities were downregulated in most treatment groups.

Animal models have been important for researchers to investigate biological responses of tissues to wear debris. There are some limitations to animal studies including variability of animals and interspecies differences [177]. Improvements in animal models can be achieved with higher quality criteria including, appropriate controls and sample size, and better particle generation techniques to ensure clinical relevance [178].

2.9 Neural cell types used in CNS modelling

The two types of cells in the Central Nervous System (CNS) are neurons and glia. Neurons are nerve cells and act as the primary functional unit of the nervous system.

Neurons process and transmit information via electrical and chemical signals. Glial cells are non-neuronal cells that provide neuron-supporting functions. Glial cells can be classified into microglia and macroglia. Microglia are considered the immune cells of the CNS and travel around the brain and spinal cord to remove waste, pathogens and other foreign substances. Macroglia have three main subtypes, including astrocytes, oligodendrocytes and ependymal cells. Astrocytes are involved in the structural support of the brain, as well as repairing damage, maintaining the blood-brain-barrier (BBB) and control neuronal communication. Oligodendrocytes are responsible for supporting and insulating neurons with myelin in the CNS. The ependymal cells are located in the walls of the ventricles and are essential in the production and circulation of cerebrospinal fluid, which functions to remove waste and protect the brain from injury.

Immortalised cell lines are primary cells, which have been manipulated to create indefinite reproduction and allows them to be passaged numerous times in cell culture [179]. Neuronal cell lines are derived from neuronal tumours or can be produced by genetic modification of healthy cells. *In vitro* research on neuronal processes and differentiation have commonly used PC-12 cells (derived from pheochromocytoma in the rat adrenal medulla) and P19 cells (derived from embryo-derived teratocarcinoma in mice) [179]. Additionally, PC-12 cells have been widely used to examine the neurotoxicity of several substances, e.g. by evaluating the impacts on cell survival or DNA damage [180]. Another cell line that has been used in neural cell culture is NG108-15. NG108-15 is a neuronal hybrid cell line from mouse neuroblastoma and rat glioma. Neuronal 3D *in vitro* co-culture involving NG108-15 cells and Schwann cells (SC) have been studied by Kraus *et al* [181] and Daud *et al* [182] as peripheral nerve models. Both studies reported neurite outgrowth, which supports the use of NG108-15 cells in 3D models for studying *in vitro* peripheral nerve regeneration [181, 182]. No studies have been conducted to investigate the biological responses of wear particles on NG108-15 cells.

Another type of neural cell line often used in modelling the CNS is the C6 glial cell line (derived from a rat glial tumour). In a previous study by Guzman and VandeVord [183], C6 rat astrocytoma and Rat2 fibroblast cell lines were utilised *in vitro* to model astrocytes and meningeal fibroblasts in 2D culture, respectively, to investigate the responses of

astrocytes and fibroblasts to biomaterial particles. Guzman and VandeVord [183] demonstrated that C6 cells responded to titanium alloy particles via differentiation into reactive astrocytes. Since glial scars are mostly comprised of reactive astrocytes in its final state, Guzman and VandeVord's [183] study was essential in showing the potential of titanium alloys in stimulating glial scar formation.

2.9 2D and 3D neural cell culture models

Cell culture is an essential *in vitro* tool utilised in biomedical research, regenerative medicine and tissue engineering. Previous *in vitro* research on investigating the biological responses to wear debris have been mainly conducted using two-dimensional (2D) cell culture. The cells in the conventional 2D cell culture grow as a monolayer, which adhere to an artificial flat surface of a flask or petri dish. The use of 2D cell culture is advantageous in terms of its simplicity and cost-effectiveness. The monolayer growth of cells in 2D cell culture, results in a homogenous distribution of nutrients and growth factors to all the cell, which allows for uniform proliferation. [184]. Even though 2D cell culture is predominantly used *in vitro* as the culture system, there are some limitations that have been demonstrated. One of the main disadvantages is the reduced cell-cell and cell-extracellular matrix interactions, which can negatively impact cell differentiation, responsiveness to mechanical stimuli and protein/gene expression [169, 185-187]. *In vitro* 2D cultures of neural cells provides a simple and efficient system for studying biological processes and CNS diseases [185]. However, the lack of *in vivo* mimicry from 2D cell culture, restricts it being a physiologically relevant model for modelling the CNS [188]. Another disadvantage is that 2D culture systems can result in changes in cell morphology, which can impact cell function, cell signalling and the internal structural organisation of the cell [185]. The limitations of 2D cell culture has resulted in recent research in the development of three-dimensional (3D) cell models.

3D cell culture allows the cells to be grown in a microenvironment, which more closely resembles the conditions and structures *in vivo* [185]. The 3D culture system provides a better cell-cell and cell-extracellular matrix connections, which allows it to be more physiologically relevant, compared to the 2D culture system [189]. 3D cell culture can be categorised into two techniques: scaffold-based cell culture and scaffold-free cell culture.

One of the scaffold-free cell culture models is the spheroid cultures, which form by aggregation of cells. 3D spheroids provide advantageous properties, including mimicking many characteristics of solid tissues, generating cell-cell and cell-extracellular matrix interactions similar to ideal physiological conditions, and being easily quantifiable, using confocal and light fluorescence microscopy [190, 191]. The advantages and disadvantages of 2D and 3D cell culture are shown in Table 2.

Table 2.4. A comparison of 2D and 3D cell culture

	Advantages	Disadvantages
2D cell culture	• Cost effective • Simple and convenient • Uniform access to nutrients, oxygen and growth factors • Well established assays	• Reduced cell-cell and cell-extracellular matrix interactions • Unable to mimic *in vivo* microenvironment • Limited complexity • Less physiologically relevant
3D cell culture	• Cell-cell and cell-extracellular matrix interactions similar to *in vivo* • Able to mimic *in vivo* microenvironment • More physiologically relevant	• Expensive • Time-consuming • Challenges in microscopic analysis and measurement

Scaffold-based 3D cell culture can be produced by seeding cells on a biodegradable 3D scaffold, or by growing cells in medium comprising of gel-like substances, followed by solidification [185, 192]. The design of 3D neural cell culture systems are divided into physical and biochemical requirements [179]. Neural tissue have low stiffness, with elastic moduli of less than 1 kPa for neurons [193] and approximately 40 – 230 kPa for

the spinal cord [194, 195]. Consequently, a scaffold with low stiffness would closely mimic the mechanical properties *in vivo*. In addition, previous researchers have demonstrated that neural cell cultures that utilise hydrogels with <80 kPa elastic modulus, have been most successful [196-198]. Additionally, scaffolds need to be biodegradable in order for cells to grow new extracellular matrix [199]. Having a porous, interconnected architecture is important for neuron growth in 3D scaffolds, because it allows the diffusion of nutrients and cell migration within the structure [179, 200]. Furthermore, the biomaterials used in scaffolds should also be bioactive to ensure cell adhesion and proliferation, via the binding of integrin or adhesion receptors to the biomaterials [179]. The most commonly used scaffolds for *in vitro* 3D neural cell culture are hydrogels, which have been successful due to their low stiffness, facile diffusion of nutrients, oxygen and waste, and cell adhesion [201]. Naturally derived hydrogels, including collagen, agarose, alginate, chitosan, hyaluronic acid have been utilised in 3D cell culture, due to their inherent biocompatible and bioactive characteristics [179, 190, 202].

Collagen (Type I) is commonly utilised substrate in 3D cell culture models and has been prevalently applied in tissue engineering research [203]. Collagen is the main fibrous protein found in the extracellular matrix and is a major element in tissues, including bone, cartilage, skin and blood vessels [204]. Collagen (Type I) have been used *in vitro* for modelling the CNS, because it stimulates significantly higher neural cell attachment and survival, compared to other hydrogel materials [205, 206]. In 3D collagen-based hydrogel cultures, Watanabe *et al* [207] reported differentiation of neural stem cells into neurons, astrocytes and oligodendrocytes. Similarly, Huang *et al* [208] demonstrated an increase in neural stem cell differentiation *in vitro* when cultured in collagen-based scaffolds, compared to neural stem cells grown in suspension. In another study using the 3D collagen hydrogel system, East *et al* [209] developed an *in vitro* model for astrogliosis (abnormal elevation of astrocytes). East *et al* [209] found that astrocytes were less reactive in 3D cell culture than in 2D, due to the downregulation of activation markers in 3D culture. Consequently, the 3D culture system provided a better astrogliosis model, as the astrocytes were able to stimulate astrogliosis from its "ground state." Collagen hydrogels have some limitations including, inadequate long-term stability, high variability of properties, and batch-to-batch variability.

Similarly, hyaluronic acid is found in many tissues, including the brain, skin and is an essential in contributing to tissue regeneration, development and disease [210]. Since hyaluronic acid is a primary component in the extracellular matrix of brain tissue, it has been attractive substrate to be utilised in neural tissue engineering [179]. Hyaluronic acid has been used in 3D cell culture to model glioblastoma. Pedron *et al* [211] successfully modelled an extracellular microenvironment for investigating the development of glioblastomas, using a hyaluronic acid-based hydrogel system. Additionally, Seidlits *et al* [212] demonstrated that hyaluronic acid hydrogels were able to guide the differentiation of neural progenitor cells, by regulating the stiffness of the hydrogel. The advantages of hyaluronic acid are its physiological relevance and being chemically modifiable. The ability of hyaluronic acid to be modified allows it to be used processed into different hydrogel systems, including 2D and 3D culture systems, as well as an injectable hydrogel. One of the limitations is the absence of integrin-mediated cell adhesion in untuned hyaluronic acid, however they are able to communicate with cell surface markers including CD44 and CD168 [213].

Alginate-based hydrogels have been utilised in applications including, tissue engineering and drug delivery. Unlike collagen, alginate requires functionalisation with adhesive ligands to promote cell attachments. Frampton *et al* [214] manufactured and optimised alginate-based hydrogels for 3D neural cell culture using cells including, astrocytes, neurons and microglia. Neural cells were reported to exhibit neurite outgrowth over a period of time in culture [214]. Additionally, Matyash *et al* [215] demonstrated the neuroprotective effects of alginate hydrogels, as neurons showed resistance to oxidative stress. Alginate-based hydrogels could be useful for neural tissue engineering applications.

Polyethylene glycol (PEG) is a synthetic polymer that has been used for *in vitro* cell culture, due to its tunability of mechanical properties, and its relative inertness [179, 210]. Previously, 3D neural cell culture studies have been conducted using PEG-based hydrogels. Wang *et al* [107] investigated the effects of the hydrogel scaffold stiffness on glioblastoma cells, and showed that higher stiffness resulted in slower cell proliferation in the hydrogel, however denser spheroids were formed by the cells, with cell projections [216]. Modified PEG hydrogels have shown to improve the efficacy of PEG [217]. One

of the limitations of PEG hydrogels is the lack of remodelling by cells. Additionally, the lack of cell adhesion in PEG hydrogel scaffolds, due to their bio-inertness is another drawback [218]. To overcome this limitation, PEG-based hydrogels modified with polylysine were able stimulate neural cell adhesion and improve the stability of neural interactions in a study by Rao *et al* [219]. Additionally, Zhou *et al* demonstrated that neurite growth in PEG hydrogels increased when the concentration of fibronectin increased [206].

Gelatin methacryloyl (GelMA) has been recently used in 3D cell culture, due to its appropriate biological properties and tailorable physical properties [220, 221]. GelMA-based hydrogels closely mimics the native extracellular matrix, due to the widespread distribution of arginine-glycine-aspartic acid (RGD) sequences, which encourage cell adhesion and proliferation [220, 222]. In addition, matrix metalloproteinase (MMP) sequences in GelMA stimulate enzymatic cleavage, which allow for cellular remodelling [220-222]. Functionalisation of materials has been recently utilised as a technique to overcome the limitations of natural materials [223]. One example is photo-crosslinking GelMA, by exposure to light irradiation, which provide tuneable physical properties [220]. Photo-crosslinkable hydrogels have been widely investigated in engineering 3D tissue constructs, bio-sensing and drug delivery [224]. GelMA hydrogels have also been used in 3D neural culture studies. Wu *et al* demonstrated that there was a critical range for the elastic modulus of GelMA hydrogels to stimulate the outgrowth of PC12 cells [225]. Similarly, Zhu *et al* [226] reported that 3D bio-printed GelMA hydrogels were successful in modelling a biocompatible microenvironment for neural stem cell survival and growth. In addition, neural stem cells encapsulated in the hydrogel displayed neuron differentiation and neurite outgrowth [226]. Furthermore, in a spinal cord injury model conducted by Fan *et al* [227], the neural stem cells grown in GelMA hydrogels, promoted neural regeneration and inhibited glial scar development [227]. Previous research on 3D neural culture systems show the potential of 3D bio-printed GelMA hydrogels in neuroregeneration and modelling spinal cord injury.

The rationale for using bioprinting techniques for developing 3D bio-constructs instead of traditional methods, includes the many advantages it presents for example, greater precision in spatial control, and increased complexity and mimicry of the *in vivo*

organisation of tissues [228, 229]. Currently, there are different methods of 3D bioprinting, including stereolithography bioprinting, inkjet-based bioprinting, laser-assisted bioprinting, extrusion-based bioprinting and electrospinning-based bioprinting. Stereolithography bioprinting utilises a laser to solidify photosensitive liquid resin through a layer-by-layer process. The principle of inkjet-based bioprinting is similar to traditional inkjet printing demonstrated in desktop ink printing, which involves the deposition of tiny droplets of bioink. Laser-assisted bioprinting utilises laser energy to deposit bioink through laser pulses in a layer-by-layer manner. In addition, electrospinning-based bioprinting utilises a high electric voltage field to support the deposition of material through a needle [230]. A summary of bioprinting techniques is displayed in figure 2.8.

One of the main bioprinting technologies is extrusion-based 3D bioprinting, which is widely utilised in tissue engineering applications [228, 229, 231]. Extrusion-based bioprinting uses a dispensing system to extrude a bioink, which is a formulation of cells, biological molecules, and biomaterials [231, 232]. Bioprinting using the extrusion technique occurs through an automated computer program. One of the advantages of extrusion-based bioprinting is the ability to bioprint highly viscous bioinks and also being able to use a variety of biocompatible bioinks including, cell-laden hydrogels and cell aggregates [231]. Another advantage is the ability to bioprint structures with high cell density [228]. Furthermore, the extrusion-based technology is easy-to-use and prints at high speed to promote scalability [231]. In this study, the BIO X and BIO X6 printers developed by CELLINK were used for the extrusion-based bioprinting of hydrogels to create a 3D cellular model. The BIO X and BIO X6 printers were chosen due to their ability to support a range of bioinks consisting of cell-laden hydrogels, and also the delivery of high precision printing while also being user-friendly.

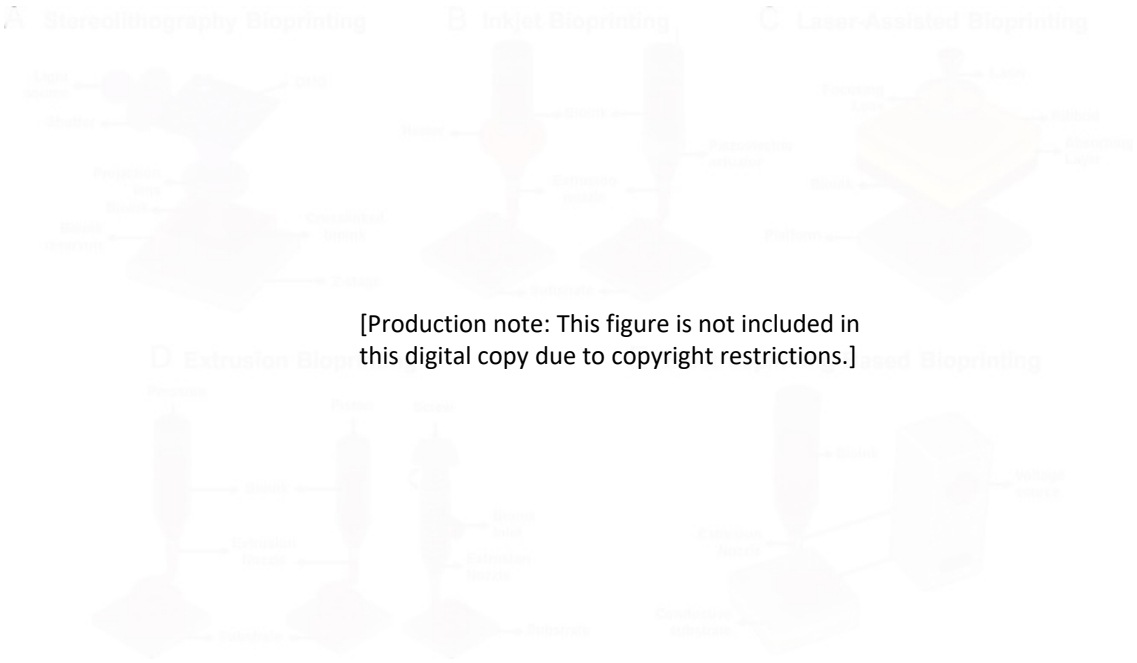

[Production note: This figure is not included in this digital copy due to copyright restrictions.]

Figure 2.8. A schematic summary of different bioprinting techniques used in 3D bioprinting. (A) Stereolithography; (B) Inkjet-based; (C) Laser-assisted; (D) Extrusion-based; € Electrospinning-based. Figure adapted from [230].

Chapter 3

Materials and Methods

3.1 Materials

The general materials used in this study are detailed in chapter 3.

3.1.1 Chemicals and reagents

The chemicals and reagents used in the study are listed in table 3.1.

Table 3.1. General chemicals and reagents used in this study.

Chemical/Reagent	**Supplier**	**Storage Conditions**
ATP Luminescence detection assay kit	Abcam	Stored at -20ºC
CellTiter-Glo 3D cell viability assay kit	Promega	Stored at -20ºC
Dimethyl Sulfoxide (DMSO)	Sigma Aldrich	Stored at room temperature (25ºC)
Dulbecco's Modified Eagles Medium (DMEM)	Gibco	Stored at 4ºC
Dulbecco's Phosphate Buffered Saline (DPBS) solution	Sigma Aldrich	Stored at 4 ºC
Ethanol	Thermofisher	Stored at room temperature (25ºC)
Foetal Bovine Serum (FBS)	Bovogen	Stored at -20ºC
Gelatin Methacrylate (GelMA) powder	CELLINK	Stored at -20ºC
Ham's F-12 Nutrient Mixture	Sigma Aldrich	Stored at 4ºC
Horse Serum	Sigma Aldrich	Stored at -20ºC
L-glutamine	Gibco	Stored at -20ºC

Lithium phenyl-2,4,6-trimethylbenzoylphosphinate (LAP)	CELLINK	Stored at -20ºC
Live/Dead cell imaging kit	Invitrogen (Thermo Fisher)	Stored at -20 C
MTT (3-(4,5-Dimethylthiazol-2-yl)-2,5-Diphenyltetrazolium Bromide) reagent & solvent	Abcam	Stored at -20ºC
Penicillin/Streptomycin	Gibco	Stored at -20ºC
Phosphate buffered Saline (PBS) solution	Gibco	Stored at 4ºC
Reactive Oxygen Species (ROS) detection assay kit	Abcam	Stored at -20ºC
Trypan Blue solution	Sigma Aldrich	Stored at room temperature (25ºC)
Trypsin-EDTA solution	Gibco	Stored at -20ºC

3.1.2 Equipment

The equipment used in this study are listed in Table 3.2.

Table 3.2. General equipment used in this study

Equipment	**Supplier**
Balance	A&D Company, Limited
Class II Biosafety Cabinet	Thermoline Scientific
Centrifuge (Multifuge X1R)	Thermo Scientific
Confocal microscope (Nikon A1 HD25)	Nikon
Cryopreservation freezer	New Brunswick
EVOS M5000 microscope	Thermo Fisher Scientific
Freezer (-20ºC)	Skope
Freezer (-80ºC)	New Brunswick
Fluorescent microscope (Olympus DP80)	Olympus Life Science

Fume cupboard	Thermoline Scientific
Image analysis software	ImageJ
Incubator (Heracell™ VIOS 160i)	Thermo Scientific
Inverted light microscope (Olympus CKX53)	Olympus Life Science
Microplate reader (Varioskan LUX)	Thermo Scientific
Oven	Skope
Plate shaker	Thermo Scientific
Refrigerator (4^{o}C)	Skope
Scanning electron microscope (EVO LS15)	Zeiss
Scanning electron microscope (Supra 55 VP)	Zeiss
Sonicator	Unisonics Australia
Water bath	Thermoline Scientific

3.1.2 Consumables

The consumables used in this study are listed in Table 3.3.

Table 3.3. General consumables used in this study

Item	Size	Supplier
Cryovial	1 mL	ThermoFisher Scientific
Falcon tubes	50 mL	Westlab
Plastic petri dishes	Various sizes	Westlab
Plastic pipette tips	10 µL, 20 µL, 100 µL, 200 µL, 1000 µL	Neptune Scientific
Plastic serological pipettes	5 mL, 10 mL, 25 mL	Sarstedt
Polycarbonate membrane filter paper	8 µm, 0.8 µm	Whatman
Syringe Filter	0.22 µm pore size	Thermofisher Scientific
Tissue culture flasks	25 cm^2, 75 cm^2	SPI Life Sciences
Tissue culture plates (Flat bottom)	6 well, 12 well, 24 well, 48 well, 96 well	Corning
Weighing boats	Various sizes	Thermofisher Scientific

The cell lines used in this study are listed in table 3.4.

Table 3.4. Cell lines used in this study.

Cell Line	Species/Origin	Supplier
C6	Rat glioma	American Tissue Culture Collection (ATCC)
NG108-15	Mouse neuroblastoma fused with rat glioma	European Collection of Cell Cultures (ECACC)

3.1.3 Particles

The particles used in this study are listed in table 3.5.

Table 3.5. Model particles used in this study.

Material	Supplier
Polyetheretherketone (PEEK) OPTIMA	Invibio Biomaterial Solutions
Polyethylene (Ceridust® 3615)	Hoescht, Germany
Zirconia Toughened Alumina (ZTA)	Inframat Advanced Materials, USA
Cobalt Chromium Molybdenum Alloy (CoCr-Mo)	American Elements, USA

3.2 Methods

The general methods used in this study are described below.

3.2.1 Sterilisation

Sterilisation of equipment was essential to ensure a sterile working environment. The different sterilisation methods used in this study are described below.

3.2.1.1 Aseptic technique

Aseptic technique was used when conducting experimental work with the class II biosafety cabinet. Before and after conducting work in the cabinet, UV light was turned on for 30 minutes each time for disinfection. The interior surfaces of the cabinet were

sprayed with 70% (v/v) ethanol, prior to use. All items were also sprayed with 70% (v/v) ethanol before entering the cabinet.

3.2.1.2 Filter sterilisation

Filtration of solution was conducted when preparing the LAP solution mixed with PBS. The LAP/PBS solution was filter sterilised using a 0.22 μm syringe filter in the class II biosafety cabinet.

3.2.2 Preparation of solutions for cell culture

3.2.2.1 Cryopreservation medium for cells

The cryopreservation media for C6 cells was Ham's F-12 nutrient mix, supplemented 20% (v/v) FBS and 10% (v/v). For NG108-15 cells, the cryopreservation media consisted of DMEM, supplemented with 20% (v/v) FBS and 10% (v/v). Before use, the cryopreservation media was warmed to 37ºC in the water bath.

3.2.2.2 Complete cell culture medium for C6 cells

Ham's F-12 nutrient mixed was supplemented with 10% (v/v) FBS, 2 mM L-Glutamine and 100 $U.ml^{-1}$ penicillin/ 100 $\mu g.ml^{-1}$ streptomycin. Complete cell culture medium was stored at 4ºC.

3.2.2.3 Complete cell culture medium for NG108-15 cells

DMEM was supplemented with 10% (v/v) horse serum, 2.5% (v/v) FBS and 100 $U.ml^{-1}$ penicillin/ 100 $\mu g.ml^{-1}$ streptomycin. Complete cell culture medium was stored at 4ºC.

3.2.3 Cell culture and maintenance

Cell culture involved thawing, maintenance, passaging, and cell counting, which were all performed in class II biosafety cabinets. Prior to cell culture, the biosafety cabinet was sterilised with ultraviolet (UV) radiation for 30 minutes. Cell culture medium media and supplements were pre-warmed to 37ºC in the water bath prior to cell culture. All cells were cultured in tissue culture flasks at 37ºC and 5% (v/v) CO_2 in the incubator.

3.2.1.2 Cell thawing and reviving

C6 and NG108-15 cell lines were cryopreserved in liquid nitrogen at -196ºC. Cells, stored in a 1 mL cryovial were thawed in the water bath (37ºC), by gently swirling the cryovial, and transferred into a 15 mL centrifuge tube. Pre-warmed cell culture medium (8 mL) was added into the centrifuge tube and cells were thoroughly mixed. The cryovial was rinsed with 1 mL of cell culture medium, to ensure all cells were taken out, and transferred to the centrifuge tube. The cells were centrifuged at 300 g for 5 minutes at room temperature to ensure separation of cells from the cryopreservation medium. After centrifugation, the supernatant was aspirated to isolate the cell pellet and resuspended in 3 mL of cell culture medium. The cell suspension was transferred to a T75 cell culture flask and an extra 7 mL of cell culture medium was added. The cells were observed under a light microscope and then the flask was placed in the incubator at 37ºC and 5% CO_2. After 24 hours, the cells were observed again under the light microscope to confirm adherence of cells to the flask.

3.2.1.3 Cell culture medium replacement

To ensure preservation of cell numbers, it was essential to change cell culture medium. This was done by aspirating the old medium and replacing it with 10 mL of fresh cell culture medium. The flasks were placed back in the incubator at 37ºC and 5% CO_2.

3.2.1.4 Cell maintenance and passaging

Cell passaging was conducted when the cells reached approximately 70 – 80% confluency in the culture flasks. Prior to passaging, complete cell culture medium and trypsin were pre-warmed at 37ºC in the water bath. The cell culture medium in the flask was aspirated and washed with PBS. Afterwards, 0.25% (v/v) Trypsin-EDTA (1 mL for T25 flask and 3 mL for T75 flask) was added into the flask and incubated at 37ºC and 5% CO_2 for 3 minutes. The flasks were gently tapped to ensure detachment of all adherent cells from the flask. Equal volumes of complete medium were added to deactivate trypsin. The cell suspension was transferred to a 15 mL tube and centrifuged for 5 minutes at 300 g. After centrifugation, the supernatant was aspirated, isolating the pellet. Fresh cell culture medium was added to the tube and thoroughly mixed by pipetting up and down. Cells

were transferred into a new cell culture flask with fresh cell culture medium. The flasks were kept in the incubator at 37°C and 5% (v/v) CO_2 for maintenance.

3.2.1.5 Cell counting

Cell counting was done by using the cells that were re-suspended in fresh cell culture medium after the centrifugation step in the cell passaging process. Cell counting was performed using the Trypan blue exclusion assay. Trypan blue 0.2% (v/v) was mixed with cell suspension at a ratio of 1:1. A volume of 10 µL of cell suspension was added to an Eppendorf and 10 µL of Trypan blue 0.2% (v/v) was thoroughly mixed with the cell suspension. A haemocytometer was cleaned using 70% (v/v) ethanol and a glass coverslip was placed on top of it. A volume of 10 µL of the Trypan blue/cell suspension mixture was pipetted into a chamber of the haemocytometer. The haemocytometer was placed under the inverted light microscope and focused on the grid lines, using a 10X magnification. The haemocytometer was moved to one set of 4 x 4 square. Cells located on the top edge and left edge of the 4 x 4 square were included in the count. Cells located on the bottom edge and right edge of the square were excluded in the cell count. After counting each corner square, the average cell number per square was calculated. Figure 3.1 shows a representation of the haemocytometer under the microscope and the areas that the cell count included.

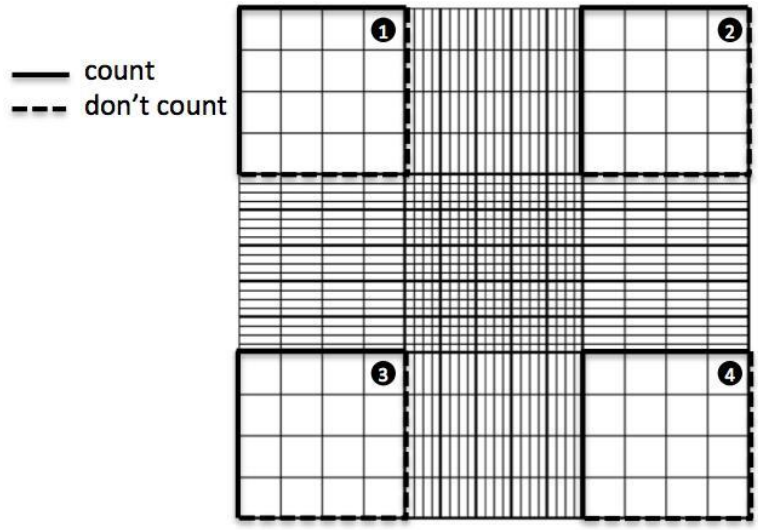

Figure 3.1. A representation of the haemocytometer as seen under the microscope. Cells lying on the solid line for squares labelled 1 – 4 are counted (top and left line) and cells lying on the broken line are not counted (right and bottom line). After cell counting, the density of the cells was calculated using this formula:

$$\frac{\text{Total number of viable cells*dilution factor*}10^4}{\text{Number of squares counted}} \text{ cells/ml}$$

The dilution factor was a two-fold dilution, when mixing equal volumes of Trypan blue and cell suspension. The dilution factor per mL was 1 x 10^4.

3.2.1.5 Cell cryopreservation

Cells were cryopreserved in liquid nitrogen at -196°C for future use. Cells were passaged using a method mentioned in section 3.2.1.3. Cells were then counted using the method mentioned in 3.2.1.4. The cell pellet obtained after centrifugation was re-suspended in 1 mL a cryopreservation medium, which consisted of 70% (v/v) complete medium, 20% (v/v) FBS, and 10% (v/v) DMSO at a cell seeding density of 1 x 10^6 cells per mL of cryopreservation medium. The cell suspension was transferred into 1 mL cryovials and were stored in a -80°C freezer. For long-term cryopreservation, cells were transferred to liquid nitrogen.

3.2.2 Microscopy

The general methods used in bright field and fluorescence microscopy are detailed below.

3.2.2.1 Bright field microscopy

An inverted microscope, Olympus CKX53 was used for bright field microscopy and was useful for cell culture applications including observing and counting cells. The inverted microscope was suitable for observing cells and samples in petri dishes, tissue culture flasks and multi-well plates.

3.2.2.2 Fluorescence microscopy

Microscopes used for fluorescence microscopy included Olympus DP80 and Nikon ECLIPSE Ti2. Fluorescence microscopy was utilised for imaging fluorescently stain cells for qualitative analysis of cell viability. The emission filters used for fluorescent imaging included green fluorescent protein (GFP, emission: 525/50 nm), red fluorescent protein

(RFP, emission: 593/40 nm) and 4',6-diamidino-2-phenylindole (DAPI, emission: 447/60 nm).

3.2.2.3 Confocal microscopy

Confocal microscopy was utilised to perform 3D imaging and Z-stacks. Z-stacks are a series of images that are obtained at different focal planes on the z-axis, which can provide a detailed representation of a sample's 3D structure. The technique of point-by-point scanning in addition with a confocal pinhole of the confocal microscope allows for improved optical sectioning, improved contrast and resolution, compared to wide field microscopy. In this study, EVOS M5000 and Nikon A1 HD25 confocal microscopes were used for imaging fluorescently stained cells in 3D bioprinted structures. Z-stacks were obtained by capturing images at incremental distances along the z-axis. For example, in this study, a total thickness of 200 µm was imaged at 5 µm intervals to obtain 40 image slices. The initial point of the z-position was determined when cells first appeared.

3.2.3 Preparation of particles

Particles of different materials, including polymers, metallic and ceramic were used in this study. Polymer particles used were Polyetheretherketone (PEEK) and polyethylene (Ceridust® 3615). The type of ceramic particle used was Zirconia Toughened Alumina (ZTA) and the type of metallic particle used was Cobalt Chromium Molybdenum Alloy (CoCr-Mo).

3.2.4 Image analysis of particles using Image J

Analysis of particle morphology and size was conducted using a computer software called ImageJ. Measurement of area, length and width of each region of interest (ROI) was enabled by installing, a plug-in called "Measure_ROI," which was downloaded from the website: https://www.optinav.info/Measure-Roi.htm. The ROI in this case refers to the outline of each particle. The installed "Measure_ROI," provided a ROI manager in ImageJ that allowed temporary storage of measurements of multiple particles that were labelled on the image. Prior to measuring particle sizes, scale calibration was performed to convert the image dimensions in pixels to physical dimensions. Each particle was

measured by drawing around the perimeter and then added to the ROI manager, where the area, length and width of each particle were recorded.

3.2.5 Preparation of GelMA hydrogel solution

The preparation of the GelMA hydrogel solution was conducted using the GelMA Kit from CELLINK, which included GelMA powder and a photoinitiator called, Lithium phenyl-2,4,6trimethylbenzoylphosphinate (LAP). The photoinitiator was dissolved in phosphate-buffered saline (PBS) and mixed at 60ºC for 20 minutes to make a solution with a concentration of 0.25% (w/v). The LAP/PBS solution was then filter-sterilised (0.22 μm) in a class II biosafety cabinet. The LAP/PBS solution was then added to the GelMA powder and mixed at 50ºC for 20 minutes to make a GelMA solution with a concentration of 5% (w/v). The GelMA solution was stored in the fridge at 4ºC for future use.

3.2.6 Bioprinting 3D GelMA hydrogel solution

The neural cells, C6 and NG108-15 cells were cultured in a flask at 37ºC and 5% (v/v) CO_2. When cells reached 80% confluence, cell culture medium was removed, and trypsin was added to the flask and incubated for 3 minutes to ensure cells were detached. Afterwards, the same volume of cell culture medium was added to neutralise the trypsin and the solution was transferred to a 15 mL falcon tube. The cell solution was centrifuged for 5 minutes at 250 G. Then, the supernatant was aspirated, and the cell pellet was resuspended in fresh cell culture medium.

The GelMA solution was placed in the incubator at 37ºC, prior to bioprinting. Cells were mixed with GelMA solution at a ratio of 1:10. For example, 1 mL of GelMA solution was mixed with 100 μL of cells. The solution was transferred to a 3 mL cartridge and a piston was placed on top of the solution. The nozzle was screwed onto the cartridge and then inserted into the print head of the bioprinter. The detailed bioprinting parameters are described in the sections 5.4.1.2 and 5.4.1.3.

3.2.7 Quantitative cell viability assays

Cell viability assays were utilised to quantitatively analyse NG108-15 and C6 cell viability. Cells were seeded into 96 well plates for quantitative analysis of cell viability. Both a MTT (3-(4,5-dimethylthiazol-2-yl)-2,5-diphenyltetrazolium bromide) assay and a Luminescent ATP detection assay were used to determine cell viability in 2D using a microplate reader. CellTiter-Glo 3D cell viability assay was utilised to investigate cell viability in a 3D cell culture model.

MTT assay is an in vitro method to assess the viability, proliferation, and cytotoxicity of cells. Cell viability is quantified by using 3-(4,5-dimethylthiazol-2-yl)-2,5-diphenyltetrazolium bromide (MTT) which involves the reduction of yellow tetrazolium by action of dehydrogenase enzymes into an insoluble, dark purple formazan. This assay allows the analysis of cell proliferation rate, cell apoptosis and cell viability. Viable cells with active metabolism have the ability to reduce the yellow coloured MTT into the dark purple formazan, while dead cells lose the ability of the purple colour formation. Solubilisation of the formazan is done by the addition of a solvent, commonly DMSO. The formation of colour is an indication of viable cells. When absorbance is measured at 590 nm, the signal produced is proportional to the metabolic activity of the cells, and thus the number of viable cells.

Luminescent ATP detection assay uses the principle that adenosine triphosphate (ATP) is the energy source of all metabolically active cells. When cells die, through apoptosis or necrosis, the ATP production significantly decreases, and the level of ATP is significantly reduced. Thus, ATP is a commonly accepted marker for viable cells. The addition of an ATP substrate (luciferase enzyme and luciferin), which undergoes a luciferase enzymatic reaction in the presence of molecular oxygen, uses ATP from lysed cells to release energy in the form of light. The intensity of light produced is proportional to the ATP concentration, which therefore is an indicator of cell viability. Similarly, the CellTiter-Glo 3D cell viability assay is a luminescent-based assay that examines the number of viable cells in 3D cell culture by quantifying the ATP present in cells.

3.2.7.1 MTT assay

Prior to conducting MTT assay experiments, cells were seeded into 96 well plates using the process described in section 3.2.1.4 and 3.2.1.5. The MTT assay was performed by adding 50 µL of MTT solution (Thiazolyl blue tetrazolium bromide) to each well containing cells in the 96 well plate. The plate was placed in a humidified incubator with 5% (v/v) CO_2 at 37ºC, for 2 – 3 hours. After incubation, 150 µL of MTT solvent solution (DMSO) was added to each well. The well plate was wrapped with aluminium foil and shaken for 15 minutes on an orbital shaker. The well plate was placed in a microplate reader and absorbance measurements at 590 nm were recorded.

3.2.7.2 Luminescent ATP detection assay

The luminescent ATP detection assay kit consisted of a detergent, a substrate buffer, and a lyophilised substrate. The pre-assay preparation involved reconstituting every lyophilised substrate vial in 5 mL substrate buffer. The required volume of the new substrate solution was aliquoted for conducting the assay. Prior to conducting the luminescent ATP detection assay, cells were seeded into 96 well plates using the process described in section 3.2.1.4 and 3.2.1.5. Luminescent ATP detection assay was conducted by adding 50 µL of detergent to each well. The plate was shaken for 5 minutes using a microplate-compatible shaker at 40 – 50 g, which allowed lysis of cells and stabilisation of ATP. Afterwards, 50 ml of substrate solution was added to the wells and the well plate were shaken again for 5 minutes at 40 – 55 g. The plate was dark adapted for 10 minutes and then luminescence was measured using the microplate reader.

3.2.7.3 CellTiter-Glo 3D cell viability assay

The quantitative analysis of cell viability for neural cells cultured in 3D cell culture models was determined by using a luminescent ATP assay kit called, CellTiter-Glo 3D Cell Viability Assay Kit. Prior to beginning the cell viability test, the well plate and CellTiter-Glo 3D reagent were equilibrated to room temperature for approximately 30 minutes. A volume of 100 µL CellTiter-Glo 3D reagent was added to the wells containing the cells. The solution was mixed for 5 minutes by pipetting up and down, to encourage cell lysis. The well plate was then covered with aluminium foil and placed on a plate shaker for 30 minutes at 100 rpm. The luminescence was measured with an integration time of 1000 ms, using a microplate reader.

3.2.8 Qualitative analysis of cell viability

The qualitative analysis of cell viability for neural cells were determined using a live/dead assay staining kit for fluorescent imaging. A working solution from the live/dead staining kit was prepared, which included calcien AM (acetomethoxy) and ethidium homodimer-1 dyes. The non-fluorescent derivate of calcien, calcien AM, permeates the cell membrane and once inside the cell the intracellular esterases break down the AM groups, which restores the fluorescent calcien molecule. The calcien emits a strong green fluorescence and since esterase activity is absent in dead cells, only live cells are labelled green. The ethidium homodimer-1 is membrane-impermeable, so it can only enter the cell if the plasma membrane becomes disrupted, indicating dying cells or dead cells.

To perform the live/dead assay of cells, firstly the cell culture medium was removed from the well plates and washed with PBS. Then, the live/dead staining solution was added to each well to cover the cells. The well plates were incubated at 37ºC and 5% (v/v) CO_2 for 30 minutes. Afterwards, the staining solution was removed, and the cells were washed with PBS. Fresh cell culture medium was added, and the cells were imaged using a fluorescent microscope, with appropriate emission filters for live cells (green) and dead cells (red).

3.2.9 Investigation of reactive oxygen species production

The reactive oxygen species (ROS) Detection assay kit was utilised to measure ROS production quantitatively, using a microplate reader. The ROS assay kit included ROS assay buffer, ROS label (1000X) and ROS inducer (250X). For experimental use, the ROS label was diluted at 1:1000 in pre-warmed ROS assay buffer to achieve a 1X final concentration. Additionally, the ROS inducer was diluted at 1:250 in pre-warmed ROS assay buffer.

Prior to performing the assay, cells were seeded into 96 well plates. The ROS assay was performed over a duration of 5 days, measuring the ROS production on three different time points. The media was aspirated, and cells were washed with ROS assay buffer. ROS label was added to the wells containing the cells and incubated for 45 minutes at 37ºC in the dark. Afterwards, the ROS label was removed, and ROS buffer was added to the wells.

The ROS inducer was used as an experimental control and was added to the cells 1 hour prior to analysis. The cells in the well plate were placed in a microplate reader to measure the fluorescence at Excitation/Emission of 495/529 nm.

3.2.9 Investigation of DNA damage in neural cells

To determine the effect of model wear particles on the integrity of astrocyte-like and neuronal cells DNA, the measurement of γ-H2AX foci levels in cells was conducted. The formation of γ-H2AX occurs when there is DNA double stranded breaks and thus is the basis for a sensitive assay to detect DNA damage. Prior to conducting the DNA damage assay, the cells were seeded in 12 well plates and were grown for at least 24 hours until cells were exposed to model particles. The well plates were incubated at 37ºC and 5% CO_2. DNA damage was measured at various time points including 1, 2 and 4 hours.

To perform DNA damage, cells were washed with PBS and permeabilised with 100 µL of 0.5% Triton X-100 solution for 3 minutes. After that, the cells were washed twice and 50 µL of primary antibody (γ-H2AX) was added to the cells and incubated in the incubator at 37ºC and 5% CO_2 for approximately 45 minutes. Next, cells were washed with PBS and 50 µL of secondary antibody was added and incubated at 37ºC and 5% CO_2 for approximately 25 minutes. After incubation, cells were washed with PBS and finally mounting media containing Hoerst solution was added that covered the cells and imaged using the fluorescent microscope.

3.2.10 Characterisation of particles using ImageJ

The size and shape of model particles for different biomaterials were measured using the ImageJ (v1.53a) image analysis software. Images obtained from scanning electron microscopy (SEM) were opened in ImageJ. Afterwards, image thresholding was applied by selecting “Image”, then “Adjust” and choosing “Threshold.” Thresholding was applied to ensure that particles were differentiated from the background. The next step was to set the image scale by selecting “Analyse” and then “Set scale.” The scale bar was measured and converted to micrometres. The measurement of particle size including area, perimeter, maximum and minimum diameter of the region of interest (ROI) was enabled by installing a plug-in called “Measure_ROI.” The ROI refers to the specific area of an

image or the outline of the particle that is used for detailed analysis. Once installed, the ROI manager was enabled in ImageJ in order simultaneously store multiple ROIs by selecting “Analyse,” then “Tools,” and “ROI Manager.” The total area of the image was measured by drawing a rectangular outline around the image. Each particle was measured by drawing an outline around the particle. Measurements were stored in the ROI manager by selecting “Analyse” and then “Measure.”

3.2.11 Statistical analysis

Statistical significance was analysed using Student’s t-test. The indication for statistical signification was determined by a p-value of < 0.05. For proportional or percentage data that does not follow a binomial distribution, an arc sine transformation was used to help normalise the distribution of data. All experiments were conducted with a minimum of three biological replicates.

Chapter 4

Clinical outcomes of lumbar total disc replacements for degenerative disc disease with a minimum of 5 years follow up

4.1 Introduction

Lumbar degenerative disc disease (DDD) is a spinal disorder indicated by the degeneration of the intervertebral discs (IVD) and is commonly associated with low back pain [233, 234]. In DDD, the IVD gradually deteriorate, due to the reduction of water content in the nucleus pulposus, which leads to progressive impairment of mechanical function and disc instability [21]. Multidisciplinary rehabilitation and pain medication are the initial treatment methods for symptomatic lumbar DDD. However, surgical procedures, including spinal fusion and total disc replacement (TDR) may be considered, if conservative pain management fails to improve symptoms.

Spinal fusion is considered to be the gold standard treatment of lumbar DDD [235-237]. However, there have been reports of spinal instability and adjacent segment degeneration from long-term follow-up results [236, 238]. Adjacent segment degeneration occurs when the spinal load from the fused vertebra is diverted to the adjacent vertebrae and results in unbalanced load distribution. Consequently, TDRs have gained traction as an alternative procedure in recent decades [239-241]. The principle behind TDRs is to replace damaged and degenerated spinal discs with an artificial disc via minimally invasive spinal surgery. The aims of TDRs are to restore spine biomechanics to allow for supporting physiological loads and relieve back pain.

The longevity of lumbar TDR may be dependent on the biomaterial properties of the components that make up the artificial disc. One of the major challenges that poses a risk to the longevity of spinal devices is the wear debris produced from articulating interfaces, e.g. polymer core and metal endplate interfaces in total disc replacements. Currently, the most considered biomaterials for lumbar TDRs are cobalt-chrome alloys, titanium alloys,

stainless steels, polyethylene and ceramics. TDRs are designed based on a bearing system and the interfaces of the implant are at risk of wear and producing wear debris particles at close proximity of neural tissue and cells of the central nervous system. Currently, common bearing couples of artificial discs that have been investigated include metal-on-metal (MoM) and metal-on-polyethylene (MoP). MoM bearings have two metal endplates, superior and inferior, which articulate on a metal core component. MoP bearings have two metal endplates, superior and inferior, which articulate on a polyethylene core component. TDRs, including the Charité (DePuy Synthes), ProDisc-L (DePuy Synthes) and activL (Aesculap Implant Systems) were approved by the Food and Drug Administration (FDA) in 2004, 2006 and 2015, respectively. MoM disc implants for lumbar TDR, including Maverick (Medtronic) and Kineflex (SpinalMotion) have been developed, but are still undergoing the process of FDA approval. The material selection in bearing systems may have an impact on the performance of lumbar TDRs in patients [148].

Although the performance of total joint replacements has been studied over the past several years [242], TDRs are relatively new compared to other joint replacements, and mid-to-long term results for different material combinations have not been thoroughly examined. Additionally, TDRs present unique challenges possibly due to challenging surgical techniques due to the complexity of the spine structure and lack of device selection. Furthermore, the design of TDRs must consider the dynamic aspects of spine kinematics, which present unique challenge compared to other joint replacements. It is also important for patients to understand the potential long-term benefits of TDRs including back pain relief, motion preservation, and improved quality of life. In addition, the design of TDRs having bearing systems have the potential to produce wear debris from articulating surfaces of biomaterials, most commonly polymers and metals. The problem with wear debris is that it has the potential to ultimately lead to implant loosening and implant failure. The focus of this chapter was to examine the clinical performance of lumbar TDRs and also evaluating the complication and reoperation rates of these implants.

4.2 Aim and objectives

4.2.1 Aim

In response to the lockdown measures implemented during the COVID-19 pandemic, this part of the PhD was conducted while working at home and also to greater understand the effectiveness total disc placements in patients with low back pain. The overall aim of this study was to systematically review the clinical outcomes, re-operation, and complication rates of different lumbar TDR at mid- to long-term follow-up studies for the treatment of lumbar DDD in patients.

4.2.2 Objectives

The specific objectives of this chapter were:

1) To determine the clinical outcomes, including pain scores, clinical success, and patient satisfaction in patients with lumbar TDRs
2) To determine the rate of complications or re-operation in patients with lumbar TDRs
3) To compare the long-term clinical outcomes and safety profile of patients with the mid-term outcomes

4.3 Methods

4.3.1 Search Strategy and Quality Analysis

A systematic search was conducted using three electronic databases (PubMed, SCOPUS and Embase) to identify follow-up articles that evaluated clinical outcomes of lumbar TDR in patients with DDD. Only articles written in English and published in English journals between 2012 and 2022 were included to provide most up-to-date research findings. The following Boolean search string was utilized: lumbar[title] AND (disc[title] OR disk[title]) AND (replacement[title] OR arthroplasty[title] OR charite[title] OR Prodisc-L[title] OR Maverick[title] OR kineflex[title] OR activ-L[title] OR acroflex[title]) AND degeneration. The titles and abstracts of potentially relevant articles were reviewed, and full texts of studies included in this systematic review were obtained. The reference lists of included studies were examined to identify any additional relevant studies. The lead author was responsible for data extraction and evaluation of selected studies, and other co-authors were involved in cross-checking as quality control.

The included studies met the following criteria: clinical trials, prospective and retrospective studies published in the last 10 years; reported data on lumbar TDR patients with degenerative disc disease; a minimum mean of 5 years post-operative follow-up; a randomized control trial; a study sample size of greater than 10 patients; patients > 18 years of age; containing clinical outcomes with at least one of, Oswestry Disability Index (ODI), Visual Analog Scale (VAS), complication or reoperation rates. ODI and VAS pain scores are commonly used to assess patients' back pain by collecting data pre-operatively and post-operatively on patients' back pain intensity. The exclusion criteria included: other treatment methods in combination with lumbar TDR; non-English manuscripts; case reports, reviews, or animal studies. The initial search generated a total of 415 citations from both PubMed and SCOPUS. After the removal of duplicates, 366 articles were included for title and abstract screening, with 40 articles deemed relevant for full-text assessment. A total of 23 studies were included for final analysis, including one study added from the review of reference lists (Fig 4.1).

Relevant information of the studies including study design, sample size, follow-up rate, mean follow-up years, age, gender, and quality of evidence was recorded in Table 1. The Oxford Centre for Evidence Based Medicine (March 2009) was utilized to categorize the levels of evidence for the included studies in this review. Level of evidence was used to assess the quality of a study, based on study design, strength of results, and applicability to patient care [243]. For example, the studies represented in each level are: level 1 – systematic reviews and RCTs; level 2 – individual cohort studies and retrospective cohort studies; level 3 – case-control studies; level 4 – case series (without control group).

Clinical outcomes in included studies comprised of clinical success rate, satisfaction rate, ODI, and VAS were examined. The ODI questionnaire involves 10 sections that address different aspects of daily life, e.g. pain intensity, walking and sleeping. Each section consists of 6 statements describing the levels of disability, ranging from 0 (no disability) to 5 (maximum disability). VAS scores are used for pain assessment of the back or leg. The VAS pain assessment uses a horizontal line normally 10 centimetres long, with 0 cm representing "no pain" and 10 cm representing "worst pain." The score is measured by the patient marking a point on the line to indicate the intensity of pain experienced. These

pain assessment scores are important tools to evaluate the patient's experience with pain and the effect of pain on daily life. The benefits of using these pain score assessments include being patient-friendly and easy-to use, as well as providing quantitative measurements on pain specific to the back. According to the Food and Drug Administration (FDA), the criteria for defining clinical success include an improvement of ODI score of at least 15 points compared to baseline, no major device-related complications or reoperations, no device failure, and maintenance of neurological status. Patient satisfaction is defined as a measure of how content patients are with the health care provided, and it is commonly measured using a point-based scale ranging from "very satisfied" to "very dissatisfied." Post-operative complication rates and reoperation rates were also analyzed. Complication rate was defined as the proportion of patients who suffered implant or non-implant related complications. Reoperation rate was defined as the proportion of patients who underwent secondary spinal surgery, related to the implant or any other unspecified indication. In addition, mid-term follow-up was defined as 5 years and long-term as at least 10 years.

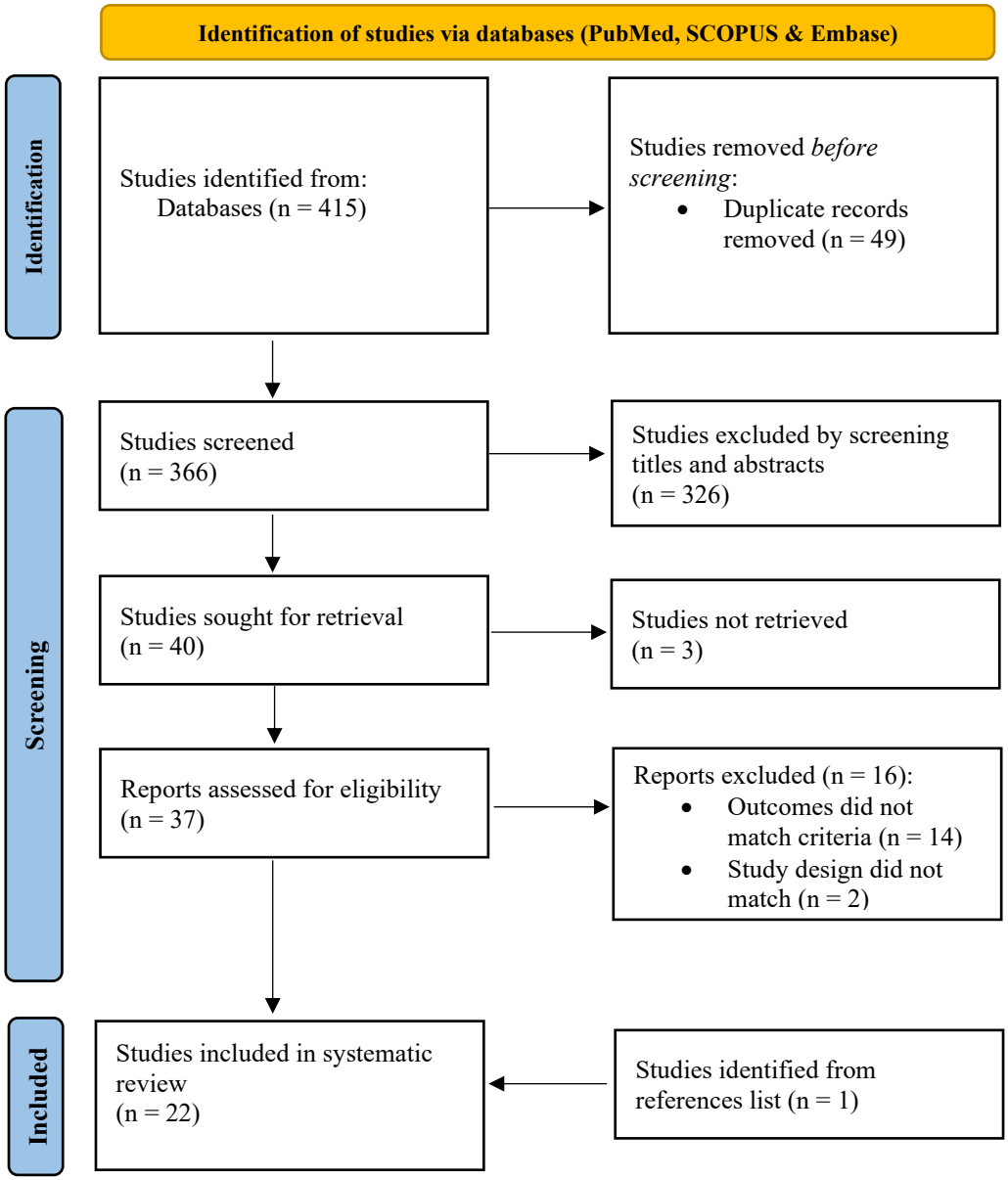

Figure 4.1. Flow diagram of study selection. Studies (n = 415) were identified from online databases (PubMed, SCOPUS and Embase). After removing 49 duplicate studies, 366 studies were screened. Non-eligible studies (n = 326) were excluded after screening titles and abstracts. Eligible studies (n = 37) were assessed, and 14 studies were excluded due to clinical outcomes measured not matching the criteria of this study, and 2 studies were excluded due to irrelevant study designs for this systematic review. Finally, 22 studies were included in the systematic review including one study identified from the reference list from another study.

4.3.2 Statistical Analysis

Analysis of data was conducted in this review on the outcomes from the 22 included studies. VAS and ODI back pain scores for different spinal implants were presented as means with 95% confidence interval (CI). The mean percentage data from clinical success and patient satisfaction rates, as well as complication and reoperation rates were arcsine transformed with 95% CI. Arc sine transformation was used to stabilize data variance, as the variance of percentages across the range (0% to 100%) was not constant. In addition, percentages are not normally distributed, and therefore arc sine transformation allows the generation of normally distributed data. The student's T-test was utilized to compare between two groups of data. Student's T-test was used to compare pre-operative and post-operative back pain scores, to compare outcomes between two different TDRs, and to compare outcomes between mid-term and long-term follow-up studies. A two-way ANOVA was used to compare differences among more than two TDRs for clinical outcomes. A p-value of <0.05 was used for statistical significance for both Student's T-test and ANOVA tests. Statistical analyses were conducted using Microsoft Excel and SPSS.

4.4 Results

4.4.1 Study Characteristics

Of the 22 included studies, 15 were prospective studies and 7 were retrospective studies. Among the 15 prospective studies, 7 were randomized controlled trials (RCT). According to the Oxford Levels of Evidence, this review consisted of seven level 1 studies, five level 2 studies, seven level 3 studies and two level 4 studies.

This study investigated the outcome data for lumbar TDR from 2284 follow-up patients from 23 published studies. The mean follow-up for this study was 8.30 years. The mean follow-up rate was 86.91%, with a range of 68.5% – 100%. The mean age of this study was 42.34 years, with a minimum and maximum age of 18 and 79 years, respectively, and a study population of 54.97% female. The lumbar TDRs examined in this study comprised of metal-on-polymer discs including, Charité, ProDisc-L, Activ-L, Acroflex, as well as metal-on-metal discs including, Maverick and Kineflex. Of the 23 included studies, 5 studies [244-248] observed different implants and bearing types

simultaneously. Only two studies [244, 246] distinguished between the implants and reported clinical outcomes. In these studies, both Radcliff *et al* [244] and Guyer *et al* [246], used RCTs to compare two different implants.

Table 4.1. Characteristics of included studies

Study	Implant (Number of patients)	Bearing type	Year	Study type	Sample size (F/I)	F/u rate (%)	Mean F/u (years)	Mean age	Male/Female (%)	Evidence level
Radcliff *et al* [244]	ActivL (160), ProDisc-L (46)	MoP, MoP	2021	Prospective RCT	206/283	72.8	7	40	52/48	1
Formica *et al*[245]	Maverick (24), ProDisc II (5), Charité (3)	MoM, MoP, MoP	2020	Retrospective case series	32/47	68.1	13.7	40.2	16.7/83.3	3
Kitzen *et al*[249]	Charité III	MoP	2020	Retrospective case series	296/405	73.1	12.3	41.25	40.9/59.1	3
Scott-Young *et al*[250]	Charité	MoP	2020	Prospective case series	122/122	100	7.8	42	63.1/36.9	4
Yue *et al*[57]	ActivL	MoP	2019	Prospective RCT	176/218	80.7	5	40	52.8/47.2	1
Lu *et al*[251]	Charité III	MoP	2018	Retrospective case series	30/35	85.7	15.4	59.4	53.3/36.7	3
Wuertinger *et al*[252]	ProDisc II	MoP	2018	Prospective case series	51/51	100	7.8	45	35.3/64.7	2
Plais *et al*[59]	Maverick	MoM	2018	Prospective case series	61/87	70.1	10	44	58.8/41.2	2
Furunes *et al*[253]	ProDisc II	MoP	2017	Prospective RCT	77/86	89.5	8	41.1	53.5/46.5	1
Laugesen *et al*[254]	ProDisc II	MoP	2017	Prospective observational cohort study	57/68	83.8	10.6	38.7	22.8/77.2	2
Guyer *et al*[246]	Kineflex-L (204), Charité (190)	MoM, MoP	2016	Prospective RCT	270/394	68.5	5	39	N/A	1
Park *et al*[255]	ProDisc II	MoP	2016	Retrospective case series	54/64	84.4	10	44.1	33.3/66.7	3
Lu *et al*[256]	Charité III	MoP	2015	Retrospective case series	32/35	91.4	11.8	41.1	43.7/56.3	3
Aghayev *et al*[247]	ActivL, Charité, Maverick, ProDisc-L	MoP, MoP, MoM, MoP	2014	Retrospective case series	218/218	100	5.6	42.35	54.8/45.2	3
Siepe *et al*[257]	ProDisc II	MoP	2014	Prospective non-RCT	181/201	90.0	7.4	43	38.7/61.3	2
Balderstone *et al*[258]	ProDisc-L	MoP	2014	Prospective case series	13/15	86.7	9.6	44.3	30.8/69.2	4
Yue *et al*[259]	ProDisc II	MoP	2013	Prospective case series	46/46	100	5	39.6	45.7/54.3	4
Skold *et al*[248]	Charité, ProDisc II, Maverick	MoP, MoP, MoM	2013	Prospective RCT	80/80	100	5	40.2	40/60	1
Mier *et al*[260]	Acroflex	MoP	2013	Prospective non-RCT	23/28	82.1	9.6	41	50/50	2
Guyer *et al*[261]	Charité	MoP	2012	Prospective RCT	90/90	100	5	40	N/A	1
Park *et al* [262]	ProDisc-L	MoP	2012	Retrospective case series	32/32	100	6	46.5	53.6/46.4	3
Zigler & Delamarter[55]	ProDisc-L	MoP	2012	Prospective RCT	137/183	85.1	5	38.7	50.9/49.1	1

4.4.2 Clinical outcomes in patients with lumbar TDR

The clinical outcomes reported in this review include, Oswestry Disability Index (ODI) scores, Visual Analog Scale (VAS) scores, clinical success rate and patient satisfaction that were assessed pre-operatively and at follow-up in patients with lumbar TDR. The ODI and VAS scores are commonly utilized to assess the efficacy of lumbar TDR in patients. The ODI is the most commonly used questionnaire for outcome measure of low back pain in patients [263]. In the included follow-up studies, the VAS and ODI scores from patients were collected pre-operatively and at the last follow-up.

The mean VAS and ODI scores are presented in Figures 1 and 2 respectively. A reduction in scores means improvement of pain in patients. The mean pre-operative and post-operative VAS pain score for all devices examined was 75.4 ± 3.5 and 24.7 ± 8.4, respectively. Patients with the ActivL, Charité and ProDisc demonstrated significant reduction (Student's t-test, p=0.01, p=0.004, p=0.000002, respectively) in VAS pain score, with 63.0 ± 12.7, 60.0 ± 12.0 and 45.90 ± 6.7, respectively. The mean pre-operative and post-operative ODI for all devices examined was 49.8 ± 5.1 and 19.4 ± 3.6, respectively. Patients with the ActivL, Charité and ProDisc demonstrated significant reduction in ODI pain score (Student's t-test, p=0.015, p=0.003, p=0.00009, respectively), with 42 ± 12.7, 30.3 ± 10.6 and 29.51 ± 9.4, respectively. The reduction in VAS and ODI scores for the Maverick device was reported in only Plais *et al* [59], which were 38.5 and 21.1, respectively. In both Radcliff *et al* [244] and Guyer *et al* [246], the authors assigned two different implants to patients. In Radcliff *et al* [244], both the activL and Prodisc-L demonstrated significant improvements from baseline in pain reduction. In Guyer *et al* [246], the TDR group consisted of patients using either Kineflex-L or Charité, however did not provide data on the specific TDR, as the authors compared the TDR group to a spinal fusion group. The findings in Guyer *et al* [246], showed a reduction in VAS and ODI pain scores of 39.6 ± 31.8 and 24.6 ± 18.1 after 5 years.

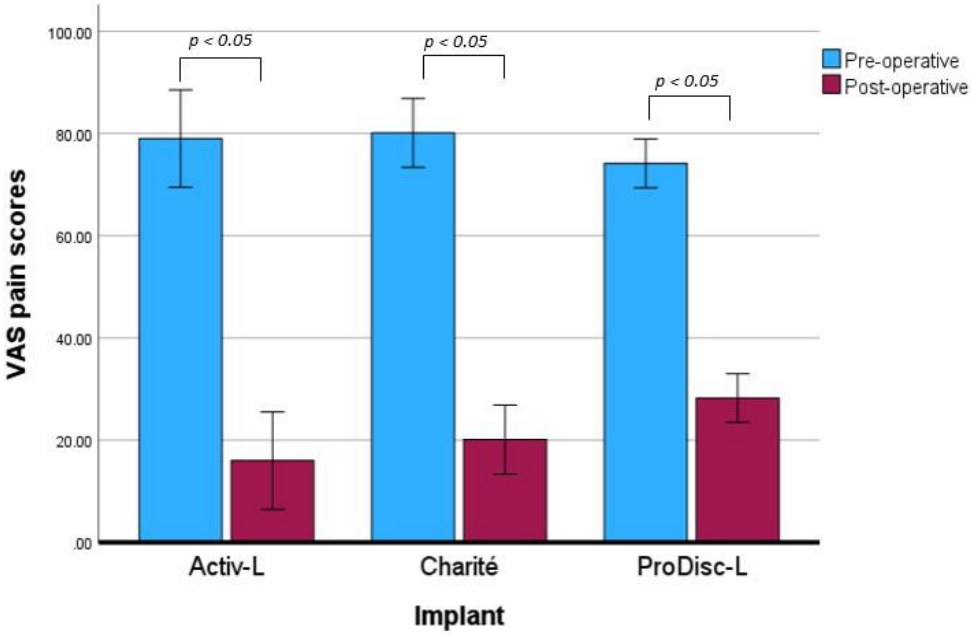

Figure 4.2. Pre-operative and post-operative VAS scores of patients with lumbar TDR. Errors bars were presented using CI of scores within each implant group. The student's t-test ($p<0.05$) showed statistical significance between preoperative and post-operative scores.

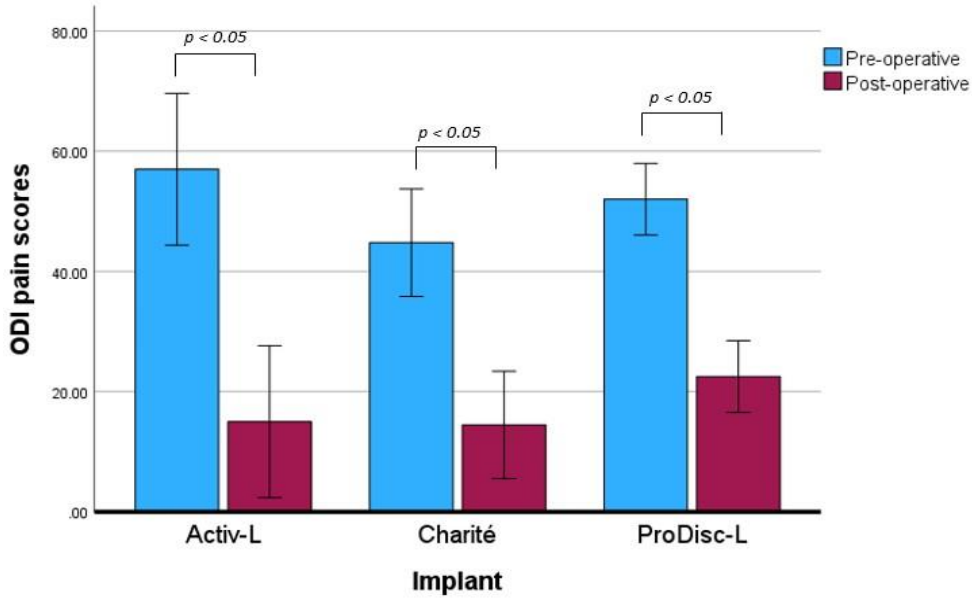

Figure 4.3. Pre-operative and post-operative ODI scores of patients with lumbar TDR. Errors bars were presented using CI of scores within each implant group. The student's t-test ($p<0.05$) showed statistical significance between preoperative and post-operative scores.

The clinical success rate was reported in 11 included studies. The mean clinical success rate was 74.79% ± 6.26%. Out of the 11 studies, four studies examined the Charité device, and four studies examined the Prodisc-L, with mean clinical success rates of 77.03% ± 18.56% and 69.20% ± 13.22%, respectively.

Patient satisfaction is an essential indicator of measuring healthcare quality [264]. The rate of patient satisfaction was reported in 13 studies, with a mean of 86.34% ± 4.38%. Out of the 13 studies, four studies [250, 255, 258, 262] used a 4-point scale of satisfaction ("very satisfied," "satisfied," "dissatisfied" and "very dissatisfied") and two studies [252, 257] used a 3-point scale ("highly satisfied," "satisfied" and "not satisfied"). In addition, Guyer *et al* [246] asked patients to choose one of six responses (ranging from "very satisfied" to "very dissatisfied") on how satisfied they were. Furunes *et al* [253] used a seven-point Likert scale ("full recovery", "much better", "slightly better", "no change", "slightly worse", "much worse" and "worse than ever") to assess the patients' satisfaction with result of treatment. The other seven studies did not state their method of assessing patient satisfaction. Out of the 13 studies, the Charité device was examined in four studies and the Prodisc-L was investigated in six studies, with mean patient satisfaction rates of 86.43% ± 12.85% and 84.55% ± 6.54%, respectively.

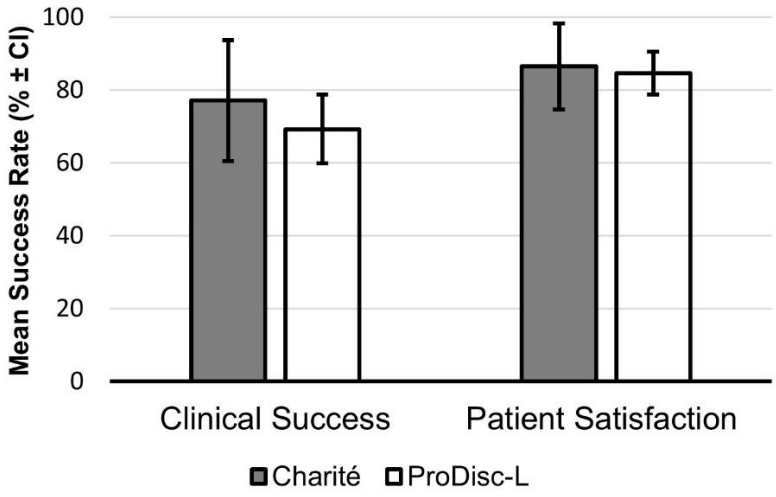

Figure 4.4. Comparison between Charité and ProDisc-L for clinical success and patient satisfaction. Errors bars were presented using CI within each implant group.

4.4.3 Complications and reoperations in patients with lumbar TDR

Complication and reoperation rates were reported in 17 studies. The mean reoperation and complication rate were 13.56% ± 3.83% and 18.53% ± 6.33%, respectively.

The mean reoperation rate for studies investigating the Charité device was 12.60% ± 7.18%, which were mostly indicated for supplemental fixation, implant replacement and treatment of continuing symptoms of chronic low back pain. Kitzen *et al* [249] reported the highest reoperation rate, with many reoperations involved in treating persistent symptoms of chronic lumbar back pain. In the study by Lu *et al*[251], the most common post-operative complication was adjacent segmentation degeneration with an incidence of 68% among patients with the Charité device.

The mean reoperation rate for studies investigating the Prodisc-L device was 16.21% ± 6.79%. The highest rate of reoperation in patients with the Prodisc-L was reported in Laugesen *et al* [254]. Zigler and Delamarter [55] reported 3.7% of patients with device failures due to complications involving, polyethylene migration and polyethylene inlay migration The majority of patients were indicated for back pain and or radiculopathy and required arthrodesis (joint fusion surgery). Park *et al* [262] and Balderstone *et al* [258], reported no device failures or major complications, with both studies examining the ProDisc-L.

Compared with Charité and Prodisc-L, fewer studies were conducted on other devices, including ActivL, Kineflex, Maverick and Acroflex. In patients with ActivL, Yue *et al* [57] reported a reoperation rate of 5% but did not state the indications for reoperations. The majority of complications reported in Yue *et al* [57] was lumbar or leg pain, which accounted for 7.80% of patients. Additionally, 1.40% of patients were reported to have implant migration. Patients with the Kineflex implant reported a reoperation rate of 11.76% in one study by Guyer *et al* [246]. The majority of reoperations consisted of treatment for pain using supplemental fixation implantations. In terms of device-related adverse events, 8.80% of patients were reported in Guyer *et al* [246]. In patients with the Maverick device, Plais *et al* [59] reported reoperation and complication rates of 4.92% and 27.20%, respectively. The long-term complications accounted for 11.20%.

Reoperation in patients with the Maverick device, who suffered long-term complications was reported in 4.80% of patients.

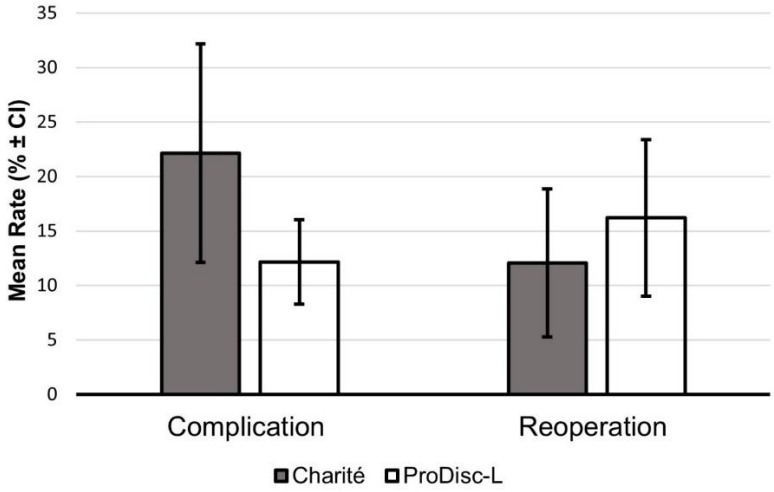

Figure 4.5. Comparison between Charité and ProDisc-L for complication and reoperation rates. Errors bars were presented using CI within each implant group.

Table 4.2 Reoperation and complication rates (%) from included studies.

Study	**Implant**	**Reoperation rate (%)**	**Complication rate (%)**
Meir *et al* [260]	Acroflex	39.3	N/A
Yue *et al* [57]	ActivL	5	36
Radcliff *et al* [244]	ActivL, ProDisc-L	4.6	N/A
Kitzen *et al* [249]	Charité III	31.1	N/A
Scott-Young *et al* [250]	Charité	6.8	N/A
Lu *et al* [251]	Charité III	5.7	N/A
Lu *et al* [256]	Charité III	5.7	34.4
Guyer *et al* [261]	Charité	7.8	22.2
Plais *et al* [59]	Maverick	N/A	27.2
Wuertinger *et al* [252]	ProDisc II	N/A	N/A
Furunes *et al* [253]	ProDisc II	16	N/A
Laugesen *et al* [254]	ProDisc II	33	N/A
Siepe *et al* [257]	ProDisc II	16	14.4
Park *et al* [255]	ProDisc II	9.3	N/A
Yue *et al* [259]	ProDisc II	N/A	N/A
Balderstone *et al* [258]	ProDisc-L	N/A	0
Park *et al* [262]	ProDisc-L	N/A	N/A

Zigler & Delamarter [55]	ProDisc-L	6.8	9.9
Guyer *et al* [246]	Kineflex-L (204), Charité (190)	11.8	9.8
Skold *et al* [248]	Charité, ProDisc II, Maverick	20	16.3
Aghayev *et al* [247]	ActivL, Charité, Maverick, ProDisc-L	4.4	23.4
Formica *et al* [245]	Maverick (24), ProDisc II (5), Charité (3)	N/A	20

4.4.4 Comparison of mid-term and long-term clinical outcomes of patients

A comparison between mid-term (5 years) and long-term (minimum 10 years) follow-up studies was investigated. Studies with a 5-year follow-up included, Guyer *et al* [246], Zigler *et al* [55], Skold *et al* [248] and Yue *et al* [57, 259]. Studies with a ≥ 10-year follow-up included, Lu *et al* [251], Park *et al* [255], Laugesen *et al* [254], Plais *et al* [59], Formica *et al* [245] and Kitzen *et al* [249]. The mean reductions for VAS pain scores for 5-year and ≥ 10-year follow-up studies were 44.68 ± 10.69 and 40.38 ± 4.55, respectively. The mean reductions for ODI pain scores for 5-year and ≥ 10-year follow-up studies were 30.76 ± 9.37 and 24.58 ± 8.68, respectively. Additionally, the mean clinical success rates for 5-year and ≥ 10-year follow-up studies were 72.80% ± 15.15% and 84.07% ± 9.99%, respectively. The mean patient satisfaction rates for 5-year and ≥ 10-year follow-up studies were 78.00% ± 0.78% and 84.10% ± 6.97%, respectively. Statistical analysis of results demonstrated no statistical significance when comparing clinical outcomes of mid-term and long-term follow-up studies.

Table 4.3. Mean reduction of VAS and ODI pain scores compared between 5-year and ≥ 10-year follow-up studies. *Student's t-test was used to compare data between groups.

	5-year follow-up	≥ 10-year follow-up	P-value*
VAS	44.68 ± 10.69	40.38 ± 4.55	0.47
ODI	30.76 ± 9.37	24.58 ± 8.68	0.42

Table 4.4. Clinical success and patient satisfaction rates compared between 5-year and ≥ 10-year follow-up studies. *Student's t-test was used to compare data between groups.

	5-year follow-up	≥ 10-year follow-up	P-value*
Clinical success rate (%)	72.80 ± 15.15	84.07 ± 9.99	0.25
Patient satisfaction rate (%)	78.00 ± 0.78	84.10 ± 6.97	0.21

The mean reoperation and complication rates for mid-term follow-up studies were 7.83% ± 2.80% and 18.84% ± 6.82%, respectively. This was higher for long-term follow-up studies, which reported mean reoperation and complication rates of 16.86% ± 9.64% and

27.20% ± 5.29%, respectively. However, the difference between mid-term and long-term follow-up studies were not statistically significant.

Table 4.5. Mean reoperation and complication rates compared between 5-year and ≥ 10-year follow-up studies**.** *Student's t-test was used to compare data between groups.

	5-year follow-up	≥ 10-year follow-up	P-value*
Reoperation rate (%)	7.83 ± 2.80	16.86 ± 9.64	0.25
Complication rate (%)	18.84 ± 6.82	27.20 ± 5.29	0.21

4.5 Discussion

This chapter of work was conducted in response to the COVID-19 pandemic when the indefinite period of lockdown was implemented in New South Wales. As an alternate to restricted access to the laboratory, a more in-depth analysis of the clinical performance of TDRs for the lumbar spine in patients with DDD. Therefore, this part of the study was aimed to investigate the clinical outcomes, re-operation, and complication rates of different lumbar TDR at mid- to long-term follow-up studies for the treatment of lumbar DDD in patients.

Although spinal fusion is currently considered as the gold standard for lumbar DDD, one of the major limitations is the loss of spinal mobility and range of motion [265]. Total disc replacement (TDR) is an alternative solution to spinal fusion, which is a surgical procedure that replaces degenerated intervertebral discs with artificial disc implants. It is essential for patients and clinicians to consider the bearing system of TDRs. The factors considered when deciding on a bearing system may include disc articulation and motion, wear resistance, biocompatibility, and surgeon preference. One of the challenges with TDRs is the potential generation of wear debris from the articulating surfaces of the TDR bearings. This chapter focussed on the clinical performance of TDRs.

Previous meta-analysis studies comparing the lumbar TDR and spinal fusion have been conducted, investigating the treatment of lumbar DDD [266-270]. Both meta-analyses

conducted by Wei *et al* [268] and Jacobs *et al* [267] reported significant safety and efficacy of TDR compared to lumbar fusion, with a follow-up of two years. However, Jacobs *et al* [267] suggested that the spine surgery community should be wary about the adoption of TDR on a large scale, due to the limited long-term data on clinical performance and the challenges of revision surgery. Whilst Wei *et al* [268] suggested the adoption of TDR on a large scale. The conflicting findings from these meta-analyses and the limited knowledge on long-term clinical outcomes of TDRs provide uncertainty about the effectiveness of lumbar TDR, which makes the decision-making process difficult for patients requiring treatment. Thus, the present study was to investigate the long-term outcomes of lumbar TDR in treating lumbar DDD.

This study analyses results from follow-up studies with a minimum of 5 years in patients with lumbar TDR. A previous systematic review conducted by Cui *et al* [271] examined follow-up studies of at least 3 years of TDR for lumbar DDD. Although Cui *et al*[271] reported improvement in quality of life in patients with lumbar TDR, however, the authors only included three RCTs studies, with the most recent follow-up study used, being published in 2017, and only included articles from the PubMed database. Thus, the current study attempted to provide a more thorough literature search and further information on long-term results in patients with lumbar TDR, examining clinical outcomes from 22 studies including 7 RCTs.

All included studies reporting VAS and ODI pain scores demonstrated improvement at follow-up compared to baseline. The Charité, Prodisc-L and ActivL devices all showed significant improvements in both VAS and ODI pain scores from baseline data. The differences in pain score variance between ODI and VAS pain scores may be attributed to the difference in measurement outcomes. For example, VAS pain assessment is a unidimensional tool for pain assessment that only focusses on pain intensity. On the other hand, ODI pain assessment, evaluates the effect that back pain has on various aspects of daily life, including social activities and physical functioning. The multidimensional aspect of the ODI pain assessment tool may result in greater variance of scores. Clinical success and patient satisfaction rates were reported mostly in studies investigating the Prodisc-L and Charité devices. Although the Charité device had a slightly higher clinical success and patient satisfaction rate than ProDisc-L, there was no significant difference

between the two devices. The highest reported clinical success and patient satisfaction rate were Activ-L and Kineflex, respectively, however, more studies on those two devices are needed to confirm these results. In two studies by Park *et al* [255] and Siepe *et al* [257], patients who reported as either "dissatisfied" or "very dissatisfied," still showed overall improvements in ODI and VAS scores, which suggests dissatisfaction in patients, despite the clinical success of the device. The factors determining patients' dissatisfaction are not clear and may need further examination. This phenomenon could be explained by unrealistic expectations set by patients of having all back pain or discomfort eliminated. In addition, even with the improvements in pain scores, the TDRs may not have fully restored normal spinal function in patients, leading to experiences of limitations in range of motion or flexibility.

Major challenges of lumbar TDR in patients include implant longevity and adverse events. Complication and reoperation rates are major factors in determining the clinical success of a device. Complications reported in follow-up studies involved both implant and non-implanted related complications. The most common non-implant related complication was lumbar, which was reported in Yue *et al* [57] and Siepe *et al* [250]. The most common implant related complication was the displacement of the implant including overall implant migration, polyethylene inlay dislodgement. The common complications reported in this study was comparable to a cross-sectional analysis conducted by Koutsogiannis *et al* [252] which reported lumbar pain and implant migration as common complications associated with the ActivL, Charité and Prodisc-L devices. Although wear was not reported in the included studies, Koutsogiannis *et al* [252] demonstrated polyethylene wear as an implant related complication associated with MoM devices including Charité and Prodisc-L. Similarly, a systematic review on clinical wear performance of TDRs conducted by Veruva *et al* [253] reported small and large polymeric wear debris generated from MoP lumbar TDRs. The authors also showed that the tissue reactions induced from wear-related damage was comparable to reactions observed in total knee replacements (TKRs). The major concern with the generation of wear debris from TDRs is the possible association with osteolysis and aseptic loosening which is the underlying cause of implant failure [253]. Furthermore, MoM TDRs including the Kineflex and Maverick were also reported by Veruva *et al* [166] to have generated metallic debris. There have also been reports by Golish and Anderson [254] that reported metallosis and formation of pseudotumours in patients with CoCr MoM

bearings. Consequently, the presence of wear debris generated from spinal implants is a significant concern in the spine. In addition, there is a need to address how various biomaterials used in spinal implants affect neural tissues in the spine considering that pain is one of the common complications for lumbar TDRs.

Compared to the clinical outcomes, the complication and reoperation rate were not as consistent among the included studies. The inconsistency could be observed from complication rates of the ProDisc-L reported in Balderstone *et al* [258] and Laugesen *et al* [254], which were 0% and 33%, respectively. No complications reported in Balderstone *et al* [258] could be resulted by the small sample size that the authors used. Additionally, the different patient selection criteria used in the included studies could also be a reason that varied complication rates were observed. Furthermore, other factors including surgical technique and post-operative patient compliance to rehabilitation could have caused the disparity in complication rates among different studies. Having appropriate candidates for TDRs and strict patient criterion could improve the consistencies of patient recorded data on complications. Although the complication and reoperation rates between the devices, showed no significant difference, it was difficult to compare results, as most data on reoperation and complication rates were reported in studies that investigated the Charité and ProDisc-L devices. Other devices including ActivL, Maverick, Kineflex and Arcoflex only had one study each that reported complication and reoperation rates, so more studies are required to gain a better understanding of the safety profile of these devices.

Currently, no studies have been conducted that compared the clinical data from mid-term follow-up studies with long-term follow-up studies. In this study, mid-term follow-up studies were defined as studies that followed up patients after 5 years post-operation, and long-term studies were defined as studies that followed up patients for at least 10 years post-operation. The comparison of clinical outcomes including VAS and ODI pain scores, clinical success rate, and patient satisfaction rate reported in mid-term and long-term follow-up studies, demonstrated no significant difference. Similarly, there was also no significant difference in the reoperation and complication rates between mid-term and long-term follow-up studies. Consequently, the results from this study suggest that the performance of TDRs can be maintained for a duration of at least 10 years.

It is important to compare the outcomes of TDRs with the current gold standard treatment, spinal fusion, to determine whether the alternative treatment is a better option for treating DDD. Skold *et al* [248] conducted a RCT investigating the clinical outcomes of lumbar TDR (ProDisc-L) with lumbar spinal fusion as a 5-year follow-up study. Although Skold *et al*[248] reported no differences in complication rates between TDRs and spinal fusion groups, patients with TDRs demonstrated significantly better improvement of back pain scores, compared with spinal fusion. Zigler and Delamarter [55] reported similar clinical outcomes in the TDR group compared to spinal fusion, which was comparable to the outcomes demonstrated in Guyer *et al* [261]. The similar improvements in back pain scores between TDR and spinal fusion observed in this study confirm the results from previous studies conducted pre-2012 [272-274]. In addition, findings from a systematic review and meta-analysis conducted by Bai *et al* [275] demonstrated significant improvement in ODI, VAS, patient satisfaction and reoperation rates for patients with TDRs compared to patients with spinal fusion [268]. Although further studies are needed on comparing TDRs and spinal fusion for longer-term, the outcomes for TDRs show that the performance is at least similar to that of spinal fusion after 5 years post-operation and may benefit patients more in reducing back pain.

In this part of the study, the key strengths were the use of more recent studies in the last 10 years and the higher number of included RCT studies, compared to previous reviews. Additionally, this was the first study to compare the clinical outcomes of mid-term follow-up studies with long-term follow-up studies. However, there are some limitations of this study. Firstly, publication bias was evident in this review, due to the articles selected only being published in English journals from three databases, within the 10-year time frame. Another limitation may be selection bias, because there was only one author reviewing the potential studies for inclusion. However, attempts to prevent this included strict inclusion and exclusion criteria. In addition, the results of this review may be affected by heterogeneity including varied study type, sample size, study subjects, and device used, as well as definitions of complication and reoperation rates. As a result, we were unable to assess the quality of the studies objectively. The implementation of more effective patient-reported clinical outcomes to enable onward analysis for evaluating the clinical performance of lumbar TDRs could be conducted by standardising clinical data

management and data collection. It would be important to develop and adopt a consensus on patient-reported outcome measures that should be implemented in all clinical trials involving patients with spinal implants. For example, the time points and intervals that pain assessment scores are obtained pre-operatively and post-operatively should be standardised across all studies to ensure constancy in data collection.

Finally, the conclusion from the comparison between mid-term and long-term follow-up studies may be limited since the outcome comparison did not take into account the baseline characteristics including demographics and implant material. In the future, further studies can investigate how long-term outcomes of TDRs compare with long-term outcomes of spinal fusion. Additionally, further studies can also compare the different types of bearings used in lumbar TDRs for mid-to-long term clinical outcomes. Finally, the concern of wear produced from the bearing surfaces of lumbar TDRs, addressed in the complications section of this study, continues to be an area that requires further study, particularly examining how biomaterial wear impacts neural tissues and cells.

Understanding that complications occur in TDRs including back pain, displacement of implant components and polyethylene wear, it is essential that further research at a tissue and cellular levels. The cause of having back pain complications in patients with spinal implants is not understood well. However, with investigations into how different materials impact the cells surrounding the area of spinal implantation, an attempt on explaining the reason behind some complications can be made. Consequently, the next chapters examine the biological impacts of different biomaterial model particles on neural cells in a 3D model cell culture model to closely represent the *in vivo* environment.

4.6 Key Findings

This chapter investigated the clinical outcomes, re-operation, and complication rates of different lumbar TDR at mid- to long-term follow-up studies for the treatment of lumbar DDD in patients. The mid-term follow-up data on clinical outcomes of lumbar TDRs were maintained at long-term follow-up. Also, similar clinical outcomes were observed between lumbar TDRs and spinal fusion. The findings from this study have significant implications on clinical settings. When examining the complications, there were instances of migration of implant components, but most of the complications reported by patients was lumbar pain. Overall, this study demonstrated that TDRs could be a reliable option for patients suffering from lumbar DDD. In the future, longer-term examination on lumbar TDR in comparison to other surgical treatments, including spinal fusion, is required to determine whether TDR is the first option for patients.

Chapter 5

Development of a 3D *in vitro* model for assessing neural cell responses to model particles

5.1 Introduction

The findings from Chapter 4 showed that complications occur in patients with lumbar total disc replacements (TDR) including back pain, dislodgement of polyethylene components, migration of implant and back pain. Although, the overall clinical performance of lumbar TDRs showed reduction in pain scores and high clinical success and patient satisfaction rates, the type of complications should be an area of concern. Since the findings from Chapter 4 were at a broader clinical level, more research should be conducted at a cellular level to examine the interactions between cells and different biomaterials used in spinal implants. With more information on the biological impacts of biomaterial particles on neural cells, recommendations of material selection can be made to clinicians and patients.

Currently, there have been limited studies investigating the neural cell responses to spinal implant wear particles *in vitro*. Biological responses to particles have been previously modelled *in vitro* using a gel encapsulation technique. In the study conducted by Green *et al* [276], the authors used a 3D model that consisted of agarose gel and a monolayer of polymer model particles. The limitation of their method was that particles were not dispersed greatly. Although 2D cell culture has the advantages of being a simple and low-cost method to observe and analyse cell activity, it does not provide an accurate representation of cellular behaviour that occurs in the human body.

Consequently, there is a need for improvement of 3D *in vitro* models to assess cellular responses in order to mimic the *in vivo* environment which incorporate more complex cell-cell and cell-extracellular matrix interactions. In a recent study conducted by Lee *et al* [12], neural cell responses to CoCr wear particles were investigated in an *in vitro* 3D model. In their study, a 3D cell culture model created with type 1 rat tail collagen gel.

Naturally derived polymers have benefits including having good biocompatibility and low cellular toxicity. However, there are some limitations of collagen including, inadequate long-term stability, high variability of properties and batch-to-batch variability. In addition, one of the limitations of agarose gel for 3D culture was the detachment of cells due to a lack of cell adhesion molecules [277]. Consequently, in this study, the rationale of using Gelatin methacryloyl (GelMA), as a semi-synthetic polymer was that it would provide the benefits of having good biocompatibility, supporting adequate cellular attachment and the tailorable physical properties which synthetic polymers exhibit. Furthermore, recently GelMA has been successfully used in spinal cord injury modelling which demonstrated neural cell viability in cell-encapsulated 3D bioprinted GelMA hydrogel constructs [278]. In this study, bioprinting techniques were used to create cell-encapsulated 3D bio-constructs. The rationale for using bioprinting techniques for developing 3D bio-constructs instead of traditional casting methods, includes the many advantages it presents for example, greater precision in spatial control for cells, and increased complexity and mimicry of the *in vivo* organisation of tissues [228, 229]. One of the main bioprinting technologies is extrusion-based 3D bioprinting, which is widely utilised in tissue engineering applications [228, 229, 231]. Extrusion-based bioprinting uses a dispensing system to extrude a bioink, which is a formulation of cells, biological molecules, and biomaterials [231, 232]. Bioprinting using the extrusion technique occurs through an automated computer program. One of the advantages of extrusion-based bioprinting is the ability to bioprint highly viscous bioinks and also being able to use a variety of biocompatible bioinks including, cell-laden hydrogels and cell aggregates [231]. Another advantage is the ability to bioprint structures with high cell density [228]. Furthermore, the extrusion-based technology is easy-to-use and prints at high speed to promote scalability [231].

In this study, NG108-15 neuronal cells and C6 astrocyte-like cells were used to model neural cell responses. NG108-15 is a neuronal hybrid cell line from mouse neuroblastoma and rat glioma. Neuronal 3D *in vitro* co-culture involving NG108-15 cells and Schwann cells (SC) have been studied by Kraus *et al* [181] and Daud *et al* [182] as peripheral nerve models. Both studies reported neurite outgrowth, which supports the use of NG108-15 cells in 3D models for studying *in vitro* peripheral nerve regeneration [181, 182]. The C6 cell line, derived from rat glial tumour was selected on the basis that it behaves similarly

to astrocytes. Astrocytes function to provide structural support and can proliferate to promote tissue repair around the site of injury or implantation in the central nervous system [279].

In this study, neural cells were exposed to commercially manufactured model particles in the 3D model. The initial plan in this study was to use wear particles generated using articulation in a pin-on-disc simulator. However, due to the unprecedented lockdowns and disruption of supply chains by the COVID-19 pandemic, there was significant delays in the procurement and commissioning of the equipment used in the wear simulation. As a result, model particles were used as an alternative and were characterised by examining the size and morphology of particles using a scanning electron microscope (SEM). Knowledge of the size distribution of wear particles is essential for investigating the biological effects on cells and tissues because the *in vivo* response differs to different particle sizes. For example, in the studies conducted by Green *et al* [16] and Ingham *et al* [108], the authors demonstrated that the size ranges of polyethylene wear particles that induced a biological response in monocytes were between 0.3 μm to 10 μm and 0.2 μm and 0.8 μm, respectively.

Consequently, this part of the study aimed to develop a 3D *in vitro* cellular model by bioprinting GelMA hydrogels, encapsulating neural cells and model particles.

5.2 Aims and Objectives

5.2.1 Aims

The overarching aim is to develop a 3D *in vitro* cellular model to investigate neural cell responses to wear particles from spinal implants and devices. The first objective was to characterise model particles of biomaterials including, metals, polymers, and ceramics. The first part of this work involved sequential filtration of model particles. The model particles were separated into clinically relevant size ranges, by conducting sequential filtration with different sized filter membranes, including micrometre and nanometre sized particles.

The second objective of this chapter was to develop a 3D cell culture model used to assess biological responses of neural cells exposed to wear particles. The novel approach in this study was the bioprinting of particles embedded in cell-laden hydrogels using an extrusion-based bioprinter.

5.2.2 Objectives

The specific objectives of this chapter were:

1. To characterise the morphology and size of model particles including polymers, ceramics and metals using scanning electron microscopy and image analysis.
2. To determine the printability of 3D GelMA hydrogels encapsulating model particles of different biomaterials.
3. To investigate the viability of neural cells including neuronal and astrocyte-like cells when encapsulated in a 3D bioprinted GelMA hydrogel construct over a duration of 7 days with and without model particles.

This chapter of the study consisted of two distinct experimental projects. Therefore, the chapter is divided into two sections. Section A details the characterisation of model particles including their size and morphology. Section B covers the process of 3D bioprinting hydrogels and optimising the printing of hydrogel containing particles, as well as evaluating the viability of neural cells in bioprinted hydrogels with and without model particles.

5.3 Section A: Characterisation of polymer, ceramic, and metal model particles.

The model particles used in this study were commercially manufactured and were in powder and resin forms. The specific materials and methodologies used to characterise model particles are detailed in the following sections.

5.3.1 Specific materials

The particles utilised in this study are listed in the Table 5.1.

Table 5.1. Particles used throughout this study and their suppliers. The materials used in this study are commonly used in the manufacture of spinal instrumentation and devices.

Material	**Supplier**
Polyetheretherketone (PEEK-OPTIMA) resin	Invibio Biomaterial Solutions
Polyethylene (Ceridust® 3615)	Hoescht, Germany
Zirconia Toughened Alumina (ZTA)	Inframat Advanced Materials, USA
Cobalt Chromium Molybdenum Alloy (CoCr-Mo)	American Elements, USA

5.3.2 Specific methods for particle characterisation

5.3.2.1 Preparation of particle filtration apparatus and filter membranes

In order to categorise particles to different size ranges and generate size distributions, the first step of particle preparation was sequential filtration. Sequential filtration of particles is a technique that involves passing different sized particles through a series of filters with decreasing pore sizes.

The set-up for filtration consisted of a glass conical flask, a vacuum base, a filter holder (including filter membrane), an aluminium clamp and a glass funnel. The set-up of the filtration apparatus is shown in Figure 5.1. The glass apparatus was washed robustly using a bristle brush with household general detergent after use. Then, the glassware was thoroughly rinsed with di-ionised water three times, and then was left to air dry at room

temperature. Finally, the glassware was sterilised using UV for 30 minutes in a biosafety cabinet.

The membrane filters used included 8 µm, 0.8 µm, 0.1 µm and had had a diameter of 25 mm. The polycarbonate membrane filters were washed with 70% (v/v) ethanol and rinsed with di-ionised water. The membrane filters were subsequently air dried at room temperature and sterilised with UV for 30 minutes.

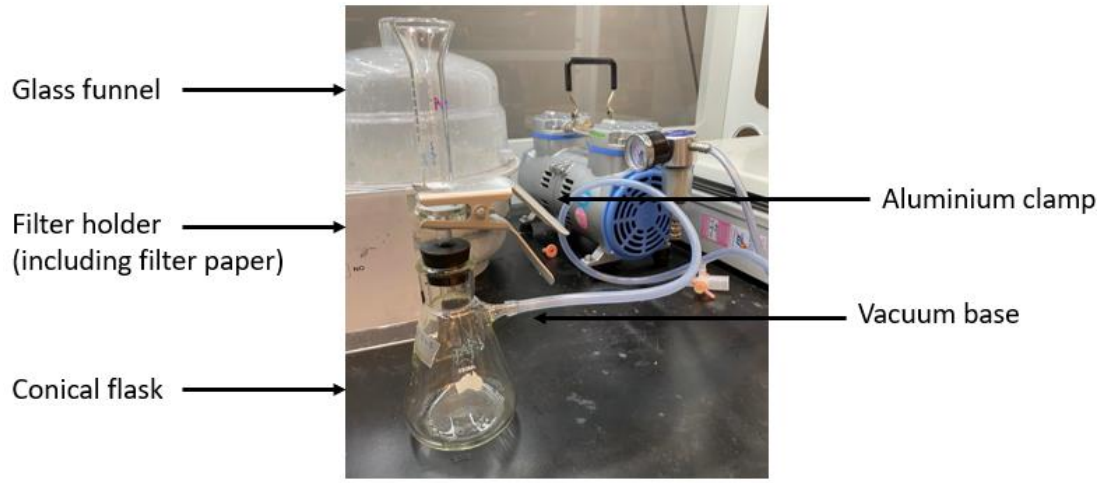

Figure 5.1. The assembly of equipment for filtration in the fume hood. The vacuum base from the conical flask was connected to the vacuum pump via a tube to allow greater rate of filtration.

5.3.1.2 Preparation of particles

The particles were stored in a storage cabinet at room temperature. A mass of 100 mg particles was weighed out using a laboratory scale. This was conducted by using a spatula to transfer the particles from the stock container onto a weighing dish. The particles were suspended in 20 mL of distilled water in a 50 mL centrifuge tube. The particles were sonicated for approximately 30 to 40 minutes to ensure dispersion of particles at a concentration of 5 mg/mL.

5.3.1.3 Sequential filtration of particles

Sequential filtration of particles was conducted in a fume hood. Prior to filtration, the surface of the fume hood was cleaned with 70% (v/v) ethanol. All equipment used for sequential filtration was sprayed with 70% (v/v) ethanol before entering the fume hood. The 8 µm polycarbonate membrane filter was handled carefully using tweezers and placed on top of the filter holder. In the next step, The filters were then cleaned by passing through 10 mL of distilled water, which also ensured that the filter was tightly sealed with the filter holder. The glass funnel was placed on top of the filter and an aluminium clamp was used to hold the glass funnel in place. Then, the vacuum pump was attached to the opening of the vacuum base. The vacuum pump was used to ensure that all liquid was drawn through the filter.

The next step was sonication, which was an important step to help reduce particle aggregation. Immediately after the particles were sonicated, the particles that were suspended in distilled water were poured through the glass funnel and filtered through the 8 µm filter and the tube was rinsed with X ml distilled water to maximise the number of particles that were filtered. The filtrate in the conical flask was passed through the next filter membrane, the 0.8 µm filter and lastly the 0.1 µm filter. After the particle samples had passed through the filter, the filter was transferred into a sterile petri dish using tweezers, with one filter per petri dish. The filters were dried in an oven at 50ºC for a minimum of 30 minutes. After drying, the filters were stored in an airtight container in preparation for SEM imaging.

5.3.1.4 Preparation of filters for field emission gun scanning electron microscopy (FEG-SEM)

All filters were mounted on individual aluminium stubs (with a diameter of either 12.6 mm or 25 mm), using double-sided carbon adhesive tabs. The 25 mm diameter aluminium stubs had the same diameter as the filters, so therefore the filters were carefully mounted onto the stub with the carbon adhesive tab, using tweezers. For the 12.6 mm diameter aluminium stubs, there were two methods of mounting. The first method was cutting the filters into smaller sections for mounting. The second method was gently pressing the stub, with the adhesive tab, on the underside of the filters. After mounting, a nitrogen spray gun was used to remove dust and debris from the surfaces of the filters.

Prior to SEM imaging, the filters were coated using a sputter coater (Leica EM ACE600). For samples of polymers or ceramics including PEEK, polyethylene and ZTA, the filters were coated with gold/palladium material using a sputter coater, and for the CoCr sample, the filters were coated with carbon. The coating was applied up to a thickness of 3 nm. After coating, the samples were immediately imaged using the FEG-SEM (Zeiss Supra 55VP). For future use, the coated samples were placed in a desiccator or in a tightly sealed container to ensure a moisture free environment.

5.3.1.5 Field emission gun scanning electron microscopy of particles

Particles including PEEK, polyethylene (Ceridust 3615®), ZTA and CoCr-Mo were imaged using a scanning electron microscope to examine their size distribution and morphology. The imaging was conducted using the Zeiss Supra 55-VP SEM at the Microstructural Analysis Unit at the University of Technology Sydney.

After the coating of filters described in section 4.3.1.4, the samples were viewed at a voltage of 5 kV or 10 kV and a working distance ranging from 4.9 mm to 21 mm. Three random fields of view were captured per magnification for each sample. The magnifications used were 100 X, 400 X, 700 X and 1500 X. A minimum of three images per magnification were collected for each filter for each material.

5.3.1.6 Image analysis and characterisation of particles

In order to generate a size and area distribution for all particles, the size and morphology of the particles imaged using SEM were analysed manually using image analysis software, Image J (version 1.53).

For each material, a minimum of 100 particles were included in the analysis. Particles that had a clear perimeter outline were included in the count and analysis. The size of each particle was manually obtained by drawing around the particle. Particles that overlapped with each other or were grouped in agglomerates were not included in the analysis.

The measurements for each material and each filter size were obtained and utilised for size distribution. The measurements obtained from Image J included area (area of the

particle), perimeter (length of particle's outline), length (Feret's diameter along major axis) and width (Feret diameter along minor axis). The measurements obtained from each filter were exported to a spreadsheet in Microsoft Excel. Then, the particles were grouped into different size ranges (< 0.1 µm, 0.1 – 0.8 µm, 1.0 – 8 µm and >8 µm). In addition, the number of particles per the area of each image (N/A) and the average area of particles in each size range (P/N) were calculated. An example of the different size ranges and calculated N/A and P/N values are shown in Table 5.2.

Table 5.2. Calculated P/N and N/A values generated from Image J of SEM images (400 X magnification) of PEEK particles on the 8 µm filter. N = number of particles, A = area of image, N/A = ratio of particles to area of image, ∑P = sum of area for particles, (∑P)/N = average area of a particle.

	N	**N/A**	**∑P**	**(∑P)/N**
<0.1 µm	0	0	0	0
0.1 µm – 0.8 µm	0	0	0	0
0.8 µm-8 µm	12	0.000192157	724.99	60.41583
>8µm	11	0.000176144	2009.66	182.6965

The size distribution and area distribution of particles were represented as histograms prepared in Microsoft Excel. The size distribution was determined by the number of particles in each size range as a percentage and the area distribution was determined by the area of particles in each size range as a percentage.

5.3.2 Results

5.3.2.1 Sequential filtration of particles

The aim of sequential filtration was to separate the particles into different size ranges using polycarbonate membrane filters. The sequence of filters used was 8 µm, 0.8 µm and 0.1 µm. This allowed the size ranges to be grouped as > 8 µm, 0.8 µm – 8 µm and 0.1 µm – 0.8 µm. The particles that were collected on the filters were imaged using the FEG-SEM. The accelerating voltages used to image the particles were either 5 kV or 10 kV.

5.3.2.2 Characterisation of PEEK model particles

PEEK-OPTIMA model particles were filtered sequentially using 8 µm, 0.8 µm and 0.1 µm filters. The PEEK-OPTIMA model particles were imaged using SEM with an accelerating volage of 5 kV and a working distance ranging of 4.9 mm. The morphologies of the PEEK-OPTIMA model particles collected on each polycarbonate membrane filter are shown in Figures 5.2, 5.3 and 5.4. PEEK particles displayed similar morphological characteristics at all size ranges, i.e. they were granular or irregular in shape. The mean size of the PEEK particles was 7.58 µm ± 3.97 µm in diameter. The size range of PEEK-OPTIMA model particles was 0.54 – 83.17 µm in diameter, with 95% of particles having a diameter less than 8 µm and 43% in the submicron range (Figure 5.5). A small proportion of the particles were greater than 8 µm in size, however these particles consisted of approximately 50% of the total area percentage of the particles.

(A) (B)

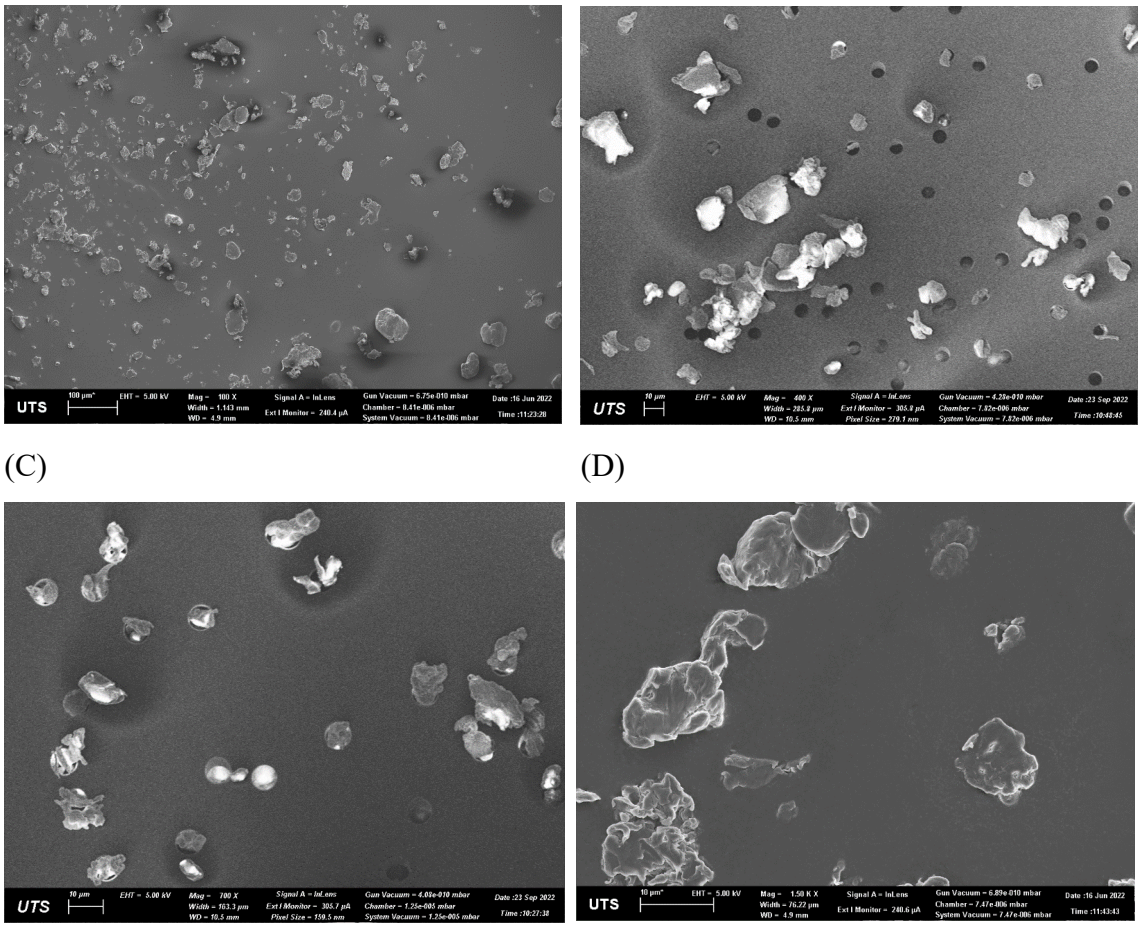

(C) (D)

Figure 5.2. Images of PEEK-OPTIMA aggregates and micro-sized PEEK-OPTIMA model particles collected on the 8 µm filter. The particles were imaged using a FEG-SEM at magnifications of (A) 100 X, (B) 400 X, (C) 700 X and (D) 1500 X. Size bars of 100 µm in image A and 10 µm for images B – D.

(A) (B)

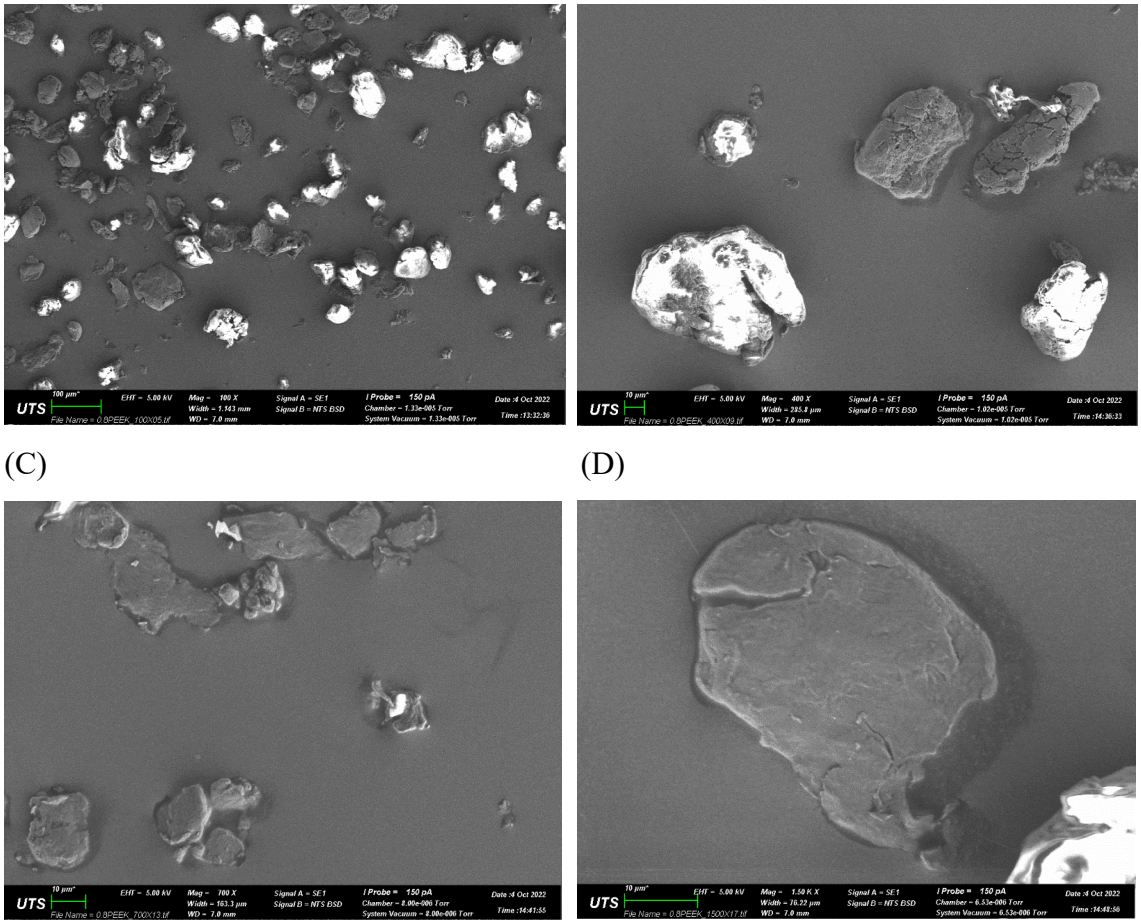

(C) (D)

Figure 5.3. Images of PEEK-OPTIMA aggregates and micro-sized PEEK-OPTIMA model particles collected with a 0.8 µm filter. The particles were imaged using a FEG-SEM at magnifications of (A) 100 X, (B) 400 X, (C) 700 X and (D) 1500 X. Size bars of 100 µm in image A and 10 µm for images B – D.

(A) (B)

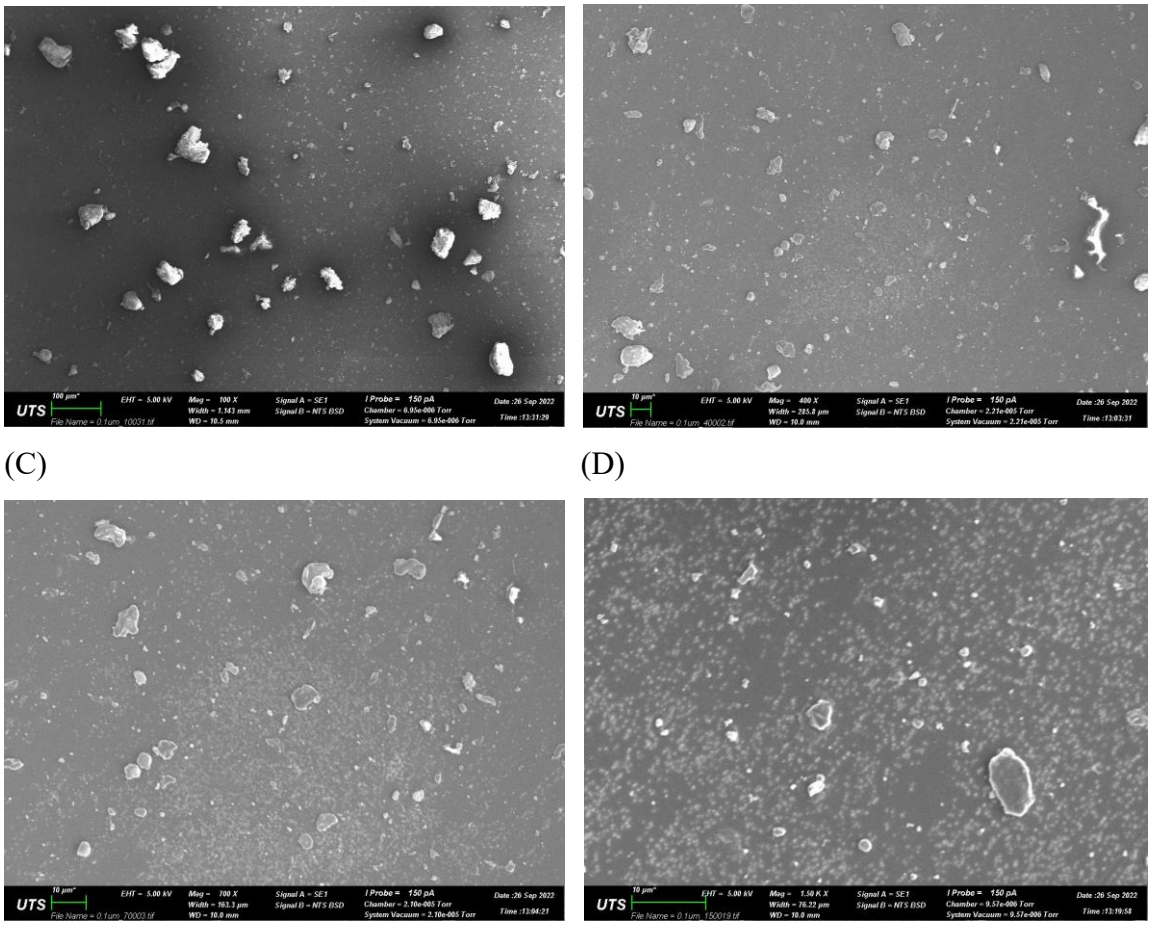

(C) (D)

Figure 5.4. Images of PEEK-OPTIMA aggregates and micro-sized PEEK-OPTIMA model particles collected with a 0.1 µm filter. The particles were imaged using a FEG-SEM at magnifications of (A) 100 X, (B) 400 X, (C) 700 X and (D) 1500 X. Size bars of 100 µm in image A and 10 µm for images B – D.

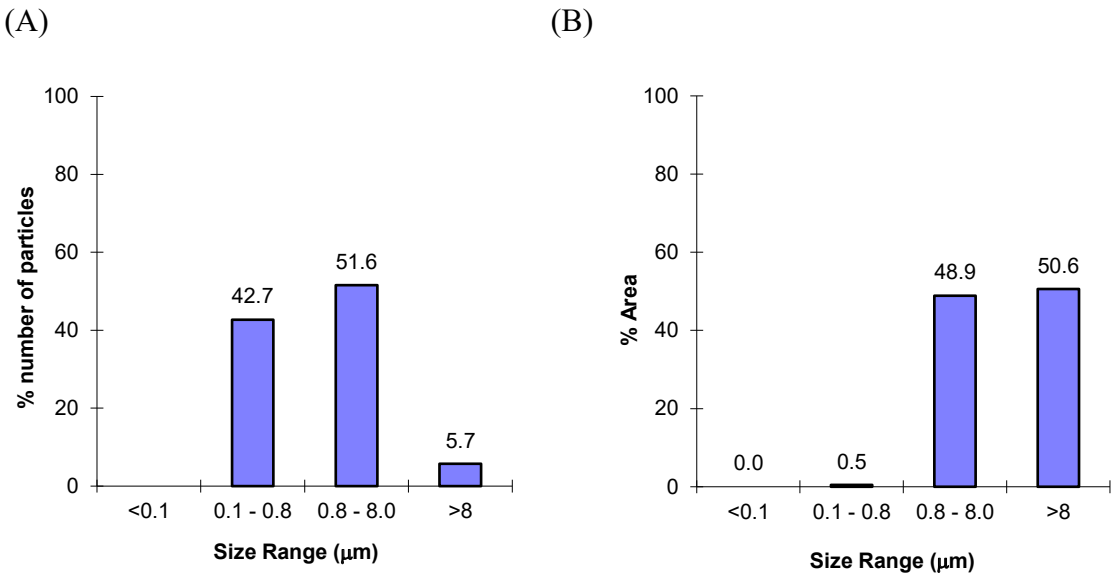

Figure 5.5. The percentage frequency and percentage area distribution of PEEK-OPTIMA model particles as a function of particle size determined from SEM images. (A) Percentage frequency distribution; (B) Percentage area distribution.

5.3.2.3 Characterisation of polyethylene model particles

Polyethylene (Ceridust 3615 ®) model particles were filtered sequentially using 8 µm, 0.8 µm and 0.1 µm filters. The Ceridust 3615® particles were imaged using SEM with an accelerating voltage of 10 kV and a working distance ranging of 17.5 mm to 21.0 mm. The morphologies of the polyethylene particles collected from each polycarbonate membrane filter are shown in Figures 5.6, 5.7 and 5.8. Ceridust 3615® model particles exhibited granular and polygonal morphology. The mean size of the Ceridust 3615® model particles was 6.43 µm ± 2.75 µm in diameter. The size range of polyethylene particles was 0.49 – 22.07 µm in diameter, with 92.31% of particles having a diameter less than 8 µm (Figure 5.9). A large proportion of the particles were in the 0.1 – 0.8 µm size range, however these particles consisted of approximately 1% of the total area percentage of the particles.

(A) (B)

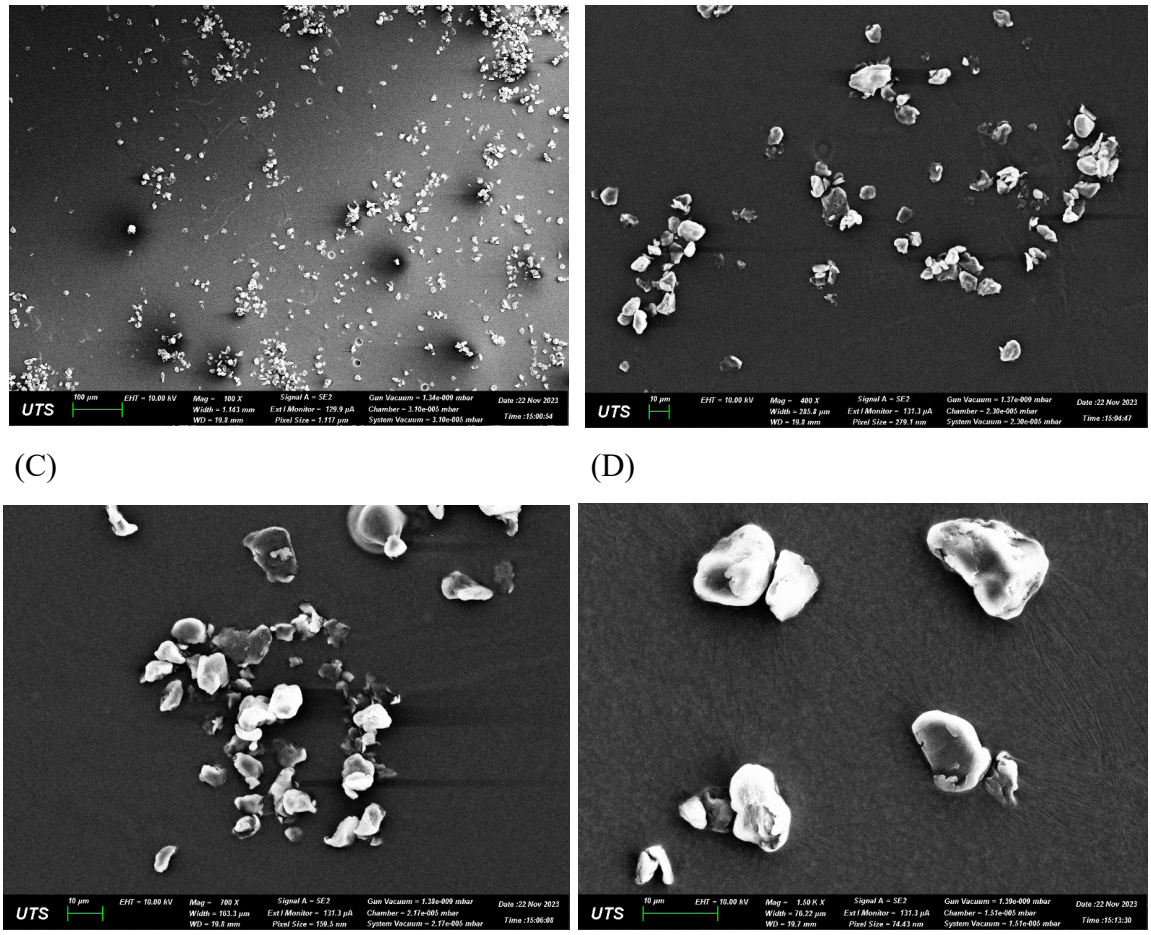

(C) (D)

Figure 5.6. Images of Ceridust 3615 ® aggregates and micro-sized Ceridust 3615 ® model particles collected with an 8 µm filter. The particles were imaged using a FEG-SEM at magnifications of (A) 100 X, (B) 400 X, (C) 700 X and (D) 1500 X. Size bars of 100 µm in image A and 10 µm for images B – D.

(A) (B)

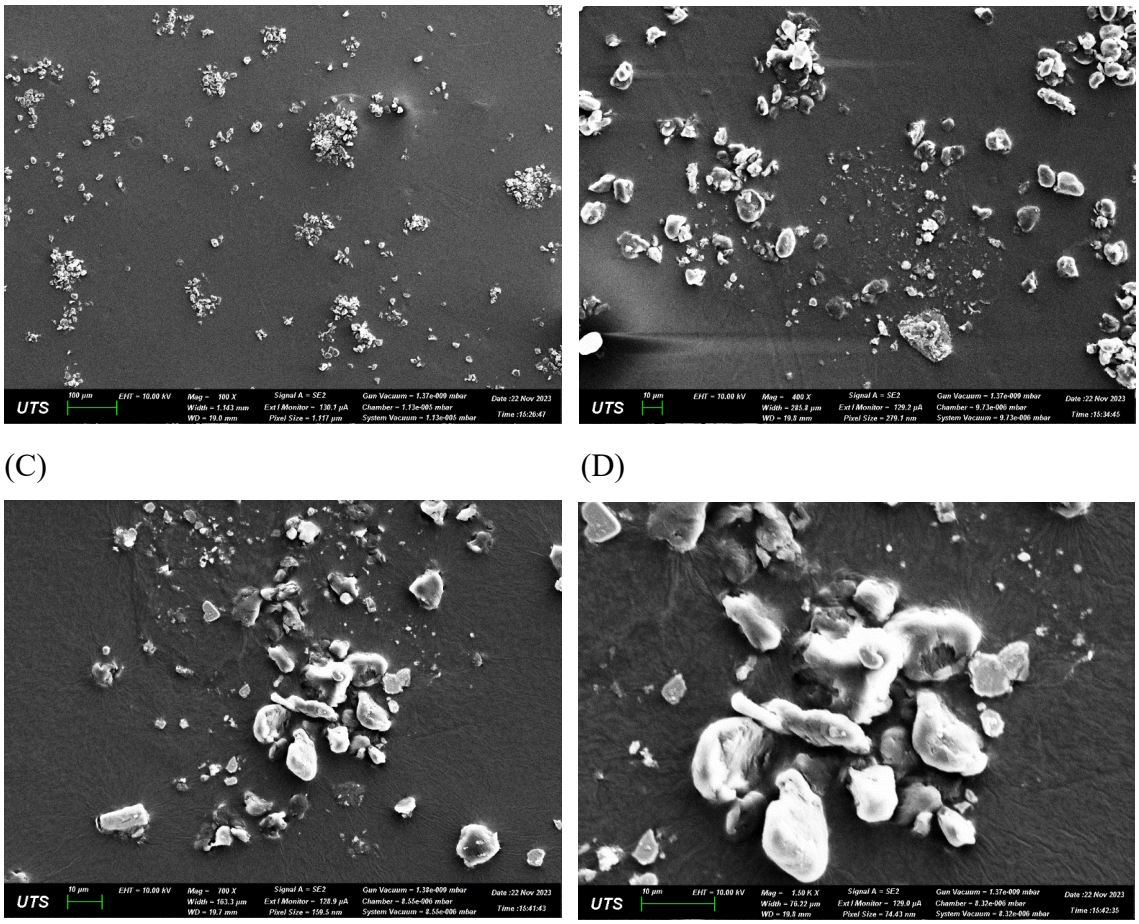

(C) (D)

Figure 5.7. Images of Ceridust 3615 ® aggregates and micro-sized Ceridust 3615 ® model particles collected with a 0.8 µm filter. The particles were imaged using a FEG-SEM at magnifications of (A) 100 X, (B) 400 X, (C) 700 X and (D) 1500 X. Size bars of 100 µm in image A and 10 µm for images B – D.

(A) (B)

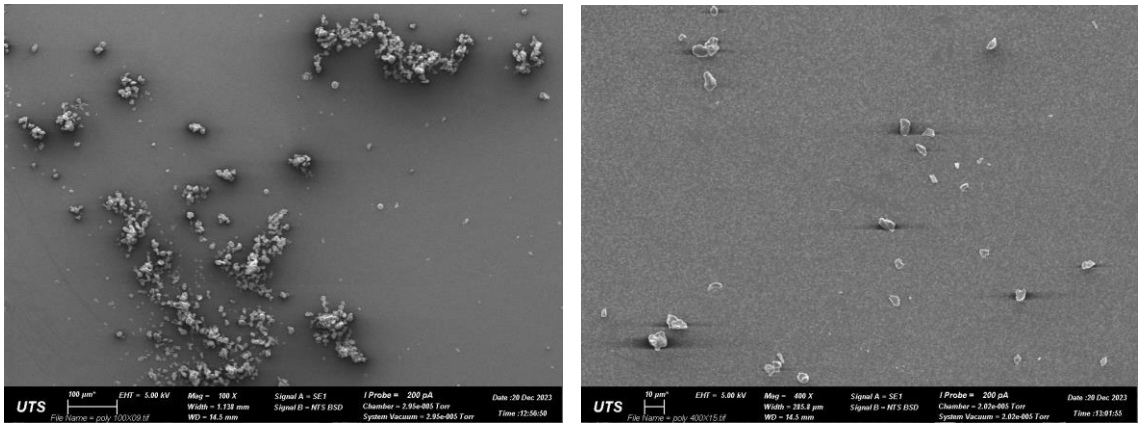

(C) (D)

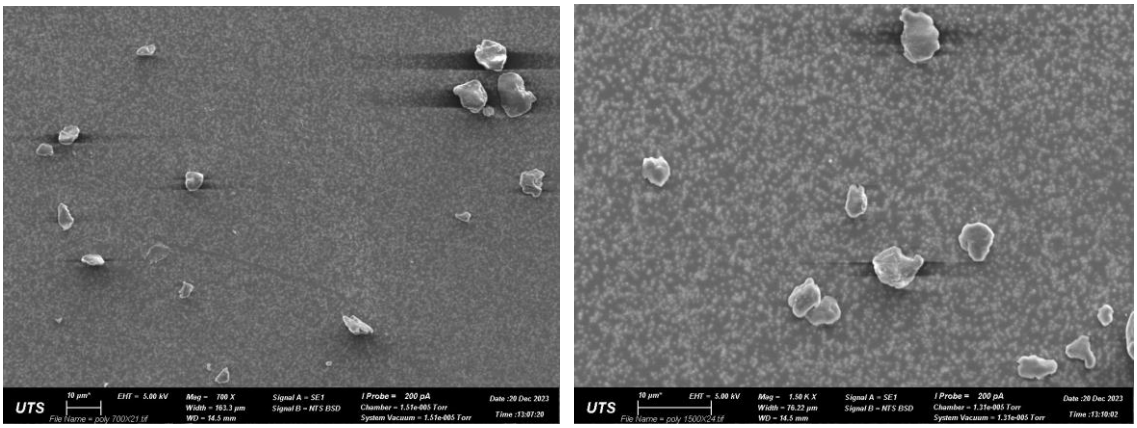

Figure 5.8. Images of Ceridust 3615 ® aggregates and micro-sized Ceridust 3615 ® model particles collected with a 0.1 µm filter. The particles were imaged using a FEG-SEM at magnifications of (A) 100 X, (B) 400 X, (C) 700 X and (D) 1500 X. Size bars of 100 µm in image A and 10 µm for images B – D.

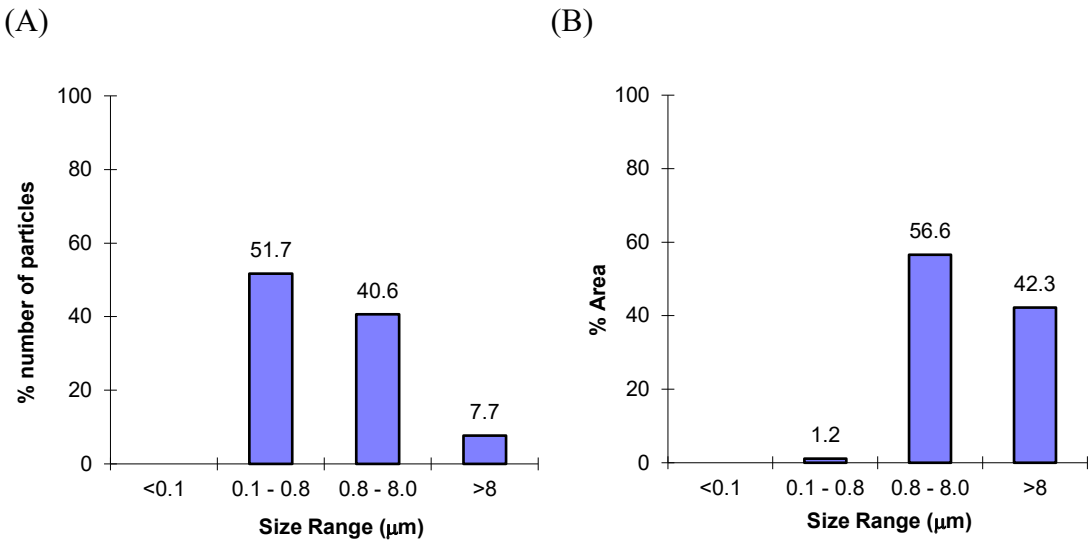

Figure 5.9. The percentage frequency and percentage area distribution of Ceridust 3615 ® model particles as a function of particle size determined from SEM images. (A) Percentage frequency distribution; (B) Percentage area distribution.

5.3.2.4 Characterisation of ZTA model particles

ZTA model particles were filtered sequentially using 8 μm, 0.8 μm and 0.1 μm filters. The ZTA particles were imaged using SEM with an accelerating voltage of 10 kV and a working distance ranging of 17.5 to 21 mm. The morphologies of the ZTA model particles collected from each polycarbonate membrane filter are shown in Figures 5.10, 5.11 and 5.12. ZTA model particles exhibited granular and polygonal morphology. The mean size of the ZTA particles was 3.69 μm ± 3.48 μm in diameter. The size range of ZTA particles was 0.45 – 20.32 μm in diameter, with 99% of particles having a diameter less than 8 μm (Figure 5.13). The ZTA model particles had a mode size of 0.8 – 8.0 μm with approximately 73% of all particles. In addition, the mode distribution of area of the particles with 99.5% were in the 0.8 – 8.0 μm size range.

(A) (B)

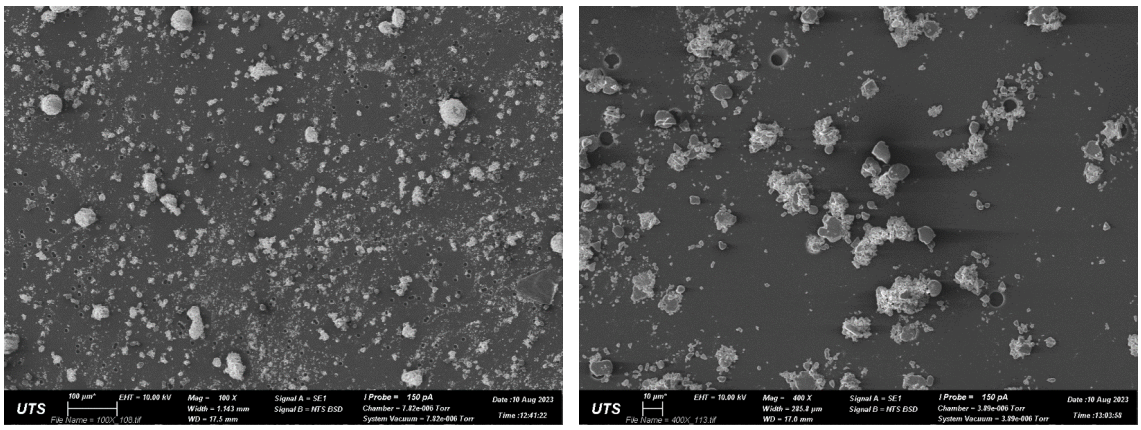

(C) (D)

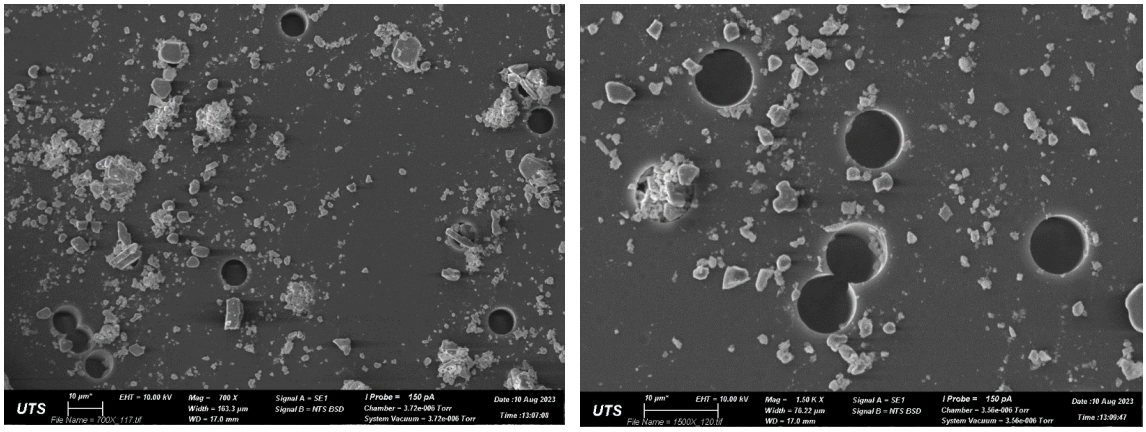

Figure 5.10. Images of ZTA aggregates and micro-sized ZTA model particles collected with an 8 µm filter. The particles were imaged using a FEG-SEM at magnifications of (A) 100 X, (B) 400 X, (C) 700 X and (D) 1500 X. Size bars of 100 µm in image A and 10 µm for images B – D.

(A) (B)

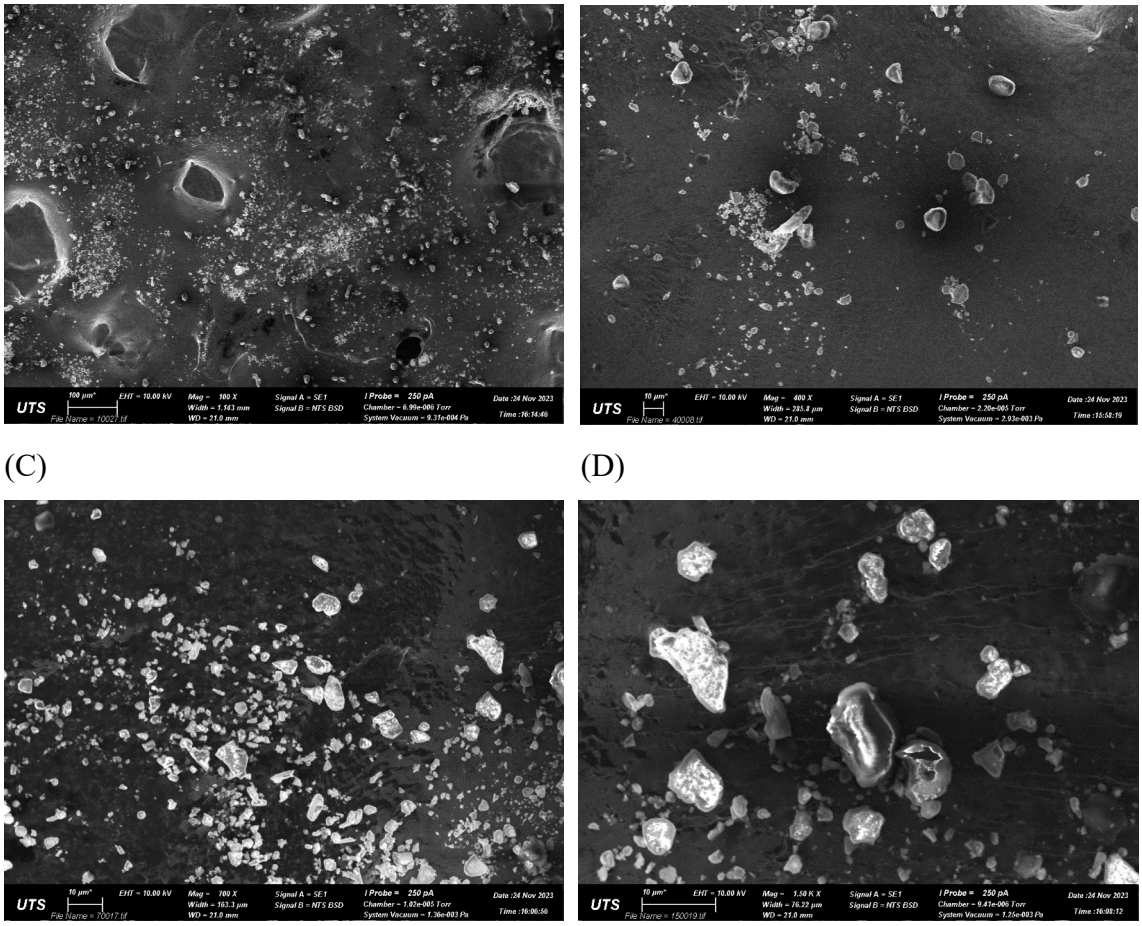

(C) (D)

Figure 5.11. Images of ZTA aggregates and micro-sized ZTA model particles collected with a 0.8 µm filter. The particles were imaged using a FEG-SEM at magnifications of (A) 100 X, (B) 400 X, (C) 700 X and (D) 1500 X. Size bars of 100 µm in image A and 10 µm for images B – D.

(A) (B)

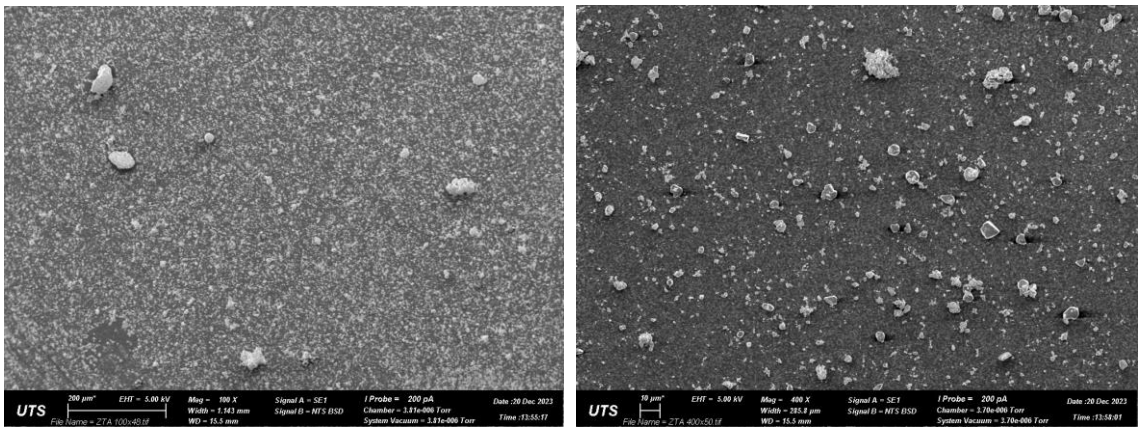

(C) (D)

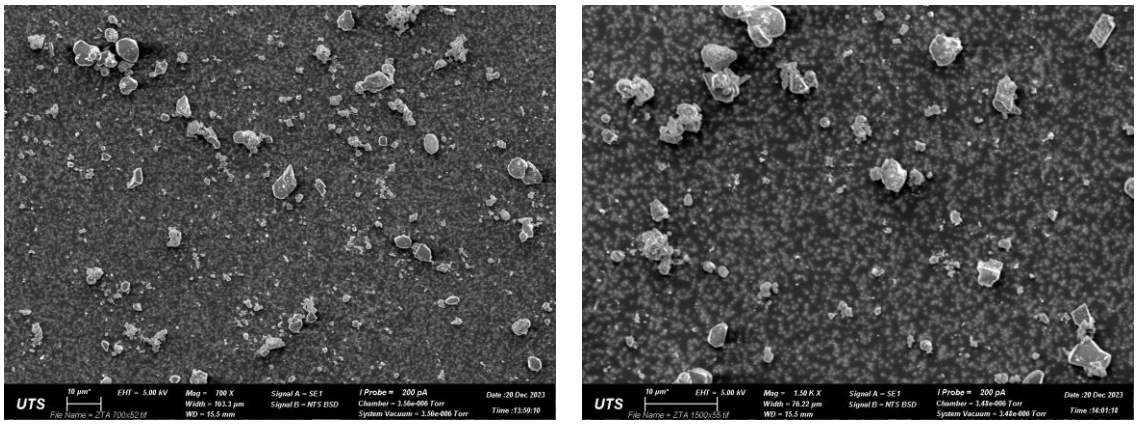

Figure 5.12. Images of ZTA aggregates and micro-sized ZTA model particles collected with a 0.1 µm filter. The particles were imaged using a FEG-SEM at magnifications of (A) 100 X, (B) 400 X, (C) 700 X and (D) 1500 X. Size bars of 200 µm in image A and 10 µm for images B – D.

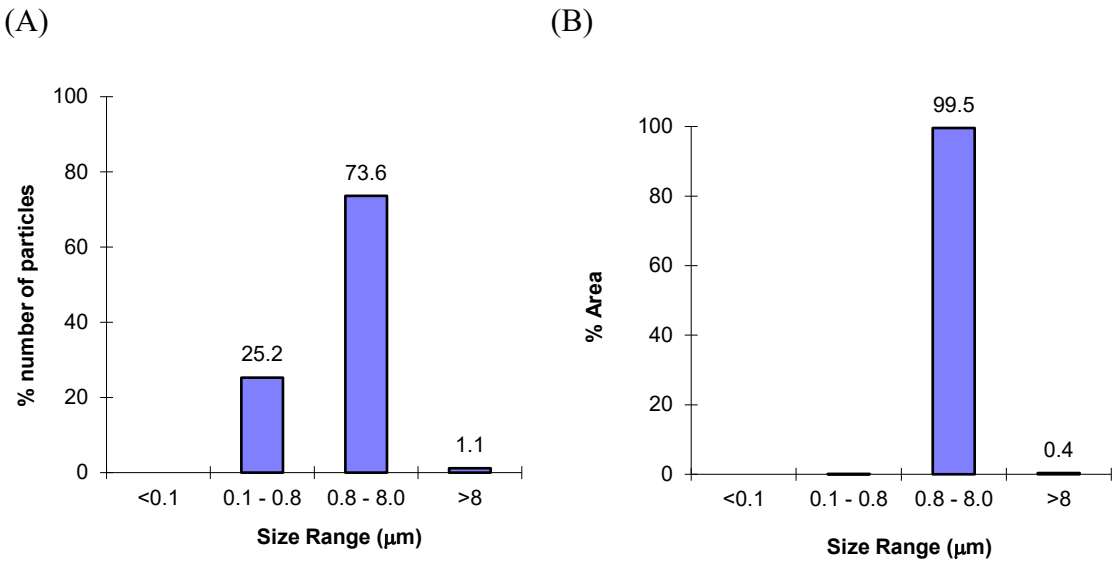

Figure 5.13. The percentage frequency and percentage area distribution of ZTA model particles as a function of particle size determined from SEM images. (A) Percentage frequency distribution; (B) Percentage area distribution.

5.3.2.5 Characterisation of metal model particles

CoCrMo model particles were filtered sequentially using 8 µm, 0.8 µm and 0.1 µm filters. The CoCrMo particles were imaged using SEM with an accelerating voltage of 5 kV and a working distance ranging of 14.5 mm to 16.0 mm. The morphologies of the CoCrMo particles collected from each polycarbonate membrane filter are shown in Figures 5.14, 5.15 and 5.16. CoCrMo model particles displayed mostly globular in shape with some being polygonal. The mean size of the CoCrMo model particles was 5.86 ± 1.20 µm in diameter. The size range of CoCrMo particles was 2.15 – 11.6 µm in diameter, with 88% of particles having a diameter less than 8 µm (Figure 5.17). The CoCrMo model particles had a mode size of 0.8 – 8.0 µm with approximately 88.5% of all particles. In addition, although a small proportion of particles (11.5%) were in the >8 µm size range, the mode distribution of area of the particles with 56.2% were in the >8 µm size range.

(A) (B)

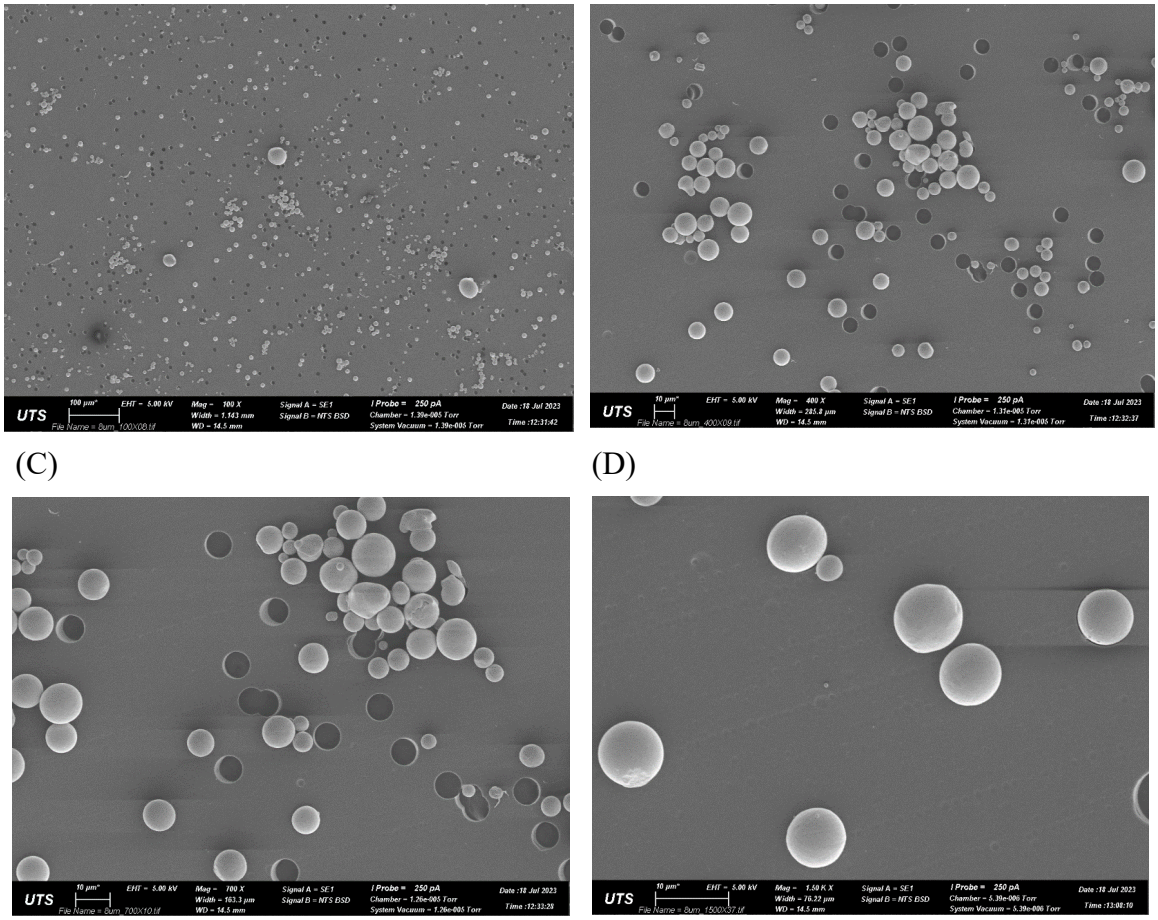

(C) (D)

Figure 5.14. Images of CoCrMo aggregates and micro-sized CoCrMo model particles collected with an 8 µm filter. The particles were imaged using a FEG-SEM at magnifications of (A) 100 X, (B) 400 X, (C) 700 X and (D) 1500 X. Size bars of 100 µm in image A and 10 µm for images B – D.

(A) (B)

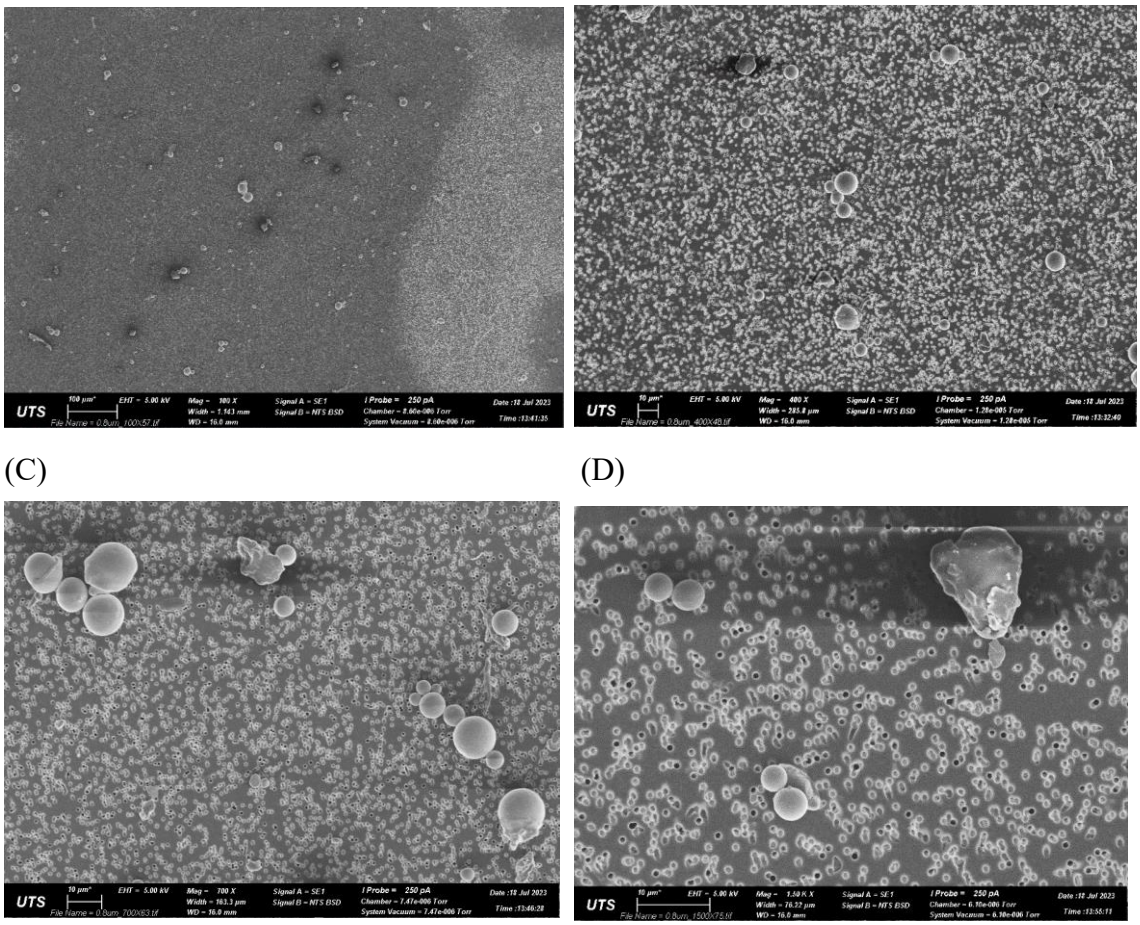

(C) (D)

Figure 5.15. Images of CoCrMo aggregates and micro-sized CoCrMo model particles collected with a 0.8 µm filter. The particles were imaged using a FEG-SEM at magnifications of (A) 100 X, (B) 400 X, (C) 700 X and (D) 1500 X. Size bars of 100 µm in image A and 10 µm for images B – D.

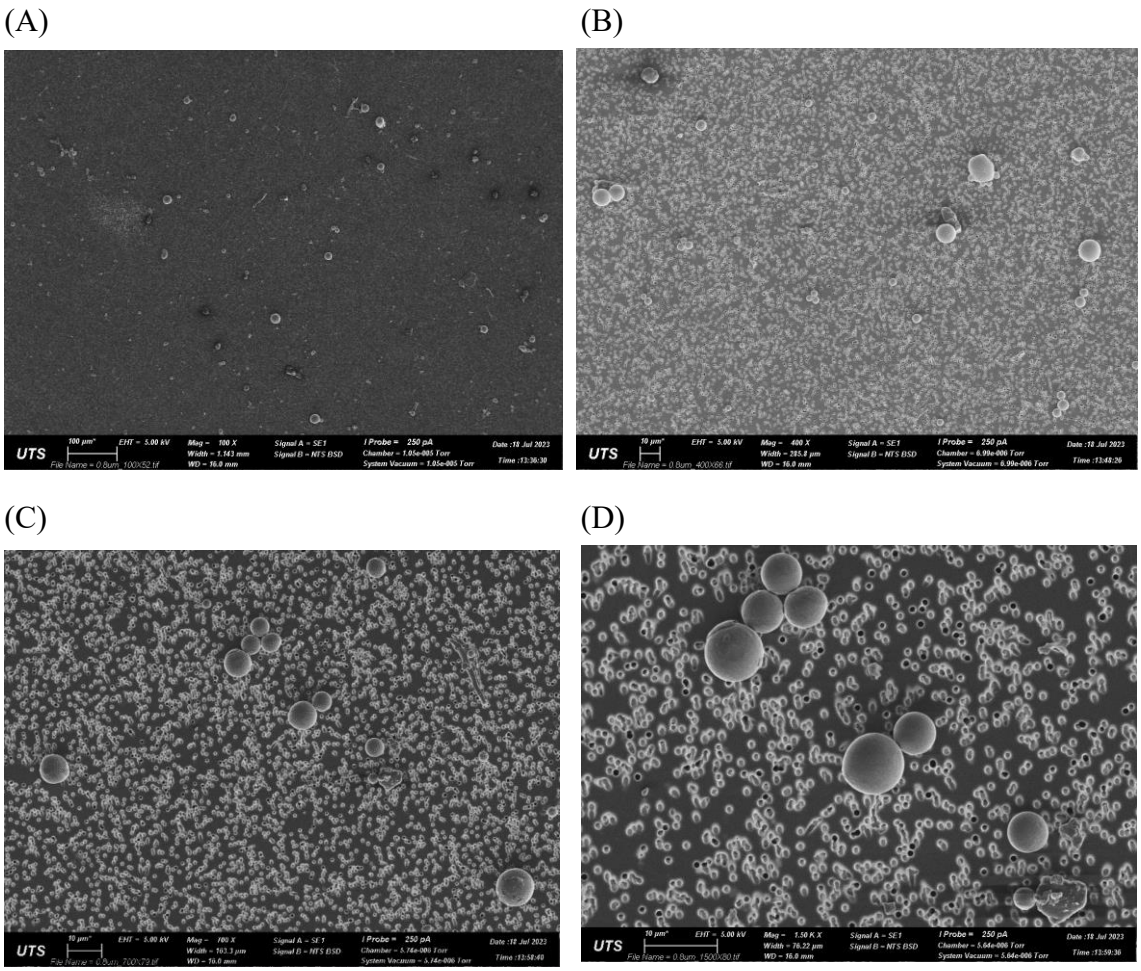

Figure 5.16. Images of CoCrMo aggregates and micro-sized CoCrMo model particles collected with a 0.1 µm filter. The particles were imaged using a FEG-SEM at magnifications of (A) 100 X, (B) 400 X, (C) 700 X and (D) 1500 X. Size bars of 100 µm in image A and 10 µm for images B – D.

(A) (B)

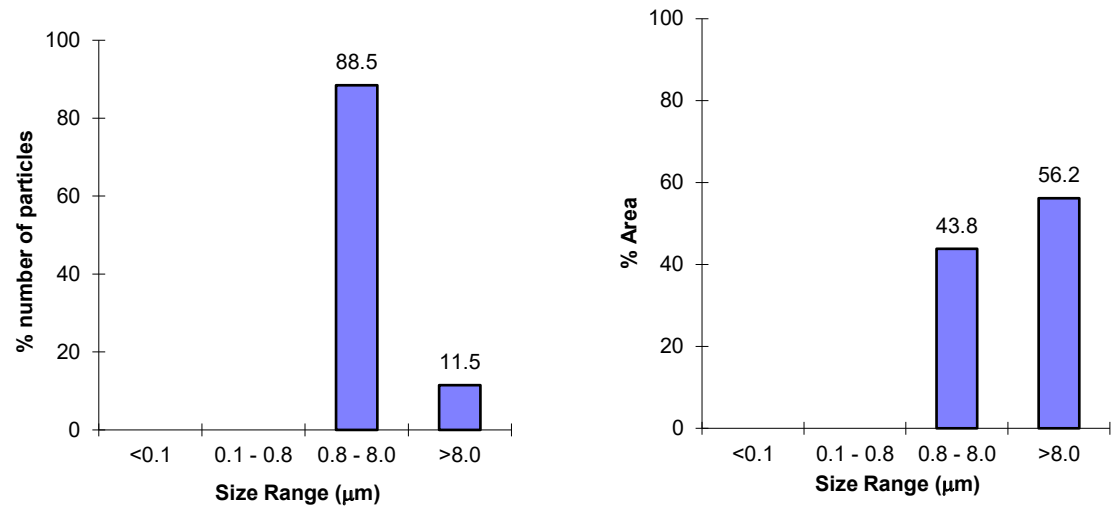

Figure 5.17. The percentage frequency and percentage area distribution of CoCrMo model particles as a function of particle size determined from SEM images. (A) Percentage frequency distribution; (B) Percentage area distribution.

5.4 Section B: Development of an in vitro 3D GelMA hydrogel model for evaluating neural cell responses to model particles

5.4.1 Specific materials

The specific materials for this section are listed in Table 5.3.

Table 5.3. Specific materials used for the development of the 3D GelMA hydrogel model

Material	**Supplier**
Gelatin Methacryloyl (GelMA)	CELLINK, Sweden
Lithium acylphosphinate (LAP)	CELLINK, Sweden
CellTiter-Glo 3D viability reagent	Promega
Calcien AM	Invitrogen
Propidium Iodine (PI)	Invitrogen

5.4.2 Specific methods

5.4.2.1 Preparation of GelMA hydrogels

In this study, the preparation method of GelMA hydrogels was conducted according to the protocol obtained from CELLINK. The materials for making GelMA were provided in the GelMA Kit from CELLINK, which included sterile freeze-dried GelMA powder and a photoinitiator, lithium acylphosphinate LAP). Firstly, to make the photoinitiator solution with a concentration of 0.25% (w/v), 250 mg of LAP powder was dissolved in 100 mL of phosphate-buffered saline (PBS). The LAP/PBS solution was mixed at 60ºC for 20 minutes on a hot plate using a magnetic stirrer. After mixing, the LAP/PBS solution was filter sterilised (0.22 μm) in a class II biosafety cabinet under dark conditions due to light sensitivity of GelMA. The tube containing the LAP/PBS solution was then covered with aluminium foil to prevent light exposure.

In this study, a GelMA hydrogel concentration of 5% (w/v) was prepared for developing the 3D model. The rationale of using 5% (w/v) was due to the findings of a previous study that demonstrated 5% (w/v) GelMA as the most optimal concentration for neuronal and astrocyte-like cell viability over a period of 7 days, at 37ºC and 5% (v/v) CO_2 [278]. To create a 5% (w/v) GelMA hydrogel solution, a volume of 10 mL LAP/PBS solution was added to 500 mg of GelMA powder and thoroughly mixed using a stirrer at 50ºC for 20

minutes on a hot plate. For future use, the GelMA hydrogel solution was stored in the fridge at 4ºC for a maximum of 3 months. To prepare for bioprinting, the GelMA hydrogel solution was transferred into a sterile, 3 mL cartridge.

5.4.1.2 Preparation of GelMA bioinks for bioprinting

The different bioinks prepared with GelMA hydrogels are shown in table 5.4.

Table 5.4. The different bioinks used in 3D bioprinting

Bioink #1	GelMA hydrogel
Bioink #2	GelMA hydrogel + particles (polymer or ceramic, or metal model particles)
Bioink #3	GelMA hydrogel + C6 astrocyte-like cells
Bioink #4	GelMA hydrogel + neuronal NG108-15 cells
Bioink #5	GelMA hydrogel + C6 astrocyte-like cells + particles (polymer, or ceramic, or metal model)
Bioink #6	GelMA hydrogel + neuronal NG108-15 cells + particles (polymer, or ceramic, or metal model)

The first step in the preparation of GelMA hydrogel bioinks containing neural cells, started with culturing C6 astrocyte-like cells and NG108-15 neuronal cells in T75 flasks at 37ºC and 5% (v/v) CO_2 as described in sections 3.2.3. When cells reached 80% confluence, cell culture medium was aspirated, and cells were washed with 10 mL of Dulbecco's phosphate-buffered saline (DPBS) solution. After removing DPBS, 3 mL of trypsin-EDTA was added to the flask and incubated for 3 minutes at 37ºC and 5% (v/v) CO_2 to detach cells, which were observed under an inverted light microscope. Following this, 3 mL of fresh complete cell culture medium, containing 10% (v/v) FBS was added to neutralise the trypsin and the cell solution was transferred to a 15 mL centrifuge tube. The cell suspension was centrifuged for 5 minutes at 300 *g*. After centrifugation, the supernatant was aspirated to isolate the cell pellet. The cell pellet was resuspended in fresh cell culture medium to be prepared to mix with GelMA hydrogel.

The GelMA hydrogel solution was pre-warmed in the incubator at 37ºC, prior to bioprinting. To create the bioinks, cells were mixed with GelMA hydrogel solution at a

ratio of 1:10. For example, 1 mL of GelMA solution was mixed with 100 µL of cells, at a concentration of 1 x 10^4 ml^{-1}. The cells and GelMA hydrogel were mixed thoroughly by aspiration in a 15 mL centrifuge tube to ensure that the cells were dispersed homogeneously in the bioink solution. The bioink was transferred to a 3 mL cartridge and a piston was placed on top to close off the opening of the cartridge. The nozzle was screwed onto the cartridge and the cartridge was inserted into the temperature-controlled print head of the bioprinter. Following this, parameters including extrusion pressure and speed of the bioprinting process, as well as the temperature were selected on the screen of the bioprinter. Simple droplet structures of GelMA hydrogels were printed in well plates. Finally, photocrosslinking of bioprinted GelMA hydrogels was required to allow for the hydrogel structures to remain intact when incubated at 37ºC and 5% (v/v) CO_2 for a duration of 7 days. The optimised conditions for photocrosslinking GelMA hydrogels (5% w/v) to support viability of neural cells were demonstrated previously by Rad *et al* [278]. These authors demonstrated the viability of C6 astrocyte-like and NG108-15 neuronal cells over 7 days when grown in bioprinted GelMA hydrogels that were photocrosslinked with UV at 365 nm (at an intensity of 19.42 $mW.cm^2$) for 120 seconds. Thus, in the current study, each bioprinted GelMA droplet encapsulating cells was photocrosslinked with UV at 365 nm (at an intensity of 19.42 $mW.cm^2$) for 120 seconds.

When preparing bioinks for GelMA hydrogels embedded with particles, particles were mixed with GelMA hydrogel solution also at a ratio of 1:10, i.e. 1 mL of GelMA solution mixed with 100 µl particle solution, containing 100 μm^3 of a PEEK-OPTIMA model particles. Embedding particles in GelMA hydrogels was a novel approach and investigating whether the inclusion of particles affected whether the extrusion of the hydrogel through the nozzle was essential for 3D model development of evaluating biological responses of neural cells exposed to particles.

5.4.1.3 The bioprinting process

Bioprinting of the GelMA hydrogels in this study was conducted using the CELLINK BIO X and BIO X6 bioprinter, which are extrusion-based bioprinters. Extrusion-based bioprinting uses a dispensing system to extrude a bioink. The components of the BIO X and BIO X6 printers are described in Table 5.5 and the displayed in Figure 5.18 and 5.19.

Table 5.5 The general components of the CELLINK bioprinters, BIO X and BIO X6

Component	**Function**
Print head/Extrusion system	The print heads are temperature-controlled that are equipped with one or more nozzles. They are used for precise deposition of bioinks during bioprinting.
Syringe/Cartridge	The syringe/cartridges are used to load bioinks (mixture of cells, supportive biomaterial and particles), which can be controlled to regulate bioink flow during bioprinting.
Print bed	The stage/platform is a stable surface for 3D bioprinting to occur on. The height of the platform can be adjusted to account for printing multiple layers.
Temperature control system	The printers are equipped with a temperature control system, which can be regulated for optimal temperature conditions for biomaterial properties and cell viability during bioprinting.
Motion control system	The printer is equipped with a motion control system that allows the movement of the print heads in the x, y and z directions. This allows for bioprinting multiple layers to create 3D structures.
Control software	The control software allows the import of 3D models and control printing parameters.
Touchscreen interface	The bioprinters have an integrated touchscreen interface that allows users to navigate and regulate printing parameters including print speed, extrusion pressure and temperature.
UV light source	The bioprinter has an integrated UV light source. It can be used as part of the photocrosslinking process, which causes gelatinisation and stabilises 3D structures.

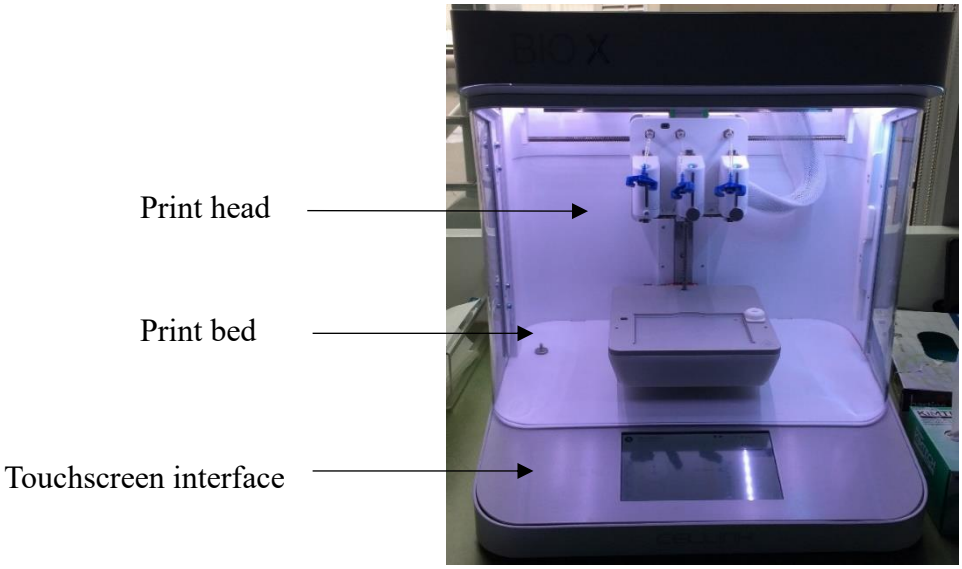

Figure 5.18. The CELLINK BIO X Bioprinter

Figure 5.19. The CELLINK BIO X6 Bioprinter

The first step in bioprinting was sterilisation of the bioprinters, achieved by turning on the chamber fans and the UV sterilisation system. When sterilisation was completed after 30 minutes, the inside of the bioprinter was cleaned using 70% (v/v) ethanol and a multi-well plate was placed on the bioprinter print bed. For printing structures, "bioprint" was selected on the start menu. On the model menu, "3D models" was selected and the 5 x 5 x 1 mm^3 (width x length x height) STL file was selected as the model for bioprinting. On the surface menu, the specific multi-well plate (e.g. 6 well plate, 12 well plate, 96 well plate, etc) and the vendor (Corning, Falcon) was selected. On the printer menu, a print bed temperature of 10^oC was selected to ensure the gelation of GelMA hydrogels once printed onto the well plates. For the tool type, pneumatic 3 mL was selected. In addition, the bioprinting parameters including, nozzle diameter (200 – 840 μm), extrusion pressure (9 – 35 kPa), print speed (5 – 11 mm/s) and print head temperature (22 – 34^oC) were selected. On the layer menu, a grid lattice with infill density of 50% was selected as the layer profile. In addition, a layer height of 0.15 mm was selected. On the print menu, all the bioprinting parameters were checked and the "print" option was selected. Finally, on the bioprint menu, calibration was selected to manually calibrate the position of the print bed in the X, Y and Z axes. After calibrating the position of the nozzle in the desired position above the well plate, the "start" option was selected to initiate bioprinting. During the bioprinting, parameters including print head temperature, print speed and extrusion pressure were able to be altered to optimise the bioprinting of GelMA hydrogels. After bioprinting, photocrosslinking was selected at 345 nm for 120 seconds for each GelMA structure. The images of the bioprinting process used with the touchscreen interface for bioprinting GelMA hydrogels are displayed in Figure 5.20.

(A)

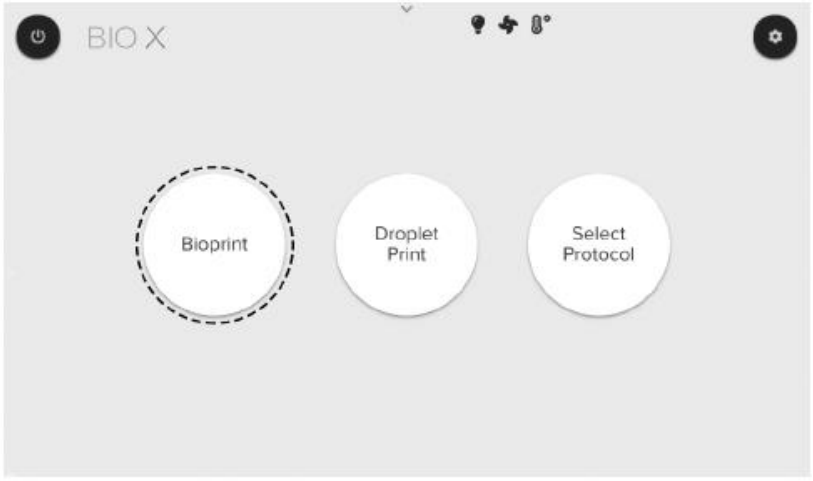
BIO X
Bioprint
Droplet Print
Select Protocol

(B)


Model
Cube10x10x5.stl
/run/media/sda1
20mmTestCube_repaired.stl
20x20x1mm.stl
Cube10x10x5.stl
HumanEar-fullsize.stl
HumanEar.stl
HumanEar_35percent.stl
Select an STL file
Model
Surface
Printer
Layers
Print

(C)

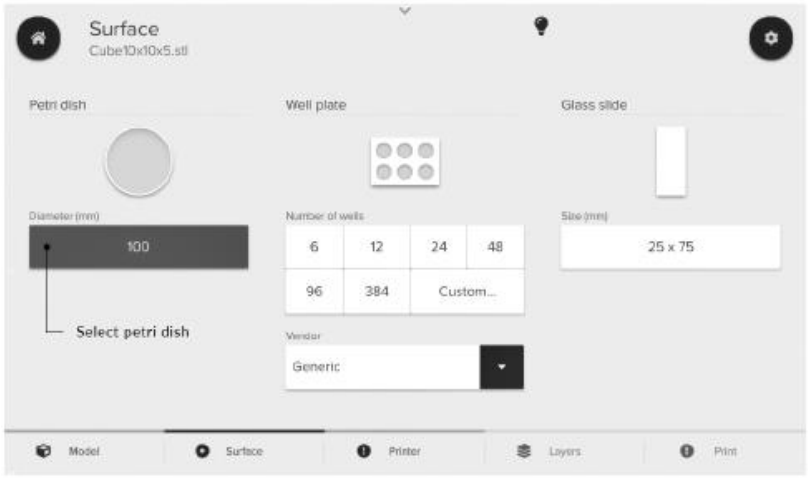
Surface
Cube10x10x5.stl
Petri dish
Well plate
Glass slide
Diameter (mm)
100
Select petri dish
Number of wells
6
12
24
48
96
384
Custom...
Size (mm)
25 x 75
Vendor
Generic
Model
Surface
Printer
Layers
Print

(D)


Printer
Cube10x10x5.stl
Printer
Tool 1
Tool 2
Tool 3
Select printhead
Tool type
Temperature Controlled
Bioink profile
CELLINK START
Photocrosslinking
Off
0.410 mm
Nozzle diameter
20 kPa
Pressure
0 and 0 ms
Pre- and postflow times
Select pressure
Off
Temperature
20 mm/s
Speed
Select print speed
Model
Surface
Printer
Layers
Print

(E)

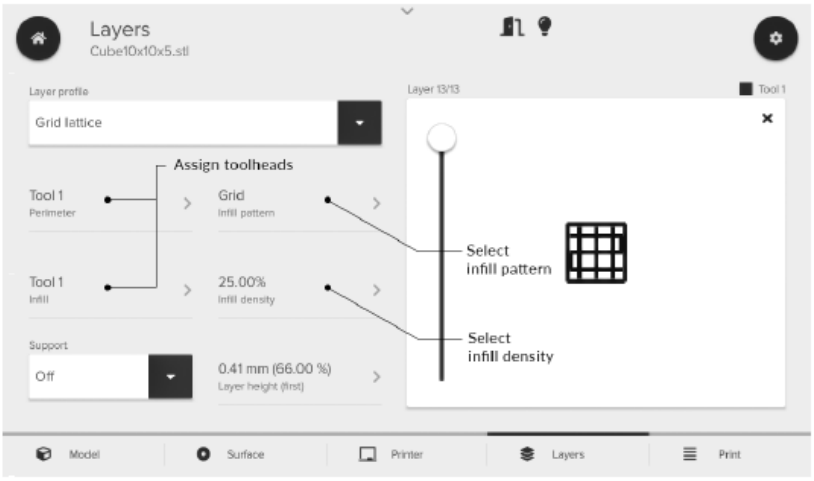
Layers
Cube10x10x5.stl
Layer profile
Grid lattice
Layer 13/13
Tool 1
Assign toolheads
Tool 1
Perimeter
Grid
Infill pattern
Select
infill pattern
Tool 1
Infill
25.00%
Infill density
Select
infill density
Support
Off
0.41 mm (66.00 %)
Layer height (first)
Model
Surface
Printer
Layers
Print

(F)


Print
Cube10x10x5.stl
Tool 1
Temperature Controlled
CELLINK START
Nozzle Ø: 0.41 mm
No photocrosslinking
Test extrusion
Tool 2
Not selected
Tool 3
Not selected
Surface
100x15 glass petri dish
Off
Temperature (41.0 °C)
20 kPa
Pressure
20 mm/s
Speed
Save
Print
Model
Surface
Printer
Layers
Print

(G)

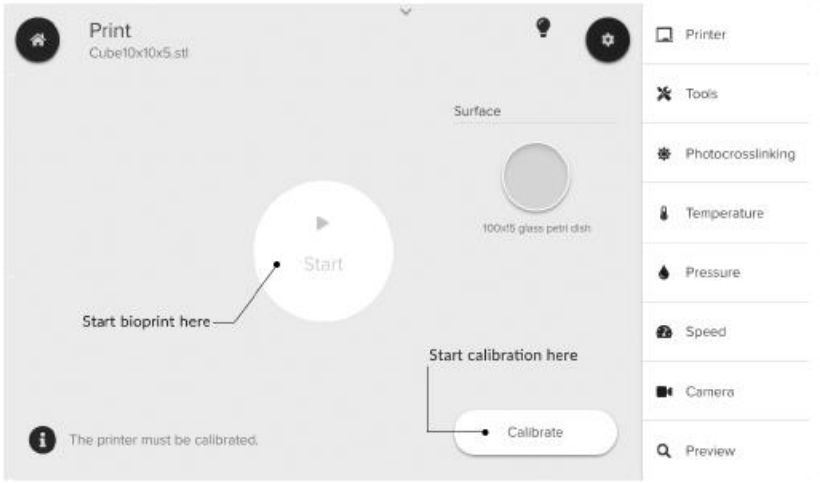

Figure 5.20. The bioprinting process of the BIO X printer.

(A) The start menu with three options (Bioprint, droplet print, Select protocol); (B) The model menu with selection of STL files; (C) The surface menu with selection of print surfaces; (D) The printer menu with selection of printing parameters including tool type, nozzle diameter, extrusion pressure, print speed, temperature, pre-flow delay and post-flow delay; (E) The layer menu with selections of infill pattern, infill density and layer height; (F) The print menu to preview print parameters and print option; (G) The Bioprint menu to initiate calibration of the system and begin bioprinting process.

5.4.2 Results

5.4.2.1 Determination of optimal printing parameters of print head temperature, print speed and extrusion pressure for GelMA hydrogels

In this part of the study, the aim was to achieve optimal printability for GelMA hydrogels by determining the most suitable printing parameters including print head temperature, print speed and extrusion pressure. The BIO X bioprinter was utilised to print GelMA hydrogels using the process described in 5.4.1.3. The first part of this experiment involved bioprinting GelMA hydrogels in a square grid structure. A square grid construct (width x length x height) of dimensions, 5 x 5 x 1 mm^3 was utilised as the model for bioprinting the GelMA hydrogels that was based off the study conducted by Rad *et al* [267]. The authors in Rad *et al* [267] determined that the optimal parameters for bioprinting 5% (w/v) GelMA hydrogels consisted of having a bed temperature, print head temperature, extrusion pressure and print speed of 10ºC, 24ºC, 12 kPa and 11$mm.s^{-1}$, respectively, and

also using a 22G nozzle size. However, in this study, when these conditions were applied the resulting bioprinted GelMA hydrogel structures were not consistent in terms of volume of hydrogel released and structural integrity, as shown in Figure 5.21. For example, there were incidences of staggered extrusion of GelMA, which resulted in irregular bead-like structures. In addition, there were occurrences of excessive extrusion of GelMA, which resulted in a circular formation of polygonal GelMA structures. As a result of inconsistent bioprinted GelMA structures with the square grid structure model, droplet printing was considered as an alternative to ensure higher consistency of structural integrity of bioprinted GelMA.

Figure 5.21. Photographic images of bioprinted GelMA hydrogels with 5% (w/v) concentration using a BIO X bioprinter. The attempted model used was a square grid construct of dimensions, 5 x 5 x 1 mm^3 with bed temperature, print head temperature, extrusion pressure and print speed of 10ºC, 24ºC, 12 kPa and 11 $mm.s^{-1}$, respectively. The bioprinted GelMA hydrogels showed inconsistency in volume of material and morphology.

When performing the first droplet printing of GelMA hydrogels with the same printing parameters of a bed temperature, print head temperature, extrusion pressure and print speed of 10ºC, 24ºC, 12 kPa and 11 $mm.s^{-1}$, respectively. As seen in figure 5.22., the structural integrity of the bioprinted droplet GelMA hydrogels were not consistent across the three wells, with the first well (bottom left corner) having a larger structure compared to the second and third well.

Consequently, for the next print the extrusion pressure was reduced to 6 kPa. The rationale behind that was to test whether it would prevent an excess amount of GelMA hydrogel being extruded from the nozzle in the first well. The other parameters including bed temperature, print head temperature and print speed were kept the same as the previous print at 10°C, 24°C, and 11 $mm.s^{-1}$, respectively. The result of this print is shown in figure 5.23. As seen in figure 5.23, the GelMA hydrogels were printed with consistency across all wells.

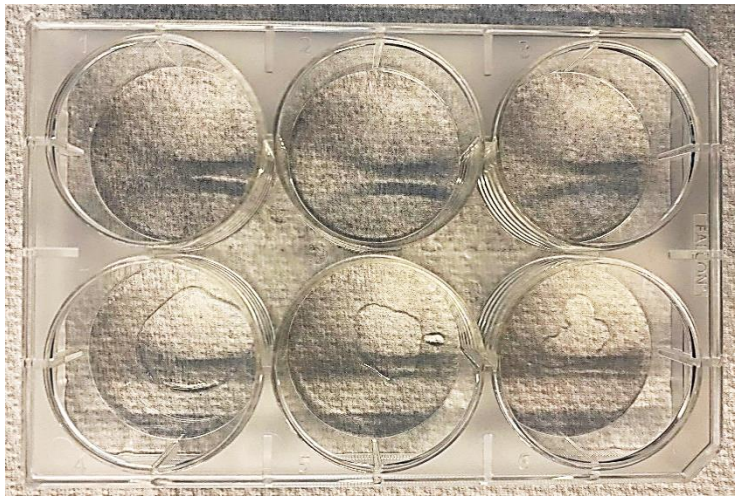

Figure 5.22. Photographic image of bioprinted droplet GelMA hydrogels with 5% (w/v) concentration using a BIO X bioprinter. The printing parameters were set for bed temperature, print head temperature, extrusion pressure and print speed at 10°C, 24°C, 12 kPa and 11 mm/s, respectively. The bioprinted GelMA hydrogel droplets showed inconsistency in terms of volume and morphology.

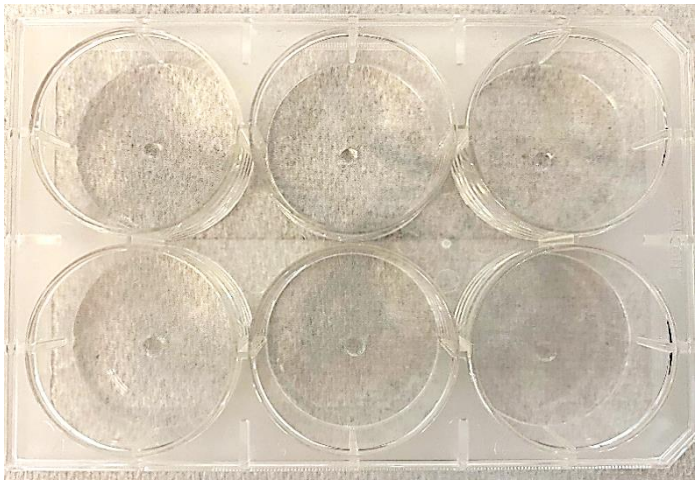

Figure 5.23. Photographic image of bioprinted droplet GelMA hydrogels with 5% (w/v) concentration using a BIO X bioprinter. The printing parameters were set for bed temperature, print head temperature, extrusion pressure and print speed at 10°C, 24°C, 6 kPa and 11 $mm.s^{-1}$, respectively. The bioprinted GelMA hydrogel droplets showed consistency in volume of material extruded and morphology.

5.4.2.2 Determination of nozzle size for bioprinting GelMA hydrogels mixed with particles

In this study, four different nozzles with different gauge sizes (20G, 22G, 25G, and 27G) were investigated for droplet printing of GelMA hydrogels mixed with particles. The print speed and extrusion pressure used were 11 $mm.s^{-1}$and 6 kPa, respectively. Nozzles with gauge sizes of 20G and 22G had inner diameters of 0.58 mm and 0.41 mm, respectively, and were able to extrude GelMA hydrogels with particles. However, the nozzles with a gauge size of 25G (0.25 mm inner diameter) and 27G (0.20 mm inner diameter) were not able to extrude the bioink plus particles consistently. A summary of the nozzle sizes tested for bioprinting GelMA hydrogel and particles are shown in table 5.5. Microscopic images of PEEK, polyethylene, ZTA and CoCrMo particles printed with GelMA hydrogels using the 22G nozzle are shown in Figure 5.37.

Table 5.6. Summary of CELLINK nozzles and needle diameters used for bioprinting GelMA hydrogels and particles using the BIO X bioprinter.

Standard nozzle	Nozzle colour	Gauge	Inner diameter (mm)	Was it able to extrude GelMA mixed with particles consistently? (Y/N)
	Pink	20G	0.58	Y
	Blue	22G	0.41	Y
	Red	25G	0.25	N
	Clear	27G	0.20	N

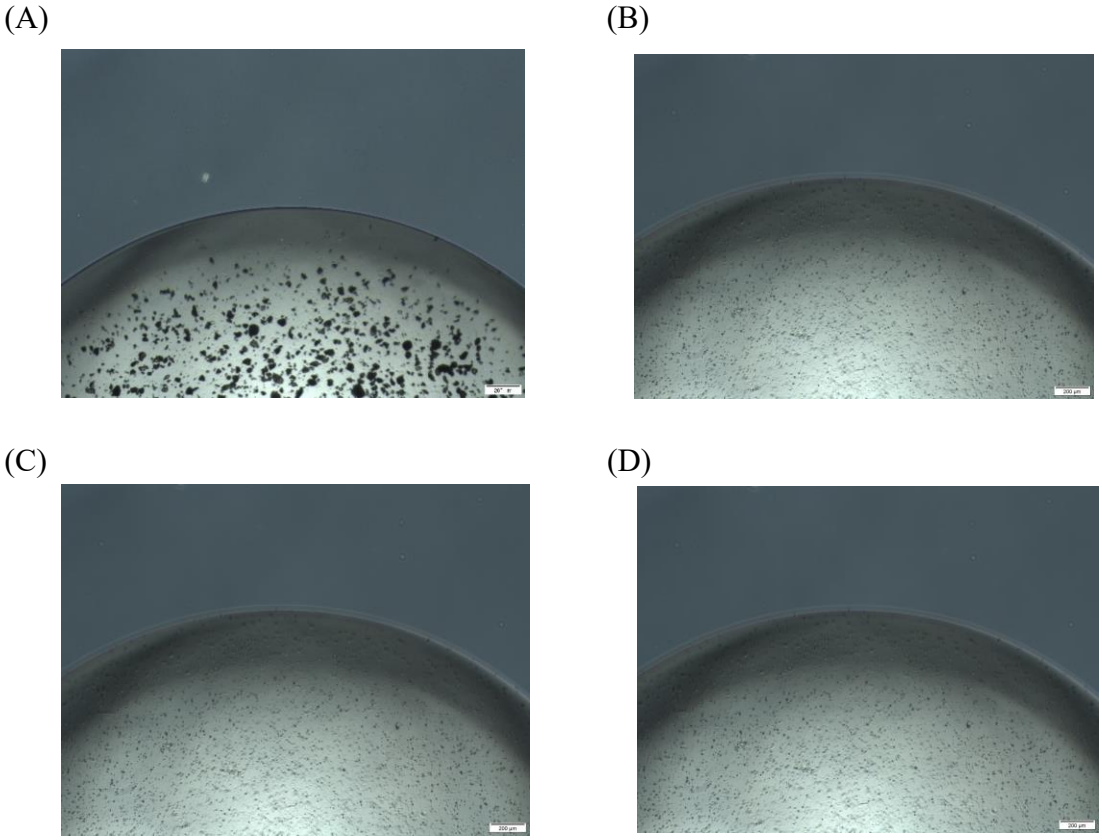

Figure 5.24. Microscopic images of bioprinted GelMA hydrogel droplets with 5% (w/v) concentration embedded with model particles. (A) PEEK-OPTIMA particles; (B) Ceridust 3615 ® particles; (C) ZTA particles and (D) CoCrMo particles. The printing parameters of nozzle temperature, extrusion pressure and speed were 24°C, 6 kPa and 11 $mm.s^{-1}$, respectively. Scale bar = 200 μm.

5.4.2.3 Cell viability of neural cells in bioprinted GelMA hydrogels

C6 astrocyte-like cells were bioprinted within 5% (w/v) GelMA hydrogels to create a 3D environment for cell culture and this was compared with C6 astrocyte-like cells cultured in the traditional 2D culture system. Bioinks with C6 astrocyte-like cells and GelMA hydrogels combined were created by mixing the cells with GelMA hydrogel solution at a ratio of 1:10. For example, 1 mL of GelMA solution was mixed with 100 μL of cells, at a concentration of 1 x 10^4 ml^{-1}. The C6 cells were cultured in 5% (w/v) GelMA hydrogels over a duration of 7 days at 37°C and 5% (v/v) CO_2. In the first experiment, images of C6 cells were taken with a bright-field microscope (Figure 5.25) and quantitative analysis of cell viability was conducted using Celltiter-Glo 3D cell viability assay at days 1, 3 and 7 (Figure 5.26). Throughout the 7 days, C6 cells cultured in GelMA hydrogels proliferated

at a similar rate to the cells only control in 2D (1 x 10^4 ml^{-1}), as seen in Figures 5.26 and 5.27. In addition, qualitative analysis of cell viability was evaluated using a live/dead stain of calcien AM and Propidium Iodine (PI). Qualitative analysis also demonstrated increased proliferation of C6 astrocyte-like cells over 7 days, as shown in Figure 5.25. On days 3 and 7, the presence of processes extended from the C6 cells could be observed. Dead cell numbers were very limited compared to the live cells.

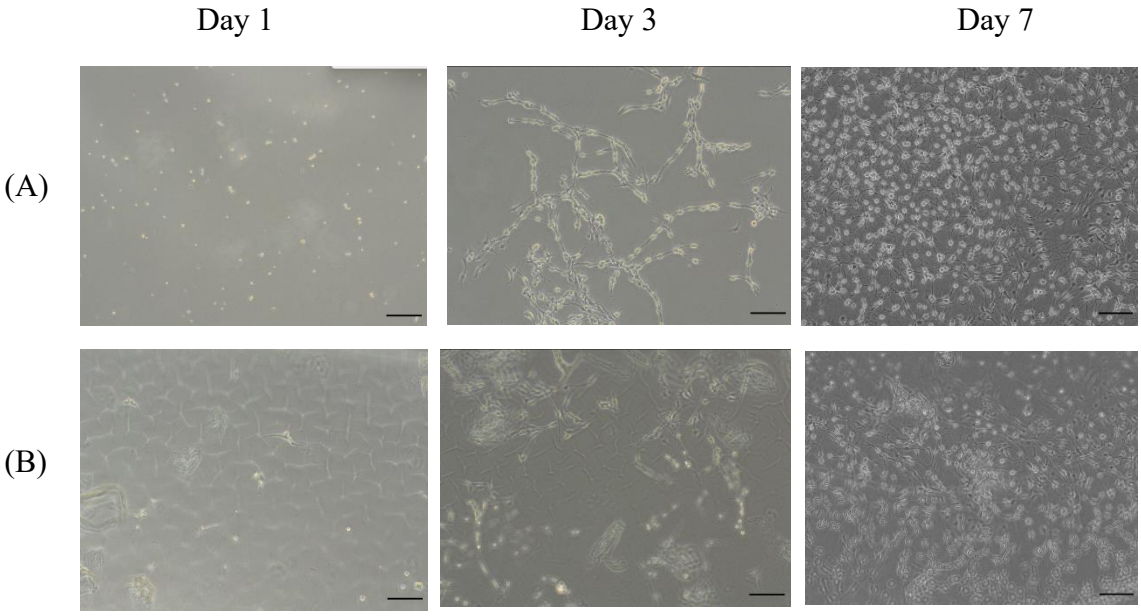

Figure 5.25. Bright-field microscope images of C6 cells (1x 10^4 ml^{-1}) in 2D cell culture compared to C6 cells in GelMA hydrogels at Day 1, 3 and 7. (A) C6 cells in 2D culture at 10 X magnification; (B) C6 cells in 3D culture at 10 X magnification; Scale bar = 100 µm

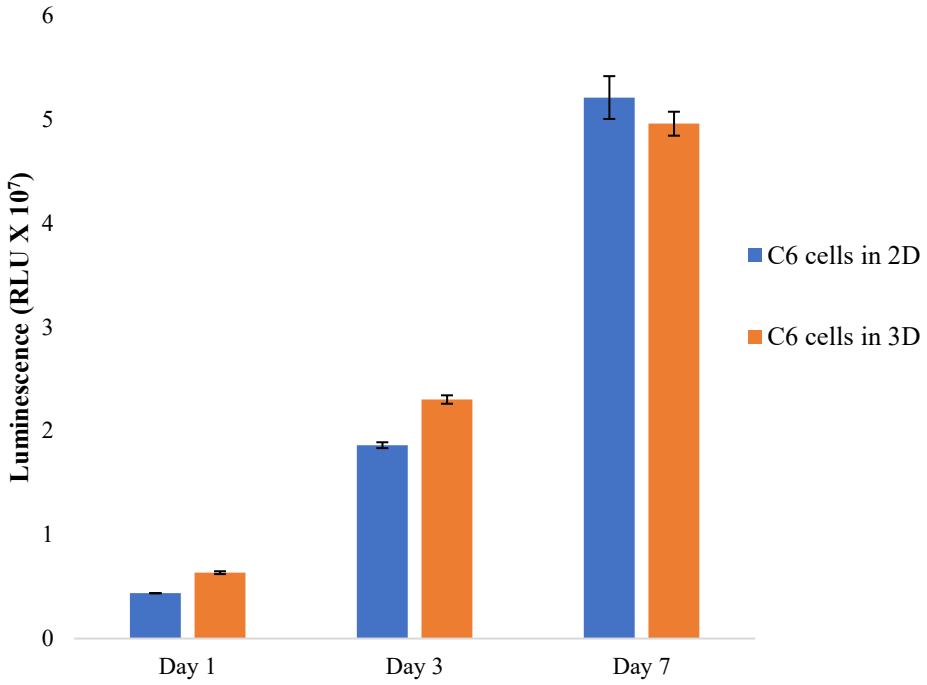

Figure 5.26. Quantitative analysis of cell viability of C6 astrocyte-like cells grown in GelMA hydrogels over 7 days. C6 astrocyte-like cells at a concentration of 1 x 10^4 ml^{-1} were encapsulated in 5% (w/v) GelMA hydrogels. The GelMA samples were incubated at 37°C and 5% (v/v) CO_2 and cell viability were assessed at days 1, 3 and 7. Error bars indicate standard deviation.

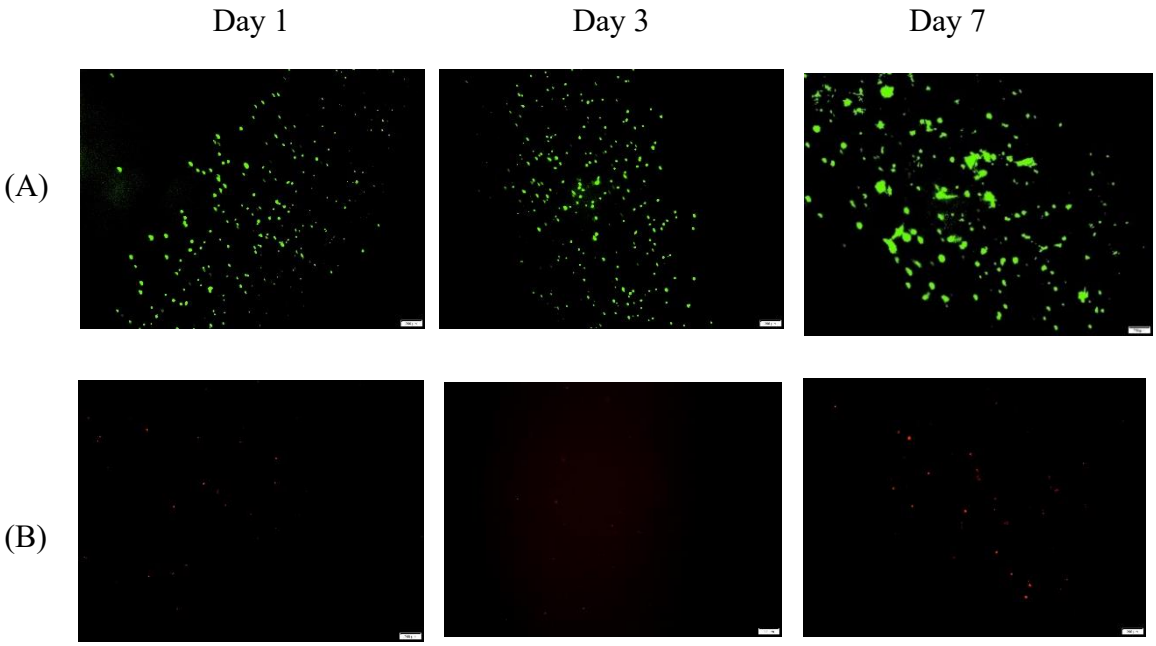

Figure 5.27. Qualitative analysis using fluorescence microscopy of 5% (w/v) GelMA, embedded with C6 cells (1 x 10^4 ml^{-1}) at days 1, 3 and 7. GelMA was immersed in cell culture medium and incubated at 37°C in 5% (v/v) CO_2. (A) C6 cells stained with Calcien AM (live cells) and (B) C6 cells stained with Propidium Iodine (dead cells). Scale bar = 200 µm.

5.4.2.4 Cell viability of neuronal cells in bioprinted GelMA hydrogels

NG108-15 neuronal cells were bioprinted with 5% (w/v) GelMA hydrogels to create a 3D environment for cell culture and this was compared with cells cultured in the traditional 2D culture system. The NG108-15 cells were cultured in GelMA hydrogels over a duration of 7 days at 37°C and 5% (v/v) CO_2. Quantitative analysis of cell viability (Figure 5.28) was conducted using a CellTiter-Glo cell viability assay at days 1, 3 and 7. In addition, qualitative analysis of cell viability was evaluated using a live/dead stain of calcien AM and Propidium Iodine (PI). Qualitative analysis demonstrated increased proliferation of NG108-15 neuronal cells over 7 days, as shown in Figure 5.29. On day 7, the presence of neurites developing from the neuronal cells could be observed. Throughout the 7 days, NG108-15 cells cultured in GelMA hydrogels proliferated at a similar rate to the cells in 2D, as seen in Figures 5.41. Similar to the experiment conducted with C6 astrocyte-like cells, the cell viability of NG108-15 cells increased over 7 days, and there were low numbers of dead cells (figure 5.29).

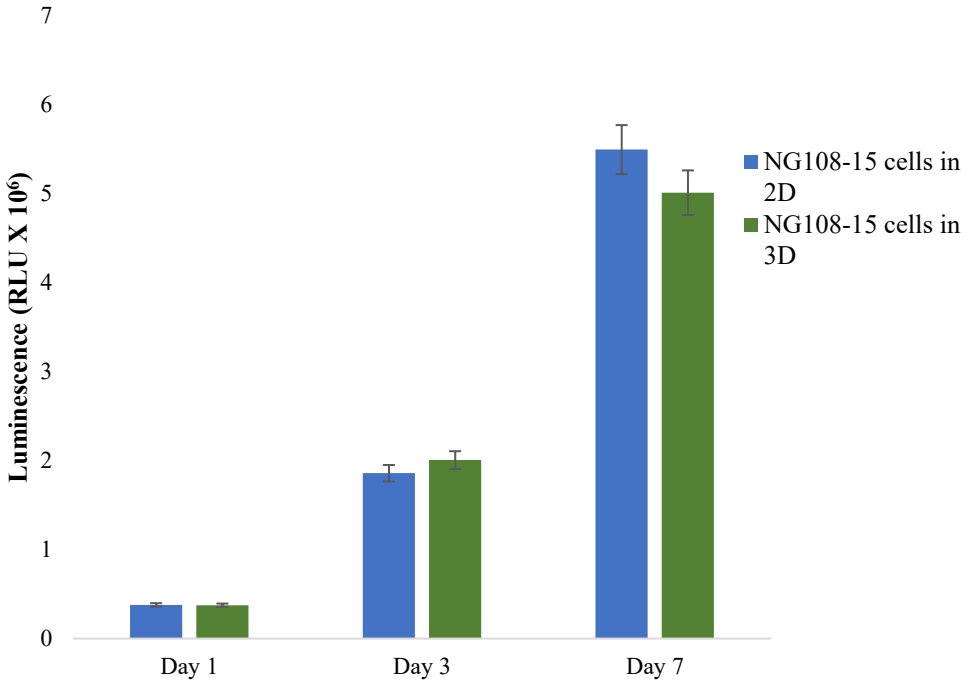

Figure 5.28. Quantitative analysis of cell viability of neuronal NG108-15 cells grown in GelMA hydrogels over 7 days. Neuronal NG108-15 cells at a concentration of 1 x 10^4 ml^{-1} were encapsulated in 5% (w/v) GelMA hydrogels. The GelMA samples were incubated at 37ºC and 5% (v/v) CO_2 and cell viability were assessed at days 1, 3 and 7. Error bars indicate standard deviation.

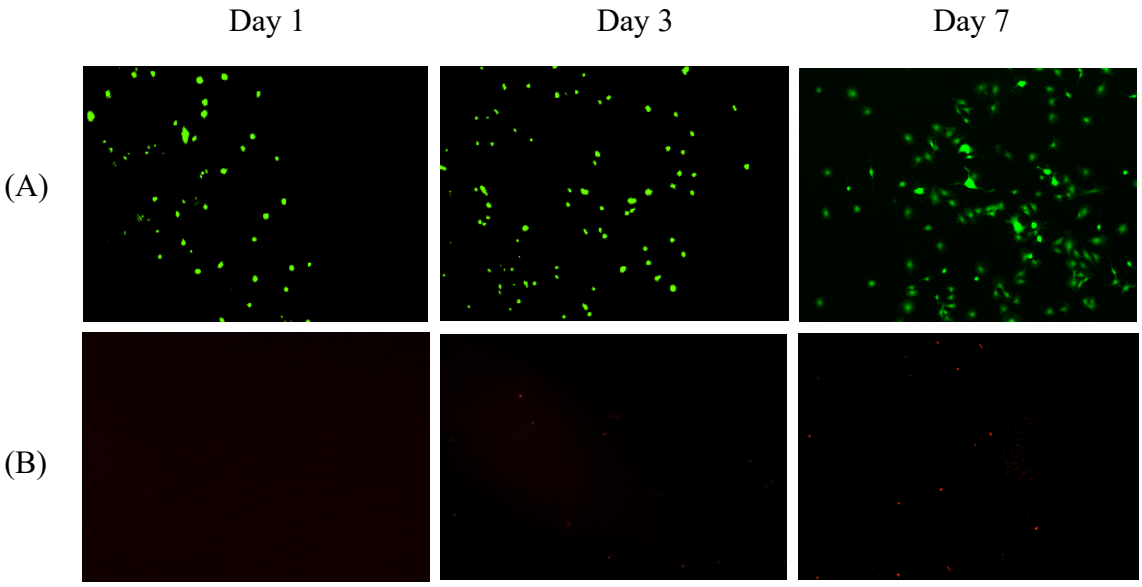

Figure 5.29. Qualitative analysis using fluorescence microscopy of 5% (w/v) GelMA, embedded with NG108-15 cells (1 x 10^4 ml^{-1}) at days 1, 3 and 7. GelMA was immersed in cell culture medium and incubated at 37°C in 5% (v/v) CO_2. (A) C6 cells stained with Calcien AM (live cells) and (B) C6 cells stained with Propidium Iodine (dead cells).

5.4.2.5 Cell viability of C6 astrocyte-like cells in bioprinted GelMA hydrogels with PEEK model particles

C6 astrocyte-like cells and model PEEK-OPTIMA particles were bioprinted with 5% (w/v) GelMA hydrogels to create a 3D environment for cell culture as a proof of concept to examine whether the model would be a viable technique to investigate future biological responses to all particle types. PEEK-OPTIMA particles were chosen as the first material to test the 3D bioprinted hydrogel model due to its excellent biocompatibility and resistance to degradation, including oxidation and hydrolysis. This ensures that the PEEK-OPTIMA particles can remain stable in the GelMA hydrogel over time. The C6 cells (1 x 10^4 ml^{-1}) were cultured in 5% (w/v) GelMA hydrogels over a duration of 7 days at 37°C and 5% (v/v) CO_2. Quantitative analysis of cell viability was conducted using a luminescent ATP assay at days 1, 3 and 7 (Figure 5.30). Throughout the 7 days, C6 cells cultured in GelMA hydrogels with PEEK-OPTIMA model particles showed cell growth.

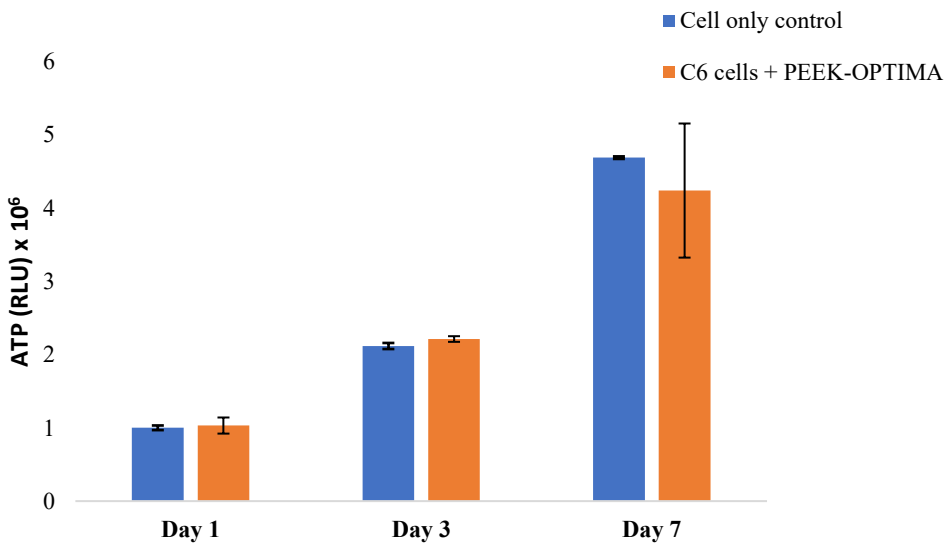

Figure 5.30. Quantitative ATP cell viability of 3D bioprinted GelMA (5% w/v), embedded with C6 astrocyte-like (1 x 10^4 ml^{-1}) cells and PEEK particles. The bioprinted GelMA was immersed in cell culture medium and incubated at 37 °C in 5% (v/v) CO_2 for a duration of 7 days. An equivalent volume of CellTiter-Glo 3D reagent was added to the well plates and transferred to a white opaque 96 well plate. The plate was shaken for 5 minutes, and the luminescence was recorded after incubating it in room temperature for approximately 25 minutes.

Furthermore, we attempted to perform optimal sectioning using confocal microscopy to observe the dispersion of C6 astrocyte-like cells in the GelMA hydrogel in 3D. The cells were stained with Hoechst stain (blue), shown in Figure 5.31.

(A) (B)

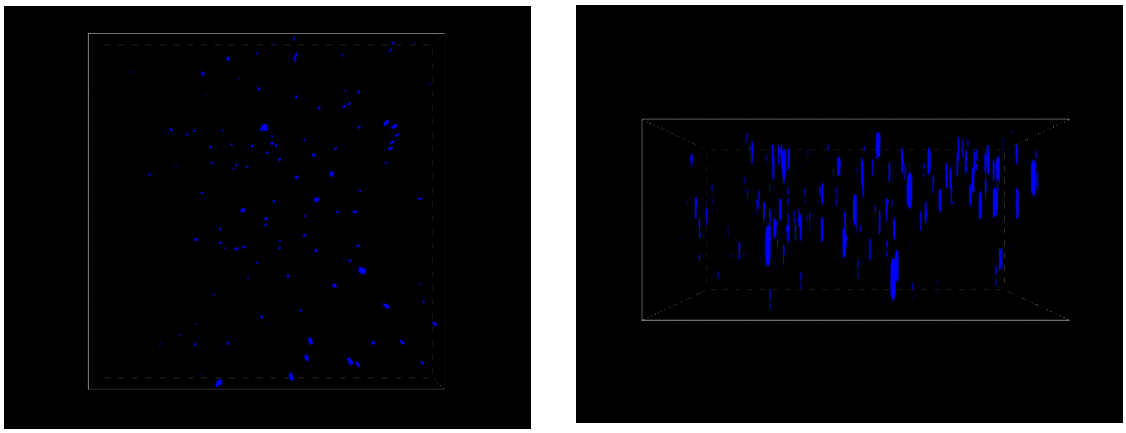

Figure 5.31. Fluorescent images of C6 astrocyte-like cells via confocal microscopy. Z-stacking was performed by obtaining horizontal cross sections of the GelMA hydrogel droplets embedded with C6 astrocyte-like cells. Cell nuclei were stained with Hoechst. (A) XY axis view of distribution of C6 astrocyte-like cells in GelMA hydrogel droplet; (B) XZ axis view of distribution of C6 astrocyte-like cells in GelMA hydrogel droplet

5.4.4 Discussion

5.4.4.1 Characterisation of model particles

In this part of the study, the aims were to characterise the size and morphology of model particles of different biomaterials, including metals, polymers and ceramics, and to develop an *in vitro* 3D bioprinted model to assess the impact of these model biomaterial particles on neural cells. Model particles were used in replacement to the originally planned wear simulated particles due to significant delays in procurement and commissioning of the essential equipment, namely the pin-on-plate wear simulator, which was caused by the COVID-19 pandemic.

The model PEEK particles used in this study, also known as PEEK-OPTIMA resin exhibited irregular and granular morphologies identified using SEM. The model PEEK particles had a mode size of 0.1 – 0.8 µm in diameter, with a mean particle size of 7.58 µm ± 3.97 µm in diameter. The majority of PEEK-OPTIMA particles (95%) were less than 8 µm in size. The reported shape of the model PEEK-OPTIMA particles were comparable to a study conducted by Du *et al* [280]. These authors reported granular shaped commercially available PEEK particles and also demonstrated that 99% of the

particles had a diameter of less than 5μm. The reported mean particle size by Du *et al* [280] was 1.05 μm, which was a lot smaller compared to the mean particle size in the present study. However, the preparation of PEEK particles by Du *et al* [280] was not described in their study. In addition, study conducted by Hallab *et al* [281] exposed PEEK-OPTIMA particles to macrophages. Their study showed that PEEK-OPTIMA particles were granular to flake-like morphologies. In terms of particle sizes, Hallab *et al* [281], reported at least 95% of PEEK-OPTIMA particles were between the 1 – 10 μm size range, similar to what was observed in the current study.

The model polymer particles selected for use and characterised in this study included the commercially available, low molecular weight polyethylene resin, Ceridust 3615®. These model polymer particles were observed using SEM, as granular in shape with some agglomerated granular particles, which were similarly observed by Liu *et al* [110]. Furthermore, a previous study conducted by Green *et al* [276] used Ceridust 3615® to evaluate responses of murine peritoneal macrophages to polyethylene particles *in vitro*. Green *et al* [276] characterised Ceridust 3615® into different size distributions by sequential filtration through 10, 1, 0.4 and 0.1 μm and the authors reported mean particle sizes of 7.2 ± 3.15 μm 4.3 ± 1.89 μm, 0.49 ± 0.11 μm, and 0.21 ± 0.069 μm, respectively. Similarly, in this study, mean particle sizes for Ceridust 3615 ® filtered with 8 and 0.8 μm, were 8.75 ± 2.35 μm and 5.27 ± 3.80 μm, respectively. This result is important because Green *et al* [276] demonstrated that polyethylene particles that were between 0.3 – 10 μm were most biologically active to induce phagocytosis by macrophages.

The model ceramic particles selected for use and characterised in this part of the study were Zirconia Toughened Alumina (ZTA) particles, commercially manufactured by Inframat Advanced Materials (USA). In this study, the ZTA particles were observed to be granular and polygonal in morphology, which was comparable to the polygonal shape reported in the study by Asif [134]. Additionally, the observations of agglomerates of ZTA particles in the present study was also reported in Asif [134]. When comparing to another type of commercially available ceramic particles, called alumina powder studied by Germain *et al* [282], the authors reported a mean size of 0.503 ± 0.19 μm, which was smaller than 3.69 ± 3.48 μm reported in this study. The disparity of the mean particle sizes could be explained by the different sized sequential filtration methods, i.e. smaller

filter membranes used to conduct sequential filtration of ceramic particles by Germain *et al* [282]. Additionally, the authors also investigated clinically relevant ceramic particles generated from the pin on plate wear simulator and reported that the mode size range was 0.3 – 0.4 μm, with most of the particles were in the 0.3 – 0.8 μm size range. The commercially manufactured ZTA particles used in the current study had a mode particle size range of 0.1 – 0.8 μm.

The model metal particles selected for use and characterised in this study were commercially available cobalt chrome molybdenum alloy (CoCr-Mo) obtained from American Elements (USA). It is essential that there is a thorough understanding of the size and morphology of metal particles, as the biological responses to these metal wear debris are dependent on particle size and shape [91]. The shape of these particles was mostly globular, and they had a mean size of 5.86 ± 1.20 μm. These results were comparable to a study conducted by Germain *et al* [282], where the authors also investigated commercially available model cobalt chrome (CoCr) particles. These authors also demonstrated particles had a uniform round morphology and reported a mean particle size of 9.87 ± 5.67 μm. However, when compared to clinically relevant CoCr particles, generated by a pin on plate wear simulator, particles were in aggregates and mostly granular in shape, with some polygonal shaped shards, demonstrated in both Germain *et al* [282] and Lee *et al* [12]. Furthermore, the mode size ranges for CoCr particles reported in Germain *et al* [282] and Lee *et al* [12] were 10 – 20 nm and 30 – 39 nm, respectively. However, the mode size range for the current study was 0.8 – 8 μm. The different mode size range reported in this study compared to previous studies using wear simulated particles is important to note when evaluating biological responses of neural cells to model CoCr-Mo particles, which will be further discussed in chapter 6.

5.4.4.2 Development of 3D bioprinted GelMA hydrogel model with model particles

The aim of this part of the study was to develop a 3D bioprinted model using GelMA hydrogels to investigate neural cell responses to model particles. The specific objective was to bioprint a mixture of GelMA hydrogels, neural cells and model particles as a droplet using extrusion bioprinting with the BIO X and BIO X6 bioprinter (CELLINK). In order to achieve this, specific parameters were required to be optimised including, bed temperature, print head temperature, extrusion pressure and printing speed. Optimised

parameters allow printing consistency, structural integrity and stability of bioprinted constructs.

In this study, bioprinting techniques were used to create cell-encapsulated 3D bio-constructs. The rationale for using bioprinting techniques for developing 3D bio-constructs instead of traditional casting methods, includes the many advantages it presents, for example, greater precision in spatial control for cells, and increased complexity and mimicry of the *in vivo* organisation of tissues [228, 229]. In this study, 5% (w/v) GelMA hydrogels and neural cells used for 3D bioprinting droplets, presents a promising approach for modelling a 3D cell culture environment for investigating neural cell responses to particles. Specifically, model particles were mixed with neural cells and GelMA hydrogels and extruded with the BIO X or BIO X6 printer as a droplet. This study demonstrated that model particles were able to be printed using extrusion bioprinting when combined with hydrogels and cells.

The basis of the printing parameters used in this study comprised of the successful use of GelMA hydrogels and neural cells including C6 astrocyte-like cells and NG108-15 neuronal cells as a 3D bioprinted model used for spinal cord injury, conducted by Rad *et al* [278]. GelMA is temperature sensitive which presents reversible gelation behaviour when responding to temperature changes. In the study conducted by Rad *et al* [278], the authors demonstrated that at higher temperatures (≥ 32 ^{o}C), higher GelMA concentrations were required, e.g. 15% (w/v), whilst lower temperatures (≤ 22 ^{o}C) required lower concentrations of GelMA, e.g. 2.5% (w/v). Additionally, extrusion pressure was an important parameter in determining consistency with structural integrity of the GelMA construct. Higher extrusion pressure causes overflow and spreading of material extruding from the nozzle. Lower extrusion pressures did not allow hydrogels to be extruded from the nozzle. Finally, nozzle size was an important parameter, as in this study, for the first time we attempted to print hydrogels with both cells and particles, with biomaterials including metals, polymers and ceramics. In this study, the smaller diameter nozzles with a sized of 25 G (0.25 mm diameter) and 27 G (0.20 mm diameter) were not able to provide consistent extrusion of droplets when particles were included in the bioinks. The unsuccessful use of these nozzles could be explained by the particles clogging inside the nozzle tip due to the smaller diameter openings. In contrast, nozzles with sizes of both 20

G (0.58 mm diameter) and 22G (0.41 mm diameter) were successfully used to extrude droplets of bioinks containing particles with consistency.

Ensuring cell viability is an important consideration when fabricating 3D bioprinted structures. In this study, the biocompatibility of bioprinted GelMA hydrogels to support the viability of both NG108-15 neuronal cells and C6 astrocyte-like cells, was evaluated *in vitro*. The results of cell viability were presented quantitatively and qualitatively and compared with the traditional 2D cell culture method. Over a duration of 7 days, similar growth of both NG108-15 neuronal cells and C6 astrocyte-like cells demonstrated cell viability and cell proliferation for both 2D and 3D cell culture methods. These results confirm the findings in Rad *et al* [278], where it was also reported that 5% (w/v) GelMA hydrogel supports cell viability over 7 days using the same cell lines as this study.

Finally, the results using model PEEK particles as the initial test particles bioprinted with NG108-15 neuronal cells and C6 astrocyte-like cells with 5% (w/v) GelMA hydrogels, showed that PEEK particles did not affect the cell viability of neural cells. Ultimately, this part of the study demonstrated the viable technique of modelling a 3D environment to test neural cell response to model particles, which consisted of bioprinting model particles with neural cells and GelMA hydrogels.

5.5 Key findings

- The majority of model particles characterised in this study were between 0.1 – 8.0 μm in size.
- The novel approach of bioprinting particles mixed with GelMA hydrogels was successful, with the smallest viable nozzle gauge of 22 G (with an inner diameter of 0.41 mm.
- For both C6 astrocyte-like cells and NG108-15 neuronal cells, embedded in 5% (w/v) GelMA hydrogels, quantitative and qualitative analyses of cell viability demonstrated cell proliferation and viability over a duration of 7 days.
- The proof of concept of bioprinting neural cells with PEEK-OPTIMA particles using a novel 3D *in vitro* bioprinted cellular model was successful.

Chapter 6

Biological impacts of model particles on astrocyte-like and neuronal cells in a novel 3D cellular model

6.1 Introduction

The incorporation of biomaterials in medical devices used in spinal applications, requires a comprehensive understanding of the biomaterial interactions with the neural environment. The increasing prevalence of spinal implants and instrumentation, intended to address spinal disorders and improve patient spinal mobility, has resulted in an essential need to investigate the biological responses induced by wear particles produced from spinal implant materials including PEEK, polyethylene, ceramics and metals. The mechanical wear that occurs over time leads to discharge of wear particles into surrounding tissue, which may affect neural cells located in close vicinity to the spinal cord.

Currently, there have been limited studies investigating the neural cell responses to spinal implant wear particles *in vitro*. The types of cells utilised in previous studies consisted of mostly fibroblasts, osteoblasts and macrophages. Even so, a previous study conducted by Lee *et al* [12] studied neural cell responses to CoCr wear particles were investigated in an *in vitro* 3D model. In their study, a 3D cell culture model created with type 1 rat tail collagen gel was used to investigate the biological responses of primary astrocytes and microglia. However, collagen gel present challenges including poor structural integrity and batch-to-batch variability. In addition, previous studies using hydrogels to develop 3D cell culture system have used the casting technique which has some limitations. One of the challenges is the difficulty of creating uniformity of the hydrogel in terms of thickness and density, e.g. the formation of bubbles when casting hydrogels. In addition, the present study aimed to overcome the challenges faced with casting hydrogels, by using extrusion bioprinting of hydrogels. One of the most important advantages of bioprinting is the improvement of precision and control over the deposition of hydrogel compared to the conventional casting method [283].

There are some advantages of using an *in vitro* model in this study compared with an *in vivo* model. The use of *in vitro* models allows a more detailed examination of specific cell types without the complexities faced with *in vivo* models including ethical considerations and animal model selection. Furthermore, *in vitro* models allow for greater fixed control of experimental conditions including temperature and nutrient concentrations compared with *in vivo* models. Finally, *in vitro* studies offer a more cost-effective and time efficient approach to experimental setup and obtaining experimental results.

Gelatin Methacryloyl (GelMA) has been used extensively used in 3D cell culture in numerous applications including, modelling drug responses in cancer cells, the development of organ-on-a-chip and modelling spinal cord injury. In recent years, GelMA hydrogels have been utilised in modelling 3D cell culture environments for neural cells. In a recent study conducted by Wu *et al* [225], neurons were cultured on GelMA hydrogel substrates to investigate the effect of hydrogel stiffness on neurone outgrowth, cell viability and adhesion. The different stiffnesses of GelMA hydrogel was prepared by altering the concentration of GelMA. The findings from their study, demonstrated that GelMA hydrogels with a concentration of 5% (w/v) had the greatest neuronal cell attachment. Similarly, the recent study conducted by Rad *et al* [278] reported that 5% (w/v) GelMA hydrogel was the optimum concentration for structural stability and cell viability of C6 astrocyte-like cells and NG108-15 neuronal cells. Consequently, the 3D cellular model in the present study utilised 5% (w/v) GelMA hydrogels to investigate neural cell responses to model particles over a duration of 5 days. Using this *in vitro* model to study the biological responses of cells to wear particles, is of great importance in examining biomaterials used in current orthopaedic implants and in the development of new implants or bearing systems.

Previous literature has demonstrated that different biological responses to model particles or wear simulated particles are dose dependent. In the study by Lee *et al* [12], increasing doses of 0.5 – 50 μm^3 CoCr wear particles per cell were used in investigating cellular responses. Their study demonstrated significant reduction in cell viability of primary astrocytes after 5 days was reported when exposed to wear simulated CoCr particles,

dosed at 50 μm^3 per cell. Thus, in the present study, CoCrMo model particles were dosed at 0.5 μm^3, 5 μm^3 50 μm^3 per cell and exposed to C6 astrocyte-like cells to observe whether the type of CoCr particle effects the bioreactivity of neural cells. Similarly, the same increasing doses from 0.5 – 50 μm^3 was also used in a study investigating the biological impact of ceramic wear particles on cells, conducted by Asif [134]. In that study, no significant reduction in cell viability was observed in fibroblast cells when exposed to ceramic wear particles, dosed at 0.5 μm^3, 5 μm^3 and 50 μm^3 per cell after 24 hours. In the present study, a concentration of 50 μm^3 per cell for ZTA model particles were used to determine whether different cell types or different particles, or longer exposure to particles effect biological responses. Furthermore, Ceridust 3615 ® model particles, dosed at 100 μm^3 per cell were examined in a study conducted by Liu *et al* [110]. Their study found no significant decrease in cell viability in peripheral blood mononuclear cells when exposed to Ceridust 3615 ® particles after 24 hours. In the current study, Ceridust 3615 ® model particles were dosed at 100 μm^3 per cell and exposed to neural cells for 5 days. Lastly, since PEEK-OPTIMA model particles have not been studied widely, there is limited information on what volumes of particles per cell exhibit cellular responses. Thus, due to the polymeric nature of PEEK-OPTIMA, the current study applied a volume of 100 μm^3 per cell, similar to Ceridust 3615 ® model particles.

6.2 Aims and objectives

6.2.1 Aims

The rationale behind this chapter is to provide new findings of how astrocyte and neuronal cells of the spinal cord respond to wear particles from spinal instrumentation and devices, because previously, this area of research has been study relatively rarely compared to other total joint replacements including, knee and hip replacements. The aim of this chapter was to use a novel 3D bioprinted model developed in chapter 5, as an advanced cell culture model to investigate the biological reactions of astrocytes and neuronal cells in response to polymer, ceramic and metal model particles.

6.2.2 Objectives

The specific objectives of this chapter of the thesis were to:

1) Determine the volume of model particles required to achieve specific dose concentrations.
2) Investigate the viability of neural cells including C6 astrocyte-like cells and NG108-15 neuronal cells, when exposed to model particles in the 3D bioprinted GelMA hydrogel model.
3) Investigate the production of reactive oxygen species (ROS) of C6 astrocyte-like cells and NG108-15 neuronal cells, when exposed to model particles in the 3D bioprinted GelMA hydrogel model.
4) Investigate DNA damage of C6-astrocyte-like cells when exposed to wear particles in the 3D bioprinted GelMA hydrogel model.

6.3 Specific materials

The specific materials used in this chapter are detailed in Table 6.1 and 6.2

Table 6.1. Assay kits used to determine the effect of polymer, ceramic and metal particles on cell viability, production of reactive oxygen species (ROS), and DNA damage.

Material	**Supplier**
CellTiter-Glo® 3D Cell Viability Assay • CellTiter-Glo® 3D Reagent	Promega
Green-fluorescent Calcein-AM	Invitrogen
Red-fluorescent ethidium homodimer-1	Invitrogen
NucBlue™ Live ReadyProbes™ Reagent (Hoechst 33342)	Life Technologies
DCFDA / H2DCFDA - Cellular ROS Assay Kit • 10X Dilution Buffer • 20 mM DCFDA • 55mM TBHP	Abcam
0.5% Triton X-100	Sigma Aldrich
Anti-gamma γ-H2AX (phospho S139) antibody	Abcam
Goat Anti-Mouse IgG H&L (Alexa Fluor® 488)	Abcam

6.4 Specific methods

The specific methods used in this part of the study are detailed below.

6.4.1 Determination of the volume of particles used for culture with C6 astrocyte-like and NG108-15 neuronal cells.

The volume of particles cultured with each neural cell type was expressed as a ratio of volume of particles (μm^3) to number of cells. For example, a ratio of 100:1 equated to 100 μm^3 of particles per cell.

The particles were suspended in cell culture medium to produce particle stock solutions (1 $mg.ml^{-1}$). The mass required for each particle was calculated using the formula below:

$$Density = \frac{Mass}{Volume}$$

The calculation of the mass of each particle required for a particle volume of 100 μm^3 using a cell seeding density of 1 x 10^4 cells per well are detailed below. To calculate the mass, the formula was rearranged to:

$$Mass = Density \times Volume$$

The density of each particle used in this study are outlined in Table 6.2.

Table 6.2. The densities of particles used in culture with neural cells.

Particle	**Density ($g.cm^{-3}$)**
PEEK (PEEK-OPTIMA)	1.3
Polyethylene (Ceridust 3615 ®)	1
Ceramic (ZTA)	5
Metal (CoCrMo)	8.4

The density units of particles was converted from g.cm^{-3} to µg.µm^{-3} using the conversion:

$$1\ gram = 1 \times 10^{-6}\ microgram$$

6.4.1.1 Volume calculation for PEEK-OPTIMA particles

The density of PEEK-OPTIMA particles was 1.3 g.cm^{-3} according to the material properties outlined by Invibio Biomaterial Solutions Ltd. For a particle dose of 100 µm^3 per cell, with a cell seeding density of 1 x 10^4 cells per well, the mass of PEEK particles was calculated using the following steps below:

1) Calculate the mass of PEEK-OPTIMA particles required per cell

$$Mass\ of\ PEEK\ particles\ required\ per\ cell = 100\ \mu m^3\ \times\ 1.3 \times 10^{-6}\ \mu g.\ \mu m^{-3}$$
$$= 1.3 \times 10^{-4}\ \mu g\ per\ cell$$

2) Calculate the mass of PEEK-OPTIMA particles required per well

$$Mass\ of\ PEEK\ particles\ required\ per\ well$$
$$= (1 \times 10^4\ cells\ per\ well) \times\ 1.3 \times 10^{-4}\ \mu g\ per\ cell$$
$$= 1.3\ \mu g\ per\ well$$

3) Volume of PEEK-OPTIMA particle stock solution required per well

$$A\ PEEK\ particle\ mass\ of\ 1.3\ \mu g\ per\ well\ means:$$

A volume of 1.3 µL of $particle\ stock\ solution\ of\ 1\ mg.ml^{-1}\ is\ required\ per\ well$

6.4.1.2 Volume calculation for Ceridust 3615 ® particles

The density of Ceridust 3615 ® particles was 1 g.cm^{-3} according to previous studies conducted by Liu *et al* [110] and Richards *et al* [123]. For a particle dose of 100 µm^3 per cell, with a cell seeding density of 1 x 10^4 cells per well, the mass of Ceridust 3615 ® particles was calculated using the following steps below:

1) Calculate the mass of Ceridust 3615 ® particles required per cell

$$Mass\ of\ \text{Ceridust 3615 ®}\ particles\ required\ per\ cell$$
$$= 100\ \mu m^3\ \times\ 1 \times 10^{-6}\ \mu g.\mu m^{-3}$$
$$= 1 \times 10^{-4}\ \mu g\ \text{per cell}$$

2) Calculate the mass of Ceridust 3615 ® particles required per well

$$Mass\ of\ PEEK\ particles\ required\ per\ well$$
$$= (1 \times 10^4\ cells\ per\ well) \times\ 1 \times 10^{-4}\ \mu g\ \text{per cell}$$
$$= 1\ \mu g\ \text{per well}$$

3) Volume of Ceridust 3615 ® particle stock solution required per well

$$A\ \text{Ceridust 3615 ®}\ particle\ mass\ of\ 1\ \mu g\ \text{per well means:}$$
$$\text{A volume of 1 µL of}\ particle\ stock\ solution\ of\ 1\ mg.ml^{-1}\ is\ required\ per\ well$$

6.4.1.3 Volume calculation for ZTA particles

The density of ZTA particles was 5 g.cm^{-3} according to material properties outlined by the supplier, Inframat. For a particle dose of 100 µm^3 per cell, with a cell seeding density of 1 x 10^4 cells per well, the mass of ZTA particles was calculated using the following steps below:

1) Calculate the mass of ZTA particles required per cell

$$Mass\ of\ \text{ZTA}\ particles\ required\ per\ cell = 100\ \mu m^3\ \times\ 5 \times 10^{-6}\ \mu g/\mu m^3$$

$$= 5 \times 10^{-4}\ \mu g\ \text{per cell}$$

2) Calculate the mass of ZTA particles required per well

$$Mass\ of\ ZTA\ particles\ required\ per\ well$$
$$= (1 \times 10^4\ cells\ per\ well) \times\ 5 \times 10^{-4}\ \mu g\ per\ cell$$
$$= 5\ \mu g\ per\ well$$

3) Volume of ZTA particle stock solution required per well

$$A\ ZTA\ particle\ mass\ of\ 5\ \mu g\ per\ well\ means:$$
$$A\ volume\ of\ 5\ \mu L\ of\ particle\ stock\ solution\ of\ 1\ mg.ml^{-1}\ is\ required\ per\ well$$

6.4.1.4 Volume calculation for metal particles

The density of CoCrMo particles was 8.4 g/cm^3 according to material properties outlined by the supplier, American Elements. For a particle dose of 100 µm^3 per cell, with a cell seeding density of 1 x 10^4 cells per well, the mass of ZTA particles was calculated using the following steps below:

1) Calculate the mass of CoCrMo particles required per cell

$$Mass\ of\ \text{CoCrMo}\ particles\ required\ per\ cell = 100\ \mu m^3\ \times\ 8.4 \times 10^{-6}\ \mu g.\mu m^{-3}$$
$$= 8.4 \times 10^{-4}\ \mu g\ per\ cell$$

2) Calculate the mass of CoCrMo particles required per well

$$Mass\ of\ \text{CoCrMo}\ particles\ required\ per\ well$$
$$= (1 \times 10^4\ cells\ per\ well) \times\ 8.4 \times 10^{-4}\ \mu g\ per\ cell$$
$$= 8.4\ \mu g\ per\ well$$

3) Volume of CoCrMo particle stock solution required per well

$$A\ \text{CoCrMo}\ particle\ mass\ of\ 8.4\ \mu g\ per\ well\ means:$$
$$A\ volume\ of\ 8.4\ \mu L\ of\ particle\ stock\ solution\ of\ 1\ mg.ml^{-1}\ is\ required\ per\ well$$

6.4.2 Impact of model particles on cell viability

Cell viability assays were utilised to quantitatively and qualitatively determine the effects of polymer, ceramic and metal particles on the viability of C6 astrocyte-like and NG108-15 neuronal cells, as well as in co-culture. Prior to cell viability assays, C6 astrocyte-like, NG108-15 neuronal cells and cells in co-culture were grown, passaged and seeded according to protocols described in section 3.2.1.4. In addition, particles were prepared according to protocols described in section 5.3.1.2. Finally, 3D GelMA hydrogel constructs embedded with neural cells and particles were bioprinted following the protocol described in section 5.4.1.3.

6.4.2.1 Qualitative analysis of viability of C6 astrocyte-like and NG108-15 neuronal cells

A live/dead assay viability kit (Invitrogen) was utilised to qualitatively analyse the impact of biomaterial particles on C6 astrocyte-like or NG108-15 neuronal cells. The live/dead assay consisted of two fluorescent dyes including a green-fluorescent calcien AM dye and an ethidium homodimer-1 dye. The live cells stained with calcien AM indicated intracellular esterase activity and dead cells stained with ethidium homodimer-1 indicated the disruption of plasma membrane integrity. In addition, the DNA of cells was stained with a blue-fluorescent Hoechst 33342 dye.

GelMA hydrogel droplets, embedded with C6 astrocyte-like, NG108-15 neuronal cells, or in co-culture were bioprinted into 48-well plates, with cell seeding density of 1 x 10^5 cells per well. GelMA hydrogel constructs were cultured at 37^{o}C and 5% (v/v) CO_2 for a duration of 5 days. The live/dead assay was conducted on days 1, 3 and 5 in accordance with the protocol described in section 3.2.8. The GelMA hydrogel constructs were imaged immediately using a confocal EVOS M5000 microscope at 10 X magnification with GFP, RFP and DAPI emission filters for calcien AM, ethidium homodimer-1 and Hoechst 33342 stains, respectively. Three replicates of GelMA hydrogel constructs were bioprinted for each particle type and a total of three images were taken for each construct.

6.4.2.2 Quantitative analysis of viability of C6 astrocyte-like and NG108-15 neuronal cells

The quantitative analysis of cell viability for neural cells cultured in 3D cell culture models was performed by using a luminescent ATP assay kit called, CellTiter-Glo 3D Cell Viability Assay Kit (Promega). The principle of the CellTiter-Glo 3D cell viability assay is to assess the metabolic activity of cells by determining the level of ATP production. The ATP from lysed cells interact with luciferase enzyme and luciferin to produce light. The intensity of light produced is proportional to the ATP concentration, which therefore is an indicator of cell viability.

For the CellTiter-Glo 3D cell viability assay, GelMA hydrogel droplets, embedded with C6 astrocyte-like or NG108-15 neuronal cells were bioprinted into 96-well plates (flat bottom), as cell viability measurements with the microplate reader can only be obtained with 96-well plate. The cell seeding density used was 1 x 10^4 cells per well and specific particle volumes (calculations described previously) from the particle stock solution were added to the GelMA mixture to create a cell/particle solution. To prepare for bioprinting, a GelMA hydrogel to cell/particle solution ratio of 10:1 was utilised, i.e. 100 μL of cell/particle solution was mixed with 1 mL of GelMA hydrogel solution. A minimum of four replicates of GelMA hydrogel constructs were bioprinted. After bioprinting the GelMA hydrogel constructs, photocrosslinking of the constructs was performed by UV exposure of 365 nm at an intensity of 19.42 $mW.cm^{-2}$ for a 120 s.

The 96-well plate set up is shown in Figure 6.1. A negative control of cell only and a positive control of 5% (v/v) DMSO was utilised. In addition, a particle only control was used to ensure that particles did not interfere with the luminescent readings for this assay. The GelMA hydrogel constructs were cultured at 37°C and 5% (v/v) CO_2 for a duration of 5 days and luminescence was measured on days 1, 3 and 5.

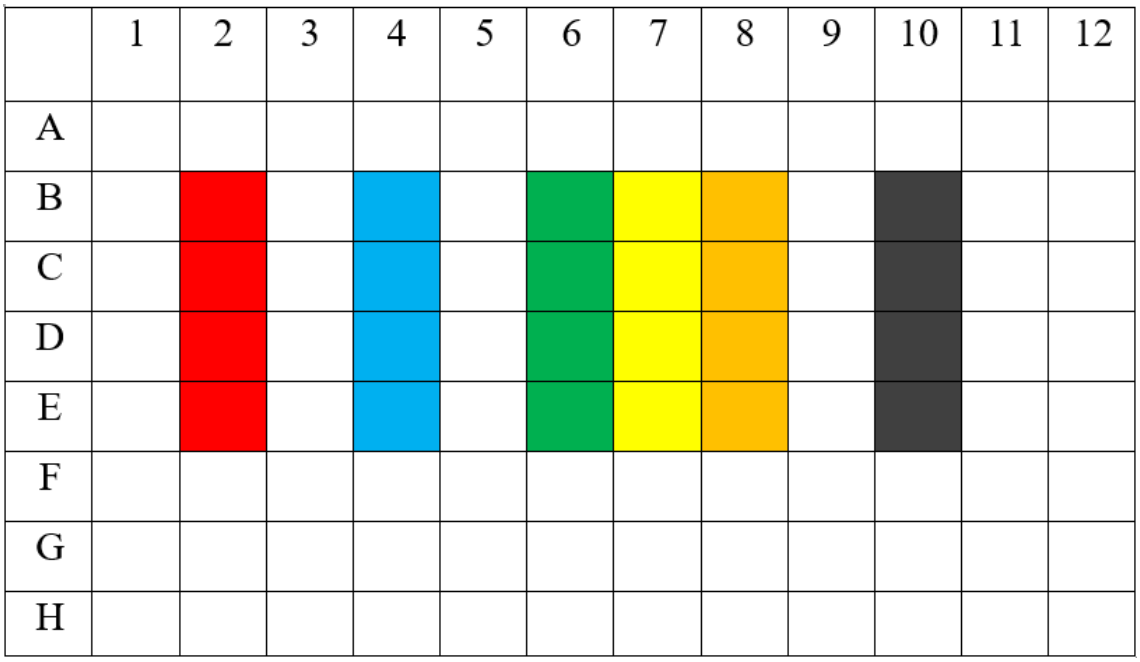

Figure 6.1. An example of the set-up of a 96-well plate for the CellTiter-Glo 3D cell viability assay investigating CoCrMo model particles. Red column = positive control, GelMA hydrogel embedded with cells cultured in supplemented cell culture medium and treated with DMSO. Blue column = negative control, GelMA hydrogel embedded with cells cultured in supplemented cell culture medium. Green column = GelMA hydrogel embedded with cells and CoCrMo model particles (0.5 μm^3/cell), cultured in supplemented cell culture medium. Yellow column = GelMA hydrogel embedded with cells and CoCrMo model particles (5 μm^3/cell), cultured in supplemented cell culture medium. Orange column = GelMA hydrogel embedded with cells and CoCrMo model particles (50 μm^3/cell), cultured in supplemented cell culture medium. Dark grey column = CoCrMo particles in cell culture medium, cultured in supplemented cell culture medium. Purple column = particle only control, GelMA hydrogel embedded with particles only.

6.4.3 Reactive oxygen species detection assay

A reactive oxygen species (ROS) detection assay was utilised to assess the oxidative stress of C6 astrocyte-like and NG108-15 neuronal cells when exposed to model particles. The ROS assay uses a fluorescent dye that is selectively sensitive to ROS. The assay kit used in this study was the DCFDA / H2DCFDA - Cellular ROS Assay Kit (Abcam), which uses 2 ,7 -Dichlorofluorescin diacetate (DCFDA) as the fluorescent probe that

measures hydroxyl, peroxyl and other ROS present within the cell. The ROS fluorescent probes are designed to permeate the cell and once inside the cell, DCFDA responds with the specific ROS. For example, in the presence of hydrogen peroxide, DCFDA undergoes oxidisation to convert DCFDA into 2 ,7 –Dichlorofluorescin (DCF) which is highly fluorescent and can be detected by fluorescence microscopy at an excitation and emission of 495 nm and 529 nm, respectively.

6.4.3.1 Preparation of reagents for reactive oxygen species detection assay

The reagents included in the DCFDA / H2DCFDA - Cellular ROS Assay kit and the preparation of reagents are described in Table 6.3.

Table 6.3. Preparation of reagents for the cellular ROS detection assay

Reagent	**Reagent preparation**	**Storage**
10 X buffer	10 X buffer was diluted with sterile water at a 1 in 10 dilution to prepare 1 X buffer	Stored at 4ºC
1 X supplemented buffer	1 X buffer was supplemented with 10% (v/v) FBS. e.g. 2 mL of FBS added to 10 mL 1 X buffer	Stored at 4ºC
20 mM DCFDA solution	20 mM DCFDA was diluted with sterile water to prepare a 25 µM final concentration of DCFDA	Stored at 4ºC
55 mM TBHP solution (positive control)	55 mM TBHP was diluted with sterile water to prepare a 200 µM final concentration of TBHP	Stored at 4ºC

6.4.3.2 Quantitative analysis of reactive oxygen species production

Prior to performing the assay, cells were seeded in bioprinted GelMA hydrogel constructs with model particles into 96 well plates. The ROS assay was performed over a duration of 5 days, measuring the ROS production on three different time points. The cell culture media was aspirated, and cells were washed with ROS assay buffer. The cells were stained with 100 µL diluted DCFDA solution and incubated at 37ºC and 5% (v/v) CO_2 for 45 minutes. The positive control was designed by exposing a column of wells to 100 µL of 200 µM TBHP and the plate was incubated for 2 hours. Subsequently, fluorescence was measured with a plate reader at excitation and emission of 485 nm and 535 nm, respectively. The TBHP positive control did not successfully produce a fluorescent signal, so hydrogen peroxide was replaced as the positive control in experiments that followed.

6.4.4 Investigation of DNA damage in neural cells

To determine the effect of model wear particles on the integrity of C6 astrocyte-like DNA, the measurement of γ-H2AX foci levels in cells was conducted. The formation of γ-H2AX occurs when there is DNA double stranded breaks and thus is the basis for a sensitive assay to detect DNA damage. Prior to conducting the DNA damage assay, cells were seeded in bioprinted GelMA hydrogel constructs with model particles in 12 well plates and were grown for at least 24 hours until cells were exposed to model particles. The well plates were incubated at 37ºC and 5% CO_2. DNA damage was measured at various time points including 1, 2 and 4 hours.

To perform DNA damage, cells were washed with PBS and permeabilised with 100 µL of 0.5% Triton X-100 solution for 3 minutes. After that, the cells were washed twice and 50 µL of primary antibody (γ-H2AX) was added to the cells and incubated in the incubator at 37ºC and 5% CO_2 for approximately 45 minutes. Next, cells were washed with PBS and 50 µL of secondary antibody was added and incubated at 37ºC and 5% CO_2 for approximately 25 minutes. After incubation, cells were washed with PBS and finally mounting media containing Hoerst solution was added that covered the cells and imaged using the fluorescent microscope.

6.5 Results

6.5.1 The effect of polymer model wear particles on the viability of C6 astrocyte-like cells in a 3D bioprinted model

C6 astrocyte-like cells and polymer model particles (PEEK-OPTIMA or Ceridust 3615®) were embedded in bioprinted 5% (w/v) GelMA hydrogel constructs. The PEEK-OPTIMA and Ceridust 3615 ® particles were dosed at 100 μm^3 per cell and compared with a negative control, which was C6 cells embedded in 3D GelMA hydrogel. Proliferation of C6 astrocytes was observed from over 5 days cells were exposed to PEEK-OPTIMA or Ceridust3615®, shown in Figure 6.2 and 6.4 respectively. In addition, over the 5 days of this experiment, the average luminescent values continued to rise for the cell only negative control as well as the PEEK-OPTIMA and Ceridust 3615 ® particles, shown in Figures 6.3 and 6.5, respectively. The luminescent values are indicative of cellular metabolic activity and therefore viability of C6 astrocyte-like cells. The average luminescent values for the cell only negative control increased approximately 4-fold in both experiments over 5 days, which was also similar to the tests with PEEK-OPTIMA and Ceridust3615®, which was indicative of cell proliferation. The cell growth of C6 astrocyte-like cells was not adversely affected ($p > 0.05$, Student's t-test) in the presence of polymer model particles of PEEK-OPTIMA or Ceridust 3615®. A significant reduction ($p < 0.05$, student's t-test) in cell viability was observed in the positive control and particle only control at each day points when compared to cell only negative control.

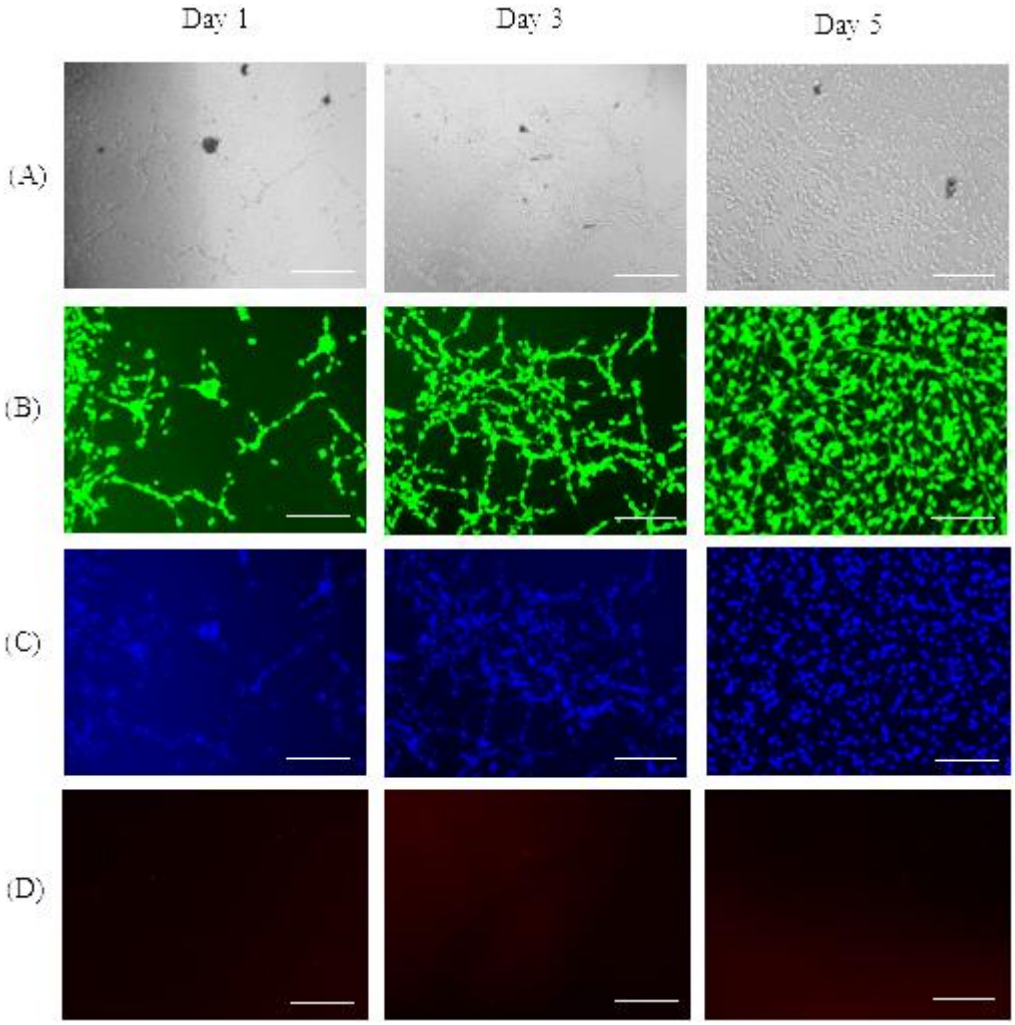

Figure 6.2. Qualitative analysis of the effects of PEEK-OPTIMA particles on the viability of C6 astrocyte-like cells in the 3D bioprinted GelMA hydrogel model. C6 Astrocyte-like cells were cultured with PEEK-OPTIMA particles for 5 days. Cell viability was determined using a green-fluorescent calcien AM stain. (A) Bright field microscopy images of C6 astrocyte-like cells with PEEK-OPTIMA particles; (B) Live cells stained with green-fluorescent calcien AM; (C) Cell nuclei stained with blue-fluorescent Hoechst; (D) Dead cells stained with red-fluorescent Propidium Iodide. Scale bar = 300 µm

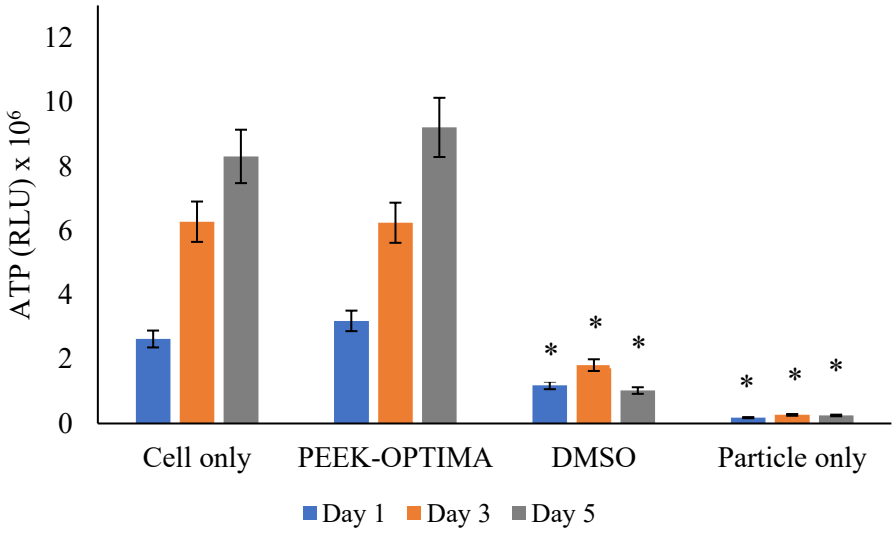

Figure 6.3. Quantitative analysis of the effects of PEEK-OPTIMA particles on the viability of C6 astrocyte-like cells in a 3D bioprinted GelMA hydrogel model. C6 cells astrocyte-like were cultured with PEEK-OPTIMA particles for 5 days. Cell viability was determined using a luminescent ATP assay. Negative controls used were C6 cell only embedded in GelMA hydrogels and particle only embedded in GelMA hydrogels. Positive control used was cells exposed to DMSO. Error bars represent ±95% confidence interval. An asterisk (*) represents statistically significant reduction ($p<0.05$, student's t-test) in cell viability in comparison to cell only negative control.

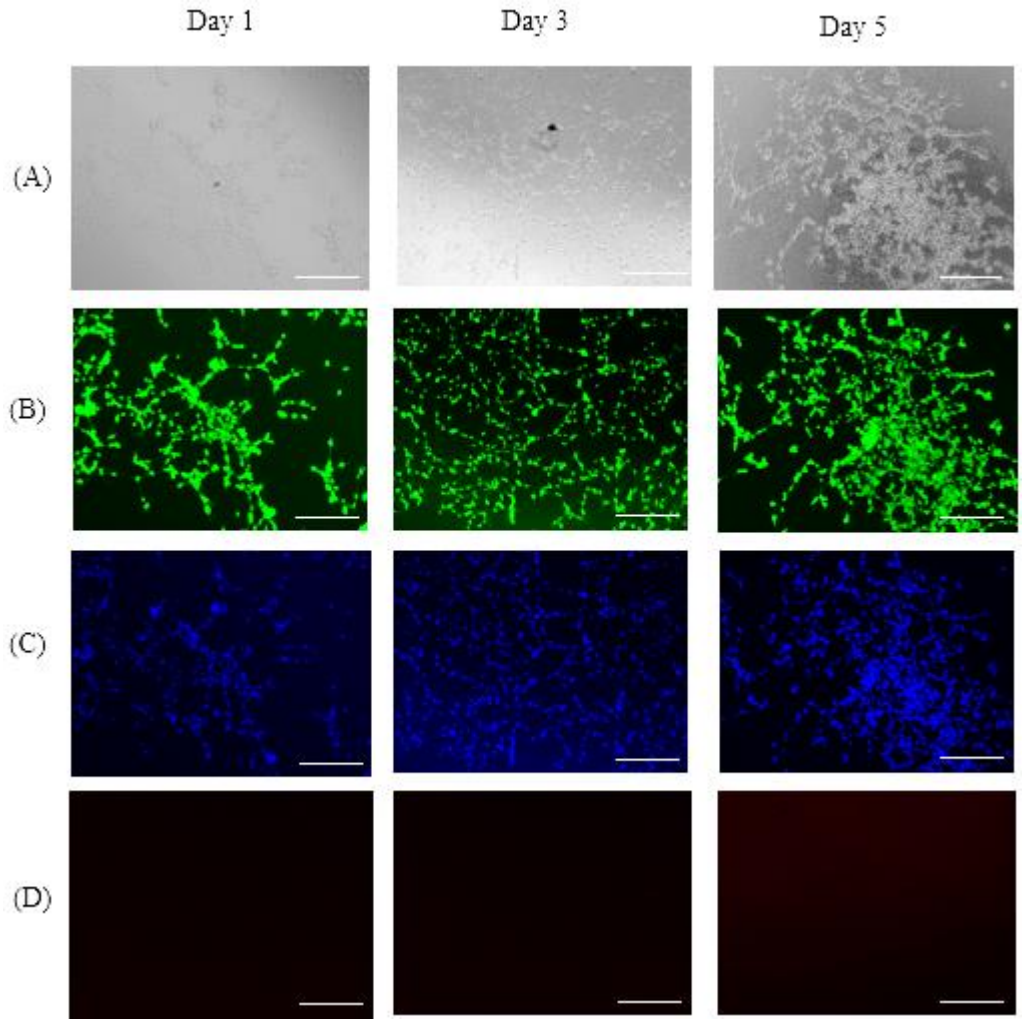

Figure 6.4. Qualitative analysis of the effects of Ceridust 3651 ® particles on the viability of C6 astrocyte-like cells in a 3D bioprinted GelMA hydrogel model. C6 astrocyte-like cells were cultured with Ceridust 3651 ® particles for 5 days. Cell viability was determined using a green-fluorescent calcien AM stain. (A) Bright field microscopy images of C6 astrocyte-like cells with Ceridust 3651 ® particles; (B) Live cells stained with green-fluorescent calcien AM; (C) Cell nuclei stained with blue-fluorescent Hoechst. (D) Dead cells stained with red-fluorescent Propidium Iodide. Scale bar = 300 µm

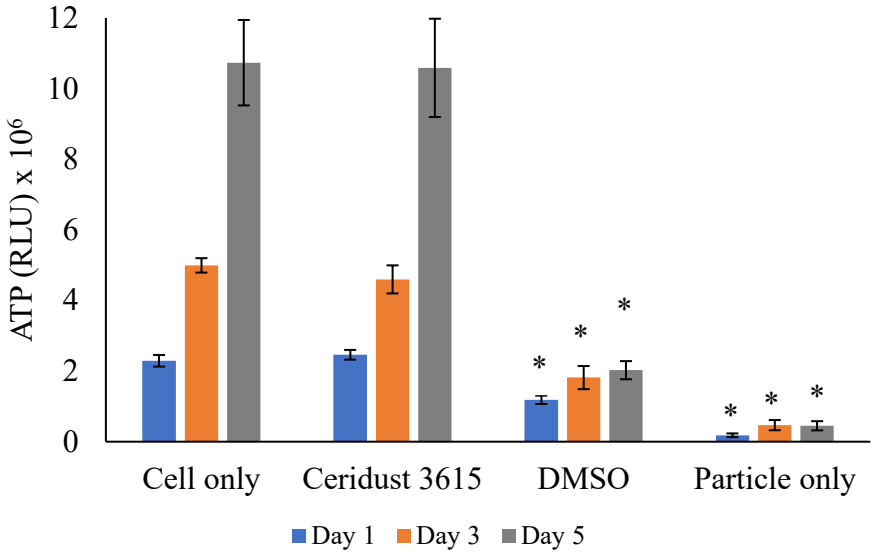

Figure 6.5.Quantitative analysis of the effects of Ceridust 3615 particles on the viability of C6 astrocyte-like cells in a 3D bioprinted GelMA hydrogel model. C6 astrocyte-like cells were cultured with Ceridust 3615® particles for 5 days. Cell viability was determined using a luminescent ATP assay. Negative controls used were C6 cell only embedded in GelMA hydrogels and particle only embedded in GelMA hydrogels. Positive control used was cells exposed to DMSO. Error bars represent ±95% confidence interval. An asterisk (*) represents statistically significant reduction ($p<0.05$, student's t-test) in cell viability in comparison to cell only negative control.

6.5.2 The effect of ceramic model particles on the viability of C6 astrocyte-like cells in a 3D bioprinted model

C6 astrocyte-like cells and ceramic model particles (ZTA) were embedded in bioprinted 5% (w/v) GelMA hydrogel constructs. The ZTA particles were dosed at 50 μm^3 per cell and compared with a negative control, which was only C6 cells embedded in 3D GelMA hydrogel. Over the 5 days of this experiment, the average luminescent values continued to rise for the cell only negative control as well as the ZTA particles, shown in Figures 6.6. The luminescent values are indicative of cellular metabolic activity and therefore viability of C6 astrocyte-like cells. The average luminescent values for the cell only negative control increased approximately 4-fold in both experiments over 5 days. The average luminescent values for the tests with the ZTA particles increased approximately 3-fold over 5 days, which was indicative of cell proliferation. The cell growth of C6 astrocyte-like cells was not adversely affected ($p > 0.05$, Student's t-test) in the presence of polymer model particles of ZTA. A significant reduction ($p < 0.05$, Student's t-test) in cell viability was measured for the positive control and particle only control when compared to cell only negative control.

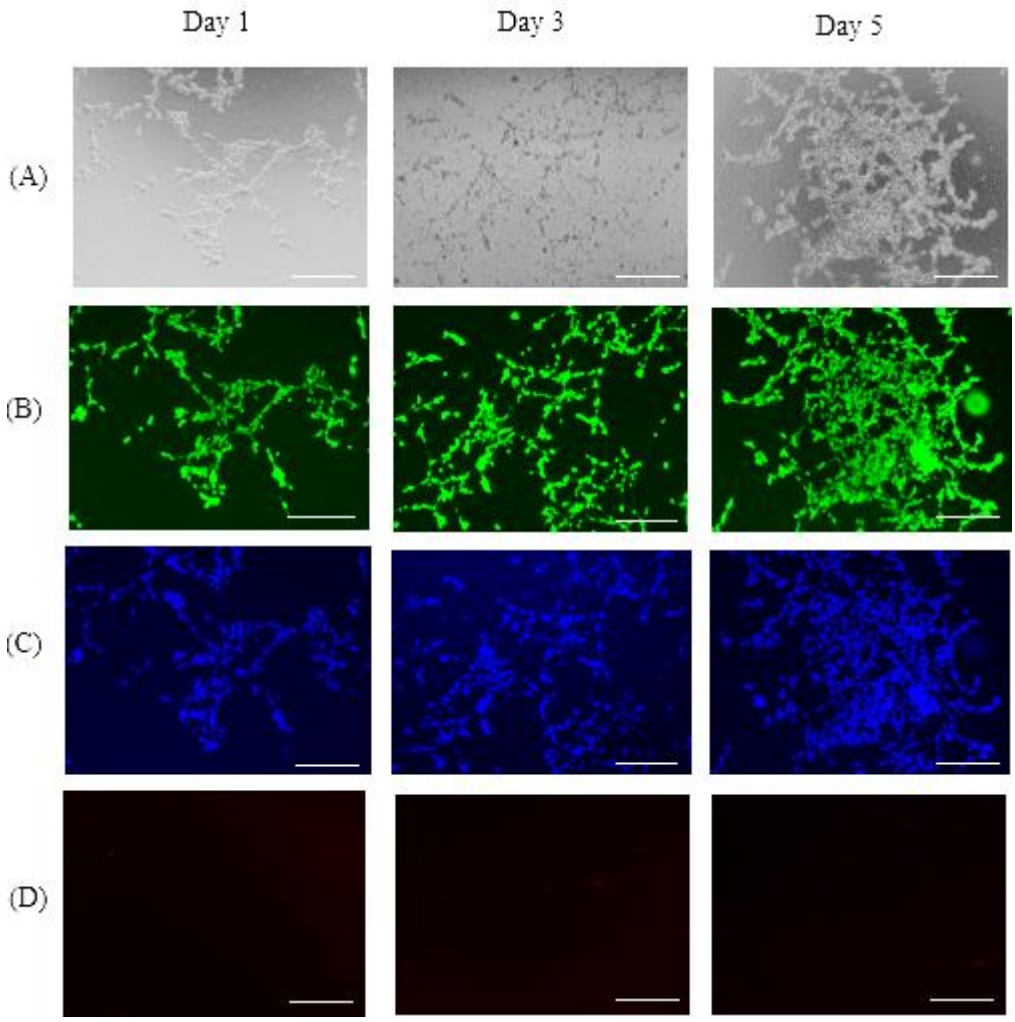

Figure 6.6. Qualitative analysis of the effects of ZTA particles on the viability of C6 astrocyte-like cells in a 3D bioprinted GelMA hydrogel model. C6 astrocyte-like cells were cultured with ZTA particles for 5 days. Cell viability was determined using a green-fluorescent calcien AM stain. (A) Bright field microscopy images of C6 astrocyte-like cells with ZTA particles; (B) Live cells stained with green-fluorescent calcien AM; (C) Cell nuclei stained with blue-fluorescent Hoechst. (D) Dead cells stained with red-fluorescent Propidium Iodide. Scale bar = 300 µm.

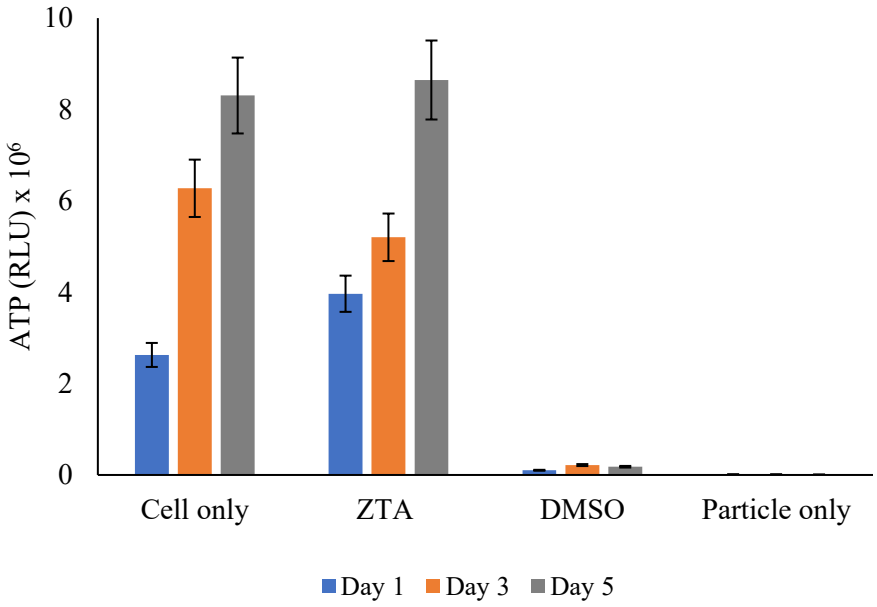

Figure 6.7. Quantitative analysis of the effects of ZTA particles on the viability of C6 astrocyte-like cells in a 3D bioprinted GelMA hydrogel model. C6 astrocyte-like cells were cultured with ZTA particles for 5 days. Cell viability was determined using a luminescent ATP assay. Negative controls used were C6 cell only embedded in GelMA hydrogels and particle only embedded in GelMA hydrogels. Positive control used was cells exposed to DMSO. Error bars represent ±95% confidence interval, n = 6. An asterisk (*) represents statistically significant reduction ($p<0.05$, student's t-test) in cell viability in comparison to cell only negative control.

6.5.3 The effect of metal model particles on the viability of C6 astrocyte-like cells in a 3D bioprinted model

C6 astrocyte-like cells and metal model particles (CoCrMo) were embedded in bioprinted 5% (w/v) GelMA hydrogel constructs. The CoCrMo particles were dosed at increasing volumes ranging 0.5 – 50 μm^3 and compared with a negative control, which was only C6 cells embedded in 3D GelMA hydrogel. Over the 5 days of this experiment, the average luminescent values continued to rise for the cell only negative control as well as the CoCrMo particles, shown in Figures 6.10. The luminescent values are indicative of cellular metabolic activity and therefore viability of C6 astrocyte-like cells. The average luminescent values for the tests with the CoCrMo increased approximately 5-fold over 5 days, which was indicative of cell proliferation. All of the different particle volumes for CoCrMo showed similar cell proliferation compared to the cell only control. There was no significant difference between the viability of C6 astrocyte-like cells exposed to CoCrMo and the cell only control ($p > 0.05$, Student's t-test). A significant reduction ($p < 0.05$, student's t-test) in cell viability was observed in the positive control and particle only control at each day points when compared to cell only negative control. Qualitative analysis was only tested for C6 astrocyte-like cells when exposed to a concentration of 50 μm^3 CoCrMo particles per cell. The results are shown in Figure 6.9.

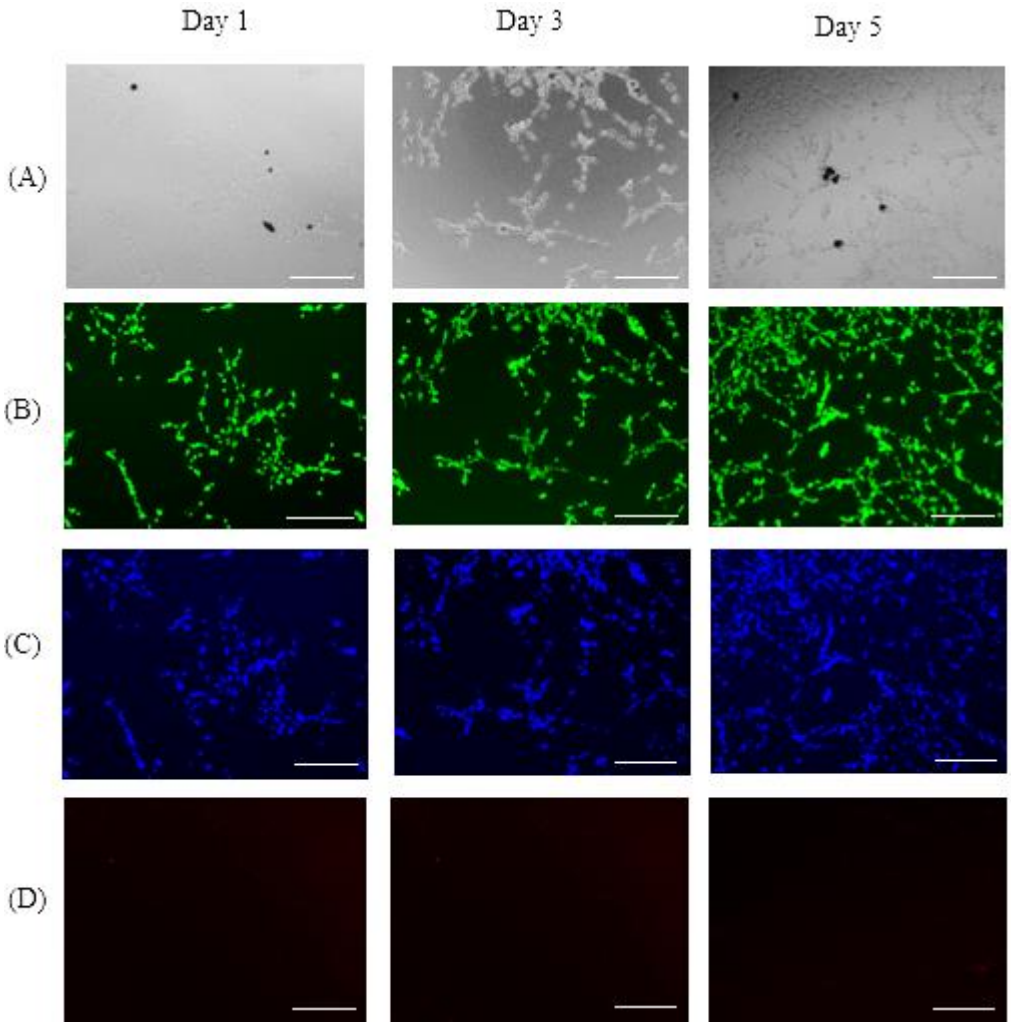

Figure 6.8. Qualitative analysis of the effects of CoCrMo particles on the viability of C6 astrocyte-like cells in a 3D bioprinted GelMA hydrogel model. C6 astrocyte-like cells were cultured with CoCrMo particles for 5 days. Cell viability was determined using a green-fluorescent calcien AM stain. (A) Bright field microscopy images of C6 astrocyte-like cells with CoCrMo particles; (B) Live cells stained with green-fluorescent calcien AM; (C) Cell nuclei stained with blue-fluorescent Hoechst. (D) Dead cells stained with red-fluorescent Propidium Iodide. Scale bar = 300 μm.

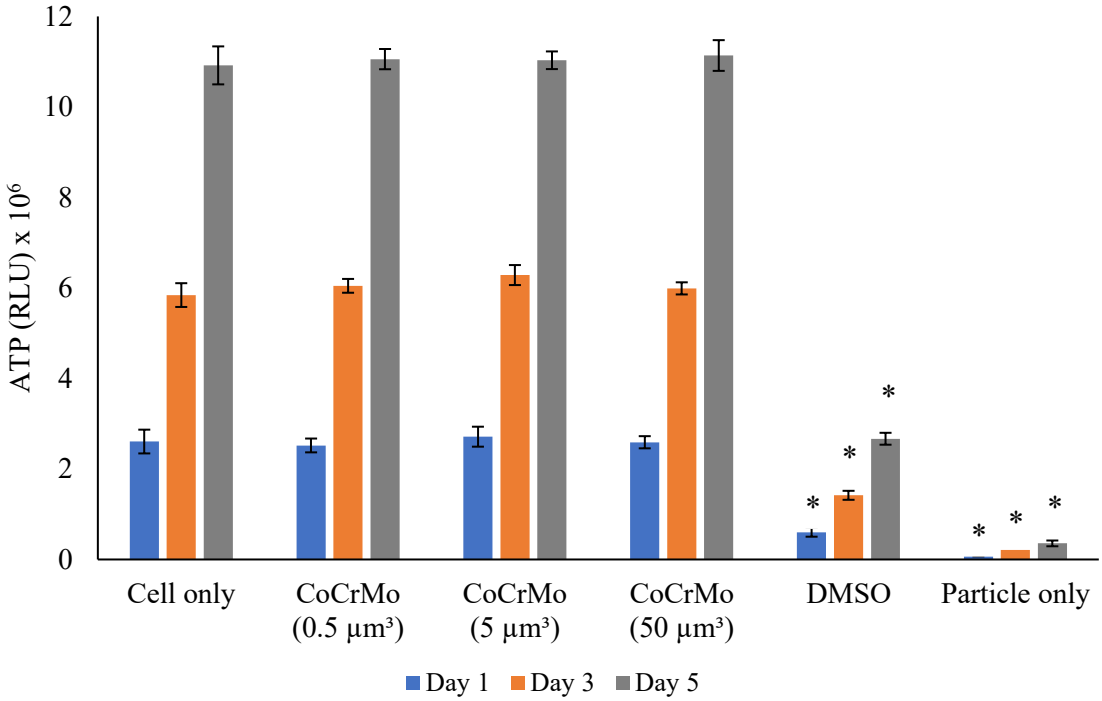

Figure 6.9. Quantitative analysis of the effects of CoCrMo particles on the viability of C6 astrocyte-like cells in a 3D bioprinted GelMA hydrogel model. C6 astrocyte-like cells were cultured with CoCrMo particles for 5 days. Cell viability was determined using a luminescent ATP assay. Negative controls used were C6 cell only embedded in GelMA hydrogels and particle only embedded in GelMA hydrogels. Positive control used was cells exposed to DMSO. Error bars represent ±95% confidence interval, n = 6. An asterisk (*) represents statistically significant reduction ($p<0.05$, student's t-test) in cell viability in comparison to cell only negative control.

6.5.4 The effect of polymer model particles on the viability of NG108-15 neuronal cells in a 3D bioprinted model

NG108-15 neuronal cells and polymer model particles (PEEK-OPTIMA or Ceridust 3615 ®) were embedded in bioprinted 5% (w/v) GelMA hydrogel constructs. In the experiment both PEEK-OPTIMA and Ceridust 3615 ® were tested at the same time using the same 96-well plates. The PEEK-OPTIMA and Ceridust 3615 ® particles were dosed at 100 μm^3 per cell and compared with a negative control, which was only C6 cells embedded in 3D GelMA hydrogel. Over the 5 days of this experiment, the average luminescent values continued to rise for the cell only negative control. In contrast, for the PEEK-OPTIMA and Ceridust 3615 ® particles, the average luminescent values decreased at day 5 from day 3, shown in Figures 6.13. The average luminescent values for the cell only negative control increased approximately 2-fold in both experiments over 5 days. The average luminescent values for the tests with the PEEK and Ceridust 3615® increased approximately 2-fold from day 1 to day 3 and decreased 14.44% and 5.56%, respectively from day 3 to day 5. The cell growth of NG108-15 neuronal cells was not adversely affected ($p > 0.05$, Student's t-test) in the presence of polymer model particles of PEEK-OPTIMA. Cell proliferation decreased for PEEK-OPTIMA and Ceridust 3615 ® at day 5, however was not statistically significant ($p > 0.05$, Student's t-test). A significant reduction ($p < 0.05$) in cell viability was measured for the positive control and particle only control.

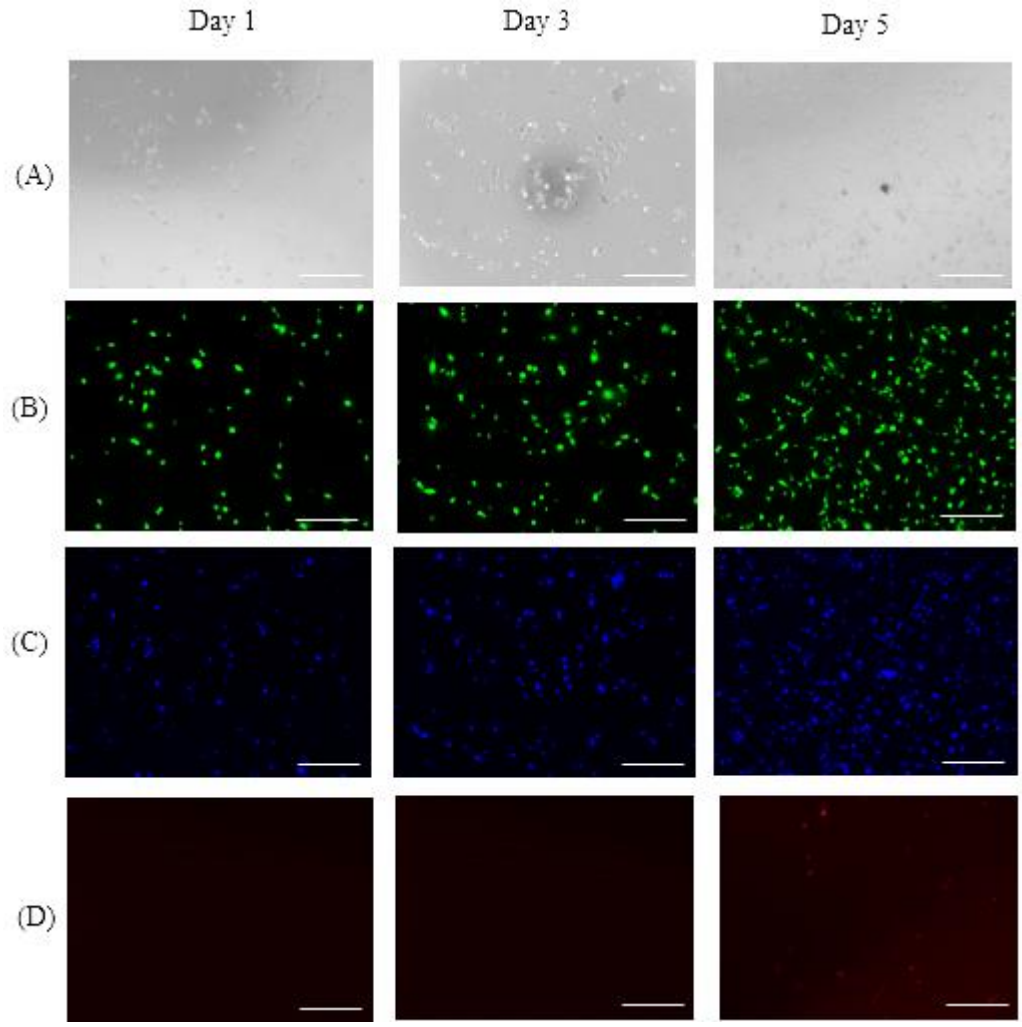

Figure 6.10. Qualitative analysis of the effects of PEEK-OPTIMA particles on the viability of NG108-15 neuronal cells in a 3D bioprinted GelMA hydrogel model. NG108-15 neuronal cells were cultured with ZTA particles for 5 days. Cell viability was determined using a green-fluorescent calcien AM stain. (A) Bright field microscopy images of NG108-15 neuronal cells with PEEK-OPTIMA particles; (B) Live cells stained with green-fluorescent calcien AM; (C) Cell nuclei stained with blue-fluorescent Hoechst. (D) Dead cells stained with red-fluorescent Propidium Iodide. Scale bar = 300 µm.

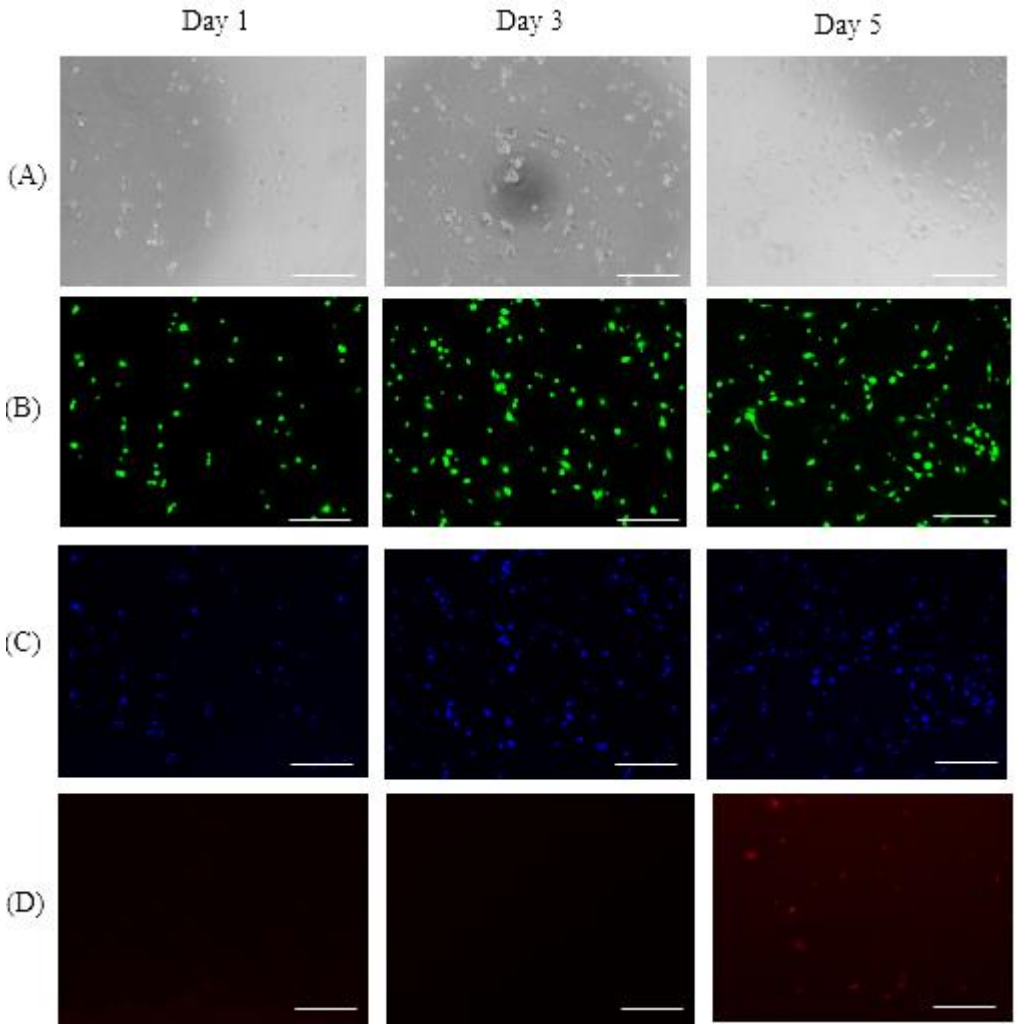

Figure 6.11. Qualitative analysis of the effects of Ceridust 3615 ® particles on the viability of NG108-15 neuronal cells in a 3D bioprinted GelMA hydrogel model. NG108-15 neuronal cells were cultured with Ceridust 3615 ® particles for 5 days. Cell viability was determined using a green-fluorescent calcien AM stain. (A) Bright field microscopy images of NG108-15 neuronal cells with Ceridust 3615 ® particles; (B) Live cells stained with green-fluorescent calcien AM; (C) Cell nuclei stained with blue-fluorescent Hoechst. (D) Dead cells stained with red-fluorescent Propidium Iodide. Scale bar = 300 µm.

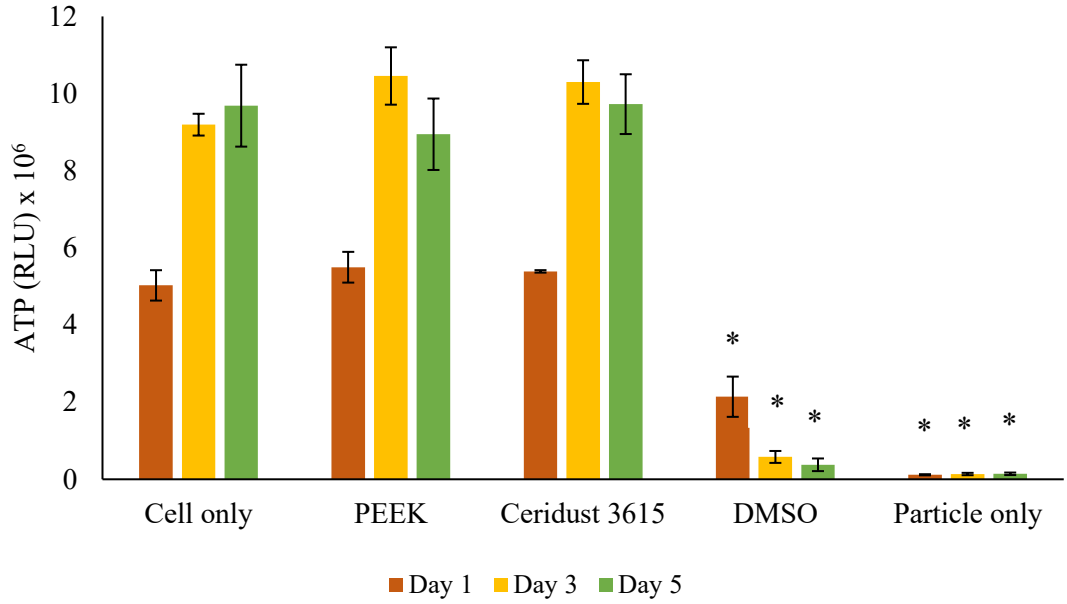

Figure 6.12. Quantitative analysis of the effects of PEEK and Ceridust 3615 ® particles on the viability of neuronal NG108-15 cells in a 3D bioprinted GelMA hydrogel model. Neuronal NG108-15 cells were cultured with PEEK or Ceridust particles for 5 days. Cell viability was determined using a luminescent ATP assay. Negative controls used were NG108-15 cell only embedded in GelMA hydrogels and particle only embedded in GelMA hydrogels. Positive control used was cells exposed to DMSO. Error bars represent ±95% confidence interval. An asterisk (*) represents statistically significant reduction ($p<0.05$, student's t-test) in cell viability in comparison to cell only negative control.

6.5.5 The effect of ceramic model particles on the viability of NG108-15 neuronal cells in a 3D bioprinted model

NG108-15 neuronal cells and ceramic model particles (ZTA) were embedded in bioprinted 5% (w/v) GelMA hydrogel constructs. The ZTA particles were dosed at 50 μm^3 per cell and compared with a negative control, which was only C6 cells embedded in 3D GelMA hydrogel. Over the 5 days of this experiment, the average luminescent values continued to rise for the cell only negative control, shown in Figure 6.15. In contrast, for the ZTA particles, the average luminescent values decreased 11.38% at day 5 from day 3, however was not statically significant ($p > 0.05$). The average luminescent values for the cell only negative control and ZTA particle test increased approximately 2-fold in both experiments over 5 days. The cell growth of neuronal NG108-15 cells was not adversely affected in the presence of polymer model particles of PEEK-OPTIMA. Cell proliferation decreased for PEEK and Ceridust 3615 ® at day 5, however was not statistically significant ($p > 0.05$, Student's t-test). A significant reduction ($p < 0.05$, Student's t-test) in cell viability was observed for the positive control and particle only control.

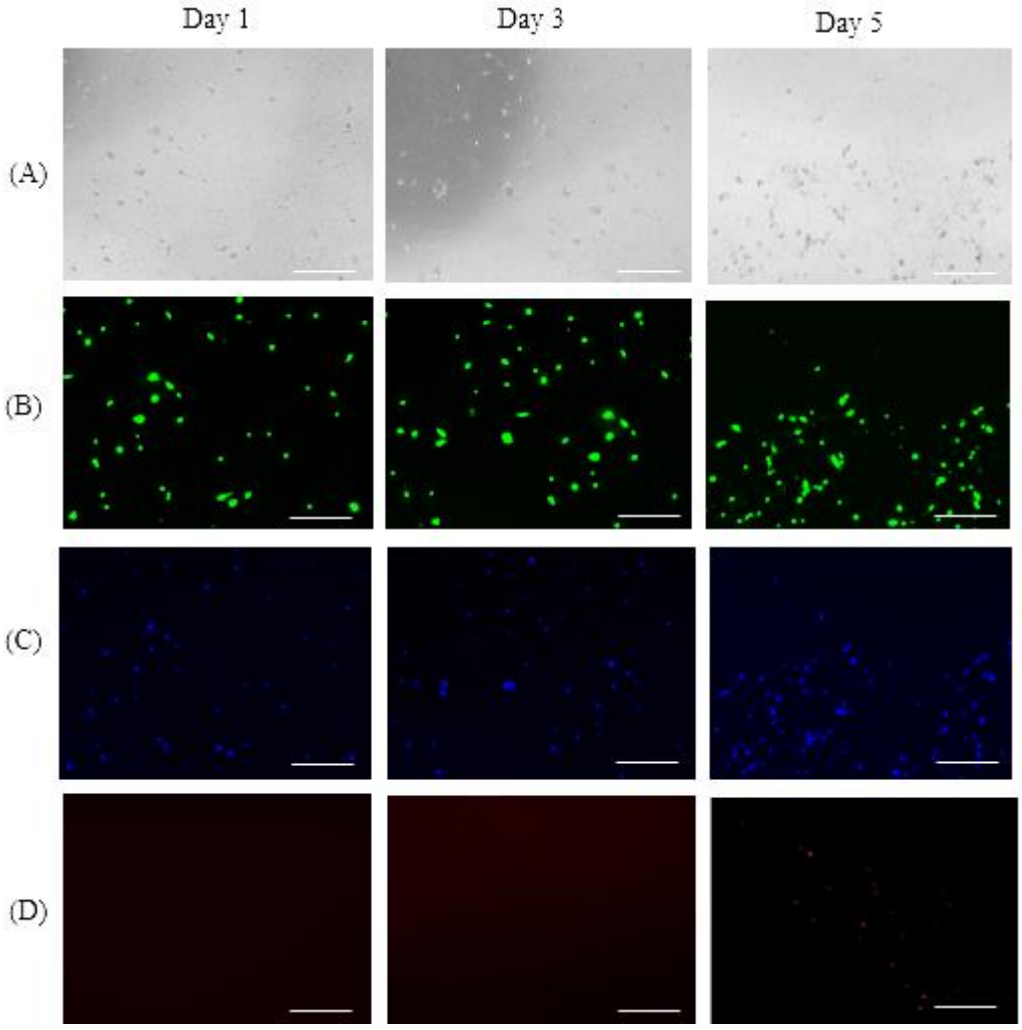

Figure 6.13. Qualitative analysis of the effects of ZTA particles on the viability of NG108-15 neuronal cells in a 3D bioprinted GelMA hydrogel model. Neuronal NG108-15 cells were cultured with ZTA particles for 5 days. Cell viability was determined using a green-fluorescent calcien AM stain. (A) Bright field microscopy images of NG108-15 neuronal cells with ZTA particles; (B) Live cells stained with green-fluorescent calcien AM; (C) Cell nuclei stained with blue-fluorescent Hoechst. (D) Dead cells stained with red-fluorescent Propidium Iodide. Scale bar = 300 μm.

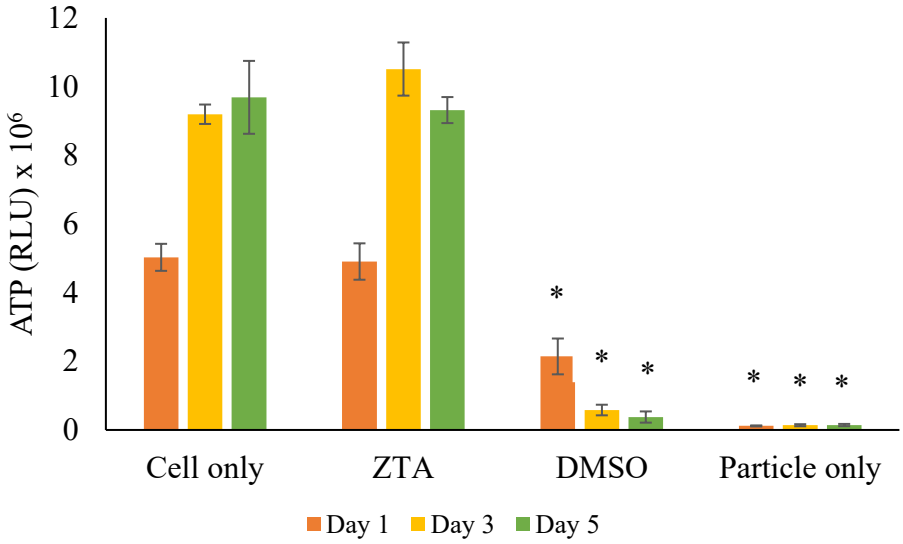

Figure 6.14. Quantitative analysis of the effects of ZTA particles on the viability of neuronal NG108-15 cells in a 3D bioprinted GelMA hydrogel model. Neuronal NG108-15 cells were cultured with ZTA particles for 5 days. Cell viability was determined using a luminescent ATP assay. Negative controls used were NG108-15 cell only embedded in GelMA hydrogels and particle only embedded in GelMA hydrogels. Positive control used was cells exposed to DMSO. Error bars represent ±95% confidence interval. An asterisk (*) represents statistically significant reduction ($p<0.05$, student's t-test) in cell viability in comparison to cell only negative control.

6.5.6 The effect of model metal particles on the viability of NG108-15 neuronal cells in a 3D bioprinted model

NG108-15 neuronal cells and model metal particles (CoCrMo) were embedded in bioprinted 5% (w/v) GelMA hydrogel constructs. The CoCrMo particles were dosed at 50 μm^3 and compared with a negative control, which was only NG108-15 cells embedded in 3D GelMA hydrogel. Over the 5 days of this experiment, the average luminescent values continued to rise for the cell only negative control, shown in Figure 6.17. In contrast, for the CoCrMo particles, the average luminescent values decreased 26.59% at day 5 from day 3, however was not statically significant ($p > 0.05$, Student's t-test). At day 5, neuronal NG108-15 cells had a statistically significant ($p < 0.05$, Student's t-test) lower luminescent value compared to the cell only negative control. In addition, a few dead cells stained with propidium iodide were observed in Figure 6.16. Overall, there was an effect of CoCrMo particles on NG108-15 neuronal cell viability over 5 days, when CoCrMo particles were dosed at 50 μm^3 per cell.

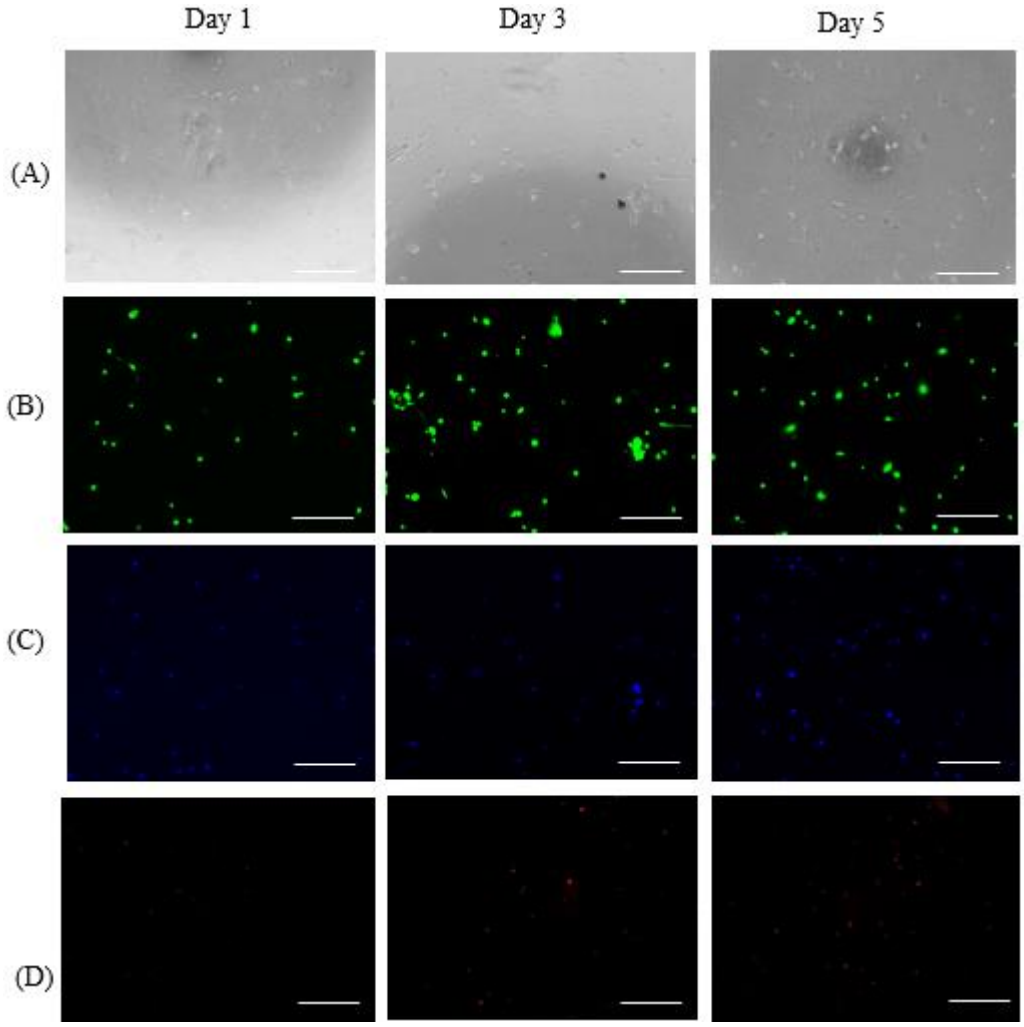

Figure 6.15. Qualitative analysis of the effects of CoCrMo particles on the viability of NG108-15 neuronal cells in a 3D bioprinted GelMA hydrogel model. Neuronal NG108-15 cells were cultured with CoCrMo particles for 5 days. Cell viability was determined using a green-fluorescent calcien AM stain. (A) Bright field microscopy images of NG108-15 neuronal cells with CoCrMo particles; (B) Live cells stained with green-fluorescent calcien AM; (C) Cell nuclei stained with blue-fluorescent Hoechst. (D) Dead cells stained with red-fluorescent Propidium Iodide. Scale bar = 300 µm.

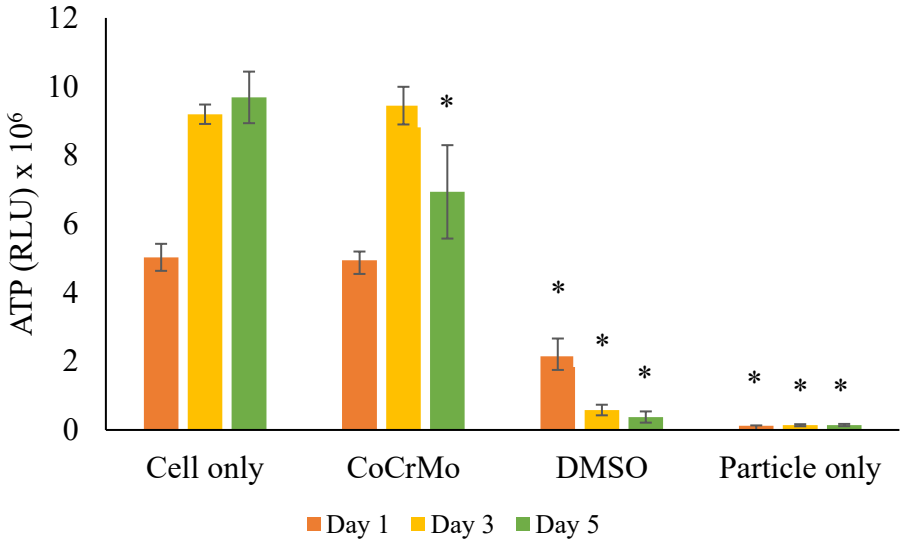

Figure 6.16. Quantitative analysis of the effects of CoCrMo particles on the viability of NG108-15 neuronal cells in a 3D bioprinted GelMA hydrogel model. NG108-15 neuronal cells were cultured with CoCrMo particles for 5 days. Cell viability was determined using a luminescent ATP assay. Negative controls used were NG108-15 cell only embedded in GelMA hydrogels and particle only embedded in GelMA hydrogels. Positive control used was cells exposed to DMSO. Error bars represent ±95% confidence interval. An asterisk (*) represents statistically significant reduction ($p<0.05$, student's t-test) in cell viability in comparison to cell only negative control.

6.5.7 The effect of model particles on the oxidative stress in C6 astrocyte-like cells

C6 astrocyte-like cells were exposed to model particles in the bioprinted 5% (w/v) GelMA hydrogel constructs, and levels of reactive oxygen species production was investigated, by comparing with a positive control. The positive control consisted of C6 astrocyte-like cells being exposed to hydrogen peroxide, which is a reagent that induces oxidative stress on cells. Oxidative stress was measured at day 3 and day 5 both quantitatively. While qualitative analysis was performed after 3 days. The positive control demonstrated higher ROS levels observed in Figure 6.18(A), indicated by the increased fluorescent intensity when compared to the cell only negative control or cells exposed to model particles. When observing the fluorescent intensity quantitatively, shown in Figures 6.19 – 6.21, there was a significant increase ($p < 0.05$, Student's t-test) in production of ROS in the positive control compared to other samples. The C6 astrocyte-like cells that were exposed to PEEK-OPTIMA and Ceridust 3615 ® particles were dosed at 100 μm^3 did not show significant increases in ROS production compared to the cell only negative control. This was similar to the results observed in cells exposed to ZTA model particles, dosed at 50 μm^3 per cell and CoCrMo model particles, dosed at 50 μm^3 per cell. Overall, the findings demonstrated that all of model particles did not induce significant levels of reactive oxygen species productions when compared to the cell only negative control.

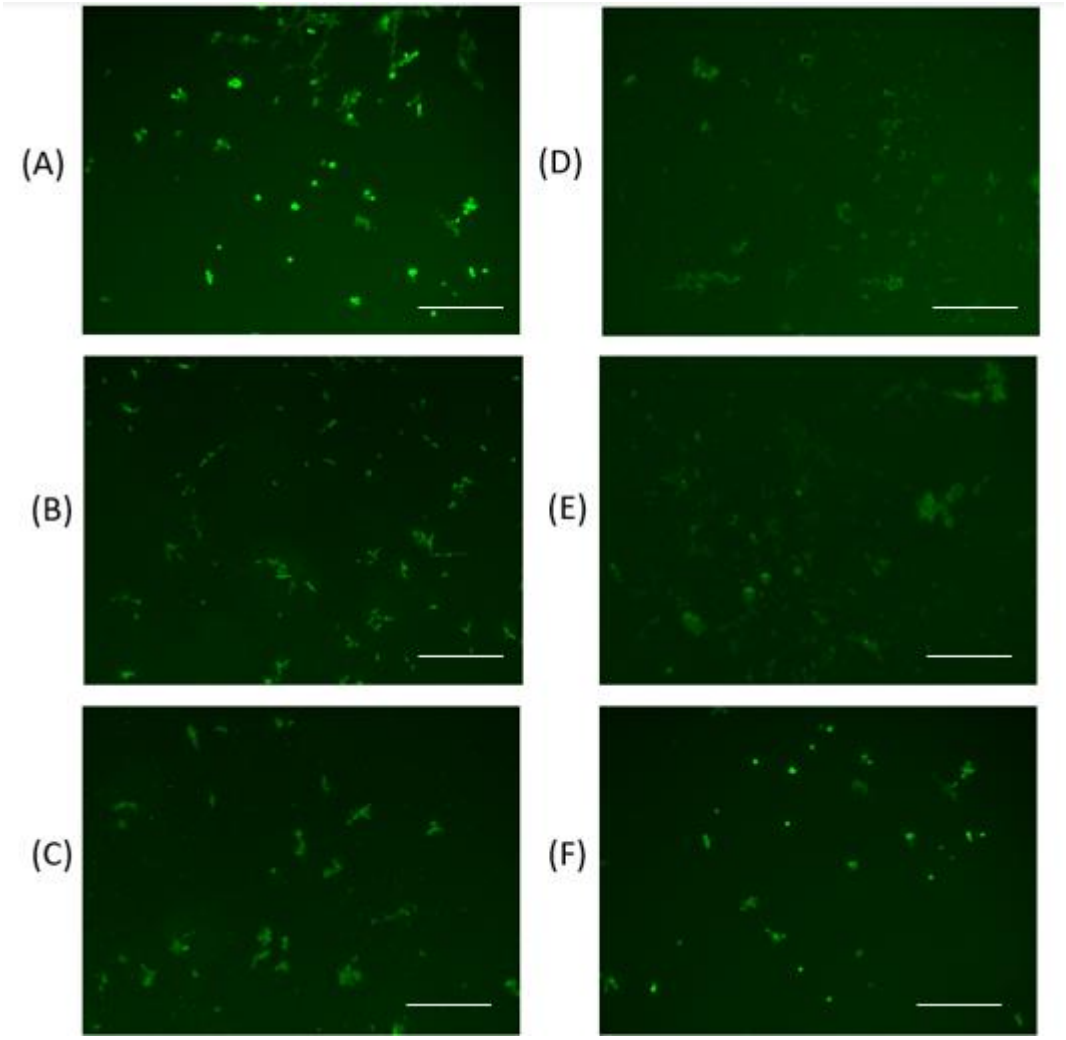

Figure 6.17. Fluorescence microscopy images of ROS in C6 astrocyte-like cells exposed with polymer, ceramic and metal model particles in 3D bioprinted GelMA hydrogels after 3 days. Oxidative stress was determined with the DCFDA probe that detects ROS activity. The production of ROS is proportional to the intensity of the green fluorescence. (A) Positive control (hydrogen peroxide); (B) Cell only control; cells exposed to (C) PEEK particles; (D) Ceridust 3615 ® particles; (E) ZTA particles; (F) CoCrMo particles. Scale bar = 200 μm

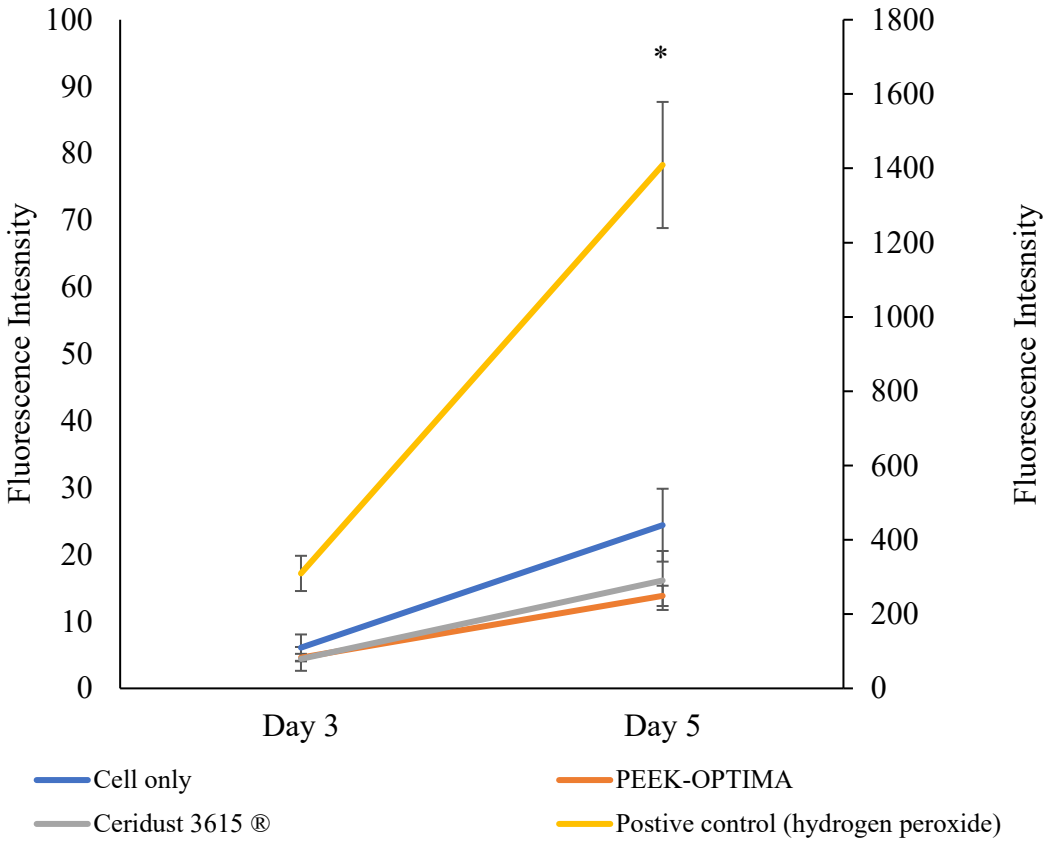

Figure 6.18.Cellular reactive oxygen species production (proportional to fluorescence level) of C6 astrocyte-like cells in response to polymer model particles (PEEK-OPTIMA and Ceridust 3615 ®), embedded in 3D bioprinted GelMA hydrogels. Oxidative stress was determined with a DCFDA fluorescent probe to detect ROS. Hydrogen peroxide was used as the positive control. Primary axis of values for fluorescence intensity correspond to the cell only negative control, PEEK-OPTIMA and Ceridust 3615 ® samples. Secondary axis intensity values correspond to the positive control. Error bars represent ±95% confidence interval. An asterisk (*) represents statistically significant reduction ($p<0.05$, student's t-test) in cell viability in comparison to cell only negative control.

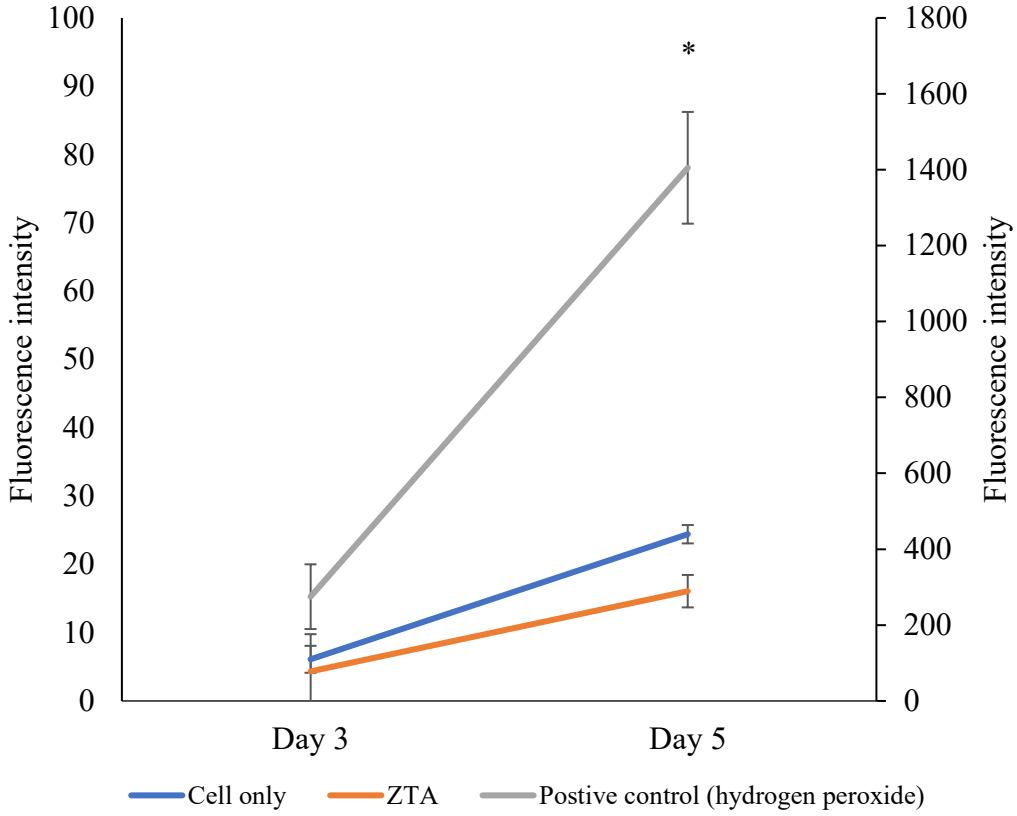

Figure 6.19. Cellular reactive oxygen species production (proportional to fluorescence level) of C6 astrocyte-like cells in response to ceramic model particles (ZTA), embedded in 3D bioprinted GelMA hydrogels. Oxidative stress was determined with a DCFDA fluorescent probe to detect ROS. Hydrogen peroxide was used as the positive control. Primary axis of values for fluorescence intensity correspond to the cell only negative control and ZTA samples. Secondary axis intensity values correspond to the positive control. Error bars represent ±95% confidence interval. An asterisk (*) represents statistically significant reduction ($p<0.05$, student's t-test) in cell viability in comparison to cell only negative control.

6.5.8 The effect of model particles on the oxidative stress in NG108-15 neuronal cells

NG108-15 neuronal cells and polymer (PEEK-OPTIMA and Ceridust 3615 ®), ceramic (ZTA) and metal (CoCrMo) model particles were embedded in bioprinted 5% (w/v) GelMA hydrogel constructs. The PEEK-OPTIMA and Ceridust 3615 ® particles were dosed at 100 μm^3 while the ZTA and CoCrMo particles were dosed at 50 μm^3. Oxidative stress was measured at day 3 and day 5 both quantitatively. While qualitative analysis was performed after 3 days. The positive control demonstrated higher ROS levels observed in Figure 6.20(A) and Figure 6.21, when compared with the cell only negative control. When C6 astrocyte-like cells were exposed to each model particle, there was no significant increase in ROS production, when compared to cell only negative control.

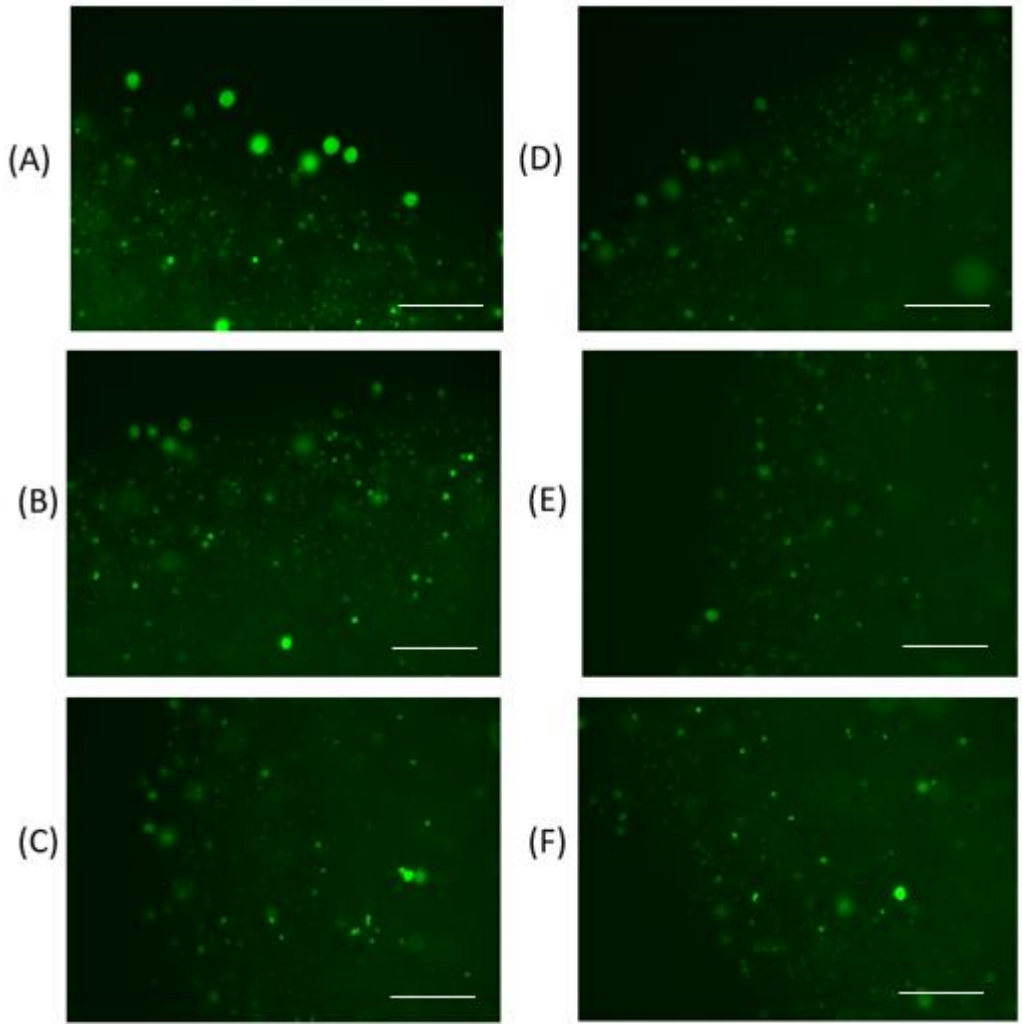

Figure 6.20. Fluorescence microscopy images of ROS in NG108-15 neuronal cells exposed with polymer, ceramic and metal model particles in 3D bioprinted GelMA hydrogels after 3 days. Oxidative stress was determined with the DCFDA probe that detects ROS activity. The production of ROS is proportional to the intensity of the green fluorescence. (A) Positive control (hydrogen peroxide); (B) Cell only control; cells exposed to (C) PEEK-OPTIMA particles; (D) Ceridust 3615 ® particles; (E) ZTA particles; (F) CoCrMo particles

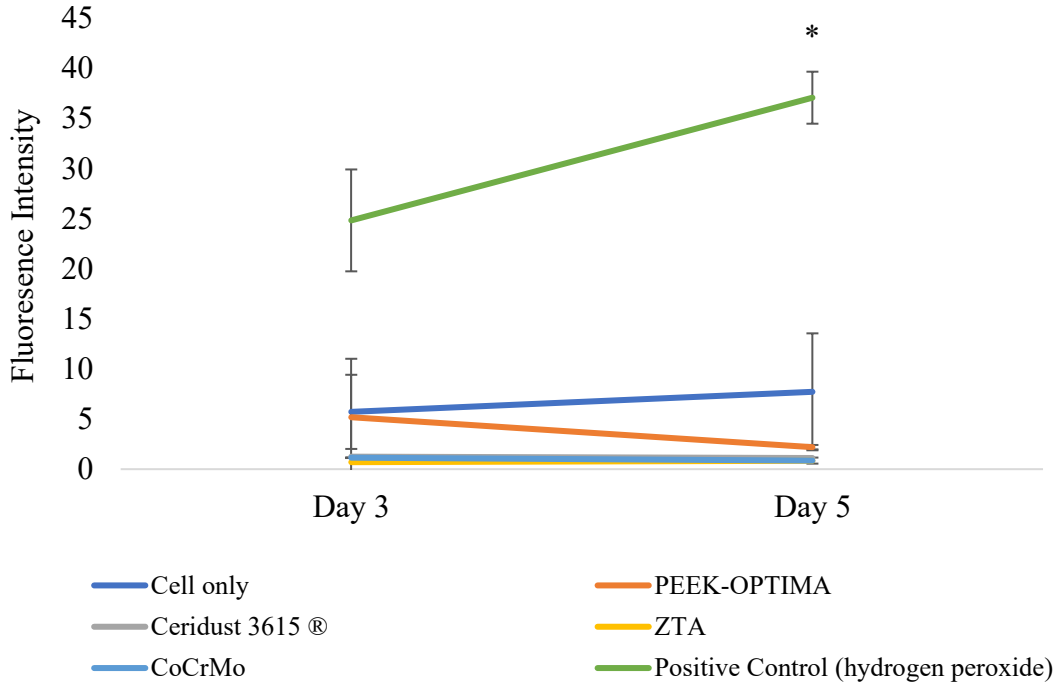

Figure 6.21. Cellular reactive oxygen species production (proportional to fluorescence level) of NG108-15 neuronal cells in response to polymer (PEEK-OPTIMA and Ceridust 3615 ®), ceramic (ZTA) and metal (CoCrMo) model particles, embedded in 3D bioprinted GelMA hydrogels. Oxidative stress was determined with a DCFDA fluorescent probe to detect ROS. Hydrogen peroxide was used as the positive control. Error bars represent ±95% confidence interval. An asterisk (*) represents statistically significant reduction ($p<0.05$, student's t-test) in cell viability in comparison to cell only negative control.

Table 6.4. Summary table of the effect of different model particles on C6 astrocyte-like and NG108-15 neuronal cell viability in the 3D bioprinted *in vitro* model. X indicates no significant decrease in cell viability and ↓ indicates a significant reduction in cell viability.

	C6 astrocyte-like cells	**NG108-15 neuronal cells**
PEEK-OPTIMA	X	X
Ceridust 3615 ®	X	X
ZTA	X	X
CoCrMo	X	↓

Table 6.5. Summary table of the effect of different model particles on reactive oxygen species production in C6 astrocyte-like and NG108-15 neuronal cells in the 3D bioprinted *in vitro* model. X indicates no significant increase in reactive oxygen species production

	C6 astrocyte-like cells	**NG108-15 neuronal cells**
PEEK-OPTIMA	X	X
Ceridust 3615 ®	X	X
ZTA	X	X
CoCrMo	X	X

6.5.9 The effect of model particles on the DNA integrity of C6 astrocyte-like cells

The DNA integrity of C6 astrocyte-like cells when exposed to model particles of PEEK-OPTIMA, Ceridust 3615®, ZTA, or CoCrMo, was investigated in the 3D bioprinted GelMA hydrogel model, using a DNA damage assay that measures γ-H2AX foci levels in cells. PEEK-OPTIMA or Ceridust 3615® model particles were dosed at a concentration of 100 μm^3 per cell. ZTA or CoCrMo model particles dosed at a concentration of 50 μm^3 per cell. DNA damage was assessed using a γ -H2AX as a quantitative DNA double-

strand break biomarker. DNA damage was assessed at 1 hour, because DNA strand breaks that are induced by genotoxic materials may occur immediately. From the images obtained from fluorescent microscopy, shown in Figure 6.23, it appears that no DNA damage occurred in C-6 astrocyte-like cells, due to the absence of γ-H2AX foci. It is important to note here that the positive control used here, C6-astrocyte-like cells exposed to 10 % (v/v), did not appear to function optimally, possibly due to cell death. Thus, the data for the positive control was not presented here.

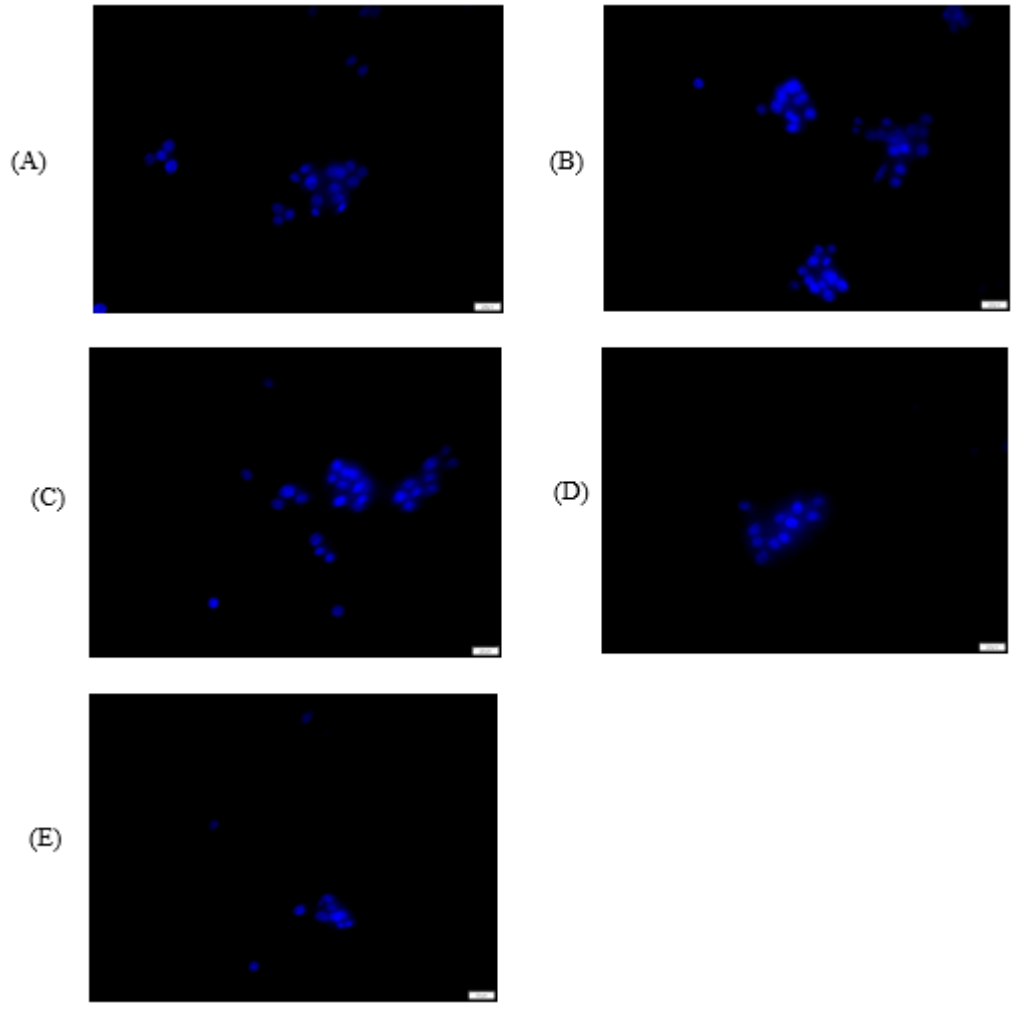

Figure 6.22. DNA damage measured by γ-H2AX immunofluorescence. C6 astrocyte-like cells were exposed to model particles and DNA damage was measured after 1 hour. Images presented here include (A) Cell only control; cells exposed to (B) PEEK-OPTIMA particles; (D) Ceridust 3615 ® particles; (E) ZTA particles; (F) CoCrMo particles

6.6 Discussion

Although the benefits of treating degenerative disc conditions with spinal implants include improving spinal stability and motion preservation, there are concerns about potential complications related to wear debris produced from the materials of the implants. Specifically, the presence of wear debris may have detrimental implications for the surrounding neural tissues and cells.

In this part of the study, the aim was to use the novel *in vitro* 3D bioprinted GelMA hydrogel model developed in Chapter 5 to investigate the biological responses of C6 astrocyte-like and NG108-15 neuronal cells, measuring the cell viability, production of reactive oxygen species and DNA damage in response to model particles including PEEK-OPTIMA, Ceridust 3615 ®, ZTA and CoCr-Mo over a period of 5 days. In addition, it was also important to compare the outcomes from this study with previous studies, specifically comparing the responses that previous studies using wear particles produced by articulation of biomaterials in a simple configuration wear simulator with the current study using model particles. This comparison was necessary to assess whether using model particles would be a viable option for future *in vitro* studies examining neural cell responses.

6.6.1 Biological responses of neural cells to PEEK model particles.

Polyetheretherketone (PEEK) offers a unique combination of mechanical properties, including resistance to fatigue, in combination with biocompatibility, and radiolucency which are beneficial for long-term device performance and improved imaging, respectively. As a result, PEEK has been widely used in the development of spinal devices and instrumentation including rods and hooks. PEEK-OPTIMA, developed by Invibio Biomaterial Solutions in the late 1990s, has been utilised in various implantable devices for spinal surgery, including spinal instrumentation, interbody spinal fusion cages and artificial discs. As a result, there is significant interest in the biological responses of neural cells to PEEK-OPTIMA model particles.

In this part of the study, both C6 astrocyte-like and NG108-15 neuronal cells were exposed to a concentration of 100 μm^3 model PEEK-OPTIMA particles per cell with 95%

of particles being with the 0.1 – 8 μm size range. Cell viability, production of reactive oxygen species (ROS) and DNA damage were investigated in an *in vitro* 3D bioprinted GelMA hydrogel model. The effect of model PEEK-OPTIMA model particles on the viability of C6 astrocyte-like and NG108-15 neuronal cells was analysed quantitatively using luminescence ATP assay, and qualitatively using a live/dead assay. When C6 astrocyte-like cells were exposed to PEEK-OPTIMA model particles over a duration of 5 days, cell viability measurements were similar to the negative control of C6 astrocyte-like cells only, with cell proliferation occurring across the 5 days. When the NG108-15 neuronal cells were exposed to PEEK-OPTIMA model particles, cell viability measurements were also similar at days 1, 3 and 5 compared to the cell only control. At day 5 for the PEEK-OPTIMA group, there was a slight reduction in cell viability compared to the cell only control group, however the reduction was not statistically significant. In addition, cell proliferation decreased from day 3 to day 5 for the PEEK-OPTIMA group but was also not statistically significant. The results from this study showed that PEEK-OPTIMA model particles did not significantly adversely affect neural cell viability when compared with cell only control. In addition, PEEK-OPTIMA model particles did not induce reactive oxygen species production or DNA damage in either C6 astrocyte-like or NG108-15 neuronal cells.

When examining previous literature, there has been very limited research conducted on investigating neural cell responses to PEEK-OPTIMA particles *in vitro*. However, one study conducted by Hallab *et al* [281] investigated macrophage reactivity using differentiated human macrophages and primary human monocytes when exposed to PEEK-OPTIMA particles compared to ultrahigh molecular weight polyethylene (UHMWPE) particles. Similarly to the present study, Hallab *et al* [281] also reported that PEEK-OPTIMA particles with sizes of 0.7 μm and 2.4 μm did not significantly reduce cell viability after 24 hours and 48 hours. The results from Hallab *et al* [281] showed similarity to the current study since 95% of the PEEK-OPTIMA particles characterised were less than 8 μm. The finding from the current study was important, as it was the first time that neural cell responses to PEEK-OPTIMA were investigated *in vitro*. Another experiment conducted in Hallab *et al* [281] was the investigation of proinflammatory cytokine release, and the authors demonstrated that PEEK-OPTIMA particles induced significant increases in proinflammatory cytokines compared to the cell media only

control, however PEEK-OPTIMA particles were significantly less inflammatory than UHMWPE particles. Although, the current study did not test for inflammatory response, it is important that future studies examine how PEEK-OPTIMA particles impact the production of proinflammatory cytokines in neural cells.

Furthermore, one previous *in vivo* study also conducted by Hallab *et al* [284] investigated PEEK-OPTIMA using a rabbit model. The authors had two test groups, with one group having the PEEK-OPTIMA placed epidurally, and the other placed intradiscally in the rabbits. Their study showed that the PEEK-OPTIMA particles did not cause neurological damage to the test subjects.

Although research on the biological responses is still limited, the findings from this study showed that PEEK-OPTIMA model particles did not have significant adverse effects on neural cells *in vitro*. These findings are encouraging as it provides more knowledge for clinicians and patients on the use of PEEK-OPTIMA in spinal implants, where the interactions with surrounding neural tissues and cells would be an essential factor in determining the safety and long-term clinical outcomes for patients.

6.6.2 Biological responses of neural cells to polyethylene model particles

Polyethylene is a commonly used material in spinal implants including the core component of total disc replacements, interbody fusion cages and components of spinal instrumentation. In this study, a commercially manufactured, low molecular weight polyethylene powder, called Ceridust 3615 ® (Hoechst, Germany) was utilised as model polymer particles. Although, the biological effect of Ceridust 3615 ® particles have been previously studied *in vitro*, there is currently limited information on the biological responses of neural cells to Ceridust 3615 ® model particles.

The biological responses to Ceridust 3615 ® particles have been previously modelled *in vitro* using a gel encapsulation technique conducted by Green *et al* [276]. In their study, Ceridust 3615 ® particles were encapsulated in 1% (w/v) agarose gel and centrifuged to produce a monolayer of particles, then murine peritoneal macrophages were seeded on top of the gel. In Green *et al* [276], Ceridust 3615 ® particles cultured at a 100 μm^3 per

cell ratio did not significantly affect cell viability compared to the cell only negative control after 24 hours. Furthermore, the technique used in Green *et al* [276] was adapted in a more recent conducted by Liu *et al* [110], where the authors used 0.4% (w/v) agarose gel and removed the centrifugation step, which allowed higher porosity of the gel and dispersed arrangement of particles in the gel, respectively. In addition, Liu *et al* [110] used human peripheral blood mononuclear cells instead of murine peritoneal macrophages. Similar to Green *et al* [276], there was no significant effect on cell viability compared to the cell only negative control after 24 hours, reported in Liu *et al* [110]. Furthermore, a study conducted by Yarrow-Wright also confirmed no significant adverse effect on viability in both human peripheral blood mononuclear and murine peritoneal macrophages when cultured in agarose and collagen gels. There have been no studies conducted previously investigating neural cell responses to Ceridust 3615 ® particles *in* vitro. Thus, in order to understand how neural tissues and cells surrounding the spine may respond to polyethylene used in spinal implants, the current study used c6 astrocyte-like and NG108-15 neuronal cells to model neural cell responses *in vitro*. In addition, the current study utilised GelMA hydrogels as the type of gel, as the study conducted by Rad *et al* [278] had demonstrated viability of C6 astrocyte-like and NG108-15 neuronal cells when cultured over 7 days. In this part of the study, both C6 astrocyte-like and NG108-15 cells were exposed to a concentration of 100 μm^3 model Ceridust 3615 ® particles per cell and the cell viability, production of reactive oxygen species (ROS) and DNA damage were investigated in an *in vitro* 3D bioprinted GelMA hydrogel model.

In the current study, 99% of characterised Ceridust 3615 ® particles were between 0.1 to 8 μm in size, with the mode size range of 0.1 to 0.8 μm, which was comparable to the particle size range of 0.21 to 7.2 μm obtained in Green *et al* [276]. Similar to the previous study, this study demonstrated also demonstrated no significant reduction in viability for C6 astrocyte-like and NG108-15 neuronal cells when compared to cell only negative control. In addition, Ceridust 3615 ® model particles did not induce reactive oxygen species production as well as DNA damage in both C6 astrocyte-like and NG108-15 neuronal cells. Although specific studies on neural cell responses to polyethylene particles may be limited, particle size could be a major contributing factor to the inactive biological responses from neural cells, as previous studies have suggested the inability of cells to uptake larger particles [12, 276]. In order to confirm this, future studies should

investigate how different particle sizes impact neural cell responses, and also aim to use particle sizes that are more clinically relevant.

In previous studies conducted by Green *et al* [276] and Liu *et al* [110], the authors also investigated the release of osteolytic cytokines from cells when exposed to Ceridust 3615 ® model particles and demonstrated that Ceridust 3615 ® model particles did not induce significant increase in osteolytic cytokine production by cells. In future studies, it is important that experiments investigating the impact of Ceridust 3615 ® model particles on osteolytic cytokine release by neural cells are conducted, which can provide extra insights into the inflammatory response in neural cells.

6.6.3 Biological responses of neural cells to ceramic model particles

The use of ceramics including alumina, zirconia and the zirconia toughened alumina (ZTA) composite material within the field of orthopaedics and neurosurgery has attracted interest due to their high corrosion and wear resistant properties. A previous study conducted by Fisher *et al* [285] compared three different bearing combinations including, metal-on-metal, metal-on-polymer and ceramic-on-ceramic, and demonstrated that the ceramic bearing produced the lowest wear. In addition, the authors showed that the generated ceramic wear debris from hip joint simulators had the lowest biological reactivity compared to metals and polymers.

The improved manufacturing methods for ceramics has allowed the development of ZTA as a material to be used in bearing surfaces for joint replacement. An example is the BIOLOX Delta ceramic femoral head which is used as a component for total hip replacement. The biological impact of BIOLOX Delta ZTA wear particles has been previously studied using fibroblast and peripheral blood mononuclear cells in Asif *et al* [134] and the authors concluded that the ZTA particles had low biological impacts and suggested that it may improve long-term clinical performance. Studies investigating the biological responses to ceramic has been very limited, since it is not as commonly used compared to other materials including, metals and polymers. Despite the improvement of toughness that zirconia provides, the application of ceramics in spinal implants is still limited. A major concern of ZTA ceramics is the brittleness of the material especially

when exposed to certain loading conditions, including excessive mechanical forces, which could cause fracture within the material [286]. Furthermore, the current state of knowledge on how ceramic wear affects neural cells remains unclear. Thus, the current study aimed at examining the biological responses of neural cells to ZTA model particles.

In this part of the study, both C6 astrocyte-like and NG108-15 cells were exposed to a concentration of 100 μm^3 model ZTA particles per cell. The mean size of the ZTA particles was 3.69 μm in diameter. The size range of ZTA particles was 0.45 – 20.32 μm in diameter, with 99% of particles having a diameter less than 8 μm. The ZTA particles had a mode size of 0.8 – 8.0 μm with approximately 73% of all particles. Biological responses of neural cells to model ZTA particles were examined by conducting experiments including, cell viability, production of reactive oxygen species (ROS) and DNA damage in the *in vitro* 3D bioprinted GelMA hydrogel model.

Previous studies investigating biological responses to commercially available ceramic powder have reported mild cytotoxic effects that was dose dependent. Thus, in the current study neural cells were exposed to ZTA model particles at a dosing range of 0.5 – 50 μm^3 and the cell viability was examined over a period of 5 days. The results demonstrated that ZTA model particles dosed at 0.5, 5 and 50 μm^3 had no significant effect on cell viability for both C6 astrocyte-like and NG108-15 neuronal cells, when compared to cell only negative control. Previous studies have not investigated neural cell responses, however, other cell types including L929 fibroblast cells also showed no significant reduction in cell viability when exposed to commercially available ceramic powder in a study conducted by Germain *et al* [282]. However, the authors demonstrated significant cytotoxic effects on U937 human macrophages when exposed to clinically relevant ceramic wear particles dosed at 50 μm^3 per cell. The absence of cytotoxic effects when neural cells were exposed to ceramic model particles in the current study was comparable to the results observed by Germain *et al* [282]. In addition, similar results were observed in the study conducted by Asif [134], where BIOLOX Delta model ceramic particles, dosed with the same range as the current study, showed no impact on the viability of L929 cells.

In addition, ZTA model particles did not induce reactive oxygen species production or DNA damage in either C6 astrocyte-like or NG108-15 neuronal cells when compared to cell only negative control. These results were comparable to the study conducted by Asif [134], who demonstrated no significant effect on oxidative stress and DNA damage in peripheral blood mononuclear cells when exposed to ceramic model particles. Similar to the results in cell viability, the use of clinically relevant ceramic wear particles, dosed at 50 μm^3 per cell demonstrated DNA damage by Asif [134], which shows the disparity of biological impact on cells between model and clinically relevant particles. Consequently, future studies on neural cell responses should use clinically relevant ceramic wear particles, dosed at 50 μm^3 per cell should be used to see whether previous cytotoxic effects in fibroblasts also occur in neural cells.

6.6.4 Biological responses of neural cells to metal model particles

Although cobalt chrome (CoCr) alloys provide many advantages as a material used in spinal implants including having high strength and durability, as well as corrosion resistance, the production of wear debris from CoCr spinal implants is an important area to consider due to its potential detrimental effect on clinical performance and patient health. Specifically, due to the close proximity of neural tissues to implanted materials in the spine, it was critical to investigate the neural cell response to CoCr wear particles.

In this study, a commercially available cobalt chrome molybdenum (CoCrMo) powder, manufactured from American Elements was utilised as model CoCr particles to be exposed to C6 astrocyte-like and NG108-15 neuronal cells in a 3D *in vitro* model. In a previous study conducted by Lee *et al* [12], neural cell responses to CoCr wear particles were investigated in an *in vitro* 3D model. In their study, a 3D cell culture model created with type 1 rat tail collagen gel was used to investigate the biological responses of primary astrocytes and microglia to increasing doses of 0.5 – 50 μm^3 CoCr wear particles per cell for a duration of 5 days. Lee *et al* [12] demonstrated significant reduction in cell viability of primary astrocytes when exposed to cobalt chrome particles dosed at 50 μm^3 per cell after two and five days. In the current study, GelMA hydrogels were used to provide the 3D cell culture environment, due to the successful demonstration of neural cell viability in GelMA hydrogels reported by Rad *et al* [278]. In addition, collagen hydrogels in

previous studies presented challenges including, poor structural integrity and batch-to-batch variability. The results from the current study demonstrated no significant reduction in viability of C6 astrocyte-like cells for all doses of model CoCr particles, ranging 0.5 – 50 μm^3 per cell over 5 days. However, there was a significant reduction in NG108-15 neuronal cell viability when exposed to model CoCr particles dosed at 50 μm^3 after 5 days compared to the cell only negative control. The difference in how model CoCr particles impacted cell viability adversely in NG108-15 neuronal cells compared to the absence of adverse response in C6 astrocyte-like cells could be due to the different sensitivity that both cells exhibit when exposed to foreign materials. The more robust response to model CoCr particles exhibited from astrocytes compared to neurons may be due to that astrocytes function to provide structural support and can proliferate to promote tissue repair around the site of injury or implantation in the central nervous system [279].

Furthermore, there was no significant effects on oxidative stress for both C6 astrocyte-like and NG108-15 neuronal cells. DNA damage was not observed in C6 astrocyte-like cells after 24 hours when exposed to model CoCr particles. These results contrast the findings from Lee *et al* [12], where the authors reported significant levels of DNA to astrocytes after 24 hours when exposed to cobalt chrome particles.

The findings from this study were dissimilar to the results reported by Lee *et al* [12]. The two main differences in the model found between the current study and Lee *et al* [12] that may have contributed to the disparity of results were the type of CoCr particles used and the particle size. In the study conducted by Lee *et al* [12], the authors used wear simulated CoCr particles that were more clinically relevant compared to the current study and had mean particle sizes in the 30 – 39 nm range. Whereas in the current study, model CoCr particles that had sizes mostly in the 0.8 – 8 μm range. In addition, the different particle shape and possibly surface characteristic may impact how neural cells uptake the particles.

Furthermore, the results from this study were consistent with a previous study conducted by Germain *et al* [282], where the authors had investigated not only wear generated CoCr particles, but also commercially available particles. Similar to Lee *et al* [12], Germain *et al* [282], demonstrated significant reduction in cell viability when exposed to wear

simulated CoCr particles dosed at 50 μm^3 per cell. However, Germain *et al* [282] reported that the commercially available CoCr particles, did not adversely affect cell viability, which was also observed in the current study. In addition, the reported mean particle sizes in the micrometre range were comparable to the sizes observed in the current study, which was contrasted to the nanometre sized particles reported in Lee *et al* [12]. Although the study by Germain *et al* [282] used other cell types including human histiocytes and fibroblast cells, the consistent absence of adverse effect on cell viability when exposed to commercially available CoCr particles, strongly supports the implication that the particle size and shape may impact how neural cells interact with model CoCr particles.

6.7 Key findings

The novel 3D bioprinted GelMA hydrogel model was successfully used to model neural cell responses to model particles including PEEK-OPTIMA, Ceridust 3615 ®, ZTA and CoCrMo. The findings from this chapter are as follows:

- Polymer model particles including, PEEK-OPTIMA and Ceridust 3615 ®, dosed at a concentration of 100 μm^3 per cell did not adversely affect the cell viability and oxidative stress levels of C6 astrocyte-like cells and N108-15 neuronal cells after 5 days. In addition, DNA damaged was not reported in C6 astrocyte-like cells when exposed to polymer model particles.

- ZTA model particles, dosed at a concentration of 50 μm^3 per cell did not adversely affect the cell viability and oxidative stress levels of C6 astrocyte-like cells and N108-15 neuronal cells after 5 days. In addition, DNA damaged was not reported in C6 astrocyte-like cells when exposed to ZTA model particles.

- CoCrMo model particles, dosed at a concentration of 50 μm^3 per cell significantly reduced cell viability of NG108-15 neuronal cells after 5 days. However, C6 astrocytes-like cell viability was not adversely affected. In addition, CoCrMo model particles did not adversely affect oxidative stress levels in C6 astrocyte-like cells and NG108-15 neuronal cells. DNA damaged was also not reported in C6 astrocyte-like cells when exposed to CoCrMo model particles.

Chapter 7

Overall Discussion

7.1 Introduction

Approximately 4 million Australians with back problems, which is 1 in 6 of the total population reported by the Australian Bureau of Statistics (ABS) in 2017 – 2018 [287]. Back pain can often have a detrimental impact on quality of life and also the economy. Back pain was ranked the third most cause of disease burden in 2023, based on the Australian Burden of Disease Study, representing 4.3% of Australia's overall disease burden [287]. People with back pain, aged 15 – 64 are less likely to be employed and be in the labour force compared to people with no back pain [287]. Management of back pain accounts for approximately $3.4 billion annually in Australia, reported in 2020 – 2021 [288]. In addition, there were 177,000 hospitalisations with people principally diagnosed with back problems, reported in 2020 – 2021, which was 690 hospitalisations per 100,000 population.

With the increased incidences of back problems globally, the use of spinal implants including total disc replacements and spinal fusion have continued to increase. Although the benefits of spinal implants are recognised for helping patients with back pain, caused by degeneration of intervertebral discs, there are challenges associated with maintaining long-term clinical performance of spinal implants. One of the major challenges that poses a risk to the longevity of spinal devices is the wear debris produced from articulating interfaces, e.g. polymer core and metal endplate interfaces in total disc replacements and screw-rod interfaces in spinal fusion, which may cause adverse biological responses. The proximity of neural tissues and cells to spinal devices poses a challenge as these tissues and cells may be damaged if exposed to wear debris.

Previous studies have investigated the cellular responses to wear particles of different biomaterials including, polymers, metals and ceramics. For example, Hallab *et al* [281] investigated biological responses of human macrophages and primary human monocytes when exposed to PEEK-OPTIMA or UHMWPE particles. Furthermore, other studies

including Green *et al* [276] and Liu *et al* [110], have investigated biological impacts of LDPE particles on murine peritoneal macrophages and human peripheral blood mononuclear cells, respectively. In addition, the biological effects of ceramic particles on fibroblast cells have been studied by Germain *et al* [282] and Asif [134]. Previous studies using different cell lines and different cell culture systems have been implemented to investigate cellular responses to wear particles. However, most studies conducted previously addressed the potential wear debris issue in total knee and hip replacements. Since similar biomaterials are also used in spinal devices and instrumentation, there is a need for more research on neural cell responses to these biomaterials. Even so, there have been a few studies that examined neural tissue and cellular responses to metal particles. The study conducted by Papageorgiou *et al* [173], demonstrated structural damages in the membrane surrounding the spinal cord caused by clinically relevant nanometre-sized cobalt chrome (CoCr) particles, modelled in an organ culture system. In addition, the study conducted by Lee *et al* [12], demonstrated that clinically relevant CoCr particles decreased glial cell viability and also caused DNA damage in glial cells, modelled in a 2D cell culture system, as well as a 3D collagen hydrogel cell culture system.

Most of the knowledge on the biological responses of neural cells to wear particles has been studied with in a 2D monolayer environment, which has the limitation of not being representative of the *in vivo* environment. As a result, 3D *in vitro* models have emerged as an alternative to study cell responses. The most recent 3D *in vitro* model conducted by Lee *et al* [12] studied neural cell responses from wear particles was developed using collagen hydrogels, which specifically examined how neural cells respond to metallic wear particles from metal-on-metal total disc replacements. However, the use of collagen hydrogels presented challenges including inadequate long-term stability, batch-to-batch variability and high variability of properties. Consequently, 3D bioprinting has recently become an attractive technique to generate 3D environments due to its greater precision in spatial control compared to traditional 3D cell culture methods.

7.2 Overall project aims

The overall aim of this study was to develop a novel 3D bioprinted *in vitro* model to examine biological responses of model particles that represented wear particles generated from spinal instrumentation and devices on neural cells. The biomaterial of model wear particles included metals, polymers and ceramics. This study was the first to bioprint GelMA hydrogel structures embedded with model particles and neural cells using extrusion-based bioprinting. A more in-depth understanding of how cells of the central nervous system (CNS) respond when exposed to wear particles would be beneficial for developing and optimising new designs for spinal implants including total disc replacements and spinal fusions that could ultimately improve the quality of life for patients with back pain.

In response to the Covid-19 pandemic and the lockdowns in New South Wales, Australia that restricted students' access to the laboratories, chapter 4 was devised as an alternative to laboratory work, which allowed the chapter to be researched and written while working at home during the lockdowns. Patients presented with symptoms of degenerative disc disease are commonly found to have low back pain. One of the common treatment methods for patients with low back pain associated with disc degenerative are total disc replacements for the lumbar spine. There was great interest in conducting an in-depth investigation into the performance of lumbar total disc replacements in patients. As a result, a systematic review was conducted as chapter 4 on lumbar total disc replacements for degenerative disc disease of patient outcomes with a minimum of 5 years follow-up.

Chapter 5 consisted of two distinct experimental projects, so it was divided into two sections. The first aim of chapter 5 was to characterise model wear particles of biomaterials including metals, polymers, and ceramics. The second aim of chapter 5 was to develop a novel 3D bioprinted *in vitro* cell culture model used to investigate biological responses of neural cells from the model wear particles.

Chapter 6 aimed to use the 3D bioprinted model developed in chapter 5 to investigate the cell viability, reactive oxygen species production and DNA damage of C6 astrocyte-like and NG108-15 neuronal cells when exposed to model particles.

7.3 Characterisation of model particles and development of a novel 3D bioprinted *in vitro* cell culture model

The first part of this study aimed to characterise model particles of different biomaterials including polymers (PEEK-OPTIMA and Ceridust 3615 ®), ceramics (ZTA) and metals (CoCrMo). The characterisation of particles followed the procedure in previous PhD students of Joanne Tipper including, Liu *et al* [110], Lee *et al* [12] and Asif [134]. Model particles were sequentially filtered with 8 μm, 0.8 μm and 0.1 μm filters. Model particles were imaged using scanning electron microscopy (SEM) and the sizes and morphologies of model particles were acquired using Image J. One of the challenges faced with determining the size distribution and morphologies of model particles was the difficulty of characterising particles that were within aggregates. Consequently, particles with the whole perimeter being able to be measured, were only counted and measured to create the size distribution. Measures were taken to prevent aggregation of particles which included extra sonication of particles during sequential filtration, and also using the nitrogen spray gun to remove any dust on the surface of the aluminium tabs where the particles were placed.

The PEEK-OPTIMA particles exhibited irregular and granular morphologies and majority of particles (95%) were in the 0.1 – 0.8 μm size range. The characterisation of PEEK-OPTIMA model particles was comparable to the study conducted by Hallab *et al* [281]. Similar to the current study, Du *et al* [280] reported similar granular shaped commercially available PEEK particles, with 99% of particles <5 μm. When comparing to a systematic review conducted by Stratton-Powell *et al* [135], the authors reported mean PEEK-based particles that ranged from 0.23 μm to 2.0 μm. Furthermore, the Ceridust 3615 ® model particles in this study demonstrated granular and polygonal, with approximately 92% of particles in the 0.1 – 0.8 μm size range, which were comparable to Green *et al* [276]. In addition, the morphology of ZTA model particles in this study was observed to be granular and polygonal, which was similar to the findings reported in Germain *et al* [282]. However, the mean particle size of ZTA model particle reported in the present study was larger than the size reported in Germain *et al* [282]. The difference in mean particle size could be related to the use of smaller filter membranes, e.g. less than 0.1 μm, in previous studies that allowed smaller particle sizes. However, when comparing

the size and morphology of CoCr model particles in the current study with commercial CoCr particles studied in Germain *et al* [282], similarities of circular particle morphology and particle sizes. Overall, most of the model particles sizes obtained from the current study were consistent with previous studies, in which the model particle sizes were within the most biologically reactive size range of 0.1 μm to 10 μm [135].

In the next part of this study, a novel *in vitro* 3D bioprinted GelMA model was developed to be utilised in investigating neural cell responses to model particles. In order to maintain consistency in bioprinted constructs, droplet printing was chosen instead of other shapes, e.g. grid lattice. Both C6 astrocyte-like and NG108-15 neuronal cells were bioprinted with 5% (w/v) GelMA as droplets via extrusion bioprinting, and viability of both cell lines were demonstrated over a duration of 7 days. The findings from this study confirmed the cell viability results demonstrated in Rad *et al* [278], who used the same GelMA concentration and neural cell lines. Previous *in vitro* studies that investigated biological effects of particles in a hydrogel model utilised the casting method, where the cells in the hydrogel mixture would be pipetted in the well plates to form the 3D model structure. In the current study, the novelty behind the current model was that model particles were bioprinted with neural cells and GelMA hydrogel, which would intend to provide a more uniform distribution of cells and particles. One of the major factors in determining successful bioprinting was the nozzle diameter. In this study, smaller nozzle diameters including 0.20 mm and 0.25 mm were not able to protrude the GelMA mixture with neural cells and particles. However, larger nozzle diameters including 0.41 mm and 0.58 mm, were able to extrude the mixture. The unsuccessful bioprinting with smaller nozzle sizes, suggests that the model particles may have clogged the nozzle preventing extrusion of the GelMA mixture. Overall, the 3D bioprinted GelMA model developed in Chapter 4 was a viable *in vitro* model used to investigate neural cell responses to model particles.

7.4 Neural cell responses to model particles

Previous studies on the investigations into the biological responses of cells to wear particles have mostly used 2D cell culture systems. The issue with the use of 2D cell culture model is the possible misrepresentation of cellular behaviour, especially cells of

the central nervous system, where the phenotype may be exhibited different in 2D and 3D culture [209]. The current study used a novel advanced 3D bioprinted cell culture system, which aimed to provide a more physiologically relevant *in vivo* environment. Model particles of different biomaterials including PEEK-OPTIMA, Ceridust 3615 ®, ZTA and CoCrMo were exposed to C6 astrocyte-like cells or NG108-15 neuronal cells in the 3D bioprinted GelMA hydrogel model. The final aim of this study was to investigate the neural cell responses to model particles, specifically investigating the effects of model particles on cell viability, oxidative stress and DNA damage.

When C6 astrocyte-like cells or NG108-15 neuronal cells were exposed to PEEK-OPTIMA model particles, there was no significant adverse effect on the cell viability and oxidative stress. Although, studies on the biological impacts of PEEK-OPTIMA have been very limited, the findings from this study were comparable with the study conducted by Hallab *et al* [281]. In their study, no significant reduction was observed in human macrophage cell viability when exposed to PEEK-OPTIMA particles after 48 hours. When C6 astrocyte-like cells or NG108-15 neuronal cells were exposed to Ceridust 3615 ® model particles, there was also no significant adverse effect on the cell viability and oxidative stress. The findings were consistent with previous studies conducted by Green *et al* [276] and Liu *et al* [110], where the authors showed no significant adverse effects on murine peritoneal macrophages. Overall, the findings from the present study suggest that polymer model particles do not affect biological response of neural cells. The biological inactivity could be related to the surface properties, which was beyond the scope of this investigation. Previous researchers have demonstrated a reduction of bioreactivity associated with elevated hydrophilicity in the surface chemistry of polymers [289]. However, further studies on surface chemistry of these polymer model particles are required to understand the relationship between polymer surface and biocompatibility.

When C6 astrocyte-like cells or NG108-15 neuronal cells were exposed to ZTA model particles, there was no significant adverse impact on cell viability and oxidative stress. The findings from this study were consistent with previous studies that used commercial ceramic particles. For example, the study conducted by Faye *et al* [290] demonstrated that commercially available ceramic particles including alumina and cerium-zirconia particles did not have harmful biological effects on fibroblastic cells. Similarly, Tsaousi

et al [291] demonstrated no significant reduction in cell viability in primary human fibroblast cells when exposed to commercially available alumina particles when compared to cell only control. Additionally, the authors also reported that the alumina particles did not cause increased levels of DNA damage, similar to the current study. In addition, the absence of oxidative stress and DNA damage observed in the present study was comparable to the results demonstrated in Asif [134], where ceramic model particles did not induce DNA damage and oxidative stress in cells. The absence of detrimental biological effects observed in neural cells when exposed to ceramic model particles, may be due to the bioinert properties of alumina ceramics, which makes it a desirable property for clinical applications in spinal surgery.

When the neural cells were exposed to CoCrMo model particles, there was no significant reduction on viability of C6-astrocyte-like cells. However, when NG108-15 neuronal cells were exposed to CoCrMo model particles, dosed at 50 μm^3 per cell, a significant reduction was observed after 5 days when compared to cell only negative control. The absence of adverse biological effects of C6 astrocyte-like cells was contrasted to the findings in Lee *et al* [12], who demonstrated significant adverse effects on cell viability and DNA damage, however, when exposed to wear simulated CoCr particles. When comparing to the study conducted by Germain *et al* [282], who used commercially available CoCr particles, there was no significant decrease in cell viability, which was similar to the results found in C6 astrocyte-like cells in the present study. The reduction in cell viability observed in NG108-15 neuronal cells was comparable a previous study conducted by Gomez-Arnaiz *et al* [292], who demonstrated decreased cell viability of SH-SY5Y neuroblastoma cells when exposed to cobalt ions at concentrations of $\geq$ 100 μM. The different effect on cell viability observed in C6 astrocyte-like and NG108-15 neuronal cells, may suggest the different sensitivity of cells when exposed to foreign material.

7.5 Limitations of this study and future work

This study did have some limitations. One of the main limitations was that the model particles used in modelling neural cell response were not clinically representative in terms of size and chemical composition. Unfortunately, wear particles were not able to be simulated due to significant delays in the commissioning and set up of the pin-on-disc tribometer in the laboratory. As a result, through consultation with the supervisory team, the candidate decided to proceed with model particles that were readily available in the laboratory. Future studies should repeat experiments using clinically relevant wear simulated particles to investigate the neural cell responses in the same 3D bioprinted GelMA hydrogel model *in vitro*. Generation of wear particles would involve using a pin-on-plate wear simulator with materials that are used from spinal devices. In addition, parameters including, normal load, sliding speed and motion type relevant to realistic spinal conditions. It would be interesting to compare the neural cell responses to model particles with clinically relevant wear simulated particles. This would involve testing the same outcomes of cell viability, ROS production and DNA damage of neural cells cultured in the novel 3D bioprinted *in vitro* model developed in this study when exposed to either model particles of wear simulated particles.

A key limitation with the characterisation of particles from images obtained from SEM, was the presence of some particle agglomeration, making it difficult to image individual particles. In order to reduce this problem in this study, images with regions that had less particle agglomeration were captured to ensure sufficient number of individual particles could be measured. Attempts should be made in the future to prevent particle agglomeration during the particle sample preparation by conducting longer sonication times of the particle solutions between each filtration step of sequential filtration. Another limitation was the time inefficiency of measuring particle sizes using the ImageJ software, as each particle measurement was obtained by drawing an outline of the particle. A new automated system of wear particle analysis has been researched and developed recently that utilises segmentation and classification algorithms to improve the speed and accuracy of wear particle characterisation [293]. There are automated image analysis systems that have more advanced capabilities than ImageJ that would improve the precision and speed of analysing particle size and shape. For example, Morphologi 4 is an automated image analysis system that utilises advanced optics and image processing to measure particle

size and shape. The advantages of this system consist of high-resolution imaging that allows precise size and shape measurements, and high throughput and reproducibility, allowing it to be ideal for high-volume particle sample processing. Furthermore, a key limitation of extrusion-based bioprinting of hydrogels with cells is the exposure of shear stress on the cells. The shear stress on cells when bioinks are pushed out through the nozzles can reduce cell viability or even cell death, particularly for sensitive cell types. To reduce shear stress exposure of cells; it would be important to consider using larger diameter nozzles reducing the pressure required to extrude the bioinks.

Another limitation was the absence of DNA damage data for NG108-15 neuronal cells. This was due to the time pressure faced because of initial difficulties and errors when setting up the DNA damage quantitative experiments for C6 astrocyte-like cells. In the future, it is important that DNA damage is examined in neuronal cells when exposed to wear particles. Assessing DNA damage in the future can be conducted using COMET assay (single-cell gel electrophoresis), which can be used as a quantitative method to analyse DNA damage. COMET assays would involve observing DNA damage as comet-like tails using fluorescence microscopy and measuring the tail length to quantify the DNA damage. Furthermore, future studies should also examine the neural cell responses to different sized particles and determine whether particle size has an impact on cell viability, ROS production and DNA damage.

Furthermore, in the current study, experimental work on the inflammatory response of neural cells was not conducted, which should be conducted in future work *in vitro* using astrocyte and neuronal cells. Inflammatory response of neural cells when exposed to particles would be investigated using an enzyme linked immunosorbent assay (ELISA), which determines the concentration of cytokines produced by cells. Additionally, it would be interesting to conduct further research on how the combination of different biomaterial wear particles impact the biological effects of neural cells, and also increasing the cellular complexity of the model by co-culturing both astrocytes and neuronal cells together.

7.6 Conclusion

In conclusion, this study developed a novel *in vitro* 3D bioprinted model using bioprinted GelMA hydrogels to investigate neural cell responses to different model particles of biomaterials used in spinal devices and instrumentation. The main findings of the study were as follows:

- The novel *in vitro* 3D bioprinted cellular model using GelMA hydrogels was successful in modelling neural cell responses to model particles.

- The nozzle size for bioprinting played a factor in consistent extrusion of GelMA containing model particles, with the smallest nozzle size being 0.41 mm in diameter.

- Both C6 astrocyte-like and NG108-15 neuronal cells demonstrated cell viability and proliferation when cultured in bioprinted GelMA hydrogels over 7 days.

- There was no significant reduction in cell viability of C6 astrocyte-like and NG108-15 neuronal cells when exposed to polymer model particles (sizes ranged 0.1 – 8.0 μm), dosed at 100 μm^3 per cell or ceramic model particles (sizes ranged 0.1 – 8.0 μm), dosed at 50 μm^3 per cell after 5 days.

- Model metal particles (sizes ranged 0.1 – 8.0 μm), dosed at 50 μm^3 did not significantly decrease cell viability of C6 astrocyte-like and NG108-15 neuronal cells. However, significantly decreased NG108-15 neuronal cells after 5 days.

- There was no adverse effect on oxidative stress levels and DNA integrity in C6 astrocyte-like and NG108-15 neuronal cells when exposed to either polymer, ceramic or metal model particles (sizes ranged 0.1 – 8.0 μm), dosed at 100 μm^3, 50 μm^3 and 50 μm^3, respectively.

References

1. Grotle, M., et al., *Lumbar spine surgery across 15 years: trends, complications and reoperations in a longitudinal observational study from Norway.* BMJ Open, 2019. **9**(8): p. e028743.
2. Hartvigsen, J., et al., *What low back pain is and why we need to pay attention.* Lancet, 2018. **391**(10137): p. 2356-2367.
3. Schoenfeld, A.J., et al., *Risk factors for immediate postoperative complications and mortality following spine surgery: a study of 3475 patients from the National Surgical Quality Improvement Program.* J Bone Joint Surg Am, 2011. **93**(17): p. 1577-82.
4. Garreau de Loubresse, C., *Neurological risks in scheduled spinal surgery.* Orthopaedics & Traumatology: Surgery & Research, 2014. **100**(1, Supplement): p. S85-S90.
5. Camino Willhuber, G., C. Elizondo, and P. Slullitel, *Analysis of Postoperative Complications in Spinal Surgery, Hospital Length of Stay, and Unplanned Readmission: Application of Dindo-Clavien Classification to Spine Surgery.* Global spine journal, 2019. **9**(3): p. 279-286.
6. Punt, I.M., et al., *Periprosthetic tissue reactions observed at revision of total intervertebral disc arthroplasty.* Biomaterials, 2009. **30**(11): p. 2079-2084.
7. Punt, I.M., et al., *Are periprosthetic tissue reactions observed after revision of total disc replacement comparable to the reactions observed after total hip or knee revision surgery?* Spine, 2012. **37**(2): p. 150-159.
8. Yang, C.-C., et al., *Metallosis after traumatic loosening of Bryan cervical disc arthroplasty: a case report and literature review.* European Spine Journal, 2018. **27**(3): p. 415-420.
9. Takahashi, S., J. Delécrin, and N. Passuti, *Intraspinal metallosis causing delayed neurologic symptoms after spinal instrumentation surgery.* Spine (Phila Pa 1976), 2001. **26**(13): p. 1495-8; discussion 1499.
10. Gaine, W.J., et al., *Late operative site pain with isola posterior instrumentation requiring implant removal: infection or metal reaction?* Spine (Phila Pa 1976), 2001. **26**(5): p. 583-7.
11. Guyer, R.D., et al., *Early Failure of Metal-on-Metal Artificial Disc Prostheses Associated with Lymphocytic Reaction: Diagnosis and Treatment Experience in Four Cases.* Spine, 2011. **36**(7): p. E492-E497.
12. Lee, H., et al., *Neural cell responses to wear debris from metal-on-metal total disc replacements.* European Spine Journal, 2019.
13. Chang, B.S., et al., *Evaluation of the biological response of wear debris.* Spine J, 2004. **4**(6 Suppl): p. 239s-244s.
14. Hu, Y.-L. and J.-Q. Gao, *Potential neurotoxicity of nanoparticles.* International Journal of Pharmaceutics, 2010. **394**(1): p. 115-121.
15. Kaiser, J.T. and J.G. Lugo-Pico, *Anatomy, Back, Spinal Cord Arteries*. 2019, StatPearls Publishing, Treasure Island (FL).
16. Waxenbaum, J.A. and B. Futterman, *Anatomy, Back, Thoracic Vertebrae*, in *StatPearls*. 2020: Treasure Island (FL).
17. Gkasdaris, G., et al., *Clinical anatomy and significance of the thoracic intervertebral foramen: A cadaveric study and review of the literature.* J Craniovertebr Junction Spine, 2016. **7**(4): p. 228-235.

18. Frost, B.A., S. Camarero-Espinosa, and E.J. Foster, *Materials for the Spine: Anatomy, Problems, and Solutions.* Materials (Basel), 2019. **12**(2).
19. Martini, F., J.L. Nath, and E.F. Bartholomew, *Fundamentals of anatomy & physiology*. 9th ed. 2012, San Francisco: Benjamin Cummings.
20. Dickson, R.A. and W.P. Butt, *Anatomy of the Spine*. The Medico-Legal Back: An Illustrated Guide. 2003: Cambridge University Press. 7-36.
21. Smith, L.J., et al., *Degeneration and regeneration of the intervertebral disc: lessons from development.* Dis Model Mech, 2011. **4**(1): p. 31-41.
22. Urban, J.P. and S. Roberts, *Degeneration of the intervertebral disc.* Arthritis Res Ther, 2003. **5**(3): p. 120-30.
23. Bron, J.L., et al., *Repair, regenerative and supportive therapies of the annulus fibrosus: achievements and challenges.* Eur Spine J, 2009. **18**(3): p. 301-13.
24. Chen, S., et al., *Meniscus, articular cartilage and nucleus pulposus: a comparative review of cartilage-like tissues in anatomy, development and function.* Cell and tissue research, 2017. **370**(1): p. 53-70.
25. Balkovec, C., et al., *Annulus Fibrosus Can Strip Hyaline Cartilage End Plate from Subchondral Bone: A Study of the Intervertebral Disk in Tension.* Global spine journal, 2015. **5**(5): p. 360-365.
26. Peng, B. and M.J. DePalma, *Cervical disc degeneration and neck pain.* J Pain Res, 2018. **11**: p. 2853-2857.
27. Adams, M.A., D.S. McNally, and P. Dolan, *'Stress' distributions inside intervertebral discs. The effects of age and degeneration.* J Bone Joint Surg Br, 1996. **78**(6): p. 965-72.
28. Adams, M.A. and P.J. Roughley, *What is Intervertebral Disc Degeneration, and What Causes It?* Spine. 2006. **31**(18): p. 2151-2161.
29. Ohshima, H. and J.P.G. Urban, *The Effect of Lactate and pH on Proteoglycan and Protein Synthesis Rates in the Intervertebral Disc.* Spine (Phila Pa 1976), 1992. **17**(9): p. 1079-1082.
30. Ishihara, H. and J.P. Urban, *Effects of low oxygen concentrations and metabolic inhibitors on proteoglycan and protein synthesis rates in the intervertebral disc.* J Orthop Res, 1999. **17**(6): p. 829-35.
31. Nachemson, A., et al., *In Vitro Diffusion of DYE Through the End-Plates and the Annulus Fibrosus of Human Lumbar Inter-Vertebral Discs.* Acta Orthopaedica Scandinavica, 1970. **41**(6): p. 589-607.
32. Bartels, E.M., et al., *Oxygen and Lactate Concentrations Measured in Vivo in the Intervertebral Discs of Patients With Scoliosis and Back Pain.* Spine (Phila Pa 1976). 1998. **23**(1): p. 1-7.
33. Stokes, I.A.F. and J.C. Iatridis, *Mechanical Conditions That Accelerate Intervertebral Disc Degeneration: Overload Versus Immobilization.* Spine (Phila Pa 1976), 2004. **29**(23): p. 2724-2732.
34. Heikkilä, J.K., et al., *Genetic and Environmental Factors in Sciatica Evidence from a Nationwide Panel of 9365 Adult Twin Pairs.* Annals of Medicine, 1989. **21**(5): p. 393-398.
35. Simmons, E.D.J., et al., *Familial Predisposition for Degenerative Disc Disease: A Case-Control Study.* Spine (Phila Pa 1976), 1996. **21**(13): p. 1527-1529.
36. Varlotta, G.P., et al., *Familial predisposition for herniation of a lumbar disc in patients who are less than twenty-one years old.* J Bone Joint Surg Am, 1991. **73**(1): p. 124-8.

37. Sambrook, P.N., A.J. MacGregor, and T.D. Spector, *Genetic influences on cervical and lumbar disc degeneration: A magnetic resonance imaging study in twins.* Arthritis and Rheumatism, 1999. **42**(2): p. 366-372.
38. Berg, A.J., et al., *The prevalence of lumbar disc degeneration in symptomatic younger patients: A study of MRI scans.* J Clin Orthop Trauma, 2020. **11**(5): p. 932-936.
39. Brinjikji, W., et al., *MRI Findings of Disc Degeneration are More Prevalent in Adults with Low Back Pain than in Asymptomatic Controls: A Systematic Review and Meta-Analysis.* AJNR Am J Neuroradiol, 2015. **36**(12): p. 2394-9.
40. Hibbs, R.A., *THE CLASSIC: An Operation for Progressive Spinal Deformities: A Preliminary Report of Three Cases From the Service of the Orthopaedic Hospital.* Clinical Orthopaedics and Related Research, 2007. **460**: p. 17-20.
41. ALBEE, F.H., *TRANSPLANTATION OF A PORTION OF THE TIBIA INTO THE SPINE FOR POTT'S DISEASE: A PRELIMINARY REPORT.* Journal of the American Medical Association, 1911. **LVII**(11): p. 885-886.
42. Garg, R.K. and D.S. Somvanshi, *Spinal tuberculosis: A review.* The Journal of Spinal Cord Medicine, 2011. **34**(5): p. 440-454.
43. Harris, I.A., et al., *Lumbar spine fusion: what is the evidence?* Internal Medicine Journal, 2018. **48**(12): p. 1430-1434.
44. McDermott, K.W., W.J. Freeman, and A. Elixhauser, *Overview of Operating Room Procedures During Inpatient Stays in U.S. Hospitals, 2014: Statistical Brief #233*, in *Healthcare Cost and Utilization Project (HCUP) Statistical Briefs*. 2006: Rockville (MD).
45. Rutherford, E.E., et al., *Lumbar Spine Fusion and Stabilization: Hardware, Techniques, and Imaging Appearances.* Radiographics, 2007. **27**(6): p. 1737-1749.
46. Nouh, M.R., *Spinal fusion-hardware construct: Basic concepts and imaging review.* World journal of radiology, 2012. **4**(5): p. 193-207.
47. Marcolongo, M., S. Sarkar, and N. Ganesh, *Trends in Materials for Spine Surgery*, in *Comprehensive Biomaterials II*. 2017, Elsevier. p. 175-198.
48. Lemaire, J.-P., et al., *Clinical and Radiological Outcomes With the Charité™ Artificial Disc: A 10-Year Minimum Follow-Up.* Journal of Spinal Disorders & Techniques, 2005. **18**(4): p. 353-359.
49. M., S.-Y., *REVISION DISC REPLACEMENT SURGERY.* Orthopaedic Proceedings, 2004. **86-B**(SUPP_IV): p. 460-460.
50. Zeegers, W.S., et al., *Artificial disc replacement with the modular type SB Charité III: 2-year results in 50 prospectively studied patients.* Eur Spine J, 1999. **8**(3): p. 210-7.
51. Punt, I.M., et al., *Complications and reoperations of the SB Charité lumbar disc prosthesis: experience in 75 patients.* European spine journal : official publication of the European Spine Society, the European Spinal Deformity Society, and the European Section of the Cervical Spine Research Society, 2008. **17**(1): p. 36-43.
52. Putzier, M., et al., *Charité total disc replacement--clinical and radiographical results after an average follow-up of 17 years.* European spine journal : official publication of the European Spine Society, the European Spinal Deformity Society, and the European Section of the Cervical Spine Research Society, 2006. **15**(2): p. 183-195.

53. Tropiano, P., et al., *Lumbar disc replacement: preliminary results with ProDisc II after a minimum follow-up period of 1 year.* J Spinal Disord Tech, 2003. **16**(4): p. 362-8.
54. Park, S.J., et al., *Long-Term Outcomes Following Lumbar Total Disc Replacement Using ProDisc-II: Average 10-Year Follow-Up at a Single Institute.* Spine (Phila Pa 1976), 2016. **41**(11): p. 971-7.
55. Zigler, J.E. and R.B. Delamarter, *Five-year results of the prospective, randomized, multicenter, Food and Drug Administration investigational device exemption study of the ProDisc-L total disc replacement versus circumferential arthrodesis for the treatment of single-level degenerative disc disease.* J Neurosurg Spine, 2012. **17**(6): p. 493-501.
56. Yue, J.J., R. Garcia, Jr., and L.E. Miller, *The activL(®) Artificial Disc: a next-generation motion-preserving implant for chronic lumbar discogenic pain.* Medical Devices (Auckland, N.Z.), 2016. **9**: p. 75-84.
57. Yue, J.J., et al., *Five-year Results of a Randomized Controlled Trial for Lumbar Artificial Discs in Single-level Degenerative Disc Disease.* Spine (Phila Pa 1976), 2019. **44**(24): p. 1685-1696.
58. Le Huec, J.C., et al., *Clinical results of Maverick lumbar total disc replacement: two-year prospective follow-up.* Orthop Clin North Am, 2005. **36**(3): p. 315-22.
59. Plais, N., et al., *Maverick total disc arthroplasty performs well at 10 years follow-up: a prospective study with HRQL and balance analysis.* Eur Spine J, 2018. **27**(3): p. 720-727.
60. Wigfield, C.C., et al., *The new Frenchay artificial cervical joint: results from a two-year pilot study.* Spine (Phila Pa 1976), 2002. **27**(22): p. 2446-52.
61. Zeng, J., et al., *Clinical and radiographic outcomes of cervical disc arthroplasty with Prestige-LP Disc: a minimum 6-year follow-up study.* BMC Musculoskeletal Disorders, 2018. **19**(1): p. 285.
62. Gornet, M.F., et al., *Cervical disc arthroplasty: 10-year outcomes of the Prestige LP cervical disc at a single level.* Journal of Neurosurgery, 2019. **31**(3): p. 317.
63. Navarro, M., et al., *Biomaterials in orthopaedics.* J R Soc Interface, 2008. **5**(27): p. 1137-58.
64. Hu, C.Y. and T.-R. Yoon, *Recent updates for biomaterials used in total hip arthroplasty.* Biomaterials research, 2018. **22**: p. 33-33.
65. Knight, S.R., R. Aujla, and S.P. Biswas, *Total Hip Arthroplasty - over 100 years of operative history.* Orthopedic reviews, 2011. **3**(2): p. e16-e16.
66. Vital, J.M. and L. Boissiere, *Total disc replacement.* Orthop Traumatol Surg Res, 2014. **100**(1 Suppl): p. S1-14.
67. Villavicencio, A.T., et al., *Spinal Artificial Disc Replacement: Cervical ArthroplastyPart I: History, Design, and Types of Artificial Discs.* Contemporary Neurosurgery, 2007. **29**(12): p. 1-5.
68. Escalas, F., et al., *Biocompatibility of materials for total joint replacement.* Journal of Biomedical Materials Research, 1976. **10**(2): p. 175-195.
69. Lemons, J.E., K.M.W. Niemann, and A.B. Weiss, *Biocompatibility studies on surgical-grade titanium-, cobalt-, and iron-base alloys.* Journal of Biomedical Materials Research. 1976. **10**(4): p. 549-553.
70. Syrett, B.C. and E.E. Davis, *In vivo evaluation of a high-strength, high-ductility stainless steel for use in surgical implants.* Journal of Biomedical Materials Research. 1979. **13**(4): p. 543-556.

71. Chen, Q. and G.A. Thouas, *Metallic implant biomaterials.* Materials Science and Engineering: R: Reports, 2015. **87**: p. 1-57.
72. HUISKES, R., H. WEINANS, and B.V. RIETBERGEN, *The Relationship Between Stress Shielding and Bone Resorption Around Total Hip Stems and the Effects of Flexible Materials.* Clinical Orthopaedics and Related Research, 1992. **274**: p. 124-134.
73. Bauer, T.W. and J. Schils, *The pathology of total joint arthroplasty.* Skeletal Radiology, 1999. **28**(9): p. 483-497.
74. Pham, M.H., et al., *Material Science in Cervical Total Disc Replacement.* BioMed research international, 2015. **2015**: p. 719123-719123.
75. Bra-nemark, P.-I., et al., *Tissue-Integrated Prostheses. Osseointegration in Clinical Dentistry.* Journal of Plastic and Reconstructive Surgery, 1986. **77**(3): p. 496-497.
76. Warburton, A., et al., *Biomaterials in Spinal Implants: A Review.* Neurospine, 2020. **17**(1): p. 101-110.
77. Hussein, M.A., A.S. Mohammed, and N. Al-Aqeeli, *Wear Characteristics of Metallic Biomaterials: A Review.* Materials, 2015. **8**(5): p. 2749-2768.
78. Merola, M. and S. Affatato, *Materials for Hip Prostheses: A Review of Wear and Loading Considerations.* Materials (Basel, Switzerland), 2019. **12**(3): p. 495.
79. Katti, K.S., *Biomaterials in total joint replacement.* Colloids and Surfaces B: Biointerfaces, 2004. **39**(3): p. 133-142.
80. Hallab, N., H.D. Link, and P.C. McAfee, *Biomaterial optimization in total disc arthroplasty.* Spine (Phila Pa 1976), 2003. **28**(20): p. S139-52.
81. Brach Del Prever, E.M., et al., *UHMWPE for arthroplasty: past or future?* Journal of orthopaedics and traumatology : official journal of the Italian Society of Orthopaedics and Traumatology, 2009. **10**(1): p. 1-8.
82. Galvin, A., et al., *Wear of crosslinked polyethylene under different tribological conditions.* J Mater Sci Mater Med, 2006. **17**(3): p. 235-43.
83. Muratoglu, O.K., *The comparison of the wear behavior of four different types of crosslinked acetabular components.* J Orthop Res, 2001. **19**(6): p. 1210.
84. Galvin, A.L., et al., *Nanometre size wear debris generated from crosslinked and non-crosslinked ultra high molecular weight polyethylene in artificial joints.* Wear, 2005. **259**(7): p. 977-983.
85. Kurtz, S.M. and J.N. Devine, *PEEK biomaterials in trauma, orthopedic, and spinal implants.* Biomaterials, 2007. **28**(32): p. 4845-4869.
86. Brantigan, J.W. and A.D. Steffee, *A carbon fiber implant to aid interbody lumbar fusion. Two-year clinical results in the first 26 patients.* Spine (Phila Pa 1976), 1993. **18**(14): p. 2106-7.
87. McEntire, B.J., et al., *Ceramics and ceramic coatings in orthopaedics.* Journal of the European Ceramic Society, 2015. **35**(16): p. 4327-4369.
88. Sorrell, C., et al., *Results of 15-year clinical study of reaction bonded silicon nitride intervertebral spacers.* Transactions - 7th World Biomaterials Congress, 2004.
89. Taylor, R.M., et al., *Silicon nitride: A new material for spinal implants.* J. Bone Jt. Surg., 2010. **92**.
90. Jin, Z., et al., *(v) Biotribology.* Current Orthopaedics, 2006. **20**(1): p. 32-40.
91. Nine, M.J., et al., *Wear Debris Characterization and Corresponding Biological Response: Artificial Hip and Knee Joints.* Materials (Basel), 2014. **7**(2): p. 980-1016.

92. Jin, Z.M., et al., *Tribology of medical devices.* Biosurface and Biotribology, 2016. **2**(4): p. 173-192.
93. St. John, K.R., L.D. Zardiackas, and R.A. Poggie, *Wear evaluation of cobalt–chromium alloy for use in a metal-on-metal hip prosthesis.* Journal of Biomedical Materials Research Part B, 2004. **68B**(1): p. 1-14.
94. Gibon, E., et al., *The biological response to orthopaedic implants for joint replacement: Part I: Metals.* Journal of Biomedical Materials Research Part B, 2017. **105**(7): p. 2162-2173.
95. Chiu, A., et al., *Review of Chromium (VI) Apoptosis, Cell-Cycle-Arrest, and Carcinogenesis.* Journal of Environmental Science and Health, Part C, 2010. **28**(3): p. 188-230.
96. Amanatullah, D., et al., *Metal in Total Hip Arthroplasty: Wear Particles, Biology, and Diagnosis.* Orthopedics, 2016. **39**.
97. Savarino, L., et al., *Ion release in patients with metal-on-metal hip bearings in total joint replacement: A comparison with metal-on-polyethylene bearings.* Journal of Biomedical Materials Research, 2002. **63**(5): p. 467-474.
98. Doorn, P.F., P.A. Campbell, and H.C. Amstutz, *Metal Versus Polyethylene Wear Particles in Total Hip Replacements: A Review.* Clinical Orthopaedics and Related Research, 1996. **329**: p. S206-S216.
99. Doorn, P.F., et al., *Metal wear particle characterization from metal on metal total hip replacements: Transmission electron microscopy study of periprosthetic tissues and isolated particles.* Journal of Biomedical Materials Research, 1998. **42**(1): p. 103-111.
100. Firkins, P.J., et al., *Quantitative analysis of wear debris from metal on metal hip prosthesis tested in a physiological hip joint simulator.* Bio-medical materials and engineering, 2001. **11**: p. 143-57.
101. Hallab, N.J., *A review of the biologic effects of spine implant debris: Fact from fiction.* SAS journal, 2009. **3**(4): p. 143-160.
102. Paré, P.E., F.W. Chan, and M.L. Powell, *Wear characterization of the A-MAV™ anterior motion replacement using a spine wear simulator.* Wear, 2007. **263**(7): p. 1055-1059.
103. Pasko, K.M., *Ceramic Coatings for Cervical Total Disc Replacement*. 2017: University of Leeds (School of Mechanical Engineering).
104. Catelas, I., et al., *Comparison of in vitro with in vivo characteristics of wear particles from metal–metal hip implants.* Journal of Biomedical Materials Research Part B: Applied Biomaterials 2004. **70B**(2): p. 167-178.
105. Reeks, J. and H. Liang, *Materials and Their Failure Mechanisms in Total Disc Replacement.* Lubricants, 2015. **3**: p. 346-364.
106. Kurtz, S.M., et al., *Polyethylene wear and rim fracture in total disc arthroplasty.* The Spine Journal, 2007. **7**(1): p. 12-21.
107. Wang, A., et al., *Lubrication and wear of ultra-high molecular weight polyethylene in total joint replacements.* Tribology International, 1998. **31**(1): p. 17-33.
108. Ingham, E. and J. Fisher, *Biological reactions to wear debris in total joint replacement.* Proc Inst Mech Eng H, 2000. **214**(1): p. 21-37.
109. Eckold, D.G., K. Dearn, and D.E.T. Shepherd, *The evolution of polymer wear debris from total disc arthroplasty.* Biotribology, 2015. **94**.
110. Liu, A., et al., *The biological response to nanometre-sized polymer particles.* Acta Biomater, 2015. **23**: p. 38-51.

111. Maloney, W.J., et al., *Isolation and characterization of wear particles generated in patients who have had failure of a hip arthroplasty without cement.* J Bone Joint Surg Am, 1995. **77**(9): p. 1301-10.
112. Campbell, P., et al., *Isolation of predominantly submicron-sized UHMWPE wear particles from periprosthetic tissues.* J Biomed Mater Res, 1995. **29**(1): p. 127-31.
113. Margevicius, K.J., et al., *Isolation and characterization of debris in membranes around total joint prostheses.* J Bone Joint Surg Am, 1994. **76**(11): p. 1664-75.
114. Tipper, J.L., et al., *Quantitative analysis of polyethylene wear debris, wear rate and head damage in retrieved Charnley hip prostheses.* Journal of Materials Science: Materials in Medicine, 2000. **11**(2): p. 117-124.
115. Scott, M., et al., *Wear particle analyses of conventional and crosslinked UHMWPE tested in an anatomic hip simulator.* Trans Orthop Res Soc, 2001. **26**: p. 1.
116. Endo, M., et al., *Comparison of wear, wear debris and functional biological activity of moderately crosslinked and non-crosslinked polyethylenes in hip prostheses.* Proc Inst Mech Eng H, 2002. **216**(2): p. 111-22.
117. Baxter, R.M., et al., *Characteristics of highly cross-linked polyethylene wear debris in vivo.* Journal of biomedical materials research. Part B, Applied biomaterials, 2013. **101**(3): p. 467-475.
118. Iwakiri, K., et al., *In vivo comparison of wear particles between highly crosslinked polyethylene and conventional polyethylene in the same design of total knee arthroplasties.* J Biomed Mater Res B Appl Biomater, 2009. **91**(2): p. 799-804.
119. Liu, A., et al., *Generation of a large volume of clinically relevant nanometre-sized ultra-high-molecular-weight polyethylene wear particles for cell culture studies.* Proc Inst Mech Eng H, 2014. **228**(4): p. 418-26.
120. Tipper, J.L., et al., *Isolation and characterization of UHMWPE wear particles down to ten nanometers in size from in vitro hip and knee joint simulators.* J Biomed Mater Res A, 2006. **78**(3): p. 473-80.
121. Lapcikova, M., et al., *Nanometer size wear debris generated from ultra high molecular weight polyethylene in vivo.* Wear, 2009. **266**(1): p. 349-355.
122. Koseki, H., et al., *Analysis of polyethylene particles isolated from periprosthetic tissue of loosened hip arthroplasty and comparison with radiographic appearance.* J Orthop Sci, 2005. **10**(3): p. 284-90.
123. Richards, L., et al., *Identification of nanometre-sized ultra-high molecular weight polyethylene wear particles in samples retrieved in vivo.* J Bone Joint Surg Br, 2008. **90**(8): p. 1106-13.
124. Visentin, M., et al., *A new method for isolation of polyethylene wear debris from tissue and synovial fluid.* Biomaterials, 2004. **25**(24): p. 5531-7.
125. Punt, I., et al., *Submicron sized ultra-high molecular weight polyethylene wear particle analysis from revised SB Charité III total disc replacements.* Acta Biomater, 2011. **7**(9): p. 3404-11.
126. Williams, P. and I. Clarke, *Ceramic Wear Debris in Total Joint Replacements: Review of Debris Morphology and Biological Response.* Key Engineering Materials - KEY ENG MAT, 2002. **218-220**: p. 591-594.
127. Kummer, F.J., S.A. Stuchin, and V.H. Frankel, *Analysis of removed autophor ceramic-on-ceramic components.* J Arthroplasty, 1990. **5**(1): p. 28-33.
128. Henssge, E.J., I. Bos, and G. Willmann, *Al2O3 against Al2O3 combination in hip endoprostheses. Histologic investigations with semiquantitative grading of*

revision and autopsy cases and abrasion measures. Journal of Materials Science: Materials in Medicine, 1994. **5**(9): p. 657-661.
129. Lerouge, S., et al., *Ceramic-ceramic and metal-polyethylene total hip replacements: comparison of pseudomembranes after loosening.* J Bone Joint Surg Br, 1997. **79**(1): p. 135-9.
130. Yoon, T.R., et al., *Osteolysis in association with a total hip arthroplasty with ceramic bearing surfaces.* J Bone Joint Surg Am, 1998. **80**(10): p. 1459-68.
131. Hatton, A., et al., *Alumina-alumina artificial hip joints. Part I: a histological analysis and characterisation of wear debris by laser capture microdissection of tissues retrieved at revision.* Biomaterials, 2002. **23**(16): p. 3429-40.
132. Tipper, J.L., et al., *Characterisation of wear debris from UHMWPE on zirconia ceramic, metal-on-metal and alumina ceramic-on-ceramic hip prostheses generated in a physiological anatomical hip joint simulator.* Wear, 2001. **250**(1): p. 120-128.
133. Imran, A., et al., *Characterisation and biocompatibility of composite ceramic particles used to manufacture ceramic-on-ceramic total hip replacements.* Frontiers in Bioengineering and Biotechnology, 2016. **4**.
134. Asif, I.M. *Characterisation and Biological Impact of Wear Particles from Composite Ceramic Hip Replacements*. 2018.
135. Stratton-Powell, A.A., et al., *The Biologic Response to Polyetheretherketone (PEEK) Wear Particles in Total Joint Replacement: A Systematic Review.* Clin Orthop Relat Res, 2016. **474**(11): p. 2394-2404.
136. Hatton, A., et al., *Effects of clinically relevant alumina ceramic wear particles on TNF-alpha production by human peripheral blood mononuclear phagocytes.* Biomaterials, 2003. **24**(7): p. 1193-204.
137. Guyer, R.D., et al., *Early failure of metal-on-metal artificial disc prostheses associated with lymphocytic reaction: diagnosis and treatment experience in four cases.* Spine (Phila Pa 1976), 2011. **36**(7): p. E492-7.
138. Oliveira, C.A., et al., *Metallosis: A diagnosis not only in patients with metal-on-metal prostheses.* European journal of radiology open, 2014. **2**: p. 3-6.
139. Drummond, J., P. Tran, and C. Fary, *Metal-on-Metal Hip Arthroplasty: A Review of Adverse Reactions and Patient Management.* Journal of functional biomaterials, 2015. **6**(3): p. 486-499.
140. Lohmann, C.H., et al., *Metallic debris from metal-on-metal total hip arthroplasty regulates periprosthetic tissues.* World journal of orthopedics, 2014. **5**(5): p. 660-666.
141. Miloŝev, L., et al., *Extensive metallosis and necrosis in failed prostheses with cemented titanium-alloy stems and ceramic heads.* J Bone Joint Surg Br, 2000. **82**(3): p. 352-7.
142. Aroukatos, P., et al., *Immunologic adverse reaction associated with low-carbide metal-on-metal bearings in total hip arthroplasty.* Clinical orthopaedics and related research, 2010. **468**(8): p. 2135-2142.
143. Mahendra, G., et al., *Necrotic and inflammatory changes in metal-on-metal resurfacing hip arthroplasties.* Acta orthopaedica, 2009. **80**(6): p. 653-659.
144. Agins, H.J., et al., *Metallic wear in failed titanium-alloy total hip replacements. A histological and quantitative analysis.* J Bone Joint Surg Am, 1988. **70**(3): p. 347-56.
145. Buly, R.L., et al., *Titanium wear debris in failed cemented total hip arthroplasty. An analysis of 71 cases.* J Arthroplasty, 1992. **7**(3): p. 315-23.

146. Winter, G.D., *Tissue reaction to metallic wear and corrosion products in human patients.* Journal of Biomedical Materials Research, 1974. **8**(3): p. 11-26.
147. S., H.F., et al., *Metal-on-metal bearings.* The Journal of Bone and Joint Surgery, 2011. **93-B**(5): p. 572-579.
148. Taksali, S., J.N. Grauer, and A.R. Vaccaro, *Material considerations for intervertebral disc replacement implants.* The Spine Journal, 2004. **4**(6, Supplement): p. S231-S238.
149. Hallab, N.J. and J.J. Jacobs, *Biologic effects of implant debris.* Bull NYU Hosp Jt Dis, 2009. **67**(2): p. 182-8.
150. Sukur, E., et al., *Particle Disease: A Current Review of the Biological Mechanisms in Periprosthetic Osteolysis After Hip Arthroplasty.* The open orthopaedics journal, 2016. **10**: p. 241-251.
151. Hallab, N.J., B.W. Cunningham, and J.J. Jacobs, *Spinal implant debris-induced osteolysis.* Spine (Phila Pa 1976), 2003. **28**(20): p. S125-38.
152. Kandahari, A.M., et al., *A review of UHMWPE wear-induced osteolysis: the role for early detection of the immune response.* Bone research, 2016. **4**: p. 16014-16014.
153. Revell, P.A., et al., *The production and biology of polyethylene wear debris.* Arch Orthop Trauma Surg, 1978. **91**(3): p. 167-81.
154. Mirra, J.M., R.A. Marder, and H.C. Amstutz, *The pathology of failed total joint arthroplasty.* Clin Orthop Relat Res, 1982(170): p. 175-83.
155. Ingham, E. and J. Fisher, *The role of macrophages in osteolysis of total joint replacement.* Biomaterials, 2005. **26**(11): p. 1271-86.
156. Schmalzried, T.P., M. Jasty, and W.H. Harris, *Periprosthetic bone loss in total hip arthroplasty. Polyethylene wear debris and the concept of the effective joint space.* JBJS, 1992. **74**(6): p. 849-863.
157. Benz, E.B., et al., *Transmission electron microscopy of intracellular particles of polyethylene from joint replacement prostheses: size distribution and cellular response.* Biomaterials, 2001. **22**(21): p. 2835-2842.
158. Pazzaglia, U.E., C. Dell'Orbo, and M.J. Wilkinson, *The foreign body reaction in total hip arthroplasties. A correlated light-microscopy, SEM, and TEM study.* Arch Orthop Trauma Surg, 1987. **106**(4): p. 209-19.
159. Murray, D.W. and N. Rushton, *Macrophages stimulate bone resorption when they phagocytose particles.* J Bone Joint Surg Br, 1990. **72**(6): p. 988-92.
160. Goodman, S.B., et al., *Cellular profile and cytokine production at prosthetic interfaces. Study of tissues retrieved from revised hip and knee replacements.* J Bone Joint Surg Br, 1998. **80**(3): p. 531-9.
161. Granchi, D., et al., *Bone-resorbing cytokines in serum of patients with aseptic loosening of hip prostheses.* J Bone Joint Surg Br, 1998. **80**(5): p. 912-7.
162. Shanbhag, A.S., et al., *Human monocyte response to particulate biomaterials generated in vivo and in vitro.* Journal of Orthopaedic Research, 1995. **13**(5): p. 792-801.
163. Green, T.R., et al., *Effect of size and dose on bone resorption activity of macrophages by in vitro clinically relevant ultra high molecular weight polyethylene particles.* J Biomed Mater Res, 2000. **53**(5): p. 490-7.
164. Ingram, J.H., et al., *The influence of molecular weight, crosslinking and counterface roughness on TNF-alpha production by macrophages in response to ultra high molecular weight polyethylene particles.* Biomaterials, 2004. **25**(17): p. 3511-3522.

165. Illgen, R.L., 2nd, et al., *Highly crosslinked vs conventional polyethylene particles--an in vitro comparison of biologic activities.* J Arthroplasty, 2008. **23**(5): p. 721-31.
166. Veruva, S.Y., et al., *Periprosthetic UHMWPE Wear Debris Induces Inflammation, Vascularization, and Innervation After Total Disc Replacement in the Lumbar Spine.* Clin Orthop Relat Res, 2017. **475**(5): p. 1369-1381.
167. Hernigou, P., et al., *Ceramic-ceramic bearing decreases osteolysis: a 20-year study versus ceramic-polyethylene on the contralateral hip.* Clinical orthopaedics and related research, 2009. **467**(9): p. 2274-2280.
168. Huo, M.H., et al., *Cementless total hip arthroplasties using ceramic-on-ceramic articulation in young patients: A minimum 5-year follow-up study.* The Journal of Arthroplasty, 1996. **11**(6): p. 673-678.
169. Li, Y., et al., *An approach to quantifying 3D responses of cells to extreme strain.* Sci Rep, 2016. **6**: p. 19550.
170. Li, J., et al., *Evaluation of biocompatibility of various ceramic powders with human fibroblasts in vitro.* Clin Mater, 1993. **12**(4): p. 197-201.
171. Kim, K.J., Itoh, T., Kumegawa, M., *Soluble factors from rabbit synovial cells in response to alumina particles stimulate osteoclast mediated bone resorption.* In Proceedings of the 45th Annual Meeting of the Orthpaedic Research Society, 1999: p. 25.
172. Meachim, G. and G. Brooke, *The synovial response to intra-articular Co-Cr-Mo particles in Guinea Pigs.* Biomaterials, 1983. **4**(3): p. 153-159.
173. Papageorgiou, I., et al., *Biological Effects of Clinically Relevant CoCr Nanoparticles in the Dura Mater: An Organ Culture Study.* Nanomaterials (Basel, Switzerland), 2014. **4**(2): p. 485-504.
174. Kekere, V. and K. Alsayouri, *Anatomy, Head and Neck, Dura Mater*, in *StatPearls*. 2020, StatPearls Publishing Copyright © 2020, StatPearls Publishing LLC.: Treasure Island (FL).
175. Cunningham, B.W., et al., *The effect of titanium particulate on development and maintenance of a posterolateral spinal arthrodesis: an in vivo rabbit model.* Spine (Phila Pa 1976), 2002. **27**(18): p. 1971-81.
176. Cunningham, B.W., et al., *Epidural application of spinal instrumentation particulate wear debris: a comprehensive evaluation of neurotoxicity using an in vivo animal model.* J Neurosurg Spine, 2013. **19**(3): p. 336-50.
177. Bracken, M.B., *Why animal studies are often poor predictors of human reactions to exposure.* Journal of the Royal Society of Medicine, 2009. **102**(3): p. 120-122.
178. Langlois, J. and M. Hamadouche, *New animal models of wear-particle osteolysis.* International orthopaedics, 2011. **35**(2): p. 245-251.
179. Hopkins, A.M., et al., *3D in vitro modeling of the central nervous system.* Progress in neurobiology, 2015. **125**: p. 1-25.
180. Wiatrak, B., et al., *PC12 Cell Line: Cell Types, Coating of Culture Vessels, Differentiation and Other Culture Conditions.* Cells, 2020. **9**(4): p. 958.
181. Kraus, D., et al., *The Neuro-spheroid—A novel 3D in vitro model for peripheral nerve regeneration.* Journal of Neuroscience Methods, 2015. **246**: p. 97-105.
182. Daud, M.F., et al., *An aligned 3D neuronal-glial co-culture model for peripheral nerve studies.* Biomaterials, 2012. **33**(25): p. 5901-13.
183. de Guzman, R.C. and P.J. VandeVord, *Variations in astrocyte and fibroblast response due to biomaterial particulates in vitro.* J Biomed Mater Res A, 2008. **85**(1): p. 14-24.

184. Duval, K., et al., *Modeling Physiological Events in 2D vs. 3D Cell Culture.* Physiology 2017. **32**(4): p. 266-277.
185. Kapałczyńska, M., et al., *2D and 3D cell cultures - a comparison of different types of cancer cell cultures.* Archives of medical science : AMS, 2018. **14**(4): p. 910-919.
186. Chitcholtan, K., et al., *Differences in growth properties of endometrial cancer in three dimensional (3D) culture and 2D cell monolayer.* Exp Cell Res, 2013. **319**(1): p. 75-87.
187. Price, K.J., et al., *Matrigel basement membrane matrix influences expression of microRNAs in cancer cell lines.* Biochem Biophys Res Commun, 2012. **427**(2): p. 343-8.
188. Centeno, E.G.Z., H. Cimarosti, and A. Bithell, *2D versus 3D human induced pluripotent stem cell-derived cultures for neurodegenerative disease modelling.* Molecular Neurodegeneration, 2018. **13**(1): p. 27.
189. Abbott, A., *Biology's new dimension.* Nature, 2003. **424**(6951): p. 870-872.
190. Joseph, J., T. Malindisa, and M. Ntwasa, *Two-Dimensional (2D) and Three-Dimensional (3D) Cell Culturing in Drug Discovery* in *Cell Culture*. 2019, IntechOpen.
191. Breslin, S. and L. O'Driscoll, *Three-dimensional cell culture: the missing link in drug discovery.* Drug Discov Today, 2013. **18**(5-6): p. 240-9.
192. Edmondson, R., et al., *Three-dimensional cell culture systems and their applications in drug discovery and cell-based biosensors.* Assay and drug development technologies, 2014. **12**(4): p. 207-218.
193. Spedden, E., et al., *Elasticity maps of living neurons measured by combined fluorescence and atomic force microscopy.* Biophysical journal, 2012. **103**(5): p. 868-877.
194. Karimi, A., A. Shojaei, and P. Tehrani, *Mechanical properties of the human spinal cord under the compressive loading.* J Chem Neuroanat, 2017. **86**: p. 15-18.
195. Chang, G.-L., T.-K. Hung, and W.W. Feng, *An In-Vivo Measurement and Analysis of Viscoelastic Properties of the Spinal Cord of Cats.* Journal of Biomechanical Engineering, 1988. **110**(2): p. 115-122.
196. Balgude, A.P., et al., *Agarose gel stiffness determines rate of DRG neurite extension in 3D cultures.* Biomaterials, 2001. **22**(10): p. 1077-1084.
197. Hopkins, A.M., et al., *Silk Hydrogels as Soft Substrates for Neural Tissue Engineering.* Advanced Functional Materials, 2013. **23**(41): p. 5140-5149.
198. Man, A.J., et al., *Neurite outgrowth in fibrin gels is regulated by substrate stiffness.* Tissue Eng Part A, 2011. **17**(23-24): p. 2931-42.
199. O'Brien, F.J., *Biomaterials & scaffolds for tissue engineering.* Materials Today, 2011. **14**(3): p. 88-95.
200. Ko, H.C., B.K. Milthorpe, and C.D. McFarland, *Engineering thick tissues--the vascularisation problem.* Eur Cell Mater, 2007. **14**: p. 1-18; discussion 18-9.
201. Tibbitt, M.W. and K.S. Anseth, *Hydrogels as extracellular matrix mimics for 3D cell culture.* Biotechnology and bioengineering, 2009. **103**(4): p. 655-663.
202. Ravi, M., et al., *3D Cell Culture Systems: Advantages and Applications.* Journal of Cellular Physiology 2015. **230**(1): p. 16-26.
203. Dong, C. and Y. Lv, *Application of Collagen Scaffold in Tissue Engineering: Recent Advances and New Perspectives.* Polymers, 2016. **8**(2): p. 42.
204. Yuan, Z., et al., *Development of a 3D Collagen Model for the In Vitro Evaluation of Magnetic-assisted Osteogenesis.* Scientific Reports, 2018. **8**(1): p. 16270.

205. Krewson, C.E., et al., *Cell aggregation and neurite growth in gels of extracellular matrix molecules.* Biotechnology & Bioengineering, 1994. **43**(7): p. 555-562.
206. Zhou, W., et al., *Comparison of neurite growth in three dimensional natural and synthetic hydrogels.* Journal of Biomaterials Science, Polymer Edition, 2013. **24**(3): p. 301-314.
207. Watanabe, K., et al., *Establishment of three-dimensional culture of neural stem/progenitor cells in collagen Type-1 Gel.* Restorative Neurology and Neuroscience, 2007. **25**: p. 109-117.
208. Huang, F., Q. Shen, and J. Zhao, *Growth and differentiation of neural stem cells in a three-dimensional collagen gel scaffold.* Neural regeneration research, 2013. **8**(4): p. 313-319.
209. East, E., J.P. Golding, and J.B. Phillips, *A versatile 3D culture model facilitates monitoring of astrocytes undergoing reactive gliosis.* Journal of Tissue Engineering and Regenerative Medicine, 2009. **3**(8): p. 634-646.
210. Caliari, S.R. and J.A. Burdick, *A practical guide to hydrogels for cell culture.* Nature Methods, 2016. **13**(5): p. 405-414.
211. Pedron, S., E. Becka, and B.A.C. Harley, *Regulation of glioma cell phenotype in 3D matrices by hyaluronic acid.* Biomaterials, 2013. **34**(30): p. 7408-7417.
212. Seidlits, S.K., et al., *The effects of hyaluronic acid hydrogels with tunable mechanical properties on neural progenitor cell differentiation.* Biomaterials, 2010. **31**(14): p. 3930-3940.
213. Dicker, K.T., et al., *Hyaluronan: a simple polysaccharide with diverse biological functions.* Acta Biomaterialia, 2014. **10**(4): p. 1558-1570.
214. Frampton, J.P., et al., *Fabrication and optimization of alginate hydrogel constructs for use in 3D neural cell culture.* Biomed Mater, 2011. **6**(1): p. 015002.
215. Marina, M., et al., *Novel Soft Alginate Hydrogel Strongly Supports Neurite Growth and Protects Neurons Against Oxidative Stress.* Tissue Engineering Part A, 2012. **18**(1-2): p. 55-66.
216. Wang, C., X. Tong, and F. Yang, *Bioengineered 3D brain tumor model to elucidate the effects of matrix stiffness on glioblastoma cell behavior using PEG-based hydrogels.* Mol Pharm, 2014. **11**(7): p. 2115-25.
217. Kong, X.-B., et al., *Polyethylene glycol as a promising synthetic material for repair of spinal cord injury.* Neural Regeneration Research, 2017. **12**(6): p. 1003-1008.
218. Zhu, J., *Bioactive modification of poly(ethylene glycol) hydrogels for tissue engineering.* Biomaterials, 2010. **31**(17): p. 4639-4656.
219. Rao, S.S., N. Han, and J.O. Winter, *Polylysine-Modified PEG-Based Hydrogels to Enhance the Neuro–Electrode Interface.* Journal of Biomaterials Science, Polymer Edition, 2011. **22**(4-6): p. 611-625.
220. Yue, K., et al., *Synthesis, properties, and biomedical applications of gelatin methacryloyl (GelMA) hydrogels.* Biomaterials, 2015. **73**: p. 254-271.
221. Zhu, M., et al., *Gelatin methacryloyl and its hydrogels with an exceptional degree of controllability and batch-to-batch consistency.* Scientific Reports, 2019. **9**(1): p. 6863.
222. Sun, M., et al. *Synthesis and Properties of Gelatin Methacryloyl (GelMA) Hydrogels and Their Recent Applications in Load-Bearing Tissue*. Polymers, 2018. **10**, DOI: 10.3390/polym10111290.

223. Lin, R.Z., et al., *Transdermal regulation of vascular network bioengineering using a photopolymerizable methacrylated gelatin hydrogel.* Biomaterials, 2013. **34**(28): p. 6785-96.
224. Choi, J.R., et al., *Recent advances in photo-crosslinkable hydrogels for biomedical applications.* BioTechniques, 2019. **66**(1): p. 40-53.
225. Wu, Y., et al., *The influence of the stiffness of GelMA substrate on the outgrowth of PC12 cells.* Bioscience reports, 2019. **39**(1): p. BSR20181748.
226. Zhu, W., B.T. Harris, and L.G. Zhang. *Gelatin methacrylamide hydrogel with graphene nanoplatelets for neural cell-laden 3D bioprinting*. in *2016 38th Annual International Conference of the IEEE Engineering in Medicine and Biology Society (EMBC)*. 2016.
227. Fan, L., et al., *Directing Induced Pluripotent Stem Cell Derived Neural Stem Cell Fate with a Three-Dimensional Biomimetic Hydrogel for Spinal Cord Injury Repair.* ACS Applied Materials & Interfaces, 2018. **10**(21): p. 17742-17755.
228. Bishop, E.S., et al., *3-D bioprinting technologies in tissue engineering and regenerative medicine: Current and future trends.* Genes & Diseases, 2017. **4**(4): p. 185-195.
229. Yu, J., et al., *Current Advances in 3D Bioprinting Technology and Its Applications for Tissue Engineering.* 2020. **12**.
230. Heinrich, M.A., et al., *3D Bioprinting: from Benches to Translational Applications.* Small, 2019. **15**(23): p. e1805510.
231. Ozbolat, I.T. and M. Hospodiuk, *Current advances and future perspectives in extrusion-based bioprinting.* Biomaterials, 2016. **76**: p. 321-343.
232. Gillispie, G., et al., *Assessment methodologies for extrusion-based bioink printability.* Biofabrication, 2020. **12**(2): p. 022003-022003.
233. Urban, J.P.G. and S. Roberts, *Degeneration of the intervertebral disc.* Arthritis Res Ther, 2003. **5**(3): p. 120.
234. Peng, B. and M.J. DePalma, *Cervical disc degeneration and neck pain.* Journal of pain research, 2018. **11**: p. 2853-2857.
235. Bai, D.-y., et al., *Total disc replacement versus fusion for lumbar degenerative diseases - a meta-analysis of randomized controlled trials.* Medicine, 2019. **98**(29): p. e16460.
236. Wu, H., Q. Pang, and G. Jiang, *Medium-term effects of Dynesys dynamic stabilization versus posterior lumbar interbody fusion for treatment of multisegmental lumbar degenerative disease.* The Journal of international medical research, 2017. **45**(5): p. 1562-1573.
237. Lee, Y.C., M.G.T. Zotti, and O.L. Osti, *Operative Management of Lumbar Degenerative Disc Disease.* Asian spine journal, 2016. **10**(4): p. 801-819.
238. Zhang, Y., et al., *Comparison of the Dynesys Dynamic Stabilization System and Posterior Lumbar Interbody Fusion for Lumbar Degenerative Disease.* PloS one, 2016. **11**(1): p. e0148071-e0148071.
239. Salzmann, S.N., et al., *Lumbar disc replacement surgery-successes and obstacles to widespread adoption.* Current reviews in musculoskeletal medicine, 2017. **10**(2): p. 153-159.
240. Vital, J.M. and L. Boissière, *Total disc replacement.* Orthopaedics & Traumatology: Surgery & Research, 2014. **100**(1, Supplement): p. S1-S14.
241. Frelinghuysen, P., et al., *Lumbar Total Disc Replacement Part I: Rationale, Biomechanics, and Implant Types.* Orthopedic Clinics of North America, 2005. **36**(3): p. 293-299.

242. Coban, D., et al., *161. Metal-on-metal vs metal-on-plastic artificial discs in 2-level anterior cervical disc replacement: a meta-analysis with follow up of 5 years or more.* The Spine Journal, 2021. **21**(9, Supplement): p. S81.
243. Burns, P.B., R.J. Rohrich, and K.C. Chung, *The levels of evidence and their role in evidence-based medicine.* Plastic and reconstructive surgery, 2011. **128**(1): p. 305-310.
244. Radcliff, K., et al., *Final Long-Term Reporting from a Randomized Controlled IDE Trial for Lumbar Artificial Discs in Single-Level Degenerative Disc Disease: 7-Year Results.* Int J Spine Surg, 2021. **15**(4): p. 612-632.
245. Formica, C., et al., *Total disc replacement for lumbar degenerative disc disease: single centre 20 years experience.* Eur Spine J, 2020. **29**(7): p. 1518-1526.
246. Guyer, R.D., et al., *Five-Year Follow-Up of a Prospective, Randomized Trial Comparing Two Lumbar Total Disc Replacements.* Spine (Phila Pa 1976), 2016. **41**(1): p. 3-8.
247. Aghayev, E., et al., *Five-year results of lumbar disc prostheses in the SWISSspine registry.* Eur Spine J, 2014. **23**(10): p. 2114-26.
248. Sköld, C., H. Tropp, and S. Berg, *Five-year follow-up of total disc replacement compared to fusion: a randomized controlled trial.* Eur Spine J, 2013. **22**(10): p. 2288-95.
249. Kitzen, J., et al., *Long-term clinical outcome of the Charité III total lumbar disc replacement.* Eur Spine J, 2020. **29**(7): p. 1527-1535.
250. Scott-Young, M., et al., *Patient-Reported Outcome Measures After Multilevel Lumbar Total Disc Arthroplasty for the Treatment of Multilevel Degenerative Disc Disease.* Spine (Phila Pa 1976), 2020. **45**(1): p. 18-25.
251. Lu, S., et al., *Long-term clinical results following Charite III lumbar total disc replacement.* Spine J, 2018. **18**(6): p. 917-925.
252. Wuertinger, C., et al., *Motion preservation following total lumbar disc replacement at the lumbosacral junction: a prospective long-term clinical and radiographic investigation.* Spine J, 2018. **18**(1): p. 72-80.
253. Furunes, H., et al., *Total disc replacement versus multidisciplinary rehabilitation in patients with chronic low back pain and degenerative discs: 8-year follow-up of a randomized controlled multicenter trial.* Spine J, 2017. **17**(10): p. 1480-1488.
254. Laugesen, L.A., et al., *Patient-reported Outcomes and Revision Rates at a Mean Follow-up of 10 Years After Lumbar Total Disc Replacement.* Spine (Phila Pa 1976), 2017. **42**(21): p. 1657-1663.
255. Park, S.J., et al., *Long-Term Outcomes Following Lumbar Total Disc Replacement Using ProDisc-II: Average 10-Year Follow-Up at a Single Institute.* Spine (Phila Pa 1976), 2016. **41**(11): p. 971-977.
256. Lu, S.B., et al., *An 11-year minimum follow-up of the Charite III lumbar disc replacement for the treatment of symptomatic degenerative disc disease.* Eur Spine J, 2015. **24**(9): p. 2056-64.
257. Siepe, C.J., et al., *Mid- to long-term results of total lumbar disc replacement: a prospective analysis with 5- to 10-year follow-up.* Spine J, 2014. **14**(8): p. 1417-31.
258. Balderston, J.R., et al., *Long-term Outcomes of 2-Level Total Disc Replacement Using ProDisc-L: Nine- to 10-Year Follow-up.* Spine (Phila Pa 1976), 2014. **39**(11): p. 906-910.

259. Yue, J., et al., *A comparison of patients who have undergone 1-Level versus 2-Level ProDisc arthroplasty: a prospective study with minimum of 5-year follow-up.* Spine (Phila Pa 1976), 2013. **38**(14): p. 1194-8.
260. Meir, A.R., et al., *Ten-year survival and clinical outcome of the AcroFlex lumbar disc replacement for the treatment of symptomatic disc degeneration.* The Spine Journal, 2013. **13**(1): p. 13-21.
261. Guyer, R.D., I. Thongtrangan, and D.D. Ohnmeiss, *Outcomes of CHARITE Lumbar Artificial Disk versus Fusion: 5-Year Data.* Seminars in Spine Surgery, 2012. **24**(1): p. 32-36.
262. Park, C.K., et al., *Clinical outcome of lumbar total disc replacement using ProDisc-L in degenerative disc disease: minimum 5-year follow-up results at a single institute.* Spine (Phila Pa 1976), 2012. **37**(8): p. 672-7.
263. Mehra, A., et al., *Oswestry Disability Index scoring made easy.* Annals of the Royal College of Surgeons of England, 2008. **90**(6): p. 497-499.
264. Prakash, B., *Patient satisfaction.* Journal of cutaneous and aesthetic surgery, 2010. **3**(3): p. 151-155.
265. Fan, H., et al., *Comparison of Functional Outcome and Quality of Life in Patients With Idiopathic Scoliosis Treated by Spinal Fusion.* Medicine (Baltimore), 2016. **95**(19): p. e3289.
266. Nie, H., et al., *Comparison of Total Disc Replacement with lumbar fusion: a meta-analysis of randomized controlled trials.* J Coll Physicians Surg Pak, 2015. **25**(1): p. 60-7.
267. Jacobs, W., et al., *Total disc replacement for chronic back pain in the presence of disc degeneration.* Cochrane Database Syst Rev, 2012(9): p. Cd008326.
268. Wei, J., et al., *Comparison of artificial total disc replacement versus fusion for lumbar degenerative disc disease: a meta-analysis of randomized controlled trials.* International orthopaedics, 2013. **37**(7): p. 1315-1325.
269. Rao, M.J. and S.S. Cao, *Artificial total disc replacement versus fusion for lumbar degenerative disc disease: a meta-analysis of randomized controlled trials.* Arch Orthop Trauma Surg, 2014. **134**(2): p. 149-58.
270. Yajun, W., et al., *A meta-analysis of artificial total disc replacement versus fusion for lumbar degenerative disc disease.* European spine journal : official publication of the European Spine Society, the European Spinal Deformity Society, and the European Section of the Cervical Spine Research Society, 2010. **19**(8): p. 1250-1261.
271. Cui, X.D., et al., *Mid- to long-term results of total disc replacement for lumbar degenerative disc disease: a systematic review.* J Orthop Surg Res, 2018. **13**(1): p. 326.
272. Gornet, M.F., et al., *Lumbar Disc Arthroplasty With MAVERICK Disc Versus Stand-Alone Interbody Fusion: A Prospective, Randomized, Controlled, Multicenter Investigational Device Exemption Trial.* Spine, 2011. **36**(25): p. E1600-E1611.
273. Guyer, R.D., et al., *Prospective, randomized, multicenter Food and Drug Administration investigational device exemption study of lumbar total disc replacement with the CHARITÉ artificial disc versus lumbar fusion: Five-year follow-up.* The Spine Journal, 2009. **9**(5): p. 374-386.
274. Zigler, J., et al., *Comparison of Lumbar Total Disc Replacement With Surgical Spinal Fusion for the Treatment of Single-Level Degenerative Disc Disease: A*

Meta-Analysis of 5-Year Outcomes From Randomized Controlled Trials. Global Spine J, 2018. **8**(4): p. 413-423.
275. Bai, J.Z., et al., *Studies of xi (2230) in J/ psi radiative decays.* Phys Rev Lett, 1996. **76**(19): p. 3502-3505.
276. Green, T.R., et al., *Polyethylene particles of a 'critical size' are necessary for the induction of cytokines by macrophages in vitro.* Biomaterials, 1998. **19**(24): p. 2297-302.
277. Namchaiw, P., et al., *An in vitro workflow of neuron-laden agarose-laminin hydrogel for studying small molecule-induced amyloidogenic condition.* PLoS One, 2022. **17**(8): p. e0273458.
278. Rad, M.A., et al., *Micromechanical characterisation of 3D bioprinted neural cell models using Brillouin microspectroscopy.* Bioprinting, 2022. **25**: p. e00179.
279. Orr, M.B. and J.C. Gensel, *Spinal Cord Injury Scarring and Inflammation: Therapies Targeting Glial and Inflammatory Responses.* Neurotherapeutics, 2018. **15**(3): p. 541-553.
280. Du, Z., Z. Zhu, and Y. Wang, *The degree of peri-implant osteolysis induced by PEEK, CoCrMo, and HXLPE wear particles: a study based on a porous Ti6Al4V implant in a rabbit model.* Journal of Orthopaedic Surgery and Research, 2018. **13**(1): p. 23.
281. Hallab, N.J., et al., *Macrophage reactivity to different polymers demonstrates particle size- and material-specific reactivity: PEEK-OPTIMA(®) particles versus UHMWPE particles in the submicron, micron, and 10 micron size ranges.* J Biomed Mater Res B Appl Biomater, 2012. **100**(2): p. 480-92.
282. Germain, M.A., et al., *Comparison of the cytotoxicity of clinically relevant cobalt-chromium and alumina ceramic wear particles in vitro.* Biomaterials, 2003. **24**(3): p. 469-79.
283. Weng, T., et al., *3D bioprinting for skin tissue engineering: Current status and perspectives.* J Tissue Eng, 2021. **12**: p. 20417314211028574.
284. Hallab, N.J., Q.B. Bao, and T. Brown, *Assessment of epidural versus intradiscal biocompatibility of PEEK implant debris: an in vivo rabbit model.* Eur Spine J, 2013. **22**(12): p. 2740-51.
285. Fisher, J., et al., *Tribology of alternative bearings.* Clin Orthop Relat Res, 2006. **453**: p. 25-34.
286. Kölle, L., et al., *Ceramics in total disc replacements: A scoping review.* Clinical Biomechanics, 2022. **100**: p. 105796.
287. Welfare, A.I.o.H.a., *Back problems.* 2020.
288. Health, A.I.o. and Welfare, *Impacts of chronic back problems*. 2016, AIHW: Canberra.
289. Smith, R.A., A. Maghsoodpour, and N.J. Hallab, *In vivo response to cross-linked polyethylene and polycarbonate-urethane particles.* 2010. **93A**(1): p. 227-234.
290. Faye, P.A., et al., *Engulfment of ceramic particles by fibroblasts does not alter cell behavior.* Biomed Mater, 2017. **12**(1): p. 015023.
291. Tsaousi, A., E. Jones, and C.P. Case, *The in vitro genotoxicity of orthopaedic ceramic (Al2O3) and metal (CoCr alloy) particles.* Mutat Res, 2010. **697**(1-2): p. 1-9.
292. Gómez-Arnaiz, S., R.J. Tate, and M.H. Grant, *Cytotoxicity of cobalt chloride in brain cell lines - a comparison between astrocytoma and neuroblastoma cells.* Toxicology in Vitro, 2020. **68**: p. 104958.

293. Kandel, S., et al., *An automated system for polymer wear debris analysis in total disc arthroplasty using convolution neural network.* 2023. **11**.